UNIVERSITAT DE BARCELONA

Making the most of imaging and spectroscopy in TEM: computer simulations for materials science problems

Catalina Coll Benejam

PhD Thesis

Making the most of imaging and spectroscopy in TEM: computer simulations for materials science problems

Catalina Coll Benejam

UNIVERSITAT DE BARCELONA

Making the most of imaging and spectroscopy in TEM: computer simulations for materials science problems

Programa de doctorat en Física

Catalina Coll Benejam

Directores:
Francesca Peiró Martinez
Sònia Estradé Albiol

Tutor:
Blas Garrido Fernández

UNIVERSITAT DE BARCELONA

A tu, que seràs sa següent.

Acknowledgements

Ha estat llarg, molt llarg, massa llarg, però aquí la tinc. Per fi però, no ho repetiria mai més de la vida. Si esteu llegint això vol dir que em coneixeu i sabeu que no ha estat gens fàcil. Tot s'hi ha posat un poc en contra: moltes beques rebutjades (per part meva), d'altres no concedides (per part seva), moments de pànic, moments de motivació, calendaris que mai s'han complert, renúncies, problemes burocràtics impossibles, auge i decadència independentista, una pandèmia mundial i una guerra (?). Però gràcies a una quantitat molt elevada de persones que ha anat apareixent, o simplement hi eren, ha estat possible. M'agradaria aprofitar aquesta ocasió per explicar unes quantes veritats.

Les més importants en tot aquest procés no poden ser altres que les meves "jefes" la Paqui i la Sònia. Elles, contràriament al que pensava la resta de professors, van creure que podia fer alguna cosa i que la podia fer bé. Quan em van oferir de fer una tesi amb elles, em va fer molta il·lusió i ,ara, no puc deixar d'agrair-los aquesta oportunitat. No només pel fet de ser o no ser doctora sinó per haver-me don't l'oportunitat d'involucrar-me en la comunitat científica i universitària. Ha estat un plaer. Ja sabeu com m'agrada estar en tot, m'ho he passat molt bé.

Formar part del LENS ha estat tot un honor. Tot i no haver format part del LENS original, he tingut el plaer de conèixer-los a tots i treballar amb ells: el Lluís Yedra, l'autèntic responsable de què jo descobrís la microscòpia, l'Alberto, qui em va fer un parell de "google it" molt durs, el Lluís López, qui sempre ha estat prop per resoldre els meus dubtes i ensenyar m'ho tot sobre estructures, el Josep, qui em va convèncer per fer doctorat (ironies de la vida), la Gemma, qui va fer tot el possible perquè anés a l'altra punta de món, i el Pau, qui més m'ha odiat i estimat. Però jo he format part del true-LENS juntament amb el Sergi, qui em resol les curiositats de cristal·lografia avançada, el Javi, qui m'ha avançat pel lateral amb un excel·lent "whateels", i el Dani, qui mai saps a quin planeta viu i segurament arribarà lluny. Finally, all the best for LENS-doubts, Bea and

Pranjal, I'm sure that you are the best future that LENS could have, ha sido un placer ayudaros en vuestros inicios.

El despatx patera potser algun dia passarà a ser una llegenda, però jo n'hauré format part. Allà he tingut la sort de treballar amb el Julià, l'Oriol, el Giovanni, el Sergio i el Juan, qui m'ha ensenyat que qualsevol cosa és realitzable amb solidworks i sempre té una abraçada disponible, i amb l'Adrià, qui m'ha ensenyat com fer-me Barcelona meva, merci A.

Pels estudiants, el departament d'electrònica és "el malo", però he comprovat que és tot el contrari. Ple de persones encantadores i essencials. M'agradaria agrair de manera especial a l'Albert Cornet i al Dani Prades, que van fer el possible perquè no em fessin fora del departament el primer dia, al Txema, que m'ha deixat controlar el campus d'informàtica, a la Roser, que ha estat essencial pels meus infinits viatges, i als informàtics, especialment a l'Àlex, per salvar-me en diverses ocasions.

La facultat, sens dubte, ha sigut casa meva gràcies a tenir-hi molt bons amics a qui sempre puc trucar per una birra o un cafè. Gràcies Javi, Pol i Joan, i totes les altres que heu passat per aquí, ja sabeu que sempre em podeu trucar.

He estat molt afortunada, ja que he tingut l'oportunitat de conèixer microscopistes de tot el món. Javi y Ramón os habéis encargado de que siempre tuviera ganas de Consoliders, MFS y otros eventos nacionales... y otros más exóticos y fríos, Nos volvemos a Canadá, Ramón? Isobel, Alex, Viktor, Gianluigi and all the others, thank you for welcoming me and helping me with my nanoparticles.

Durant el doctorat, Barcelona s'ha convertit un poc en ca meua, i perquè negar-ho, a Sant Andreu m'hi sent a casa. El principi va ser dur i no hauria estat possible sense l'Aula d'Estudi. Gràcies, Raúl per confiar en jo tot i no tenir cap referència, i a totes les famílies que heu anat confiant en mi, m'ho heu fet tot més fàcil. Però el que ho fa casa sempre és la gent, gràcies Dario, Iuri, Martí, gent des Ghetto i tota la gent que em somriu quan sent el meu accent.

Però Menorca és i serà sempre el més important, allà ho tenc tot. Sé que no té sentit per voltros res del que he fet, però tot així sempre m'animau a seguir. Gràcies a Ladies i ses noves mini incorporacions per donar més motius per acabar. Gràcies, Joan, Lluís, Iria, Tòfol, Maria per fer de

qualsevol celebració una tradició. Gràcies, Benejam's i gràcies, Coll's. Gràcies a ses àvies, a s'àvia Llucia que mai ha entès perquè estudiï física si soc tant patosa i que només vol que torni i a s'àvia Aguedita que s'ha encarregat que mai hi falti bon embotit menorquí a ca meua. Gràcies, papà i mamà per deixar-me partir quan tenia 18 anys a estudiar una carrera que clarament me faria mal. Heu confiat sempre en es fet que aconseguiria tot allò que començés; tot i així, voltros confiàveu en què tornés, esper que encara hi confieu.

Llucia, d'aquí res tu seràs doctora i escriuràs uns agraïments molt millors que es meus. Segurament, quasi et fa més il·lusió a tu que a jo, que sigui doctora, merci. T'estim little sister!

Charlie, tu sempre has confiat en jo, sorprenentment per una vegada tenies raó. Gràcies a tu, i a n'Ànec, per estar sempre aquí. No tothom té sa sort de compartir sa vida amb es seu millor amic i una tortuga. T'estim.

Al llarg d'aquests n anys he après moltes coses, respecte com fer/intentar/destruir/polir/acabar tesis doctorals, i una cosa està claríssima, qualsevol que l'obri/la descarregui farà el que sempre es fa, llegir els agraïments. Per altra banda, és una de les poques coses que em venia de gust escriure. Gràcies gent!

Barcelona, Març 2022

Table of contents

Acknowledgements ..... **i**

Table of contents ..... **v**

Chapter 1: Motivation and objectives **1**

1.1 Motivation **1**

1.2 Thesis objectives **6**

1.3 References **8**

Chapter 2: Introduction to computer simulations for TEM **9**

2.1 Multislice method **10**

2.1.1 Electron description 13

2.1.2 Thick specimens 14

2.1.3 Thin specimen approximation 16

2.1.4 Specimen potential 17

2.1.5 Applications: STEM/CTEM 18

2.1.6 Software 20

2.2 Density functional Theory **22**

2.2.1 Fundamentals of DFT 24

2.2.2 DFT algorithm 28

2.2.3 Periodic solids 29

2.2.4 DFT for EELS 34

2.3 Boundary Element Method **45**

2.3.1 Theoretical approximations 48

2.3.2 BEM: fundamentals 49

2.3.3 Dielectric function 52

2.3.4 Model construction 57

2.3.5 Simulating data from EELS experiments 58

2.4 References **60**

Chapter 3: GaInP: the effect of atomic ordering on the electronic configuration **71**

3.1 State of the art – Motivation **72**

3.2 Material and preliminary characterization **73**

3.3 Microscopic ordering assessment: phase and diffraction contrast imaging **75**

3.4 Z-constrast imaging 80
3.4.1 Planes alternation and dumbbells polarity 81
3.4.2 Ordered domains 81
3.4.3 HAADF image simulations 82
3.5 In situ measurements 85
3.6 Density Functional Theory calculations 86
3.6.1 Cell modelling and structure relaxation 87
3.6.2 Density of states: bandgap optimization 88
3.6.3 Optical properties: inter-band transitions 89
3.6.4 Effective mass and band structure 92
3.7 Conclusions 94
3.8 References 96

Chapter 4: Oxygen Vacancies in Bismuth Oxide 103
4.1 State of the art – Motivation 104
4.2 Material and preliminary characterization 106
4.3 TEM characterization 108
4.3.1 Electron Energy Loss Spectroscopy 111
4.4 DFT calculations of bismuth oxide 113
4.4.1 Density of states 114
4.4.2 Low loss EELS: phase identification 115
4.4.3 Core loss EELS: oxygen vacancies 116
4.5 Conclusions 123
4.6 References 125

Chapter 5: Understanding the Verwey transition 133
5.1 State of the art – Motivation 134
5.1.1 Material and preliminary characterization 136
5.2 TEM Characterization 138
5.2.1 In-situ cooling experiment 140
5.3 Structural analysis 143
5.4 Electron configuration: Density Functional Theory 145
5.4.1 Structural relaxation 145
5.4.2 Density of states 146
5.4.3 ELNES 150
5.5 Conclusions 158
5.6 References 160

Chapter 6: Plasmonic Nanoparticles: gold nanodomes 167
6.1 State of the art – Motivation 168

6.2 Material and preliminary characterization 169
6.3 Morphologic and structural characterization 170
6.3.1 Tomographic reconstruction 171
6.4 EELS analysis 172
6.5 BEM simulations for low loss EELS comparison 175
6.5.1 Isolated nanodomes models 177
6.5.2 Nanodome dimer model 180
6.6 Conclusions 183
6.7 References 185

Chapter 7: General conclusions 189

Appendix A: Acronyms and Abbreviations 193

Appendix B: Complementary information 197
B.1 Definitions and concepts 198
B.2 Crystallographic files 200
B.3 Space group list 202
B.4 References 203

Appendix C: Scientific Curriculum 205
C.1 Education 205
C.2 Grants awarded 205
C.3 Journal publications 205
C.4 Conference contributions 206
C.5 Research Stage 213
C.6 Workshops and schools 213
C.7 Supervision of research projects 214

Appendix D: Resum en català 215

Chapter 1: Motivation and objectives

1.1 Motivation

Transmission Electron Microscopy (TEM), since its first implementation by Ernst August Friedrich Ruska and Max Knoll in 1931, has been an essential technique in the nanoscience and nanotechnology field. In the beginning, the real resolution was just a small fraction of the potential resolution expected by the fact of using electrons as a "light" source. The wavelength of the electrons accelerated at hundreds of electronvolts would, theoretically, involve a subatomic resolution; however, the aberrations related to electromagnetic lenses caused a dramatic resolution decrease. In addition, the energy resolution was highly affected by the chromatic aberration of the electron beam. Nowadays, all these initial problems have been solved by the development of image aberration correctors and monochromators. Since atomic resolution together with 10 meV energy resolution, are a reality for researchers, new and higher horizons have been set for transmission electron microscopy, such as orbital imaging[1], phonon imaging[2], or real time atom monitoring[3] amongst others. TEM could be described at its most fundamental as the analysis of the result of impacting electrons with a specific compound or structure[4], as schematized on Figure 1.1. From this impact, different data can be obtained which can be rapidly classified between imaging and spectroscopy.

Three main operation modes produce as a result an image: phase contrast, Z-contrast and diffraction contrast. The first one, phase contrast mode, collects the image generated by the interference of the diffracted beams produced by the interaction of the parallel electron beam with the crystalline sample due to elastic scattering with the sample. The most common type of image generated is the High Resolution TEM (HRTEM) image. In the second one, Z-contrast mode, the image is generated by the incidence of a highly focused electron beam on the sample and the collection of the scattered electrons by an annular detector; the intensity in each pixel of the final image is roughly proportional to the square of the atomic number of the atoms present as the beam scans the sample. The Annular Dark Field

(ADF) and High-Angle Annular Dark-Field (HAADF), depending on the angle of the detector, images are the usual Z-contrast images. On the other hand, the diffraction contrast images are the ones whose contrast is highly dependent on the specific crystallographic orientation and specific diffraction spot selected by a small aperture; the most common ones are the Bright Field (BF) and the Dark Field (DF) images, depending on whether they include (BF) or not (DF) the direct beam; however, more specific configurations can be used like two-beam conditions when just one reflection is considered.

Regarding spectroscopies in the TEM, even if several detectors can be installed in the column to carry out Energy Dispersive X-ray (EDX) or Cathodoluminescence (CL) analysis, Electron Energy Loss Spectroscopy (EELS) is the spectral technique with better energy and spatial resolution which can be performed inside the TEM column[5]. EELS consists in analyzing the number of electrons that have lost a given amount of energy, the number of electrons per energy channel. Once the sample is irradiated with the electron beam, most of the electrons go through it without losing energy, originating the Zero-Loss Peak (ZLP), but the others have lost part of their energy. Thus, EELS is strongly correlated with the electrons which

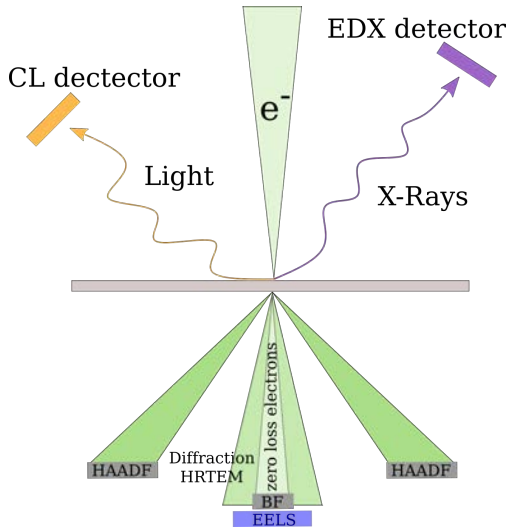

Figure 1.1 Scheme of basic signals upon electron-matter interaction.

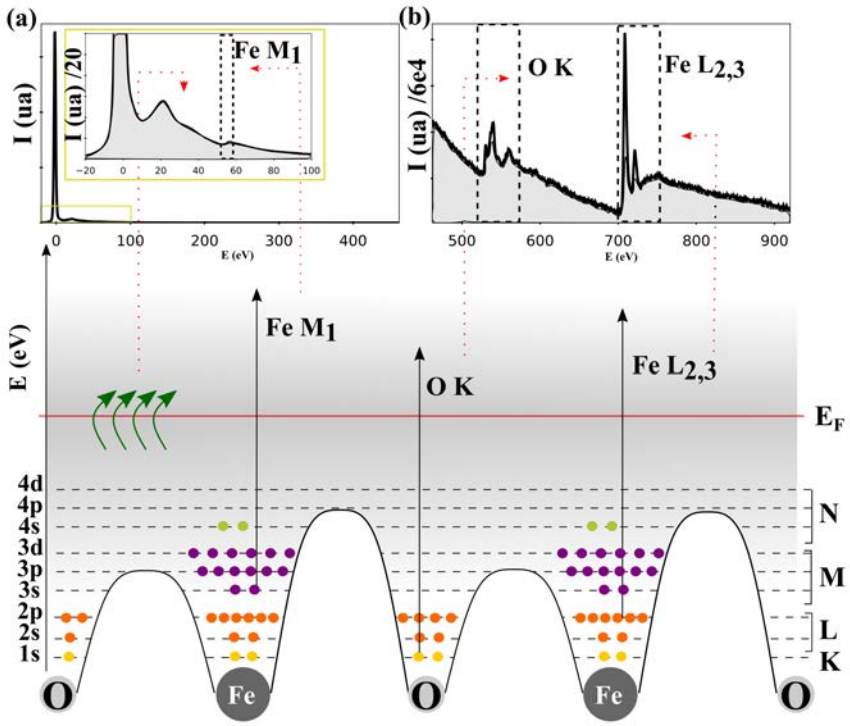

Figure 1.2 EELS Spectrum: the different regions of the spectrum are displayed at the top: the low loss (a) and the core loss (b). At the bottom the electron subshell distribution of an idealistic Fe-O compound is shown. In low loss the ZLP and the bulk plasmon appear at lower energy; the M_1 of Fe at 54 eV is related with the 3s electrons. (b) The core loss zooming in the intensity axis highlights the O K (532 eV) and the Fe $L_{3,2}$ (708 eV) transitions.

have suffered inelastic scattering; however, it is not fully independent of the elastic scattering.

The EEL spectrum covers the whole range of energy losses, from 0 eV to thousands of electronvolts. Depending on the range of energy the low loss and the core loss regimes can be distinguished; as can be easily understood, the low loss corresponds to the low energy losses, from zero to around 80 eV, and the core loss to the rest of the spectrum. Nevertheless, the difference between low and core loss lies in the information they contain; at low energies the inelastic scattering of the outer-shell electrons is the main contribution, while at higher energy losses their contribution decreases, and the ionization edges of the inner-shell electrons appear as the most striking

features. The ionization edges are a fingerprint of the elements present in the analyzed sample and the Electron Energy Loss Near Edge Structure (ELNES) contains the information corresponding to the oxidation state and the orbital configuration, which means that the analysis of the fine structure found after the onset of the edge is very important. Figure 1.2 summarizes the information in an EEL spectrum, which is divided into the low loss and core loss regions. The presented EELS spectrum corresponds to an idealized iron oxide; the direct relation between the spectrum and the density of states is also shown at the bottom, where the outer-shell electrons are highlighted in green, and the rest of electronic states are also seen in a simplified scheme as the splitting has not been considered; (a) corresponds to the low loss spectrum where the ZLP is the main feature, zooming in the first hundreds of electronvolts, the bulk plasmon can be distinguished, a $M_{2,3}$ edge of iron, corresponding to the ionization of electrons at M shell (n = 3), can be seen at 54 eV. (b) panel, rescaling the intensity axis, shows the core loss spectrum with the K edge of the oxygen (n=1) and the $L_{3,2}$ of the iron (n = 2).

With the recent increases in energy and spatial resolution, a huge amount of information can be directly extracted from very large experimental datasets; however, for a deeper understanding, most of the times the support from theoretical calculations is also needed[6,7]. Solid state physics with quantum considerations can contribute to an accurate description of the studied systems.

Whereas in the past materials science, solid state physics, quantum mechanics and chemistry were considered as separated disciplines, nowadays they merge in the field of nanoscience and nanotechnology. When the object size is reduced to the nanoscale the quantum effects cannot be neglected anymore, any change on the synthesis can in turn change the structure which plays an essential role on the compound properties[8].

Thus, modelling has become an essential step in the materials synthesis and characterization. The knowledge of the structure allows to compute the interaction of the electrons with any well described crystalline structure and generate images and spectra comparable with experimental data, not just as a check, but to gain deeper insight. The interaction of the electrons with matter must be computed by solving the Schrödinger equation of the

electrons interacting with the sample[9–11]. The sample, the system, can be considered as a periodic potential.

Imaging, measuring, modelling and manipulating matter are the basis of the promising field of nanoscience, and they can be carried out using a TEM, with the continuous support of theoretical calculations to obtain the most.

The present Thesis uses three main types of calculations to interpret TEM data: atomic simulations applied to imaging, Boundary Element Method (BEM) based calculations for surface plasmon distributions and Density Functional Theory (DFT) for EELS analysis. Even if they will be presented separately, they are not independent; the essence is always the same but depending on the desired results different considerations are needed.

Atomic simulations appear as a solution to obtain images comparable with the TEM data. In atomic simulations the sample is modelized as a periodic potential determined by the atomic potential of each element in the sample, computed by ab-initio calculations. The results are obtained by the interaction between the electrons, considered as a plane wave, and sample periodic potential. Multislice is the most used method to simplify the problem.

DFT based calculations are the most used ones when solving a many bodies problem. DFT simplifies the problem by finding the electron density of the whole system instead of working with each electron individually. Then, once the electron density is found, the electronic structure of the compound is directly obtained, and the optoelectronic properties can be computed for comparison with experimental data. Thus, the theoretical calculations allow to go deeper in the electronic configuration besides generating reference data to be compared with the experimental one.

BEM, instead of considering the sample as an atomic arrangement, defines boundaries according to the nanoobject which plasmonic response needs to be studied. By using the dielectric function of the different materials involved, obtained from DFT or experimentally, the model is fully defined. The plasmonic response is found by solving the Maxwell equations of the defined system.

Nevertheless, the essential logic of all of them is the same, the "sample" (the compound of interest) is modelized using atomic arrangement or boundary descriptions, the electron beam is described according to the experimental conditions in which the experiment has been performed and, finally, the physics of the many-body problem is introduced. The observable to be simulated will determine the accuracy in the formulation of the calculations.

1.2 Thesis objectives

The main goal of the present PhD Thesis is to complement the analysis of experimental TEM data with opportune computer simulations enabling the rationalization of some material science unknowns. In this sense, the objectives of the Thesis are the following:

- **Reviewing the simulation methods to be used for TEM data.** The fundamentals of the three types of calculations used in this Thesis, namely, multislice, density functional theory and boundary element method, for TEM images, EEL spectra and plasmon EELS analysis, respectively, will be discussed in detail. (Chapter 2)

- **Assessment of the $CuPt_B$ ordering effects on GaInP by TEM complemented with first principles calculations.** The second objective is addressing the physical implications of the $CuPt_B$ ordering in GaInP thin films using experimental TEM complemented with image simulations and DFT calculations. This includes the whole study of the ordering, from an understanding of the contrast modulations arising from the order, by imaging, to the electronic configuration of the ordered phase and the effects of ordering anisotropy using First Principles calculations. (Chapter 3)

- **Use of DFT calculations for the determination of oxygen vacancies in Bi_2O_3 using EELS data.** This

objective comprehends the whole modelling of the O K edge of α-Bi_2O_3 by DFT simulations with a two-fold aim: on one hand, understanding the physical effect of the oxygen vacancies on the O K, and, on the other hand, obtaining spectra that can be used as references for the compound with and without O vacancies, as there are none reported. (Chapter 4)

- **Study of the Verwey transition from the EELS Fe L_3 edge analysis.** This objective focuses on an in-depth study of the effects of the magnetite structure distortion, due to the Verwey transition, using DFT, and, from this, to determine the fingerprint of the Verwey transition in the Fe L_3 ELNES. (Chapter 5)

- **Modelling of the plasmonic response of gold nanodomes using BEM calculations.** The last objective is centred on unveiling the origin of low loss EELS features of exotic nanoobjects, namely, gold nanodomes. As it is observed experimentally, the plasmonic response is strongly size- and shape- dependent; thus, the goal is to get the best approximation of the actual size and shape of the nanobjects enabling an accurate plasmonic response simulation in correlation with the experimental measurements, with the aim to gain control on the design of nanoplasmonic entities with specific optical properties. (Chapter 6)

1.3 References

[1] L. Pardini, S. Löffler, G. Biddau, R. Hambach, U. Kaiser, C. Draxl, P. Schattschneider, Mapping Atomic Orbitals with the Transmission Electron Microscope: Images of Defective Graphene Predicted from First-Principles Theory, (2016). https://doi.org/10.1103/PhysRevLett.117.036801.

[2] R. Qi, N. Li, J. Du, R. Shi, Y. Huang, X. Yang, L. Liu, Z. Xu, Q. Dai, D. Yu, P. Gao, Four-dimensional vibrational spectroscopy for nanoscale mapping of phonon dispersion in BN nanotubes, Nature Communications. 12 (2021). https://doi.org/10.1038/s41467-021-21452-5.

[3] R. Manzorro, Y. Xu, J. Vincent, R. Rivera, D. Matteson, P. Crozier, Atom Detection in Time-resolved TEM Image Series: Application of Computer Vision Techniques to Noise-degraded Frames, Microsc. Microanal. 27 (2021). https://doi.org/10.1017/S1431927621008011.

[4] D.B. Williams, C.B. Carter, Transmission Electron Microscopy, 2012. https://doi.org/10.1007/978-1-61779-415-5_23.

[5] R.F. Egerton, Electron Energy-Loss Spectroscopy in the Electron Microscope, Springer US, 2011. https://doi.org/10.1007/978-1-4419-9583-4.

[6] P.E. Batson, N. Dellby, O.L. Krivanek, Sub-angstrom resolution using aberration corrected electron optics, Nature. 418 (2002) 617–620. https://doi.org/10.1093/oxfordjournals.jmicro.a050032.

[7] M. Haider, S. Uhlemann, E. Schwan, H. Rose, B. Kabius, K. Urban, Electron microscopy image enhanced, Nature. 392 (1998) 768–769.

[8] R.P. Feynman, There's Plenty of Room at the Bottom, XXIII (1960).

[9] J.G. Lee, Computational Materials Science, 2017. https://doi.org/10.1016/s1380-7323(04)80014-1.

[10] E.J. Kirkland, Computation in electron microscopy, Acta Crystallographica Section A: Foundations and Advances. 72 (2016) 1–27. https://doi.org/10.1107/S205327331501757X.

[11] E. Aharon-Shalom, a. Heller, Computation of Transmission Electron Micrographs, 1982. http://scholar.google.com/scholar?hl=en&btnG=Search&q=intitle:No+Title#0.

Chapter 2: Introduction to computer simulations for TEM

This chapter is devoted to present and explain all the fundamentals needed to understand how and why computer simulations can be used to complement experimental transmission electron microscopy. The chapter is divided into three big sections which have been ordered considering the complexity of the physics used in it and the Transmission Electron Microscopy (TEM) technique that they complement. First multislice calculations to generate TEM images are presented, then, the density functional theory calculations are introduced to obtain electron energy loss spectra from which the computed electron density will be computed and, finally, the boundary element method is explained as a tool to compute low loss electron energy loss spectroscopy of specific nanoobjects.

2.1 Multislice method

Image simulations, also called atomic simulations, consider, a priori, the elastic scattering of the electrons with the specimen. As happens inside the Transmission Electron Microscope (TEM) column, the electrons impact with the specimen, thin enough, and go all through the sample and contribute to the image formation. Thus, since the thickness of the specimen will not be smaller than 10 Å, most of the electrons will suffer plural scattering. Therefore, the kinematic scattering theory will not be enough to describe the electron behavior and dynamic scattering has to be taken into account.

The dynamic scattering was treated for the first time by Bethe in 1928[1], when describing the electron diffraction. He proposed to solve the Schrödinger equation by considering the Bloch waves, periodic wave functions with the periodic information of the sample. That solution fulfilled all the requirements and was able to describe the three-dimensional electron wave function for a periodic crystal. Since the first introduction on electron diffraction, it was applied to describe different electron related phenomena, such as reciprocal space or scanning TEM (STEM) microscopy.

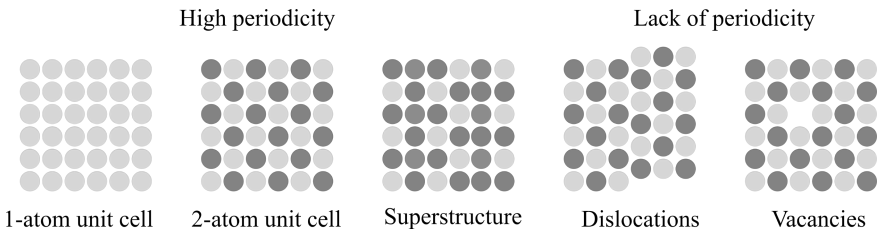

Figure 2.1 2D idealistic crystal with defects that produce a lack of periodicity.

Despite the good results obtained with the Bloch wave method there was a main drawback which made it necessary to look for better points of view. The Bloch wave calculations lose their efficiency if the studied systems have more than a few atoms, meaning that it is not possible to treat non-perfectly symmetric compounds. Once the studied system presents defects or extra periodicities (Figure 2.1), it cannot be described with the small high symmetry unit cell used to describe the bulk materials and new

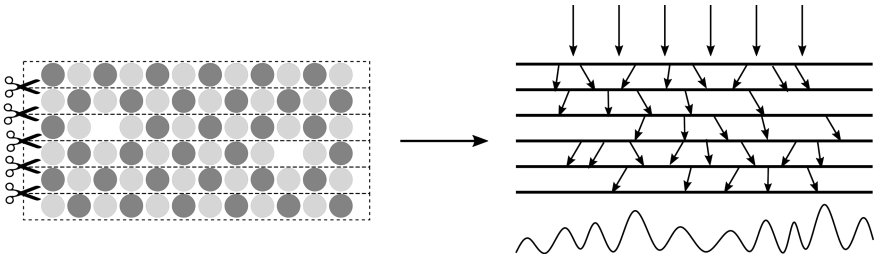

Figure 2.2 Multislice approach: cut the sample into slices which can be considered thin specimens and propagate the wave function through them.

conventional structures with more atoms should be considered to describe the system.

Multislice method emerges as an alternative to the Bloch method, as it can be more efficient. It was developed, mainly, by Cowley and Moodie. It treats the dynamic scattering with a physical optics point of view[2]. The electron wave is transmitted to a specimen which is cut into thin-enough slices and, thus, the transmitted wave is propagated to the next slice by Fresnel diffraction (Figure 2.2). This method was quickly numerically implemented and tested with good results for the interpretation of High Resolution TEM (HRTEM) images. In addition, to improve the efficiency, the calculation of the transmission and propagation was done by Fast Fourier transform (FFT), and the computational time was considerably reduced. Since 1957, when it was introduced for the first time, several improvements and extra considerations have been added by the community, like introducing the thermal diffuse scattering or taking into account the relativistic effects[3].

In this section the multislice method will be explained from the fundamental point of view; for that, the needed approximations and considerations will be presented and then the whole algorithm will be explained. To conclude, the available applications and code-packages will be summarized.

Considerations

Several considerations and approximations must be done to describe properly the electron-matter interaction.

- Non-relativistic Schrödinger equation: For transmission electron microscopy, the electrons are usually accelerated at

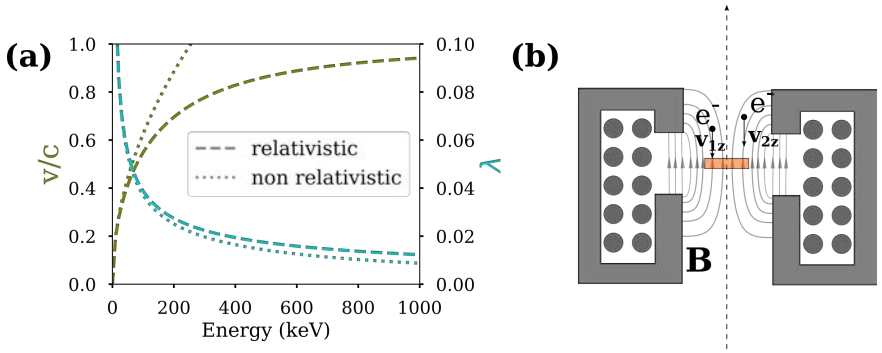

Figure 2.3 (a)Comparison between the velocity (green) and the wavelength (cyan) of the electrons computed in a relativistic (dashed line) and non-relativistic (dotted line) way. (b) Objective lens magnetic field.

hundreds of keV, thus, a priori, they would need a relativistic description. However, it has been demonstrated that, if the non-relativistic Schrödinger equation is solved considering the relativistic mass and wavelength for the electrons, a good approximation is reached for energies lower than 100 keV[4]. The validity of this assumption is illustrated in Figure 2.3(a) where the calculation of electron speed and wavelength considering relativistic or non-relativistic theory are compared. Whereas the relativistic correction is relevant for the speed, for voltages higher than 100 keV, it is not so significant for the wavelength. Furthermore, the electrons can be considered to fulfil the non-relativistic Schrödinger equation as the difference will be compensated when all the microscope aberrations and lenses are considered.

- Z movement: Inside the column, the specimen is placed just in the objective lens, which generates a magnetic field of about 1 T focused the electrons on the focal plane. Consequently, at the specimen plane, the magnetic field is, mainly, perpendicular to it and the electrostatic interaction is important only in the z direction. Thus, the magnetic forces on the other directions can be neglected (Figure 2.3(b)). From the same argument it can be deduced that the main component of the electron velocity would be the one parallel to the optic axis of the microscope, it is, the z component.

2.1.1 Electron description

Inside the TEM column the electrons travel at high speed, thus, they are considered fast electrons. Despite the fact that the time dependent Schrödinger equation would reach an exact solution as it describes the movement of charged particles moving fast, it involves a computing complexity that should be avoided. Instead, the time independent Schrödinger equation could be used as, for most of the cases, TEM images can be considered stationary.

Thus, the travelling electrons can be described by the time independent non-relativistic Schrödinger equation and their movement is mainly considered along the z direction.

If the Schrödinger equation is approximated for fast electrons the main consideration is that the speed in the z direction is the main contribution to the kinetic energy of the electrons.

Thus, taking into account the approximations, the wave function of the electrons can be expressed as the product of a plane wave on the tree-dimensions and the contribution of kinetic energy in the z direction included in the exponential term.

$$\psi_f(x,y,z) = \psi(x,y,z)\exp\left(\frac{2\pi i z}{\lambda}\right) \tag{1}$$

With that, the small perturbations are defined by the plane wave while the acceleration voltage, the electron wavelength, determines the z movement by the exponential term.

Finally, the Schrödinger equation can be written in a differential form as

$$\frac{\partial \psi_f(x,y,z)}{\partial z} = \left[\frac{i\lambda}{4\pi}\nabla_{xy}^2 + i\sigma V(x,y,z)\right]\psi\,(x,y,z) \tag{2}$$

where $\sigma = \frac{2me\lambda}{4\pi\hbar^2}$ is the interaction parameter and $V(x,y,z)$ is the atomic potential.

Bloch waves solution

By using Bloch waves the solution for the Schrödinger equation for a periodic crystal can be expressed as a linear combination of the Bloch waves:

$$\psi(\vec{r}) = \sum_j \alpha_j\, b_j\left(\mathbf{k_j}, \mathbf{r}\right) \tag{3}$$

Where α_j are the linear coefficients and $b_j(\mathbf{k_j}, \mathbf{r})$ is the Bloch wave that describes the periodic specimen, j is the summation for all the atoms. Thus,

$$\left[-\frac{\hbar^2}{2m}\nabla^2 - e\,V(x,y,z)\right] b_j(\mathbf{k_j}, \mathbf{r}) = E\; b_j(\mathbf{k_j}, \mathbf{r}) \quad (4)$$

with m as the relativistic mass of the electron, e the electron charge, $V(x,y,z)$ the potential of the specimen and E the total energy of the electron, which will remain constant as elastic scattering is assumed.

From that, and assuming the previous considerations about the electron's movement, the Bloch waves can be expressed as

$$b_j(\mathbf{k_j}, \mathbf{r}) = \exp(2\pi i\ \mathbf{k_j}\ \mathbf{r}) \sum_G C_{G_j} \exp(2\pi i\ \mathbf{G}\,\mathbf{r}) = \sum_G C_{G_j} \exp(2\pi i(\mathbf{k_j} + \mathbf{G})\ \mathbf{r}) \quad (5)$$

Where $\mathbf{G} = \left(\frac{h}{a}, \frac{k}{b}, \frac{l}{c}\right)$ corresponds to the reciprocal lattice vector. Just one solution exists for the coefficients as they take into account the periodicity of the specimen and fit with the incident plane wave.

The Bloch wave algorithm can be summarized in the following summarized in Figure 2.4:

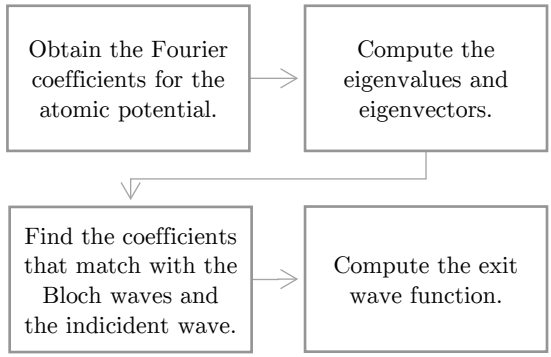

Figure 2.4 Summary of the Bloch wave algorithm.

Keeping in mind that the process must consider every position in the sample, the computational time increases proportional to N^3, with N being the number of atoms. If the symmetry is taken into account, fewer positions have to be considered, however this is a limitation to treat compounds with defects, for instance.

2.1.2 Thick specimens

The multislice simulation method is based on cutting the specimen into slices and transmitting the electron wave through all of them (Figure 2.2).

The solution for this process could be achived by obtaining the transmitted function for every Δz. Starting from the differential electron wave, integrating it for the specimen thickness (z) and expressing it as a function of Δz, with some rewriting the following expression is obtained:

$$\psi\,(x,y,z+\Delta z) = \left\{\exp\left[\frac{i\lambda}{4\pi}\,\Delta z\,\nabla^2_{xy}\right]\exp[i\sigma v_{\Delta z}(x,y,z)]\right\}\psi\,(x,y,z) + \vartheta(\Delta z^2) \quad (6)$$

From the electron wave function, two main components can be distinguished: the propagation function $\exp\left[\frac{i\lambda}{4\pi}\,\Delta z\,\nabla^2_{xy}\right]$ and the transmission function $\exp[i\sigma v_{\Delta z}(x,y,z)]$, from now on $p(x,y,z)$ and $t(x,y,z)$, respectively. The final term $\vartheta(\Delta z^2)$ represents the error associated to the approximation which is proportional to the square of the slice thickness.

The expression can be rewritten in the following way:

$$\psi\,(x,y,z+\Delta z) = p(x,y,z) \otimes [t(x,y,z)\psi\,(x,y,z)] + \vartheta(\Delta z^2) \quad (7)$$

For the numerical implementation of multislice the specimen will be sampled, and the electron function computed for each pixel. In addition, to

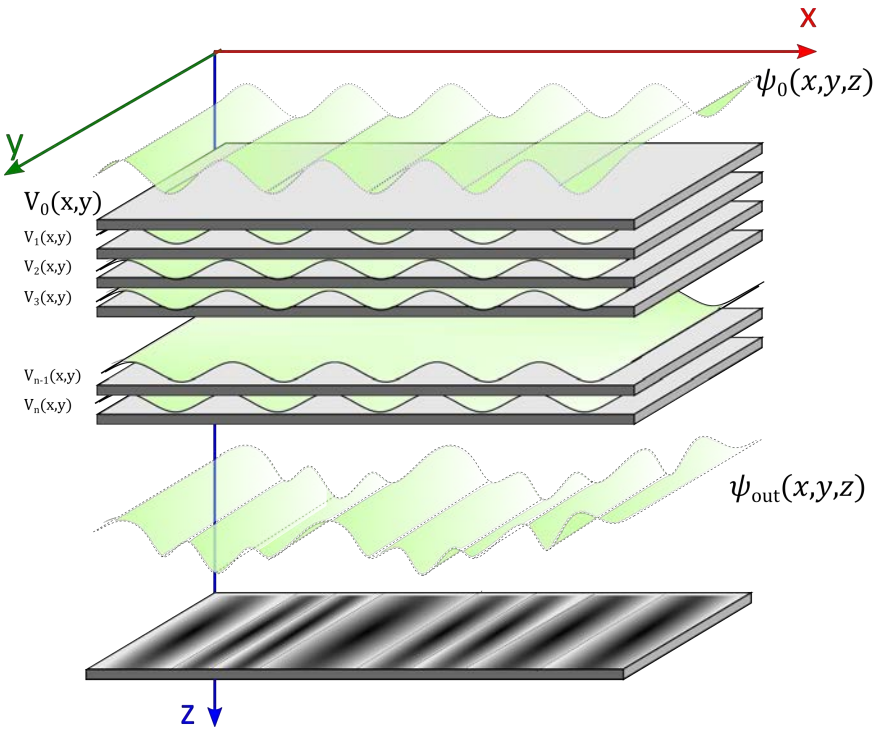

Figure 2.5 Multislice approach scheme.

calculated the convolution product in a more efficient way, it is computed in the Fourier space.

In summary, multislice starts from an electron wave which is determined by the wavelength of the electrons, the acceleration voltage, and the potential which describes the periodicity of the sample for each position (pixel); from that, the transmission function (p) is computed and propagated to the next slice (t) through Fresnel diffraction. This procedure is repeated for all the slices, until the specimen thickness is reached. The final result is the exit wave function for each position. The whole procedure is illustrated in Figure 2.5 and summarized in Figure 2.6.

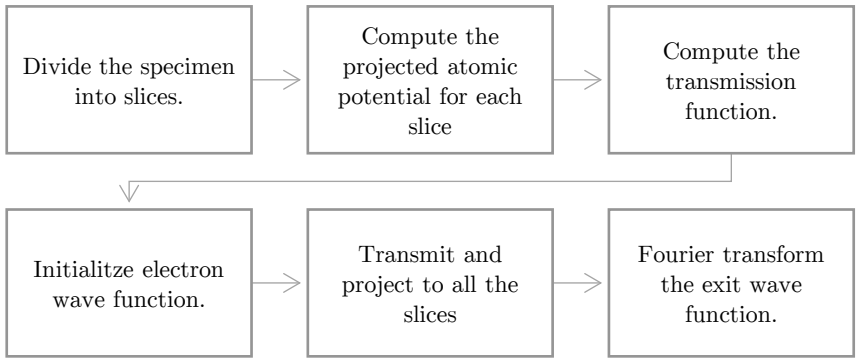

Figure 2.6 Workflow of the multislice algorithm.

2.1.3 Thin specimen approximation

Until this point, a description of the interaction of the whole sample with the electron beam has been done. However, it is important to analyze in more detail what happens to each of these thin slices.

For each slice, the specimen can be considered as a 2D object, meaning that the thickness is neglected, and this is known as thin specimen approximation. Because of the effect that the atomic potential has on the incident wave, this approximation can be called kinematic or phase grating. As before, the non-relativistic Schrödinger equation can be used, assuming the accelerating voltage is around 100 keV, to simplify the calculations.

To define the interaction between the electron beam and the specimen, the incident beam is considered a wave function of one plane wave travelling along the z direction with a specific relativistic wavelength (λ).

$$\psi_0\,(\mathrm{x}) = \exp(2\pi i\, k_z z) = \exp(2\pi i z/\lambda) \tag{8}$$

The initial wave function travels into the vacuum, until it reaches the specimen, which has a specific potential defining uniquely all the atomic positions and their composition (V_s). The presence of the atomic potential induces a change on the electron wavelength. Depending on the sign of the potential in each position, the change involves an increase or a decrease of its wavelength. Thus, while the electron is crossing the specimen the wave functions can be represented by the following expression:

$$\psi_s\,(\mathrm{x}) = \exp(2\pi i\, k_z z)\exp(i\sigma V_s z) \tag{9}$$

where σ is the interaction parameter, with m as the relativistic mass. The interaction parameter presents hyperbolic behaviour with the kinetic energy, with an almost constant region from 300 keV on.

Thus, if the specimen is thin enough the specimen acts as a weak phase object and the out-wave function can be expressed as the incident one times the atomic potential term, which can be called transmission function, $t(x) = \exp(i\sigma V_s z)$.

Summing up, the thin specimen approximation can be used directly to one slice transmission of the multislice problem. In multislice, this procedure is repeated as many times as necessary to define the whole thickness, as has been explained before.

2.1.4 Specimen potential

The definition of the specimen potential is the key point of the calculations, as the potential and charge distribution for atomic position has to be given. In order to reduce the complexity of the problem, instead of computing the potential for the whole specimen, the specimen is considered as a periodic distribution of atoms, from which the potential and charge distribution are computed. Thus, the atoms are considered single and isolated.

Starting from single isolated atoms the charge and potential distribution has to be computed using first principles calculations, as it is described in depth in the DFT section. The most precise method is the Hartree-Fock

approximation. However, the exact solution is just feasible for low Z-elements, because, as the number of electrons increases, the problem quickly increases its complexity and, for simplicity, instead of the electrons the orbitals are considered.

From the single atom description, the total potential of the specimen can be defined as the linear superposition of all the individual projected potentials ($v_{z_j}(\mathbf{x})$) considering all the atomic positions (x_i, y_i).

$$v_z(\mathbf{x}) = \sum_{j=1}^{N} v_{zj}(\mathbf{x} - \mathbf{x_j}) \tag{10}$$

This description has a main lack, because the bonds between the atoms are not considered whereas these bonds are essential for the description of the scattering. The scattering factors have to be also accounted for. The scattering factors represent the amplitude of scattering of each single atom, and, as always, there are different approximations to compute them with an increasing degree of complexity. The simplest but functional way is the first-order Born approximation, but they can be obtained from first principle calculations[5]. For image simulation the first-order Born approximation is considered enough for most cases.

From here, the projected potential is obtained by integrating the specimen potential of each slice between z and Δz.

2.1.5 Applications: STEM/CTEM

The fundamentals of multislice calculations have been explained. However, as mentioned in the introduction, using multislice different results can be obtained. Depending on the final result expected, some considerations will be taken into account. Here we will distinguish between the Conventional Transmission Electron Microscope (CTEM) mode, also referred as HRTEM, and the STEM mode. The simplified scheme of both operation modes can be seen in Figure 2.7; on both, the sample/specimen is represented by the orange-coloured rectangle and the apertures are represented in gray. In the HRTEM mode (left) the image is formed by the interference of the diffracted beams on the imaging plane. In the STEM mode the sample is scanned by a highly focused beam and then the elastic

scattering information is collected on the High-Angle Annular Dark-Field (HAADF) detector (pink).

For this kind of simulations, the input consists of the atomic position of all the atoms of a periodic structure. Thus, if the sample of interest does not have any defect, the whole crystal can be obtained by replication of the unit cell; however, if the objective is to obtain the image of interfaces, boundaries or 3D shapes, bigger models must be created.

Therefore, moving to the computer implementation, the main difference is the way by which the electron wave - sample interaction is described; in the HRTEM/CTEM mode the wave function encounters the whole atomic potential, and this interaction will be computed at each point. In the STEM mode a wave function will interact with each point of the sample, so j wave functions/probes will be considered, where j are the specimen scanned points. In a more technical description, for the HRTEM simulations the desired number of pixels of the final image will be the ones discretized on the incident wave function, while for the STEM mode a number of pixels will be chosen for the probe, another one for the sample and a third one for

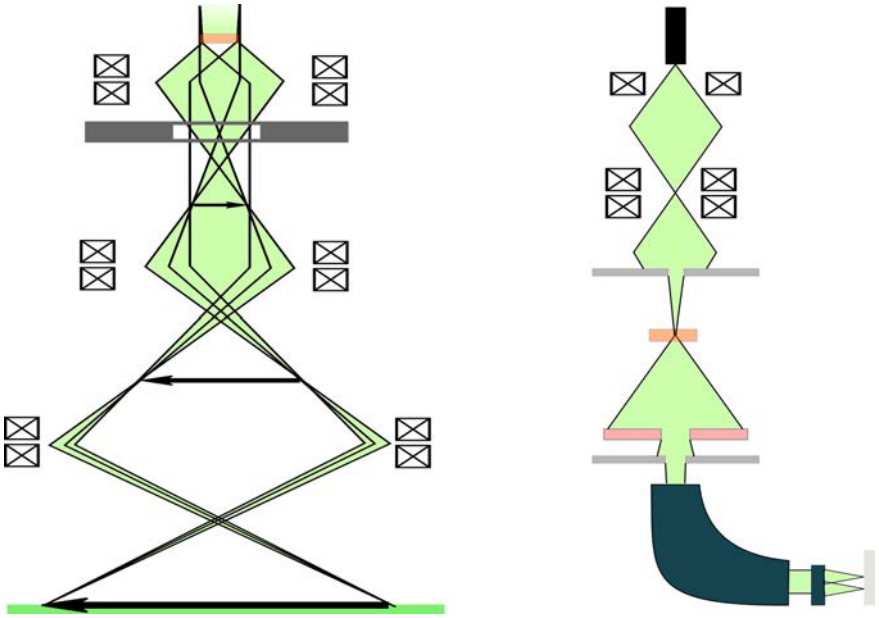

Figure 2.7 Simplified scheme of the imaging modes in TEM. (left) HRTEM and (right) STEM-HAADF and EELS. In both the specimen is colored in orange and the apertures in gray. On the STEM, the HAADF detector is highlighted in pink.

the final image. The choice of the adequate number of pixels is a tricky point to avoid artifacts and wrong images. They are mainly produced if the aliasing is not avoided.

To get a trustworthy result and avoid misinterpretations it is important to choose an adequate slicing, avoid the aliasing and be careful in the treatment of structure anomalies. The aliasing is produced by the wrong choice of the number of pixels in a periodic signal inducing the reconstruction of a signal different to the original one. The best way to prevent this is to fulfil the Nyquist criterion for which the sampling frequency has to be twice the maximum frequency of the original data. In the case of periodic structures, it would be determined by the size of the model used (a, b), the wavelength of the electrons (λ) and the angle of the Annular Dark Field-STEM (ADF-STEM) detector considered (θ_d).

$$N_x > \frac{2a\theta_d}{\lambda} ; N_y > \frac{2b\theta_d}{\lambda}$$

By using FFT, the storage memory is limited by the sampling; however, the computation time for large specimens is lower than for Bloch waves as it is proportional to $N \log_2(N)$, where N is the number of atoms.

2.1.6 Software

Multislice simulations can be used to compute HRTEM or STEM images but also to obtain the diffraction pattern and even, combined with Density Functional Theory, Energy Filtered TEM (EFTEM) maps can be obtained. The community has developed a big number of packages which offer the possibility of obtaining HRTEM, HAADF or even holographic images of a specific sample. Most of them also compute the diffraction for the model.

Table 2.1 recaps all the available software for multislice simulations applied to materials analyzed by TEM. It should be noticed that the evolution of the multislice packages is the same as for most of the scientific software. They started with Fortran or C+ based codes, and nowadays are Python based and can run on GPU systems to improve their efficiency.

Code	Year	Authors	Hardware
xHREM[62]	1977	Ishizuka	
EMS, JEMS[63,64],	1987	Stadelmann	
computem[65]	1998	Kirkland	CPU par
QSTEM[66]	2008	Koch	Still updtaing
STEMSIM[67]	2008	Rosenauer & Schowalter	
MacTempas[68]	2009	Kilaas	CPU
STEM_CELL[69,70]	2013	Carlino, Grillo et al.	CPU par
uSTEM[71]	2014	D'Alfonso et al.	GPU par., inelastic
MULTEM[72]	2015	Lobato & Van Dyck	GPU par
FDES [73]	2015	Van den Broek et al.	multi-GPU par
STEMsalabim [74]	2017	Oelerich et al.	CPU par
Prismatic[75,76]	2017	Ophus, Pryor, Rangel Dacosta, Brown, et al.,	multi CPU GPU, PRISM
Dr. Probe [77,78]	2018	Barthel & Houben	CUDA
stemcl[79,80]	2018	Radek, Tenberge, Hilke, Wilde, Peterlechner	OpenCL GPU and CPU

Table 2.1 Software available for multislice simulations sorted in chronological order. Table inspired on https://prism-em.com/resources-sim-codes/-.

2.2 Density functional Theory

Our field of study are nanomaterials, crystalline or polycrystalline materials with a specific degree of periodicity in their structure. TEM and the related techniques are used to look in detail into their structure, their composition and their interaction with the electron beam to analyze their properties. Moving into the simulation field, the first step is to model the system which at first approximation can be considered as a huge number of atoms. For example, a water molecule consists of three atoms, but a gold nanocluster of 10Å contains approximately 200 atoms. In addition, as the quantum effects have to be taken into account, the atoms cannot be considered as neutral solid spheres, as the electron configuration of each of them is not negligible. Thus, the problem to solve is nothing different from a many-body problem, and the solution consists in solving the Schrödinger equation for our system:

$$i\hbar\frac{\partial}{\partial t}|\psi(t)\rangle = \hat{H}|\psi(t)\rangle \tag{11}$$

The most general Schrödinger equation presents a time dependence that describes the evolution of the system with time. However, some solutions can be deduced assuming different approximations. For example, if the system can be considered stationary, the time dependence can be neglected, and the time independent Schrödinger equation can be solved:

$$i\hbar\frac{\partial}{\partial t}|\psi\rangle = \hat{H}|\psi\rangle \tag{12}$$

In the present Thesis, different simulation methods to be compared with TEM and Electron Energy Loss Spectroscopy (EELS) experimental data will be presented, depending on the final expected result. Thus, depending on the experiment to be modelized, different approximations of the Schrödinger equation should be applied.

Whilst finding the exact solution of the Schrödinger equation can be found, for example, for the hydrogen atom, where the problem is just a two-body problem (one positive and one negative charge), solving the equation for any possible system is an impossible mission as a lot of charges are involved. As the number of atoms increases other methods which include different levels of approximations can be used, such as Hartree-Fock[6,7] which works for a low number of atoms. However, none of these solutions

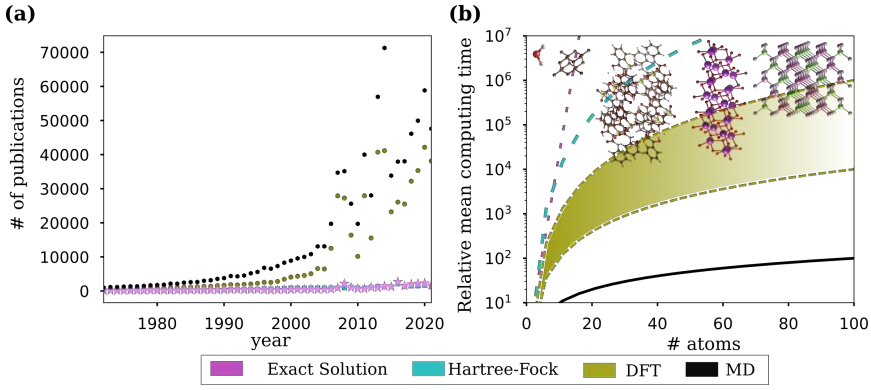

Figure 2.8 Methods to solve the Schrödinger equation for crystalline systems. (a) Number of publications about each of the methods applied to the crystalline system in the last decades. (b) Approximate computing time for each method depending on the number of atoms of the system[14].

work for nanomaterials. Additional approximations are needed to treat real solids and Density Functional Theory satisfies all the requirements.

As can be seen in Figure 2.8(a), since the beginning of the development of the solid-state theories about crystals, the exact solution has not been the preferred one, neither the Hartree-Fock (HF) method. Density Functional Theory (DFT) as well as Molecular Dynamics (MD) have been the most used ones; however, they do not offer the same information. MD is adequate for the interactions between one "big" system and another "small" system which are close enough, for example a carbon nanotube and a water droplet[8], or for the study of amorphous materials[9]. The data about the number of publications has been extracted from [10].

The estimated computing time used by each method as a function of the number of atoms is represented in Figure 2.8(b)[14]. There is a clear pattern regarding the time needed and the publications using every given method, as the time in this kind of calculations is the critical issue. When solving the Schrödinger equation in an exact way, the time increases exponentially with the number of atoms; using Hartree-Fock method it increases by N^4. Using DFT the time can be reduced as it increases by N^3or N^2, depending on the particular method used. DFT has reasonable times for systems of hundreds of atoms (working with a well parallelized machine), however, if the system is larger, MD methods are needed.

Thus, focusing on the objective of solving the Schrödinger equation for crystalline systems, DFT has been demonstrated to be the most suitable method.

2.2.1 Fundamentals of DFT

DFT, as an ab initio (First Principles) method, considers the nuclei and the electrons the basic particles to describe events at the subatomic level. It was proposed in 1965 by Kohn and Sham[11] after the breakthrough introduced by the presentation of two fundamental theorems by Hohenberg and Kohn (1964)[12].

DFT meant a change in the approach to solve the Schrödinger equation for a many-body system. The simplification consisted in considering the n-electron problem as an electron density problem. Instead of having n electrons in the three dimensions of the space, it deals with a three-dimensional density of electrons; this drastically reduces the computational effort needed.

In quantum physics the quantum state is perfectly defined by the wave function. In DFT the electron density ($\rho(\boldsymbol{r})$) will be the variable which defines the whole system (Figure 2.9). Basically, $\rho(\boldsymbol{r})$ is the distribution of electrons around the nuclei, the closer ones correspond to the core electrons while the further ones can be identified as the valence electrons. Obviously, if it is integrated over the volume of the system, the total number of electrons will be retrieved.

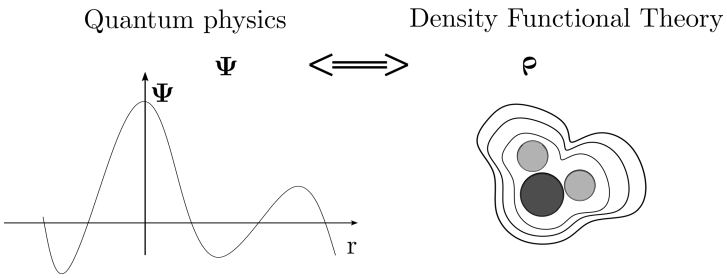

Figure 2.9 From quantum physics to DFT: the wave function (left) is the essential unit to define each building block of a quantum system; DFT proposes to use the electron density to define the system as a whole (right).

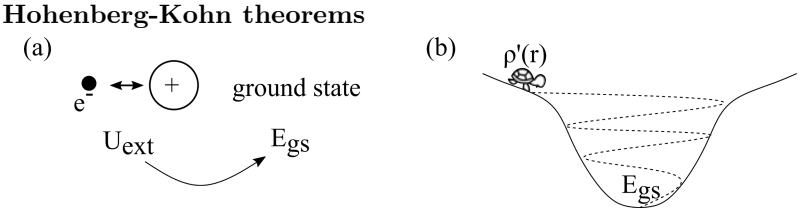

Figure 2.10 Hohenberg-Kohn theorems. (a) First theorem and (b) second theorem.

In DFT the electrons are considered independent, they do not interact among them. To connect the electron density with the Hamiltonian, the external energy and the wave function, the Hohenberg-Kohn theorems are essential.

The first theorem postulates that there is a unique external potential U_{ext} determined by the ground-state electron density. This external potential is in fact the interaction between the electron and the nuclei, but it is called external as it is seen from the electron point of view (Figure 2.10(a)).

Thus considering $\rho(\boldsymbol{r})$ of the previously defined non-interactive system the external potential is independent from it. Summarizing, knowing the electron density at a given external potential all the ground state properties of the system are defined. The electron density plays the main role in the system.

The second theorem proposes the way to find the electron density. The theorem states that $\rho(\boldsymbol{r})$ can be found by the variational principle, meaning that the electron density is modified in order to minimize the total energy of the system, the minimum corresponding to the ground state (Figure 2.10(b)).

Kohn-Sham approach

With both statements one electron systems could be well represented; however, to solve the real n-electron problem some functionals and

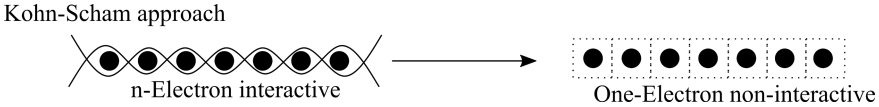

Figure 2.11 Kohn-Sham approach.

approximations need to be considered. Kohn-Sham (KS) approach assumes that each electron is noninteracting with the others and that the system is at the ground state. Figure 2.11 pretends to illustrate the situation where all the electrons were interacting between them, but with the Kohn-Sham approach it is similar to confining them into individual boxes, they are at the same position but no interaction occurs between them.

From that, the energy of the n-electron system can be expressed as the energy of one-electron systems (noninteractive) under a given external potential.

Energy terms

The total energy of the system can be expressed in the following way:

$$E = E_{kin}^{non} + U_{ext} + U_H + U_{xc} \quad (13)$$

Where E_{kin}^{non} represents the noninteractive kinetic energy, U_{ext} the external potential, U_H the Hartree potential and U_{xc} includes all the exchange correlation energies. From that, the KS Hamiltonian can be expressed in the following way representing the basis of DFT calculations.

$$\hat{H}_{K-S} = \nabla^2 + U_{eff} \quad (14)$$

U_{eff} is the effective potential and it includes the three potential terms explained above.

Each energy term does not have the same contribution to the total energy of the system: the kinetic energy represents almost half of the total energy, while the Hartree-Fock, external energy and exchange potential represent the other half. Figure 2.12 illustrates the weight of each energy term on the total computation of the energy.

Three of the four energy terms can be found by solving the Kohn–Sham equations. By KS equations, the Schrödinger equation of a system considered in agreement with the KS approach (a non-interactive one-electron system) is known. Thus, the solution of the KS equation would be the KS orbitals which will be used to find most of the energy terms. Yet it is not possible to solve it for the exchange term.

Figure 2.12 Energy contributions to the total energy of the system.

Exchange-correlation energy

Thus, the key point when performing a DFT calculation is to control the exchange-correlation term (XC) as the other terms can be solved by the KS equations. The XC includes all the quantum effects of the system, which makes it essential even if it corresponds only to a 10% of the total energy, as it can induce important modifications once the spectroscopic, band gap or spin polarization properties, for example, are computed. The XC can be expressed as the sum of the exchange energy (E_x) and the correlation energy (E_c). The exchange term represents the energy transfer between electrons of the same spin and the correlation, the exchange between opposite spin electrons.

$$E_{xc} = E_{x\uparrow\uparrow} + E_{c\uparrow\downarrow} \quad (15)$$

Several functionals have been proposed to approximate the XC potential and throughout the years, their relative popularity has experienced ups and downs. However, the more renowned and used are the Local Density Approximation (LDA) and Generalized Gradient Approximation (GGA) ones, which is not to imply that they are the ones that work more precisely. In fact, the precision highly depends on the analyzed system.

LDA assumes that the n electrons present in the system see the same environment; from that, the system can be cut in as many pieces as electrons it has in it. A uniform electron density is assigned to each of them. Summing up over all local energies from each electron density the total exchange energy is obtained. This simplest approximation has many drawbacks, like overbinds of the atoms, overestimation of cohesive energies, underestimation of the spin and orbital moments and bandgaps, and it cannot describe strongly correlated system. Even if it works well for covalent systems and simple metals, it overestimates E_x while it underestimates E_c.

GGA overcomes the problems of LDA due to the excessively simple approximations in the latter by adding an additional term. Real systems are not homogeneous in the three dimensions. For that, GGA adds an extra term to take into account the local and semilocal information. The XC functional accounts for the electron density and its gradient at a given point. Usually, GGA is expressed based on the LDA with an additional enhancement factor that modifies the LDA energy.

$$E_{xc}^{GGA}[\rho(r), s] = \int \varepsilon_{xc}^{LDA}[\rho(r)], \nabla\rho(r)]dr = \int \varepsilon_{xc}^{LDA}[\rho(r)]\rho(r)F(s)dr \quad (16)$$

A few different modifications have been applied to GGA to reduce its computational cost. The most extensively used is the proposed by Perdew, Burke and Ernzerhof (PBE)[13], which does not have empirical elements. PBE includes the local electron density and its gradient and second-order gradient in the introduction of factors. This functional is the most used one due to its accuracy and computational efficiency. GGA, with all of its modifications, presents enough advantages versus LDA to be used for most cases, but the bandgap problem is still there. It is usual for all the exchange potentials used in DFT to underestimate the energy bandgap on most of the semiconductors, To solve this underestimation problem, hybrid functionals have been developed such as Modified Becke–Johnson (mBJ)[14–16], presented as a way to improve the bandgap of compounds with semi local states, and LDA+U[17,18], used for systems with strongly correlated electrons. All the exchange potentials are in continuous development and improvement. Even if most of them were presented before having enough computer power to be useful for realistic systems. Nowadays the idea behind is still the same.

From Kohn-Sham equations to orbitals

With the XC functionals and considering the system as non-interacting, KS equations can be solved. The solution of KS equations, known as the KS orbitals, must be reached in a self-consistent way. KS orbitals, electron densities and the Hamiltonian are strongly related, thus all the characteristics have to be taken into account to reach convergence.

Basically, the KS orbitals determine one electron density, from that, the KS Hamiltonian is computed and, then a new electron density is obtained; this process is repeated until it converges. The convergence criterium is the minimum energy reached by the variational principle.

2.2.2 DFT algorithm

Summarizing, the DFT calculations have to be performed in an iterative self-consistent cycle which must follow the algorithm displayed in Figure 2.13.

Starting from a guessed electron density and the exchange potential function of the electron density, the KS Hamiltonian of the system can be solved and the KS orbitals are obtained. From the KS orbitals the electron density of the "system" can be estimated. This process is repeated until the difference between the new electron density and the initial guess is small enough. Then the forces and the atomic positions are optimized in order to minimize the energy of the system. In order to converge them, the Hamiltonian has to be solved and new orbitals are obtained. Once the density and forces are converged the cycle is finished and the properties can be computed.

The iterative way of finding the electron density supposes a huge computing time cost for complex structures, but as it has been noticed at the beginning of the section, solving it in an analytical way is not a possible solution.

2.2.3 Periodic solids

In materials science and solid-state physics, DFT is used to compute the electronic structure of the materials and from that, to obtain an estimation of their properties. The key point to apply DFT to a given solid

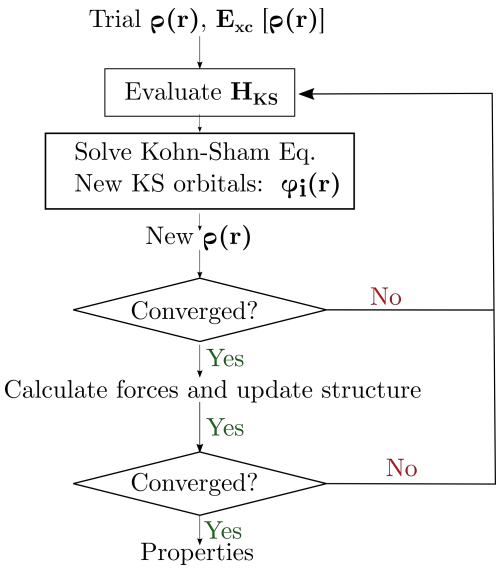

Figure 2.13 DFT algorithm

are the simplifications that can be assumed as correct. The crystalline solids are described by symmetry operations (represented by the space group), which allow to build the bulk material from a unit cell of a few atoms. The higher the symmetry, the fewer atoms will be needed to define the structure. For DFT, periodicity is a great advantage, although it is not the only source of possible simplifications. Another important aspect that can be applied to solids is the use of pseudopotentials.

Pseudopotential approach

The pseudopotential (PP) approach can be used to decrease the computational cost of the calculation. PP consists in generating a potential which mimics the real potential of the system. The strategy is based on building up a potential by considering each atom independently. The PP would be simpler than the real one, however the result will be accurate enough.

To generate the PP three approximations are used: distinguishing between core and valence electrons, frozen nucleus and pseudizing the wave functions.

Distinguishing between core and valence electrons consists in treating differently the electrons depending on their position with respect to the nucleus. The electrons are thus divided into groups. The core electrons, located closer to the nucleus, are considered to be "part of" the nucleus which means that the total charge is compensated and the only perturbations that they can suffer are the ones that also affect the nuclei; they do not affect the bonding properties. The valence electrons, which are further away, are the ones which play a role in most of the interactions, such as bonding, conductivity, or ionization.

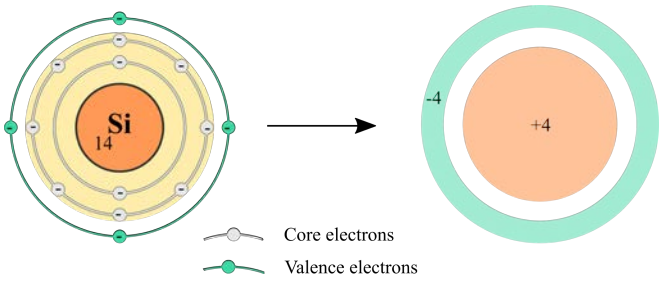

Figure 2.14 Scheme of frozen nucleus approximation for a silicon atom.

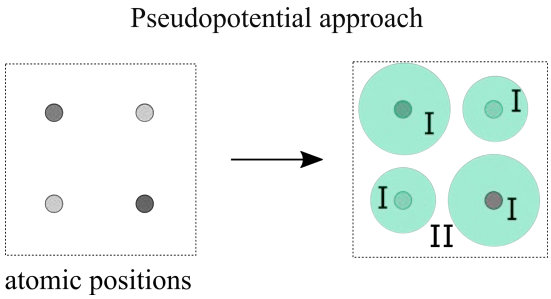

Figure 2.15 Pseudopotential approach: difference between core and interstitial regions.

Using this PP approach, the number of electrons is drastically reduced. As an example, when applied to a silicon atom, the 1s and 2s/2p electrons can be considered as core electrons, while the 3s/3p electrons can be considered valence electrons. Thus, the transformation produces a "nucleus" of 4 positive charges and a "halo" of 4 negative charges. In Figure 2.14 the silicon atom with its electron shells is represented, the K and L shells (of 1 and 2 principal quantic numbers) are fully occupied while the L (n = 3) is partially occupied; applying the frozen nucleus approximation a new simpler configuration is obtained.

This approximation is called Plane Augmented Wave (PAW) and it is a frozen core All-Electron (AE) potential which stands out because of its well-balanced efficiency and accuracy. In it, the core electrons are treated as a radial function and the valence electrons as a plane wave expansion.

Additionally, a "pseudizing" procedure can be applied to the wave functions in order to smooth them. Different types of pseudizing methods exist, depending on the type of function used to smooth the wave functions of the system, however their goal is the same: to replace the atomic orbitals of the core region by some smooth pseudo-orbitals.

With all the PP approach the system is simplified as is schematized in Figure 2.15: instead of describing the system as a net of atomic positions it is described as the core regions and the interstitial region.

K-space

The final consideration that must be taken into account to simulate a solid is to perform the calculations in the reciprocal space, k-space. The Fourier theorem states that if any function is periodic in the real space it can be expanded in the reciprocal space as a Fourier series. Applied to DFT on solids, it means that plane waves can be transformed into a Fourier series. A sampling of the first Brillouin Zone (BZ) is done. This is important because the higher the symmetry, the lower the amount of k points needed to properly define the system. Although, the wave functions are periodic in the real and reciprocal space, working in the reciprocal space reduces the problem to a smaller volume represented by a certain amount of k-points

Real space – direct lattice	Reciprocal space – reciprocal lattice
$\{\mathbf{a}, \mathbf{b}, \mathbf{c}\}$	$\{\mathbf{a}^*, \mathbf{b}^*, \mathbf{c}^*\}$
$\mathbf{R} = n_1\mathbf{a} + n_2\mathbf{b} + n_3\mathbf{c}$	$\mathbf{G} = h\boldsymbol{a}^* + k\mathbf{b}^* + l\mathbf{c}^*$
Ω_d	Ω_r
$\mathbf{a}^* = \frac{2\pi}{\Omega_d}\mathbf{b} \times \mathbf{c};\ \mathbf{b}^* = \frac{2\pi}{\Omega_d}\mathbf{c} \times \mathbf{a};\ \mathbf{c}^* = \frac{2\pi}{\Omega_d}\mathbf{a} \times \mathbf{b}$	

Table 1.2 Transformation from the real space to the reciprocal space.

which represent the compound on all the directions. The computational cost is dramatically reduced.

As is widely known, to move from the real (direct) space to the reciprocal space mathematically consists in computing the Fourier Transform (Table 1.2).

The Brillouin Zone (BZ) is the unit cell of the reciprocal space. It is defined by the surface perpendicular to all the $\mathbf{g_i}$ vectors of the first neighbors. This BZ presents a certain degree of symmetry correlated with the original structure. Considering this symmetry operation, the irreducible BZ (iBZ) can be defined, which corresponds to the smallest unit cell of the reciprocal space. The DFT calculation of periodic solids is performed on a mesh defined on this iBZ (Figure 2.16).

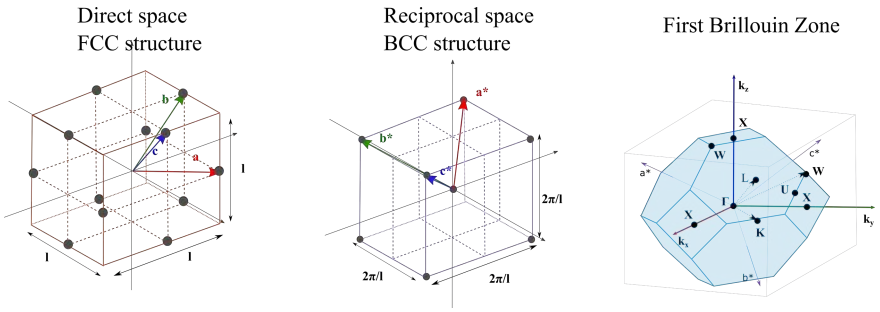

Figure 2.16 From real to reciprocal space for a face centered cubic structure (FCC).

In 1973, Chadi and Cohen presented the special points[19]. The special points are a wise choice of k-points of the BZ which allow to find the wave functions in a more simple and accurate way taking advance of the symmetry of the system. Then the energy, charge, dipole moments... can be calculated. Each crystal has its own k-points depending on its symmetry. Usually, they are placed in the centre of the faces, edges or vertexes of the BZ. The nomenclature of these k-points is arbitrary and should be checked for any structure. By solving the Hamiltonian, the energy for each energy level, or band, is a function of **k**. Later, it will be shown that the band structure takes advantage of using these discrete k points. The relationship between the k-points and the g vectors is not straightforward and the symmetry has to be taken into account.

For the calculation of other properties, different types of meshes have been developed, the most common ones being the Monkhorst and Pack and the tetrahedron.

The Monkhosrt and Pack [20] was developed just after the presentation of the special k-points to generate an equidistant mesh of the Brioullin Zone. The position of k-points is determined by the following relation:

$$\mathbf{k_{prs}} = u_p\mathbf{a}^* + u_r\mathbf{b}^* + u_s\mathbf{c}^*$$
$$u_i = \frac{2r - q_i - 1}{2q_i}$$
$$i = 1,2,3..q_i \qquad (17)$$

Where $\mathbf{a}^*, \mathbf{b}^*, \mathbf{c}^*$ are the reciprocal lattice vectors and q_i are the number of k-points in one specific direction. With that mesh q^3 equally spaced k-points are obtained.

Summarizing, to define the k-mesh just the structure and the number of k points in each direction have to be given. This kind of mesh is used for the general self-consistent cycle of the calculation.

The linear tetrahedron method[21,22] consists in dividing the BZ into tetrahedrons, interpolating the function and integrating according to the interpolation. This mesh is highly used in the calculation of the density of states and matrix element properties like the dielectric function calculation. However, it has some drawbacks like the fact that the symmetry is lost, which increases the computational time, and the under-/over- estimation of the function values.

Solving the KS equations

As a last step, for solids the KS would be resolved at each k-point of the defined mesh and the KS orbitals defined. The KS orbital energy is calculated and from that the properties computed. Some of them, like band structure or density of states would be just a question of choosing the proper k-mesh, but other ones, like optic or excitation ones, need additional calculations.

2.2.4 DFT for EELS

From all that, the electron density should be found for any compound by the self-consistency method. The immediate properties to be obtained from the electron density are the Density of States (DOS) and the band

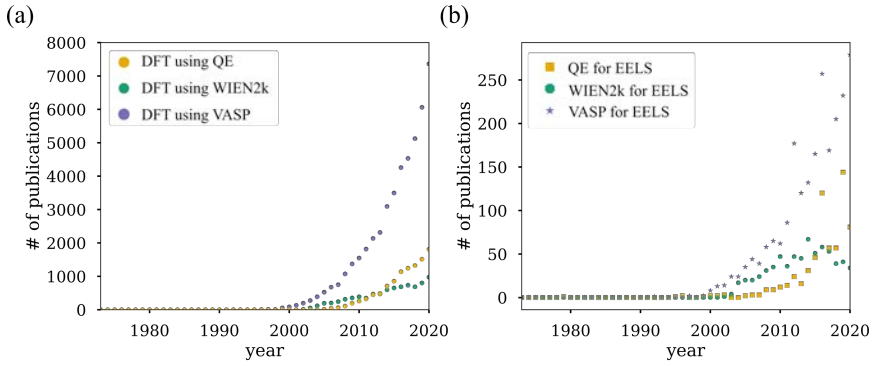

Figure 2.17 Evolution of DFT on the scientific community. (a) Publications depending on the code used. (b) Publications about EELS which include DFT calculations with each of the main codes.

structure; however extra properties can be retrieved like the dielectric function and consequently the Low Loss EELS or the Energy Loss Near Edge Structure (ELNES).

Nowadays several commercial and open-source codes are available to realize all the procedures described in the previous section in a certain user-friendly way. The most known and used ones are Quantum Espresso (QE)[23,24] (open source), Vienna Ab initio Simulation Package (VASP)[25,26] and WIEN2k[27,28]. The importance on TEM field of each of them has changed over time as shown in Figure 2.17. Even if VASP has always been the most used and reported one, WIEN2k, developed at the TU Wien in collaboration with other groups around the word, had a big importance at the beginning. Both of them are commercial packages. Since a decade ago, however, one huge competitor has appeared: Quantum Expresso, Quantum open-Source Package for Research in Electronic Structure, Simulation, and Optimization. It started as a project of CNR-IOM DEMOCRITOS National Simulation Center in Trieste (Italy) and its partners, in collaboration with different centers worldwide such as MIT, Princeton University, the University of Minnesota and the Ecole Polytechnique Fédérale de Lausanne.

The basic differences between all the codes are the pseudopotentials used and the sub-routines that allow to compute some properties or others. To make the DFT simulations useful to complement TEM studies, the possibility of obtaining ELNES would be a crucial point and WIEN2k is the only one that offers it; however, the others allow to compute Low loss EELS.

In this section, the description and the procedure to obtain the most relevant properties discussed in the context of this Thesis will be given. Due to its importance in this Thesis, the EELS related ones will be explained in more detail.

Band structure

The band structure represents the electronic configuration of the solid. In a solid crystal, different energy levels which are known as bands exist. Each band is characterized by the energy level (n) and the wave vector ($\mathbf{k}$). In the description of a solid, bands are equivalent to what electron shells would be in the case of an isolated atom (Figure 2.18). Thus, the energy of

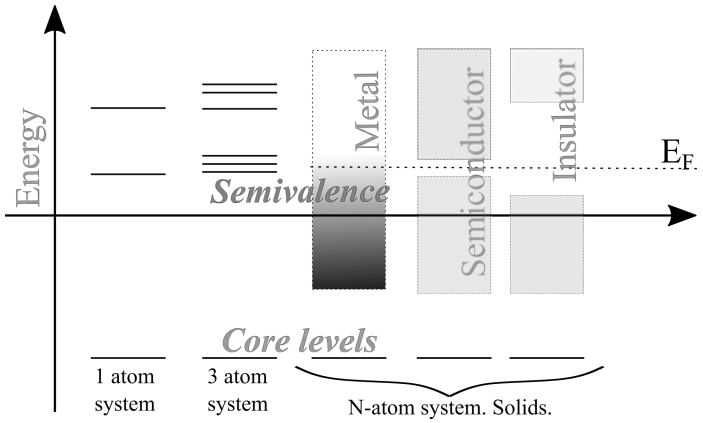

Figure 2.19 Band structure of a solid.

each band presents a dependence with the wave vector and the energy level, $E_n(\mathbf{k})$.

Even if it is not straightforward, from the symmetry, the irreducible representation of each KS eigenvalue is found; this added to the non crossing rule and the compatibility makes it possible to obtain the bands. The non-crossing rule states that the potential energy curves corresponding to electronic states of the same symmetry can not cross. It was formulated by von Neumann and Wigner after they applied the Hund theorem to

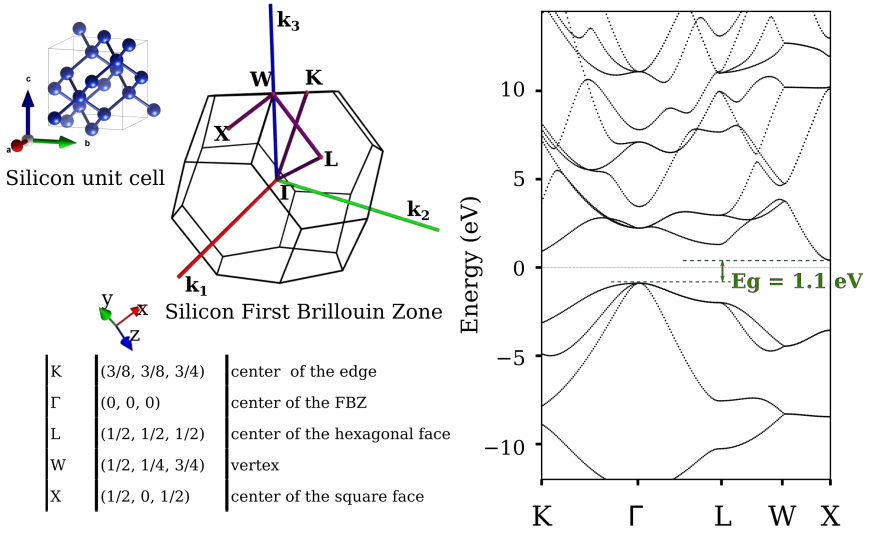

Figure 2.18 Silicon band structure computed along the k-path {K, Γ, L, W, X}. The k-path selection corresponds to strategic locations on the FBZ.

molecules[29]. In addition, there is chemical bonding information which can be also added to the representation.

To compute the band structure a specific k-path is needed. The electron density is recomputed along this special k-path and from the energy eigenvalues the band structure is built. The chosen k-path will connect the special k-points for the studied structure, as they correspond to the high symmetry points. In Figure 2.19, the silicon band structure computed along K-Γ-L-W-X k-path is shown. The FBZ obtained from the silicon unit cell is represented with the k-points marked in red and the k-path in purple; the table explains these high symmetry points. In order to define the mesh, the chosen k-points are given, as well as the number of divisions between them. To simplify the task some packages are available, for example SeeK-path[30].

Density of states

The DOS is another representation of the electronic configuration in the solid, but unlike the band structure, it is an indicator of the occupancy as a function of the energy.

The DOS can be computed from the KS eigenvalues calculated in a dense tetrahedron k-mesh using the tetrahedron method. The DOS can be decomposed in atoms and orbitals to obtain the partial DOS (PDOS). Depending on the nature of the compound and on the bonds of its atoms, the orbitals will suffer a different type of splitting. The splitting of the orbitals is studied by the Crystal Field Theory (CFT).

The CFT was proposed by Bethe and Van Vleck in 1930 [31,32]. Its main goal is to describe the degeneration of the electron orbitals due to the presence of a surrounding charge. The transition metals are the first candidates to present this kind of splitting due to the presence of d and f orbitals with a huge amount of charge. A metal cation in the presence of ordered ions needs to split its d or f orbitals. The splitting of the orbitals is determined by the nature of the metal and ion, the coordination, the oxidation states and the distribution of the ligands. The geometry is the main factor that determines the type of splitting, the most known being the octahedral and the tetrahedral ones.

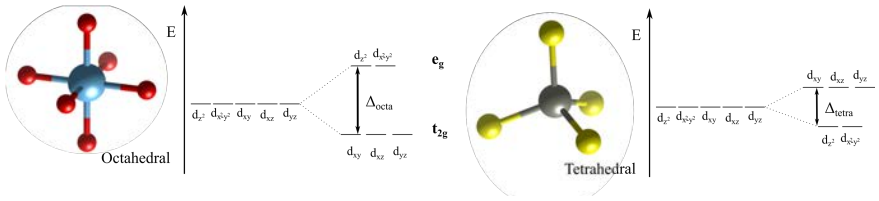

Figure 2.20 Crystal field splitting (left) octahedral and (right) tetrahedral.

The octahedral one occurs when the metal cations are surrounded by six ions (Figure 2.20 (left)). The d-orbitals will split in two, d-e_g and d-t_{2g}; the d-e_g states have higher-energy and include d_{z^2} and $d_{x^2-y^2}$ and the d-t_{2g} have lower-energy and include d_{xy}, d_{xz} and d_{yz}. For the tetrahedral one the metal is surrounded by 4 ions in a tetrahedral arrangement (Figure 2.20(right)); the splitting of the orbitals will be also between d_{z^2} / $d_{x^2-y^2}$ and d_{xy} -/d_{xz} / d_{yz} however the splitting will be of a lower amount of energy and the lower spin will be the d_{z^2} / $d_{x^2-y^2}$ and the higher the d_{xy} -/d_{xz} / d_{yz}.

The PDOS reflects all the orbital splitting as the occupancy of each element and each orbital as a function of its energy. The DOS (in gray) and PDOS (in colours) of the $SrTiO_3$ is plotted in Figure 2.21; however, the bandgap is underestimated for the compound. The STO has a perovskite structure, ABO_3, where the B element, Ti, presents d-e_g/d-t_{2g} splitting due to its octahedral coordination. The graph shows how the p orbitals are in the valence band, while the d orbitals of Sr and Ti are in the conduction band; in addition, the splitting of the low energy Ti:d-t_{2g}, from 2 to 4.5 eV, and high energy Ti:d-e_g, from 4.5 to 8.5 eV, is clearly seen.

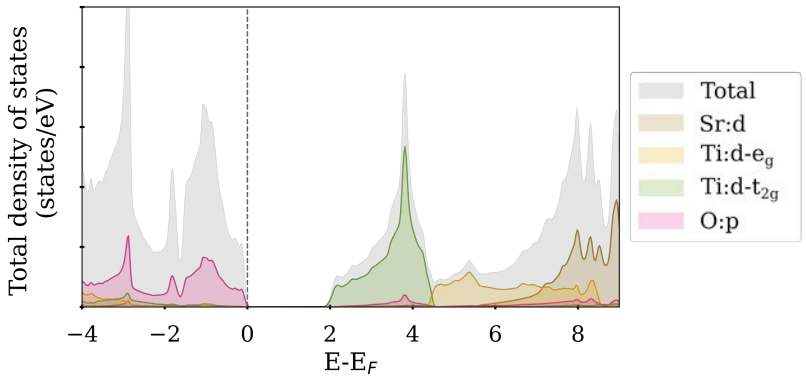

Figure 2.21 DOS and PDOS of strontium titanate

Complex dielectric function: Energy loss function

Low Loss EELS corresponds to the region of low energy losses (4 eV to 40 eV) mostly related to outer shell electrons. It contains the information about single electron excitations (inter-band and intra-band transitions) and from the collective phenomena (plasmon resonance) which will describe all the optical properties of the compound. Thus, the ground state description that DFT gives is not enough. To overcome this, Random Phase Approximation (RPA) of the dielectric function has been implemented. RPA applied to the KS states has demonstrated to work well in all-electron codes [33,34] for screening calculations and obtaining the optical properties of the solids. RPA can be implemented directly on the Linearized Augmented Plane Wave (LAPW) potential obtaining the direct transitions between occupied and unoccupied states, expressed as a function of k[35]. It can be expressed in terms of the KS eigenvalues. The original density of states is modified by the transition probability which is given by the square momentum matrix elements:

$$M = \langle n'\boldsymbol{k}|A \cdot p|n\boldsymbol{k}\rangle \tag{18}$$

where $n'\boldsymbol{k}$ is the unoccupied state, $n\boldsymbol{k}$ is the occupied state and p is the momentum. By applying the selection rules, the intensity of the optical spectra is determined and the allowed transitions are seen. As a final result the real (ε_1) and the imaginary (ε_2) part of the Complex Dielectric Function (CDF) on all the non-equivalent directions, regarding the symmetry of the material, are obtained (Figure 2.22). From the CDF, Energy Loss Function (ELF) can be extracted. In addition, other properties can be computed, as the refractive index and the extinction coefficient (this will be demonstrated on the next section).

ELF is defined as $L_{ij} = \Im m\left(-\frac{1}{\varepsilon_{ij}}\right)$. It can be correlated with ELF extracted from the experimental low loss EELS with Kramers-Kronig analysis [36,37] (Figure 2.23).

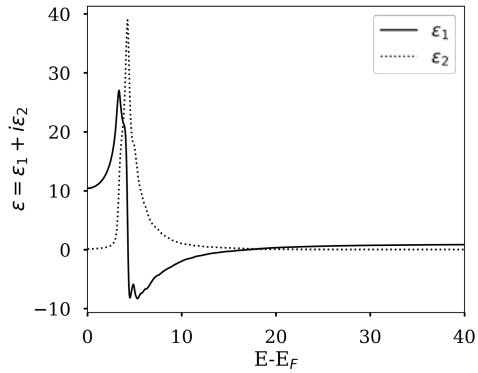

Figure 2.23 Complex dielectric function computed for silicon. The real part (ε_1) is represented by the solid line and the imaginary part (ε_2) by the dashed line.

Even if it works pretty well, it can produce artifacts that are not realistic depending on the nature of the material. For metals, an additional Drude term should be added to consider the free-electron intra-band transitions. Considering this term is essential to reach a fit with the experimental data. For semiconductors, no modifications are needed; however, the main drawback of DFT, the underestimation of the bandgap, would affect the result and must be taken into consideration. To solve this problem there are two types of solutions. The blunt one is the scissors operator, which increases the separation between the conduction- and valence-band, and the fine one is using a hybrid or modified potential. The most used hybrid potentials are the mBJ[14,38] or the GGA+U[39,40] depending on the material; however, they can reach reasonable bandgap value, but they also

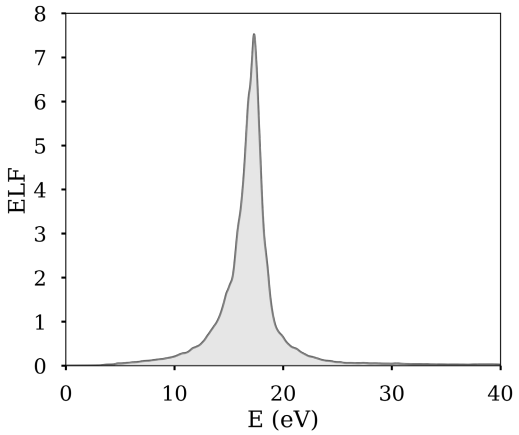

Figure 2.22 Silicon Energy Loss Function obtained from the computed CDF.

can add modifications on the band which will modify the optical properties of the compound, as has been mentioned in the exchange potential section.

The OPTIC package of WIEN2k computes momentum matrix elements for a specific k-path, and from that the CDF is obtained. Other codes include the possibility of computing the dielectric function and its optical properties, for example CASTEP includes OptaDOS[41] or VASP includes LOPTICS[42–44]. The available software is summarized in Table 1.3.

Package	Task	Approach
WIEN2k	OPTIC	DFT
CASTEP	OPTADOS	DFT
VASP	LOPTICS	DFT
Quatum espresso	TurboEELS	DFT
FFEF8	FEFF8	Multiple scattering

Table 1.3 Packages available for low loss calculations.

Energy loss near edge spectroscopy (ELNES)

EELS represents the transition of an electron between two states; as DFT works with the ground state, in principle it is an ill-poised problem. However, some workarounds can be done to get the EELS data.

Once the band structure approach is used, ELNES is computed within the first-order Born approximation. Thus, the incoming and outgoing fast electrons are plane waves with the wave vectors $\mathbf{k_i}$ and $\mathbf{k_f}$. Bethe expressed the double differential scattering cross-section (DDSCS) using the following expression[1]:

$$\frac{\partial^2\sigma}{\partial\Omega\,\partial E} = \left[\frac{4\gamma^2}{a_0^2 q^4}\right]\frac{\mathbf{k_f}}{\mathbf{k_i}} \sum_{i,f}\left|\langle f|e^{i\,\mathbf{qr}}|i\rangle\right|^2 \delta\left(E - E_f + E_i\right) \qquad (19)$$

Where $\mathbf{q} = \mathbf{k_i} - \mathbf{k_f}$ is the moment transfer, a_0 is the Bohr radius, E is the energy loss and $\gamma = \sqrt{1-b^2}$ is the relativistic factor. Rewriting the expression to be computed by DFT, the initial and final state, $|i\rangle$ and $|f\rangle$, will correspond to the ground state, obtained by the self-consistent calculation, and to the one occupied by the target electron in the conduction band after the interaction, respectively. Thus, the electron density would be recomputed considering the hole left due to the transition.

$$\frac{\partial^2\sigma}{\partial\Omega\,\partial E} = \left[\frac{4\gamma^2}{a_0^2 q^4}\right]\frac{\mathbf{k_f}}{\mathbf{k_i}} \sum_{l'=0}^{\infty}\sum_{\lambda=|l-l'|}^{l+l'}(2\lambda+1)\times\begin{pmatrix} l & \lambda & l' \\ 0 & 0 & 0\end{pmatrix}^2 (\langle j_\lambda(q)\rangle_{nl\varepsilon' l'})^2\,\chi_{l'}^{t}(\varepsilon') \quad (20)$$

Where $\chi_{l'}^{t}(\varepsilon')$ is the local partial density of states at energy per atom (t) at a given energy (ε') and $\langle j_\lambda(q)\rangle_{nl\varepsilon' l'}$ involves the radical parts of the one electron functions and the interaction operator.

If relativistic effects have to be taken into account, the DDSCS would look as follows:

$$\frac{\partial^2\sigma}{\partial\Omega\,\partial E} = \left[\frac{4\gamma^2}{a_0^2} - \frac{1}{\left(q^2 - q_z^2\beta^2\right)^2}\right]\frac{\mathbf{k_f}}{\mathbf{k_i}} \times \sum_{i,f}\left|\left\langle f\left|e^{i\,\vec{q}\,\vec{r}}\left(1-\frac{\mathbf{p}\,\mathbf{v_0}}{mc^2}\right)\right|i\right\rangle\right|^2 \delta\left(E - E_f + E_i\right) \quad (21)$$

Where $\mathbf{p}$ is the momentum operator, $\mathbf{v_0}$ the velocity of the incoming fast electron, q_z is the momentum transfer projected into the direction of the fast electrons, m is the mass of the electron and c is the speed of light. For the isotropic case, this term is compensated but it is dramatically important for the anisotropic case[45]. In the same line, the effect of working at magic angle conditions in the simulations has been studied for DFT simulations[46]. The magic angles conditions are values of the collection angle that allow to avoid any contributions of the sample tilting on the acquired spectra.

Thus, the ELNES for each non-equivalent atom could be obtained from the electron density of the ground state. However, to get reliable results some improvements can be done. The one which demonstrated better results is the core-hole approach. As its name indicates, it consists in creating a hole in the valence band by removing one electron, or half of it, in order to mimic the ionized state; to do that it is important to break the symmetry of the system, if not, the removed electron would have its equivalent electrons removed as well.

Part of the EELS community has been collaborating with de DFT developers in order to get packages dedicated to compute the ELNES, however they are not widely extended. The most important package has been developed by Cécile Hébert's group[47]. The package, called TELNES3[48], is a part of WIEN2k and allows to compute the ELNES of the desired peak for each atom of the structure. In addition, it includes the possibility of analyzing its orientation dependence[49]. Nevertheless, TELNES3 is not the only one. Some other groups have developed ad-hoc codes for ELNES calculations. Table 1.4 summarizes the available software.

Package	**Approach**
WIEN2k-TELNES	DFT
Castep[81]	DFT
MADNESS[82]	DFT
Yambo[83]	DFT
Elk[84]	DFT
ONETEP [85]	DFT
FEFF[86]	Multiple scattering

Table 1.4 Software available for ELNES calculations.

In practice, when using WIEN2k for the calculation of ELNES spectra comparable with the experimental spectra, some considerations have to be taken into account. As a result of the calculation, TELNES returns the pure ELNES and ELNES convoluted with both the spectrometer gaussian broadening and Lorentzian core hole lifetime broadening. Both data are important because sometimes once the broadening is applied differences or small features can be hinted. In addition, TELNES computes the ELNES for a specific atom, thus the same calculation must be repeated for all the non-equivalent atoms of the same element in the unit cell, as in the experimental spectra the contribution of all of them will probably be present. Then, the total ELNES can be computed by weight averaging all the contributions considering the multiplicity of each atomic position. These aspects added to the number of k points optimization, the use or not of a core-hole and the experimental parameters considered are crucial for the good quality of the computed ELNES. Nevertheless DFT is always a ground

state approach and will always exist. The possibility of never reaching a realistic enough spectrum always exists.

2.3 Boundary Element Method

Plasmons are the coherent oscillation of the conduction electrons in a metal. This oscillation occurs once the metal is irradiated, with photons or electrons, and it is characterized by the resonance frequency which depends on the density of the conduction electrons, the elementary charge (the electron mass) and the permittivity. The plasmon energy can be estimated by the free electron model in terms of the plasmon frequency[50].

$$E_P = \hbar \sqrt{\frac{ne^2}{m\varepsilon_0}} = \hbar\omega_P \tag{22}$$

Two main types of plasmon phenomena can be distinguished: the bulk plasmons and the surface plasmons. As can be deduced from the name, the first just depends on the compound while the Surface Plasmons (SP) appear at the interfaces between areas with different dielectric functions.

Bulk plasmon

The bulk plasmons can be described by the Drude-Sommerfield model, which assumes the free electron model, considering free electron approximation, independent electron approximation, relaxation time and the Pauli exclusion principle.

In a pure compound, bulk plasmons present zero magnetic field and longitudinal electric field, $\boldsymbol{\nabla} \times \boldsymbol{E} = 0$; thus, they present a trivial solution for the Maxwell equations removing any dependency with the permittivity. However, for a metal-dielectric interface the plasmons are confined and they are called surface plasmons.

Bulk plasmons' energy can be deduced from the complex dielectric function, at the energy value where the real part complex function crosses the zero with a positive slope. It appears in the energy loss function as an important peak. The bulk plasmon depends on the composition of the system and its crystalline structure. DFT considering the random phase approximation is a good option to compute it theoretically.

Surface plasmons

As has been mentioned before, surface plasmons occur on surfaces. Depending on the type of materials, defining that surface, the behavior will

be different and it is important to differentiate between Surface Plasmon Polaritons (SPP) and Localized Surface Resonance Plasmons (LSRP).

The **surface plasmon polaritons** consist in an electromagnetic wave that travels along the interface between a metal and a dielectric, which could be air in the simplest case. It takes place in "infinite" surfaces that separate a metallic medium and a dielectric one. Infinite has to be understood as the fact that one of the directions is much extended than the others. Figure 2.24 illustrates surface plasmon polaritons that occur in an interface between a metal (ε_m) and a dielectric (ε_d).

As its name suggests, the SPP are a combination of two different phenomena: the surface plasmon, which is the charge movement, and the

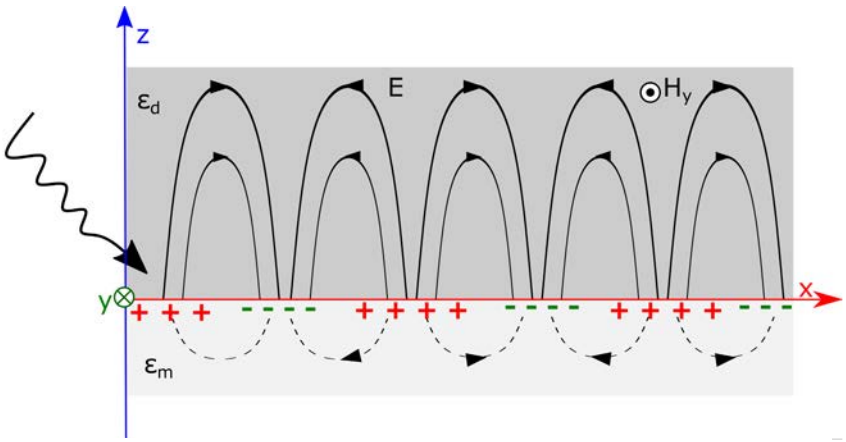

Figure 2.24 Surface plasmons polaritons.

polaritons, which represent the electromagnetic wave. The polariton decreases as the distance from the interface increases.

SPP can be excited by photons or electrons. In the context of the present Thesis, only the electron interaction will be described. The electrons reach the surface and scatter inelastically, thus the energy is transferred to the bulk plasmon, while the scattering component parallel to the surface generates the polariton.

On the other hand, **localized suface resonance plasmons** are non-propagating excitations of the conduction electrons of the metallic nanoobjects coupled with the electromagnetic field (Figure 2.25). The interaction of the electromagnetic field and the metallic nanostructures

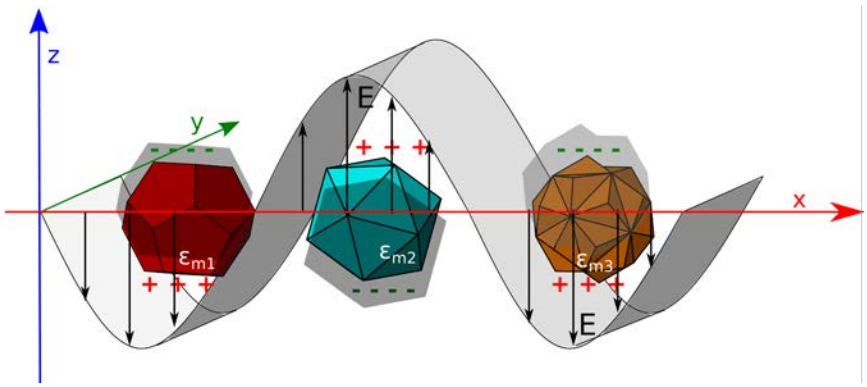

Figure 2.25 Localized surface resonance plasmons.

produces a plasmonic resonance which will depend on the material and also on the shape.

In order to define the optical properties of the plasmonic nanoobjects, the Maxwell equations should be solved for the particular system. Surface plasmons correspond to the solution of the Maxwell equations for a metallic-dielectric interface.

$$\nabla \times \boldsymbol{E}(\boldsymbol{r},t) = -\frac{\partial \boldsymbol{B}(\boldsymbol{r},t)}{\partial t} \tag{23}$$

$$\nabla \times \boldsymbol{H}(\boldsymbol{r},t) = \frac{\partial \boldsymbol{D}(\boldsymbol{r},t)}{\partial t} + \boldsymbol{j}(\boldsymbol{r},t) \tag{24}$$

$$\nabla \boldsymbol{D}(\boldsymbol{r},t) = \rho(\boldsymbol{r},t) \tag{25}$$

$$\nabla \boldsymbol{B}(\boldsymbol{r},t) = 0 \tag{26}$$

where $\boldsymbol{E}(\boldsymbol{r},t)$ is the electric field, $\boldsymbol{H}(\boldsymbol{r},t)$ is the magnetic field, $\boldsymbol{D}(\boldsymbol{r},t)$ is the electric displacement and $\boldsymbol{B}(\boldsymbol{r},t)$ is the magnetic induction. The electric current is $\boldsymbol{j}(\boldsymbol{r},t)$ and the density charge is $\rho(\boldsymbol{r},t)$.

In the context of this Thesis, the plasmonic response of nanoobjects will be analyzed using EEL spectroscopy and then theoretical simulations will be performed and compared with the experimental data. Thus, along this section, a formal description of the plasmonic responses will be given to introduce the Boundary Element Method (BEM)-based calculation which will be used to obtain simulated EELS data from the range of energy of interest.

2.3.1 Theoretical approximations

The theoretical calculations to predict plasmonic excitations can be performed using different approaches depending on the accuracy needed, as the size or complexity of the object would be a limiting factor (Figure 2.26).

The exact solution can be obtained analytically for simple structures with spherical symmetry by Mie solutions, and, if the structure has an ellipsoidal symmetry, the Mie-Gans solution can be used[51]. For arbitrarily shaped objects, numerical approximations are required. There are two main branches of numerical methods to solve the Maxwell equations: differential methods and integral methods, which solve the differential/integral Maxwell equations.

Amongst the differential methods, the most used are the Finite Difference Time Domain approximation (FDTD), the Finite Elements Method (FEM) and the discontinuous Garlerkin time-domain method. The FDTD, the most used one, consists in discretizing the space and the time into "cells"; thus, each time-cell represents the time that the electromagnetic wave needs to move from one space-cell to the next. The same discretization, time and space, is done on the Maxwell equations. From that the differential form of Maxwell equations has to be solved. This method can be applied to any object shape and any dielectric or metallic material for which the complex dielectric function is computed.

From the integral methods, boundary element method will be explained as it is the one used in the following sections. BEM solves the Maxwell equations for systems composed by a combination of homogeneous and dielectric regions separated by a boundary, meaning that the surface of a metallic nanoparticle will be considered as the boundary inside which the media is the metal and outside of which the dielectric media (i. e. air) is found.

Also, Discrete Dipole approximation (DDA) should be mentioned [52,53]. DDA consists in representing each atom as an induced dipole of different polarizability in the directions out of plane and along the tangent plane of the atomic shells. The atomic polarizability is obtained from the dielectric function of the bulk material. This method would be a good option for systems with low number of atoms, like molecules.

A completely different approach to evaluate the excitation response of a nanoobject is obtaining the full electronic description of the system using multiple scattering or band structure methods. However, this method has a huge limitation: as the number of atoms increases the computational time grows rapidly. Despite their limitations, multiple scattering studies have been performed and some works study the plasmonic response as a function of the local density of states[54,55].

2.3.2 BEM: fundamentals

Starting from the Helmholtz theorem, the electromagnetic fields (E and B) can be related with the scalar and vector potentials (ϕ and $\boldsymbol{A}$)

$$\boldsymbol{E} = ik\,\boldsymbol{A} - \nabla\phi \tag{27}$$

$$\boldsymbol{B} = \nabla \times \boldsymbol{A} \tag{28}$$

With the Lorentz gauge condition, the Maxwell equation can be expressed as the Helmholtz equations:

$$\nabla^2\phi + k^2\epsilon\phi = -4\pi\rho \tag{29}$$

$$\nabla^2\boldsymbol{A} + k^2\epsilon\boldsymbol{A} = -\frac{4\pi}{c}\mathbf{j} \tag{30}$$

Where k is the wavenumber, ϵ is the permittivity, ρ is the charge density, $\mathbf{j}$ is the current density and c is the speed of light.

The equation will be solved for each side of the boundary, considering the proper media on both sides, and the continuity at the boundary is imposed. To solve the Helmholtz equations, Green functions are used. To conserve the continuity at the boundary, extra charge and currents at the

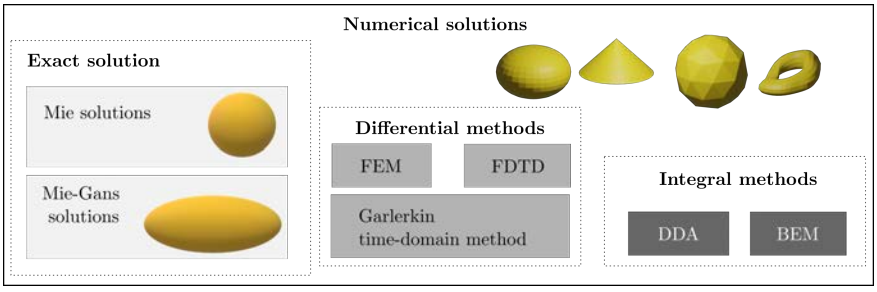

Figure 2.26 Theoretical approaches to solve the Maxwell equations for a nanobject.

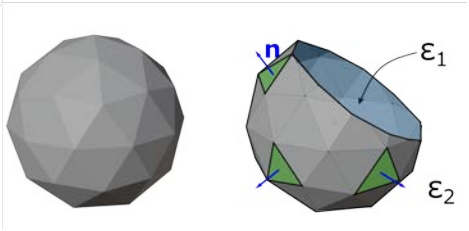

Figure 2.27 Discretization of the nanoobject surface.

surface have to be introduced, as the electromagnetic fields present discontinuity at the interface.

$$\phi(\mathbf{r}) = \int_{\partial S_j} G_j(\mathbf{r},\mathbf{s}')\sigma_j(\boldsymbol{s}')d\boldsymbol{s}' + \frac{1}{\epsilon_j \int G_j(\mathbf{r},\boldsymbol{r}')\rho(\mathbf{r}')dr'} = \int_{\partial S_j} G_j(\mathbf{r},\mathbf{s}')\sigma_j(\boldsymbol{s}')d\boldsymbol{s}' + \phi_e(\mathbf{r}) \quad (31)$$

$$A(\mathbf{r}) = \int_{\partial S_j} G_j(\mathbf{r},\mathbf{s}')\mathbf{h}_j(\boldsymbol{s}')d\boldsymbol{s}' + \frac{\mu_j}{c \int G_j(\mathbf{r},\boldsymbol{r}')j(\mathbf{r}')dr'} = \int_{\partial S_j} G_j(\mathbf{r},\mathbf{s}')\mathbf{h}_j(\boldsymbol{s}')d\boldsymbol{s}' + \mathbf{A}^e(\mathbf{r}) \quad (32)$$

where $A^e(\mathbf{r})$ and $\phi^e(\mathbf{r})$ are the vector and scalar potentials, respectively, for the external perturbation.

To numerically implement this concept, the integral is approximated to a sum, and in this way the electric - magnetic fields for each portion of the surface are obtained. The surface is divided into as many pieces as are needed to have a good representation of the whole volume, each of these pieces being identified by its position (Figure 2.27).

To determine the surface charge and current, the Maxwell theory conditions are imposed.

The continuity of the non-tangential electric field implies a continuity on the scalar potential. The field induced inside the medium is produced by the surface charge. The continuity of the normal component of the magnetic induction involves a continuity on the potential vector, $\mathbf{A}(\mathbf{r})$.

From that, the surface charge (σ_i) and current ($\mathbf{h_i}$) at both sides of the surface (medium 1 and medium 2), inside and outside of the boundary can be expressed:

$$\sigma_1 = G_1^{-1}(G_2\sigma_2 + \varphi) \quad (33)$$

$$\mathbf{h}_1 = G_1^{-1}(G_2\mathbf{h_2} + \mathbf{a}) \quad (34)$$

$$\sigma_2 = G_2^{-1}\Sigma^{-1}[D^e + ik\mathbf{n}(L_1 + L_2)(\Sigma_1 - \Sigma_2)^{-1}\boldsymbol{\alpha}] \quad (35)$$

$$\mathbf{h}_2 = G_2^{-1}(\Sigma_1 - \Sigma_2)^{-1}[ik\mathbf{n}(L_1 - L_2)G_2\sigma_2 + \alpha] \quad (36)$$

where G_i are the Green functions for each dielectric medium, φ is the difference between ϕ_i^e, $\mathbf{a}$ is the difference between $\boldsymbol{A}_i^e$, $\mathbf{n}$ is the normal vector which points outside of the medium 1, α comes from the continuity of the tangential component of the magnetic field, Σ^i is equal to $H_i G_i^{-1}$ and L_i is equal to $G_i \epsilon_i G_i^{-1}$. The other used terms can be expressed as:

$$\begin{cases} D^e = \epsilon_1\left(ik\mathbf{n}\mathbf{A_1^e} - \phi_1^{e\prime}\right) - \epsilon_2\left(ik\mathbf{n}\mathbf{A_2^e} - \phi^{e\prime}{}_2\right) - \Sigma_1\varphi + ik\mathbf{n}L_1\mathbf{a} \\ \boldsymbol{\alpha} = \mathbf{a}' + ik\mathbf{n}(\epsilon_1\phi_1^e - \epsilon_2\phi_2^e) - \Sigma_1\mathbf{a}\, ik\mathbf{n}\, L_1\varphi \\ \Sigma = \Sigma_1 L_1 - \Sigma_2 L_2 + k^2\mathbf{n}\,(L_1 - L_2)(\Sigma_1 - \Sigma_2)^{-1}\mathbf{n}(L_1 - L_2) \end{cases} \tag{37}$$

From that, the vector and scalar potentials are fully defined, and the electric and magnetic fields can be obtained. Using the Poynting vector ($\mathbf{S} = \mathbf{E} \times \mathbf{B}$) the optical cross sections can be expressed as:

$$P_{abs} = P_{ext} - P_{sca} \begin{cases} P_{sca} = n_b \oint Re\left(\mathbf{n}(\mathbf{E} \times \mathbf{B}^*)\right)da \\ P_{ext} = -\dfrac{1}{n_b}\oint Re\left(\mathbf{n}(\mathbf{E} \times \mathbf{B}_{\mathbf{inc}}^* + \mathbf{E}_{\mathbf{inc}}^* \times \mathbf{B})\right)da \end{cases} \tag{38}$$

where n_b is the refractive index of the dielectric background, and $\mathbf{E_{inc}}, \mathbf{B_{inc}}$ are the incident electric and magnetic vectors of the incident wave.

In the case that the nanoobject is much smaller than the incident wavelength all the points at the surface suffer the interaction simultaneously: this is a non-quasistatic approximation of the BEM.

As the interaction takes place instantaneously, the relation between $\mathbf{E}, \mathbf{B}$ disappears, so the Helmholtz equation can be reduced to the Poisson equation, which can be solved using quasistatic Green functions and the boundary conditions. In the same way, surface charge has to be defined and is determined by applying the Maxwell boundary conditions. The continuity of the tangential electric field involves that the charges on both sides of the boundary are equal and, taking into account the continuity of the electric displacement, the surface charge can be determined.

Finally, following the same procedure, the optical cross sections can be calculated:

$$P_{ext} = P_{sca} + P_{abs} \begin{cases} P_{sca} = \dfrac{8\pi}{3}\, k^4 |d_\lambda|^2 \\ P_{abs} = 4\pi k\, \Im m(\hat{\mathbf{e}}_\lambda d_\lambda) \end{cases} \tag{39}$$

BEM is fully implemented in the MNBEM code developed by the group of Ulrich Hohenester of University of Graz[56–58]. MNPBEM is a free license complete package for MATLAB. It allows to compute the response of metallic nanoparticles that interact with the electromagnetic waves. It includes a specific module to compute directly the EELS response of such nanoparticles, which makes it almost the software of choice for the EELS community. However, other software packages are available, most of them not as direct for EELS analysis. As it is usual to combine EELS experiments with cathodoluminescence (CL), the same happens with the theoretical calculations: BEM calculations can be compared with DDA or FDTD.

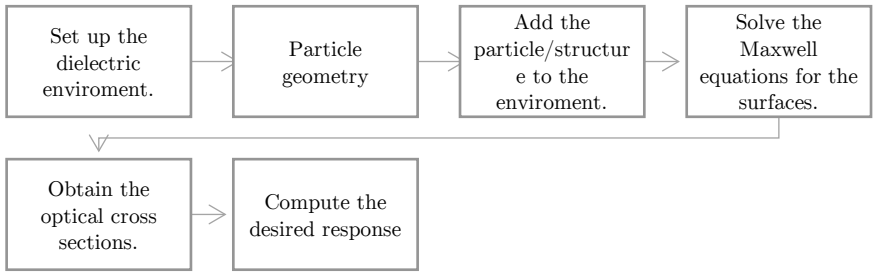

Figure 2.28 Workflow used by the MNPBEM package.

The workflow of the MNPBEM is divided into three main parts: the boundary determination, creating the structures and defining the dielectric functions at each side of the boundary; the resolution of the Maxwell equations (by BEM); and the representation of the interaction from the optical cross sections. The process is summarized in Figure 2.28.

For the simulation, two main inputs have to be given: the material information, which is defined by its dielectric function, and the nanostructure shape. For both cases different approximations can be used, and in the next section both will be explained in detail.

2.3.3 Dielectric function

In order to describe the dielectric environment of a full system, all its components have to be also described by their dielectric functions. The dielectric function is the determining factor to understand the polarizability of a material in the presence of an external field. This dependence is intrinsic

of each material and can be linear or not. Depending on the material it can be necessary to use one specific approximation to the dielectric function.

Macroscopically, by Maxwell notation, the effect of an external electromagnetic field on a dielectric may be described by the electric displacement field expression:

$$\boldsymbol{D} = \varepsilon_0 \boldsymbol{E} + \boldsymbol{P} \tag{40}$$

where ε_0 is the vacuum permittivity, $\boldsymbol{E}$ is the electric field applied and $\boldsymbol{P}$ is the polarization. In addition, taking into account the susceptibility (χ), the polarization is described as:

$$\boldsymbol{P} = \varepsilon_0 \chi \, \boldsymbol{E} \tag{41}$$

Thus,

$$\boldsymbol{D} = \varepsilon_0 \varepsilon_r \, \boldsymbol{E} \tag{42}$$

where ε_0 is the dielectric permittivity of the vacuum, ε_r is the relative permittivity and ε is the absolute permittivity. ε describes the relationship between the applied electric field and the electric displacement induced, as has been said before.

Microscopically, in the atomic world, the interaction between the electromagnetic wave and the atoms can be modelized by an harmonic model and connected to the polarization of the whole material. This approximation is known as the Lorentz model.

The polarization in a material can be considered as the sum of all the dipole moments induced by the electric displacement, which can be expressed as

$$\boldsymbol{P} = N \, q \, \boldsymbol{r} \tag{43}$$

where N is the number of electrons, q is the electric charge and $\boldsymbol{r}$ is the induced displacement due to the interaction.

Considering the atom as an oscillator, once an external field acts on the electron, three different forces are balanced: the restoring force, the electric field and the damping.

$$m \frac{\partial^2 r(t)}{\partial t} = -kr - m\gamma \frac{\partial r(t)}{\partial t} + q \, E(t) \tag{44}$$

Considering $\omega_0 = \sqrt{\frac{k}{m}}$ as the fundamental frequency and reordering, the following differential expression is reached:

$$\frac{\partial^2 r}{\partial t^2} + \gamma \frac{\partial r}{\partial t} + \omega_0^2 r = \frac{q}{m} E(t) \tag{45}$$

It can be solved considering the general solution for $E(t) = E_0 e^{i\omega t}$ and $r(t) = re^{i\omega t}$.

$$r(\omega) = \frac{q}{m} \frac{E_0}{(\omega_0^2 - \omega^2) + i\,\gamma\omega} \tag{46}$$

Thus, the polarization can be rewritten considering $r(\omega)$:

$$P = \varepsilon_0 \chi E = \frac{Nq^2}{m} \frac{E_0}{\left(\omega_0^2 - \omega^2\right) + i\,\gamma\omega} \tag{47}$$

$$\varepsilon(\omega) = 1 + \frac{\omega_p^2}{(\omega_0^2 - \omega^2) + i\,\gamma\omega} = \begin{cases} \varepsilon_1 = 1 + \dfrac{\omega_P^2(\omega_0^2 - \omega^2)}{(\omega_0^2 - \omega^2) + \gamma^2\omega^2} \\ \varepsilon_2 = \dfrac{\omega_P^2 \gamma\omega}{(\omega_0^2 - \omega^2) + \gamma^2\omega^2} \end{cases} \tag{48}$$

where $\omega_P = \sqrt{\frac{ne^2}{\varepsilon_0 m}}$ is the plasma frequency.

Linear:

The dielectrics which have a polarizability proportional to the electric field are considered linear dielectrics with a characteristic dielectric constant independent on the electric field frequency. They are, also, considered isotropic.

In practice this consideration can be assumed for air or the substrate where the nanoparticles are placed.

Approximation by Drude-Lorentz model:

As explained before, the Drude-Lorentz model is the simplest way to define the nonlinear dielectrics. Nonlinear dielectrics are all the materials that have a response that depends on the frequency and momentum of the incident field. This kind of dielectrics have a complex dielectric function. Usually, it is decomposed into the refractive index and the extinction coefficient as they can be measured experimentally.

$$n_{ii} = \sqrt{\frac{|\varepsilon_{ii}| + Re\,(\varepsilon_{ii})}{2}}\;;\; k_{ii} = \sqrt{\frac{|\varepsilon_{ii}| - Re(\,\varepsilon_{ii})}{2}} \tag{49}$$

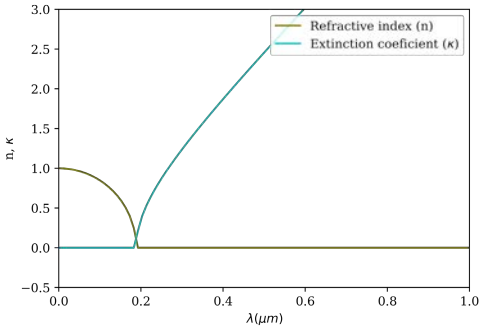

Figure 2.29 Refraction index and extinction coefficient computed for an idealistic metal by the Drude model approximation. The plasmon resonance (ω_P) has been set to $10^{16} rad/s$ and the collision time (τ) to $10^{-14} s$.

In Figure 2.29 the refractive index and the extinction coefficient for an idealistic metal are plotted. First, the complex dielectric function is obtained considering a plasmon resonance (ω_P) of $10^{16} rad/s$ and a collision time (τ) of $10^{-14} s$, then n and κ are obtained as a function of the wavelength.

Experimental/tabulated:

To have a precise description of the dielectric function, experimental data can be used. For the most common materials, the dielectric function information can be found in the bibliography (https://refractiveindex.info/ [59]).

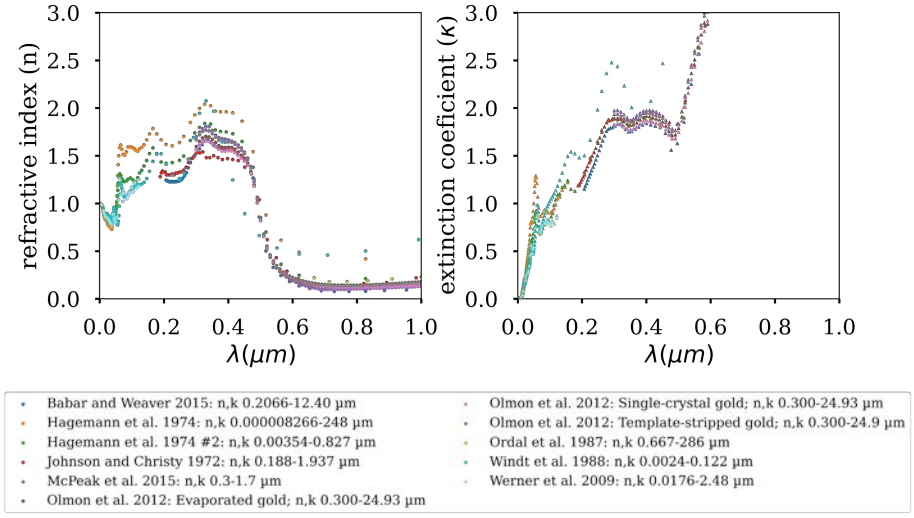

Figure 2.30 Experimental tabulated dielectric function for gold.

Figure 2.30 has been made from reported experimental data for gold (Au) from different bibliographic references, from 1974 to 2015. As can be seen, they all agree but present some difference as the sample is not the same. The choice of one or another will be determined by the energy range desired.

Random Phase Approximation – DFT

All the options presented before are subject to the fact that someone has studied the same compound and reported all the information before. This is usual, as most of the compounds have been repeatedly studied during the years; however, sometimes the compound is not the same. If the compound presents defects, superstructures or the energy range available does not fit as the plasmon resonance is expected at lower energy, more theoretical calculations have to be done. The dielectric function of any material with a known structure can be computed from DFT using the random phase approximation (as explained in the DFT section).

Figure 2.31 compares n and κ of gold obtained from DFT calculations in comparision with all the experimental ones shown before. Here, the representation is done in log-log scale. They present very good agreement.

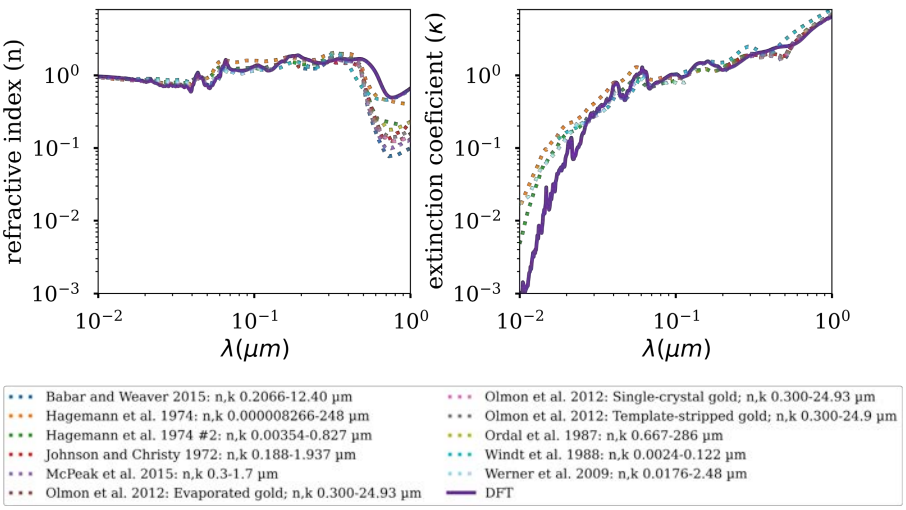

Figure 2.31 DFT obtained refraction index and extinction coefficient for gold (solid line) compared with the tabulated data from different references (dotted line). The plot is represented in a log-log scale.

2.3.4 Model construction

As it has been introduced before, the separation between materials is done by defining a surface. Depending on the geometry of the system, the separation can be done by:

- Closed boundary: to define nanoparticles or core shell nanoparticles.
- Layered structure: this is essential to define the substrate where the nanoobject is placed. For example, on top of the TEM grid, which has a different permittivity than the vacuum.

The closed boundaries can be built directly using the class particle integrated in the MNPBEM package which defines the vertices and faces of the boundary elements in accordance with the Matlab Face-Vertex structure. This approach is useful if the object of interest has a simple shape; however, if the shape is more complex, it would be advisable to construct the system in a more useful way.

It is possible to build the system using a 3D designer interface. The models presented in this work have been constructed using Blender (https://www.blender.org/ [60]). Once the model is constructed and saved in .stl format, it can be imported and converted to be compatible with MNPBEM.

Even if by using Blender a great control on the shape of the nanoobjects is achived, the most realistic boundary to model the nanoobject is to use the object itself. From the tomographic reconstruction of the object an .stl file can be extracted and simplified to be used as the input of MNPBEM simulations.

Figure 2.32 illustrates the fact that if the object of interest is a somewhat "spherical" nanoparticle, most of the times, considering just a perfect sphere will not be enough. By performing a tomographic reconstruction and using it as the basis for building a model the essence of the shape is preserved.

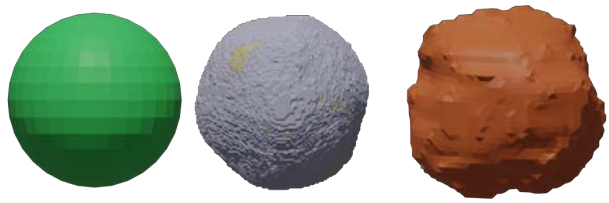

Figure 2.32 Spherical nanoparticles. (a) ideal sphere, (b) core-shell nanoparticle and (c) Fe_2O_3 hollow nanoparticle.

2.3.5 Simulating data from EELS experiments

EEL spectra correspond to the probability of energy loss after crossing a sample. Thus, in order to simulate the low loss of the plasmonic nanoobjects, the problem can be thought as fast electrons, external charge, travelling close and through the defined surfaces.

As explained before, BEM defines the sharp surfaces between regions with different dielectric functions. The EELS problem could also be simplified by decomposing both the bulk and the boundary contributions.

The fast electron which reaches the sample suffers an energy loss due to the induced electric field on its trajectory. The electrons are considered to have a straight-line trajectory with a constant velocity. Due to the force exerted by the induced electric field, a part of the energy will be lost. The loss probability as a function of the frequency can be expressed as follows:

$$\Gamma(\omega) = \frac{1}{\pi\hbar\omega}\int dt\, \Re e\{e^{-i\omega t}\, \mathbf{v}\, \mathbf{E}^{\mathbf{ind}}[r_e(t),\omega]\} + \Gamma_{bulk}(\omega) \qquad (50)$$

where $\mathbf{E}^{\mathbf{ind}}$ corresponds to the induced electric field, r_e to the electron trajectory and Γ_{bulk} to the loss function of the bulk which can be directly deduced from the complex dielectric function $\propto \Im m[\varepsilon(\omega)]$. Only the trajectories of the electrons inside and at the boundaries have to be considered, and they can be expressed as a function of the parameters calculated by BEM (ϕ^e, A^e, α *and* D^e). The induced electric field can be computed from the charge and current distributions, introduced before.

The final consideration is to decide if the problem should be solved in a quasistatic or retarded approach. The quasistatic approach does not consider the retardation effects of a charged particle moving fast enough;

however, in some cases, this is not a very relevant effect[61]. The present version of MNPBEM allows to select the option that suits the problem better.

Finally, the last input needed to perform the simulations of the EEL spectra corresponding to surface plasmons are the microscope parameters of the given experiment.

2.4 References

[1] H. Bethe, Zur Theorie des Durchgangs schneller Korpuskularstrahlen durch Materie, Ann Phys. 397 (1930) 325–400. https://doi.org/10.1002/andp.19303970303.

[2] J.M. Cowley, A.F. Moodie, The Scattering of Electrons by Atoms and Crystals. I. A New Theoretical Approach, 1957.

[3] S.J. Majert, Simulation of atomically resolved elemental maps with a multislice algorithm for relativistic electrons, 2018.

[4] A. Rother, K. Scheerschmidt, Relativistic effects in elastic scattering of electrons in TEM, Ultramicroscopy. 109 (2009) 154–160. https://doi.org/10.1016/j.ultramic.2008.08.008.

[5] R.S. Pennington, C. Coll, S. Estradé, F. Peiró, C.T. Koch, Neural-network-based depth-resolved multiscale structural optimization using density functional theory and electron diffraction data, Physical Review B. 97 (2018). https://doi.org/10.1103/PhysRevB.97.024112.

[6] J.C. Slater, A simplification of the Hartree-Fock Method, Physical Review. 81 (1951) 385–390.

[7] J.C. Slater, Note on Hartree's Method, Physical Review. 35 (1930) 210. https://doi.org/10.1103/PhysRev.35.210.2.

[8] T. Werder, J.H. Walther, R.L. Jaffe, T. Halicioglu, P. Koumoutsakos, On the Water-Carbon Interaction for Use in Molecular Dynamics Simulations of Graphite and Carbon Nanotubes, (2003). https://doi.org/10.1021/jp0268112.

[9] K. Mazeau, L. Heux, Molecular Dynamics Simulations of Bulk Native Crystalline and Amorphous Structures of Cellulose, (2003). https://doi.org/10.1021/jp0219395.

[10] Dimensions | The Next Evolution in Linked Scholarly Information,. https://www.dimensions.ai/ (accessed September 25, 2021).

[11] W. Kohn, L.J. Sham, Self-consistent equations including exchange and correlation effects, Physical Review. 140 (1965). https://doi.org/10.1103/PhysRev.140.A1133.

[12] P. Hohenberg, W. Kohn, Physical Review Physical Review, 1964.

[13] J.P. Perdew, K. Burke, M. Ernzerhof, Generalized Gradient Approximation Made Simple, PHYSICAL REVIEW LETTERS. 77 (1996) 3865–3868.

[14] D. Koller, F. Tran, P. Blaha, Improving the modified Becke-Johnson exchange potential, Physical Review B - Condensed Matter and Materials Physics. 85 (2012) 155109. https://doi.org/10.1103/PhysRevB.85.155109.

[15] D. Koller, F. Tran, P. Blaha, Merits and limits of the modified Becke-Johnson exchange potential, PHYSICAL REVIEW B. 83 (2011) 195134. https://doi.org/10.1103/PhysRevB.83.195134.

[16] A.D. Becke, E.R. Johnson, A simple effective potential for exchange, Journal of Chemical Physics. 124 (2006) 221101. https://doi.org/10.1063/1.2213970.

[17] V.I. Anisimov, J. Zaanen, O.K. Andersen, Band theory and Mott insulators: Hubbard U instead of Stoner I, Physical Review B. 44 (1991) 943–954. https://doi.org/10.1103/PhysRevB.44.943.

[18] P. Novák, J. Kuneš, L. Chaput, W.E. Pickett, Exact exchange for correlated electrons, Physica Status Solidi (B) Basic Research. 243 (2006) 563–572. https://doi.org/10.1002/pssb.200541371.

[19] D.J. Chadi, M.L.C. Cohen, Special Points in the Brillouin Zone, Physical Review B. 8 (1973) 5747–5753.

[20] H.J. Monkhorst, J.D. Pack, Special points for Brillonin-zone integrations, Physical Review B. 13 (1976) 5188–5192.

[21] O. Jepsen, O.K. Andersen, The electronic structure of hcp Ytterbium, Solid State Communications. 9 (1971) 1763–1767.

[22] G. Lehmann, M. Taut, On the Numerical Calculation of the Density of States and Related Properties, Physica Status Solidi (B). 54 (1972) 469–477. https://doi.org/10.1002/pssb.2220540211.

[23] P. Giannozzi, O. Baseggio, P. Bonfà, D. Brunato, R. Car, I. Carnimeo, C. Cavazzoni, S. de Gironcoli, P. Delugas, F. Ferrari Ruffino, A. Ferretti, N. Marzari, I. Timrov, A. Urru, S. Baroni, Quantum ESPRESSO toward the exascale, Journal of Chemical Physics. 152 (2020) 154105. https://doi.org/10.1063/5.0005082.

[24] P. Giannozzi, S. Baroni, N. Bonini, M. Calandra, R. Car, C. Cavazzoni, D. Ceresoli, G.L. Chiarotti, M. Cococcioni, I. Dabo, A.

Dal Corso, S. de Gironcoli, S. Fabris, G. Fratesi, R. Gebauer, U. Gerstmann, C. Gougoussis, A. Kokalj, M. Lazzeri, L. Martin-Samos, N. Marzari, F. Mauri, R. Mazzarello, S. Paolini, A. Pasquarello, L. Paulatto, C. Sbraccia, S. Scandolo, G. Sclauzero, A.P. Seitsonen, A. Smogunov, P. Umari, R.M. Wentzcovitch, QUANTUM ESPRESSO: A modular and open-source software project for quantum simulations of materials, Journal of Physics Condensed Matter. 21 (2009) 395502. https://doi.org/10.1088/0953-8984/21/39/395502.

[25] J. Hafner, Materials simulations using VASP-a quantum perspective to materials science, Computer Physics Communications. 177 (2007) 6–13. https://doi.org/10.1016/j.cpc.2007.02.045.

[26] J. Hafner, G. Kresse, The Vienna AB-Initio Simulation Program VASP: An Efficient and Versatile Tool for Studying the Structural, Dynamic, and Electronic Properties of Materials, Properties of Complex Inorganic Solids. (1997) 69–82. https://doi.org/10.1007/978-1-4615-5943-6_10.

[27] P. Blaha, K. Schwarz, F. Tran, R. Laskowski, G.K.H. Madsen, L.D. Marks, WIEN2k: An APW+lo program for calculating the properties of solids, Journal of Chemical Physics. 152 (2020) 74101. https://doi.org/10.1063/1.5143061.

[28] P. Blaha, K. Schwarz, G. Madsen, D. Kvasnicka, J. Luitz, WIEN2k: An Augmented Plan Wave Plus Local Orbitals Program for Calculating Crystal Properties, 2014.

[29] J. von Neumann, E.P. Wigner, Über das Verhalten von Eigenwerten bei adiabatischen Prozessen, Physikalische Zeitschrif. 30 (1929) 467–470. https://doi.org/10.1007/978-3-662-02781-3_20.

[30] Y. Hinuma, G. Pizzi, Y. Kumagai, F. Oba, I. Tanaka, Band structure diagram paths based on crystallography, Computational Materials Science. 128 (2017) 140–184. https://doi.org/10.1016/j.commatsci.2016.10.015.

[31] H. Bethe, Termaufspaltung in kristallen, Ann Phys. 395 (1929) 133–208. https://doi.org/10.1002/andp.19293950202.

[32] J.H. van Vleck, Theory of the variations in paramagnetic anisotropy among different salts of the iron group, Physical Review. 41 (1932) 208–215. https://doi.org/10.1103/PhysRev.41.208.

[33] R. Abt, C. Ambrosch-Draxl, P. Knoll, Optical response of high temperature superconductors by full potential LAPW band structure calculations, Physica B: Physics of Condensed Matter. 194–196 (1994) 1451–1452. https://doi.org/10.1016/0921-4526(94)91225-4.

[34] R.J. Mathar, J.R. Sabin, S.B. Trickey, Electronic stopping of protons for lithium in the dielectric formulation obtained from first-principles calculations, Nuclear Instruments and Methods in Physics Research, Section B: Beam Interactions with Materials and Atoms. 155 (1999) 249–271. https://doi.org/10.1016/S0168-583X(99)00295-5.

[35] C. Ambrosch-Draxl, J.O. Sofo, Linear optical properties of solids within the full-potential linearized augmented planewave method, Computer Physics Communications . 175 (2006) 1–14.

[36] R.F. Egerton, Electron Energy-Loss Spectroscopy in the Electron Microscope, Springer US, 2011. https://doi.org/10.1007/978-1-4419-9583-4.

[37] G. Brockt, H. Lakner, Nanoscale EELS analysis of dielectric function and bandgap properties in GaN and related materials, Micron. 31 (2000) 435–440. https://doi.org/10.1016/S0968-4328(99)00121-3.

[38] W. Li, C.F.J. Walther, A. Kuc, T. Heine, Density functional theory and beyond for band-gap screening: Performance for transition-metal oxides and dichalcogenides, Journal of Chemical Theory and Computation. 9 (2013) 2950–2958. https://doi.org/10.1021/ct400235w.

[39] M. Forti, P. Alonso, P. Gargano, G. Rubiolo, Transition Metals Monoxides. An LDA+U Study, Procedia Materials Science. 1 (2012) 230–234. https://doi.org/10.1016/j.mspro.2012.06.031.

[40] S.L. Dudarev, G.A. Botton, S.Y. Savrasov, Z. Szotek, W.M. Temmerman, A.P. Sutton, Electronic structure and elastic properties of strongly correlated metal oxides from first principles: LSD A + U, SIC-LSDA and EELS study of UO2 and NiO, Physica Status Solidi (A) Applied Research. 166 (1998) 429–443.

[41] R.J. Nicholls, A.J. Morris, C.J. Pickard, J.R. Yates, OptaDOS - A new tool for EELS calculations, Journal of Physics: Conference

Series. 371 (2012). https://doi.org/10.1088/1742-6596/371/1/012062.

[42] I. Souza, J. Íñiguez, D. Vanderbilt, First-Principles Approach to Insulators in Finite Electric Fields, Physical Review Letters. 89 (2002). https://doi.org/10.1103/PhysRevLett.89.117602.

[43] M. Gajdoš, K. Hummer, G. Kresse, J. Furthmüller, F. Bechstedt, Linear optical properties in the projector-augmented wave methodology, Physical Review B - Condensed Matter and Materials Physics. 73 (2006). https://doi.org/10.1103/PhysRevB.73.045112.

[44] R.W. Nunes, X. Gonze, Berry-phase treatment of the homogeneous electric field perturbation in insulators, Physical Review B - Condensed Matter and Materials Physics. 63 (2001) 1551071–15510722. https://doi.org/10.1103/physrevb.63.155107.

[45] P. Schattschneider, C. Hébert, H. Franco, B. Jouffrey, Anisotropic relativistic cross sections for inelastic electron scattering, and the magic angle, Physical Review B - Condensed Matter and Materials Physics. 72 (2005). https://doi.org/10.1103/PhysRevB.72.045142.

[46] C. Hébert, P. Schattschneider, H. Franco, B. Jouffrey, ELNES at magic angle conditions, Ultramicroscopy. 106 (2006) 1139–1143. https://doi.org/10.1016/j.ultramic.2006.04.030.

[47] C. Hébert, Practical aspects of running the WIEN2k code for electron spectroscopy, Micron. 38 (2007) 12–28. https://doi.org/10.1016/j.micron.2006.03.010.

[48] K. Jorissen, The ab initio calculation of relativistic electron energy loss spectra, 2007.

[49] C. Hébert-Souche, P.H. Louf, P. Blaha, M. Nelhiebel, J. Luitz, P. Schattschneider, K. Schwarz, B. Jouffrey, The orientation-dependent simulation of ELNES, 2000. https://doi.org/10.1016/S0304-3991(99)00168-0.

[50] F.J. García De Abajo, Optical excitations in electron microscopy, Reviews of Modern Physics. 82 (2010) 209–275. https://doi.org/10.1103/RevModPhys.82.209.

[51] F.J. García De Abajo, A. Howie, Relativistic Electron Energy Loss and Electron-Induced Photon Emission in Inhomogeneous Dielectrics, 1998.

[52] M. N'Gom, S. Li, G. Schatz, R. Erni, A. Agarwal, N. Kotov, T.B. Norris, Electron-beam mapping of plasmon resonances in electromagnetically interacting gold nanorods, Physical Review B - Condensed Matter and Materials Physics. 80 (2009) 1–4. https://doi.org/10.1103/PhysRevB.80.113411.

[53] C. Colliex, M. Kociak, O. Stéphan, Electron Energy Loss Spectroscopy imaging of surface plasmons at the nanometer scale, Ultramicroscopy. 162 (2016) A1–A24. https://doi.org/10.1016/j.ultramic.2015.11.012.

[54] S.I. Bozhevolnyi, V.S. Volkov, Multiple-scattering dipole approach to modeling of surface plasmon polariton band gap structures,. www.elsevier.com/locate/optcom (accessed November 30, 2021).

[55] T. v Shahbazyan, Local Density of States for Nanoplasmonics, (2016). https://doi.org/10.1103/PhysRevLett.117.207401.

[56] U. Hohenester, A. Trügler, MNPBEM - A Matlab toolbox for the simulation of plasmonic nanoparticles, Computer Physics Communications. 183 (2012) 370–381. https://doi.org/10.1016/j.cpc.2011.09.009.

[57] J. Waxenegger, A. Trügler, U. Hohenester, Plasmonics simulations with the MNPBEM toolbox: Consideration of substrates and layer structures, Computer Physics Communications. 193 (2015) 138–150. https://doi.org/10.1016/j.cpc.2015.03.023.

[58] U. Hohenester, Simulating electron energy loss spectroscopy with the MNPBEM toolbox, 2014. https://doi.org/10.1016/j.cpc.2013.12.010.

[59] RefractiveIndex.INFO - Refractive index database,. https://refractiveindex.info/ (accessed November 4, 2021).

[60] B. Foundation, blender.org - Home of the Blender project - Free and Open 3D Creation Software, Blender.Org. (2018). https://doi.org/10.1002/adfm.201304036.

[61] F.J. García de Abajo, A. Howie, Retarded field calculation of electron energy loss in inhomogeneous dielectrics, Physical Review B - Condensed Matter and Materials Physics. 65 (2002) 1154181–11541817. https://doi.org/10.1103/PhysRevB.65.115418.

[62] K. Ishizuka, N. Uyeda, A new theoretical and practical approach to the multislice method, Acta Crystallographica Section A. 33 (1977) 740–749. https://doi.org/10.1107/S0567739477001879.

[63] JEMS,. https://www.jems-swiss.ch/ (accessed May 21, 2021).

[64] P.A. Stadelmann, EMS - a software package for electron diffraction analysis and HREM image simulation in materials science, Ultramicroscopy. 21 (1987) 131–145. https://doi.org/10.1016/0304-3991(87)90080-5.

[65] E.J. Kirkland, Advanced Computing in Electron Microscopy, 2010. https://doi.org/10.1088/1751-8113/44/8/085201.

[66] QSTEM: Quantitative TEM/STEM Simulations-Strukturforschung / Elektronenmikroskopie,. https://www.physics.hu-berlin.de/en/sem/software/software_qstem (accessed May 21, 2021).

[67] A. Rosenauer, M. Schowalter, STEMSIM—a New Software Tool for Simulation of STEM HAADF Z-Contrast Imaging, Microscopy of Semiconducting Materials 2007. (2008) 170–172. https://doi.org/10.1007/978-1-4020-8615-1_36.

[68] MacTempasX Version 2,. https://www.totalresolution.com/Tempas.htm (accessed May 21, 2021).

[69] V. Grillo, E. Rotunno, STEM_CELL: A software tool for electron microscopy: Part I-simulations, Ultramicroscopy. 125 (2013) 97–111. https://doi.org/10.1016/j.ultramic.2012.10.016.

[70] V. Grillo, F. Rossi, STEM_CELL: A software tool for electron microscopy. Part 2 analysis of crystalline materials, (2012). https://doi.org/10.1016/j.ultramic.2012.10.009.

[71] L.J. Allen, A.J. D'alfonso, S.D. Findlay, Modelling the inelastic scattering of fast electrons, (2014). https://doi.org/10.1016/j.ultramic.2014.10.011.

[72] I. Lobato, D. van Dyck, MULTEM: A new multislice program to perform accurate and fast electron diffraction and imaging simulations using Graphics Processing Units with CUDA, Ultramicroscopy. 156 (2015) 9–17. https://doi.org/10.1016/j.ultramic.2015.04.016.

[73] W. van den Broek, X. Jiang, C.T. Koch, FDES, a GPU-based multislice algorithm with increased efficiency of the computation of the projected potential, (2015). https://doi.org/10.1016/j.ultramic.2015.07.005.

[74] J.O. Oelerich, L. Duschek, J. Belz, A. Beyer, S.D. Baranovskii, K. Volz, STEMsalabim: A high-performance computing cluster friendly code for scanning transmission electron microscopy image simulations of thin specimens, Ultramicroscopy. 177 (2017) 91–96. https://doi.org/10.1016/j.ultramic.2017.03.010.

[75] Prismatic Software For STEM Simulation - Documentation, tutorials, and source code for the software package Prismatic, a GPU implementation of image simulation algorithms in scanning transmission electron microscopy (STEM),. https://prism-em.com/ (accessed May 24, 2021).

[76] L. Rangel DaCosta, H.G. Brown, P.M. Pelz, A. Rakowski, N. Barber, P. O'Donovan, P. McBean, L. Jones, J. Ciston, M.C. Scott, C. Ophus, Prismatic 2.0 – Simulation software for scanning and high resolution transmission electron microscopy (STEM and HRTEM), Micron. 151 (2021). https://doi.org/10.1016/J.MICRON.2021.103141.

[77] Dr. Probe - STEM image simulation software,. https://er-c.org/barthel/drprobe/index.html (accessed May 24, 2021).

[78] J. Barthel, Dr. Probe: A software for high-resolution STEM image simulation, (2018). https://doi.org/10.1016/j.ultramic.2018.06.003.

[79] GitHub - stemcl/stemcl: GPU accelerated multislice simulation,. https://github.com/stemcl/stemcl (accessed May 24, 2021).

[80] M. Radek, J.G. Tenberge, S. Hilke, G. Wilde, M. Peterlechner, STEMcl–A multi-GPU multislice algorithm for simulation of large structure and imaging parameter series, Ultramicroscopy. 188 (2018) 24–30. https://doi.org/10.1016/j.ultramic.2018.02.004.

[81] S.J. Clark, M.D. Segall, C.J. Pickard, P.J. Hasnip, M.I.J. Probert, K. Refson, M.C. Payne, First principles methods using CASTEP, Zeitschrift Fur Kristallographie. 220 (2005) 567–570. https://doi.org/10.1524/zkri.220.5.567.65075.

[82] L.E. Ratcliff, W.S. Thornton, ´ Alvaro, V. Mayagoitia, N.A. Romero, Combining Pseudopotential and All Electron Density Functional Theory for the Efficient Calculation of Core Spectra using a Multiresolution Approach.

[83] D. Sangalli, A. Ferretti, H. Miranda, C. Attaccalite, I. Marri, E. Cannuccia, P. Melo, M. Marsili, F. Paleari, A. Marrazzo, G. Prandini, P. Bonfà, M.O. Atambo, F. Affinito, M. Palummo, A. Molina-Sánchez, C. Hogan, M. Grüning, D. Varsano, A. Marini, Many-body perturbation theory calculations using the yambo code, Journal of Physics Condensed Matter. 31 (2019). https://doi.org/10.1088/1361-648X/ab15d0.

[84] J.K. Dewhurst, S. Sharma, L. Nordström, F. Cricchio, O. Grånäs, E.K.U. Gross, The Elk Code Manual Version 7.2.42.

[85] J.C.A. Prentice, J. Aarons, J.C. Womack, A.E.A. Allen, L. Andrinopoulos, L. Anton, R.A. Bell, A. Bhandari, G.A. Bramley, R.J. Charlton, R.J. Clements, D.J. Cole, G. Constantinescu, F. Corsetti, S.M.M. Dubois, K.K.B. Duff, J.M. Escartín, A. Greco, Q. Hill, L.P. Lee, E. Linscott, D.D. O'Regan, M.J.S. Phipps, L.E. Ratcliff, Á.R. Serrano, E.W. Tait, G. Teobaldi, V. Vitale, N. Yeung, T.J. Zuehlsdorff, J. Dziedzic, P.D. Haynes, N.D.M. Hine, A.A. Mostofi, M.C. Payne, C.K. Skylaris, The ONETEP linear-scaling density functional theory program, Journal of Chemical Physics. 152 (2020). https://doi.org/10.1063/5.0004445.

[86] G. Editor, J. Anton van Bokhoven, J.J. Rehr, J.J. Kas, F.D. Vila, M.P. Prange, K. Jorissen, D.E. Ramaker, D.C. Koningsberger, P. Chem, P. Ghigna, S. Pin, G. Spinolo, M.A. Newton, M. Zema, S.C. Tarantino, G. Capitani, F. Tatti, R.M. van der Veen, C.J. Milne, V.-T. Pham, A. el Nahhas, F.A. Lima, D.A. Vithanage, R. Abela, M. Chergui, A.M. Beale, B.M. Weckhuysen, M. Bauer, C. Gastl, P. Chem Chem, S.A. Wyrzgol, S. Schäfer, S. Lee, B. Lee, M. di Vece, X. Li, S. Seifert, R.E. Winans, M. Stutzmann, J.A. Lercher, S. Vajda, S. Villaume, U. Ekström, H. Ottosson, P. Norman, N.B. Muddada, U. Olsbye, L. Caccialupi, F. Cavani, G. Leofanti, D. Gianolio, S. Bordiga, C. Lamberti, D. Cabaret, A. Bordage, A. Juhin, M. Arfaoui, E. Gaudry, D. Ferri, M. Santosh Kumar, R. Wirz,

A. Eyssler, O. Korsak, P. Hug, A. Weidenkaff, B.D. Patterson, R. Abela, G. Silversmit, B. Vekemans, S. Nikitenko, S. Schmitz, T. Schoonjans, F.E. Brenker, J. Singh, R.C. Nelson, B.C. Vicente, S.L. Scott, J.A. van Bokhoven, N. Guo, B.R. Fingland, W. Damion Williams, V.F. Kispersky, J. Jelic, W. Nicholas Delgass, F.H. Ribeiro, R.J. Meyer, J.T. Miller, T. Anniyev, H. Ogasawara, M.P. Ljungberg, K.T. Wikfeldt, J.B. MacNaughton, L.-Å. Näslund, U. Bergmann, S. Koh, P. Strasser, L.G. Pettersson, A. Nilsson, M. Tada, Y. Uemura, R. Bal, Y. Inada, M. Nomura, Y. Chen, C. Xie, Y. Li, C. Song, T.B. Bolin, M.P. Prange bc, Parameter-free calculations of X-ray spectra with FEFF9, Phys. Chem. Chem. Phys. 7 (2010) 52. https://doi.org/10.1039/c0cp90010a.

Chapter 3: GaInP: the effect of atomic ordering on the electronic configuration

In this Chapter, the effect of a special kind of ordering on the optoelectronic properties of a semiconductor compound is presented to be studied in depth. In particular, the CuPtB order in GaInP thin films is revisited combining new and traditional techniques. The chapter summarizes the whole study done on a set of GaInP thin films with different degrees of ordering and how it can be related to their electronic behavior. To reach a complete and self-consistent comprehension, different experimental techniques and theoretical approximations are needed. The chapter starts by introducing the samples and their macroscopic optical characterization. After that, the ordering and its consequences are studied from an experimental point of view by Transmission Electron Microscopy techniques and from a theoretical approach using Density Functional Theory calculations.

3.1 State of the art – Motivation

Gallium Indium Phosphide (GaInP) is an important member of the III-V semiconductors family as it presents a high electron mobility[1] and a wide bandgap, which can be easily controllable by the growth conditions. It is relevant for the fabrication of III–V optoelectronics and microelectronics, and is used currently in a variety of semiconductor devices, namely, Heterojuntion Bipolar Transistors (HBTs)[2], High-electron Mobility Transistors (HEMTs)[3], Light-Emitting Diode (LEDs)[4], lasers[5] and solar cells[6]. In the particular field of Multijunction Solar Cells (MJSCs), GaInP is the material of choice for the top subcell in a variety of designs (i.e. lattice matched triple-junction GaInP/Ga(In)As/Ge, inverted metamorphic, upright metamorphic, wafer bonded and lattice-matched using dilute-nitride solar cells). During the last decades, the improvement of the efficiency of multijunction solar cells based on III-V semiconductors has been on the focus, going from the 33% obtained in the 90s [7–9] to the current values which are closer to 50% [10]. Therefore, a deep understanding of the interplay between the growth conditions and the material microstructure is fundamental to further improve the performance of the aforementioned devices.

GaInP presents a zinc-blende type crystallographic structure, with a F-43m (216) space group (as GaP or InP) with half of the places of group III occupied by Ga and the other half by In. For this particular composition ($Ga_xIn_{1-x}P$ with x=0.5), gallium indium phosphide usually presents CuPt type B ordering. This ordering consists of alternating Ga- and In-rich {111} planes in the zinc-blende structure. For (001)-oriented substrates, the ordering affects the $(\bar{1}11)$ and $(1\bar{1}1)$ planes, i.e. a $CuPt_B$ type with two variants that can be selected by substrate misorientation. In particular, a misorientation of the (001) substrate by a few degrees towards (111) favors the formation of a single variant [11].

The alternance of In-rich and Ga-rich planes on $(1\bar{1}1)$ planes in a single variant $CuPt_B$ type is in fact a superstructure that can be easily detected by electron diffraction by the presence of the satellite spots appearing at multiples of $1/2(1\bar{1}1)$ over the expected diffraction pattern for a zinc-blende structure along the [110] zone axis, whereas no satellite spots will appear on the $[\bar{1}10]$ zone axis.

The degree of order is described by the so called order parameter (η), a conventional value between 0 (fully disordered sample, this is In and Ga randomly distributed on group III sites) and 1 (fully ordered sample, with perfect alternation of In and Ga on the {111} planes) that can be estimated from the measurements of the bandgap (E_g) of the material[12,13], since it has been demonstrated that E_g shrinks as the ordering increases. On the other hand, the degree of order can be controlled by the use of a surfactant (usually Sb)[14]. Therefore, the band gap of GaInP can be indirectly tuned using different surfactant concentrations during the growth.

In this chapter, a set of GaInP layers grown by metalorganic vapor phase epitaxy (MOVPE) using different Sb concentrations in the P flux during the growth will be analyzed in depth using transmission electron microscopy techniques. The evidence of the ordering will be assessed using Selected Area Electron Diffraction (SAED). Ordered domains and domain boundaries will be assessed by two-beam imaging conditions, enabling the quantification of the Antiphase Boundaries between ordered Domains (APDB) distribution. The polarity of the material (III and V element location in the dumbbells projected in [110] orientation) will be observed by atomic resolution High Angle Annular Dark Field (HAADF) Scanning Transmission Electron Microscopy (STEM). Then, atomistic simulations will be performed to estimate the variation of the HAADF-STEM image contrast when ordered and disordered domains overlap. Furthermore, in-situ electrical measurements will be carried out to evaluate the potential conductivity anisotropy induced by the asymmetrical single variant $CuPt_B$ ordering. Finally, DFT calculations will be used to carefully analyze the effect of the atomic ordering on the electronic configuration.

3.2 Material and preliminary characterization

GaInP thin films were prepared by the Instituto de Energía Solar de Madrid (IES). Four thin films of GaInP were grown using different fluxes of Sb, from 0 ppm to 1721 ppm[15].

The samples consisted of a thin film of GaInP:Sb grown by MOVPE, on top of a germanium substrate with a misorientation of 6° towards the nearest [111] axis. A nucleation layer of GaInP was previously grown, between the GaInP:Sb layer and the substrate, and, on top, an overbuffer of GaInAs:Si was deposited as sketched in Figure 3.1(b). Further details on the growth can be found in [16,17].

Sb/P (ppm)	Eg (eV)	η
0	1.855	0.53
411	1.880	0.48
728	1.904	0.44
1721	1.949	0.31

Table 3.1 Description of the samples set: Sb/P flux expressed in ppm, degree of order, η, and energy bandgap (E_g) in eV.

Photoluminescence experiments were carried out, and the changes in the energy bandgap (E_g) were measured. The obtained results are summarized in the Table 3.1.

In the table, the degree of order is also given; it was approximatively calculated following equations (51) and (52) from [18]:

$$E_g(\eta) = E_g(\eta = 0) - \eta^2 \Delta E_g \tag{53}$$

$$\eta = \sqrt{\frac{1991 - PL_{peak}at\ 20K}{471}} \tag{54}$$

where η is the degree of order, $E_g(\eta = 0)$ is the bandgap in a fully disordered sample (estimated to be 1.991 eV [19]), and ΔE_g is the bandgap reduction of the fully ordered alloy.

Thus, the dependence of the degree of order with the Sb content is clearly evidenced by the macroscopic characterization. The inverse relationship of the bandgap energy with the degree of order (it decreases as the degree of order increases), agrees with previously reported works on the same compound[12,14,20,21].

3.3 Microscopic ordering assessment: phase and diffraction contrast imaging

The effects and consequences of the ordering were analyzed locally using different TEM techniques. In order to have access to the orientations where the order was visible, and not visible, for each sample, two FIB lamellas

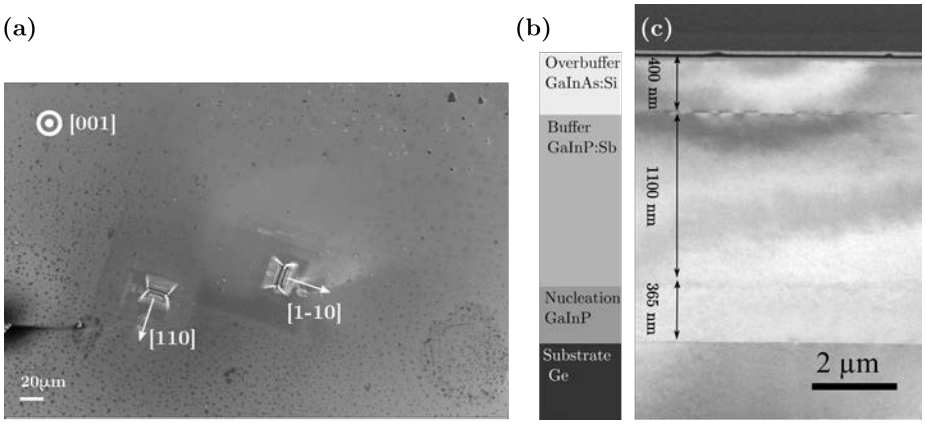

Figure 3.1 (a) FIB-SEM image of lamella preparation. Two lamellas of each sample were prepared one, on [110] zone axis and the other on $[1\bar{1}0]$. (b) Sketche of the multilayer stack. (c) Low magnification image with the identification of the three layers.

were prepared along two perpendicular zone axes, [110] and $[\bar{1}10]$, as is shown in Figure 3.1 (a).

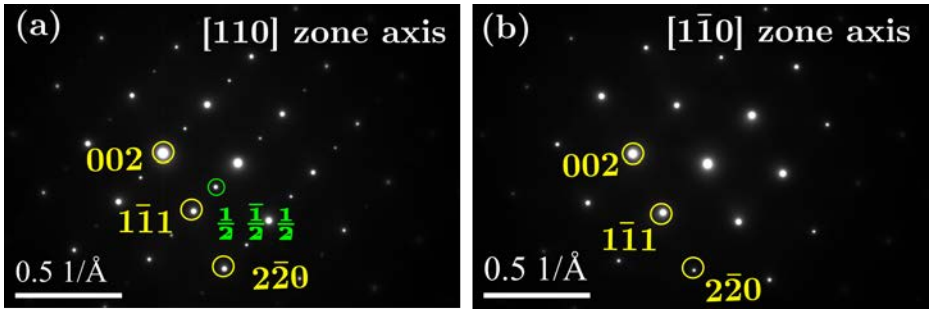

Figure 3.2 SAED of the same sample oriented on the direction (zone axis) in which the order is visible, [110], and the perpendicular one, on wihich it is not visible, $[1\bar{1}0]$. On both the zinc blende diffraction pattern is observed, but in (a) the extra satellite spot appears at $\boldsymbol{g} = \frac{1}{2}(1\bar{1}1)$.

The samples were analyzed by conventional TEM to identify and to check the thickness of all the layers of the structure (Figure 3.1 (c)). Conventional dark field (DF) and SAED observations were carried out in a JEOL 2100 system operated at 200 kV.

SAED of the GaInP:Sb layer was acquired to assess the presence or absence of the superstructure. As it has been mentioned before, GaInP presents a cubic zinc-blende structure, thus from [110] and [$\bar{1}$10] the same diffraction pattern should be retrieved, as they are completely equivalent. The presence of an alternation of the (1$\bar{1}$1) planes, however, appeared as an extra spot in that particular [110] direction. The periodicity of the alternation is double of the periodicity of the (1$\bar{1}$1) planes, so the extra spot appears at half the distance of the **g** vector. The SAED of the GaInP:Sb layer on the [110] zone axis shows the zinc-blende diffraction pattern with the satellite spot at 1/2 (1$\bar{1}$1) (Figure 3.2(a)); however, on the orthogonal direction, [1$\bar{1}$0], only the pure zinc-blende pattern is observed (Figure 3.2(b)).

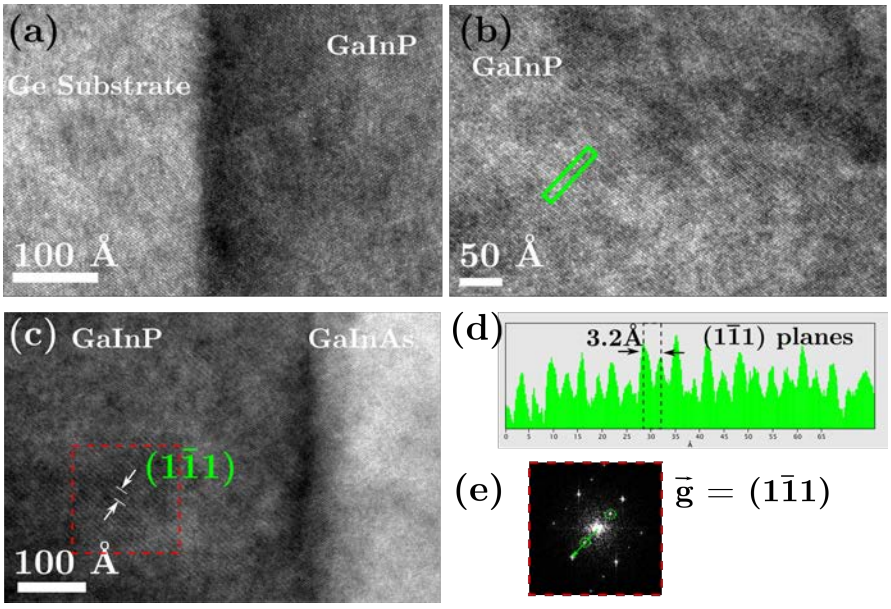

Figure 3.3 HRTEM images: (a) interface between the Ge substrate and GaInP nucleation layer, (b) GaInP:SB layer with an intensity profile depicted in (d), (c) interface between the GaInP:Sb, from which the FFT is computed (e), and the GaInAs overbuffer.

By HRTEM the good epitaxial growth of the layers was checked as was the good crystallinity. Figure 3.3 collects HRTEM images of the different layers and interfaces of a sample oriented on the [110] zone axis, where the ordering is observed. The interface between the germanium substrate and the nucleation layer of GaInP is shown in Figure 3.3 (a). Both substrate and layer present good crystallinity and no defects or dislocations can be appreciated. The main layer, GaInP:Sb, is shown in Figure 3.3 (b). The GaInP:Sb also presents a good epitaxy with the GaInAs overbuffer layer as shown in Figure 3.3 (c). Even if the phase contrast does not allow to detect changes in composition, the superstructure can still be seen. If a profile is acquired perpendicular to the planes (highlighted in green) the interplanar distance of the {111} planes is retrieved, as is shown in Figure 3.3 (d). In addition, by computing the Fast Fourier Transform (FFT) the satellite spot is detected along the $(1\bar{1}1)$ **g** vector, in the same way as for the experimental SAED (e).

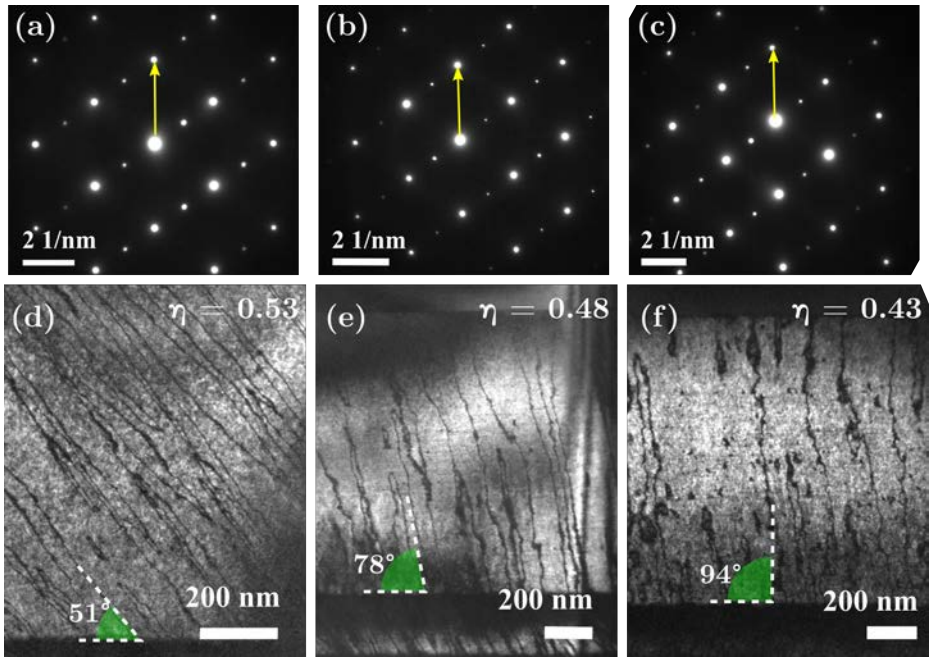

Figure 3.4 (a-c) correspond to the electron diffraction pattern along the [110] zone axis for the samples with 0 ($\eta = 0.53$), 411 ($\eta = 0.48$) and 728 ($\eta = 0.43$) ppm Sb/P (ppm). The growth direction is highlighted In yellow. Below, (d-f) two beam DF images of each of the samples can be seen. In green the angle of APDB is highlighted.

The homogeneity of the ordering was assessed by performing dark field two beam condition TEM selecting the satellite spot. For each sample on [110] zone axis, where the order is visible, as is demonstrated by the SAEDs (Figure 3.4 (a-c)), the DF image of the whole GaInP:Sb layer was acquired (Figure 3.4 (d-f)). As the DF images come from the extra satellite spot the bright contrast corresponds to the regions with order. The dark narrow regions can be identified as APB between the ordered domains. Thus, these dark field two beam images prove the presence of boundaries between the ordered domains (APBD) (Figure 3.4 (d-f)). We name them as APBD to avoid confusion with the antiphase boundaries (APB) separating domains of different polarity, that are usually seen in III-V semiconducting materials. The orientation, extension and width of the domains were quantified in order to detect any possible existing relationship with the degree of order. In addition, the lineal density of APDB was quantified, considering it as the number of APDB divided by the total length of a profile.

Figure 3.5 (a) illustrates how these measurements were done: the angle of the domain boundaries was measured counter clockwise from the interface with the nucleation layer (orange); the ordered/boundary fraction area was quantified in segmented images by applying an intensity threshold to

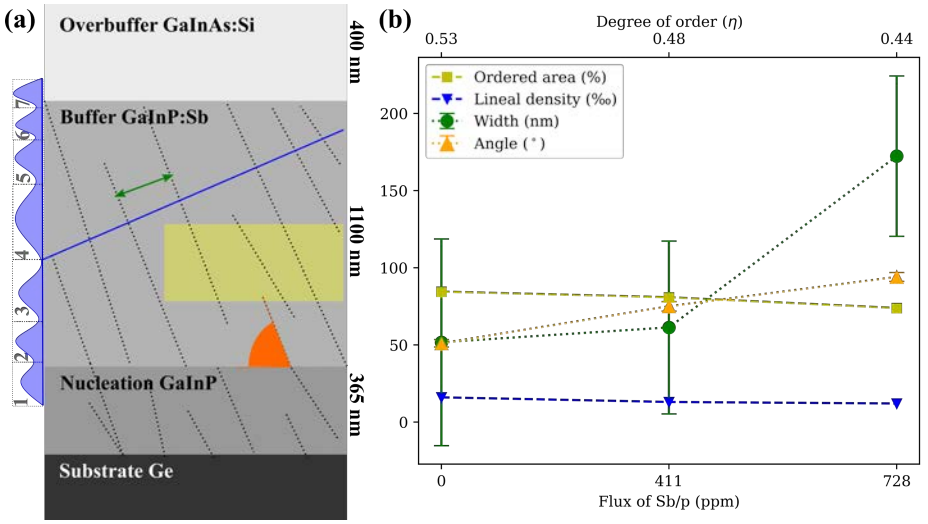

Figure 3.5 Scheme of the samples general appearance with the notation indicating how the domain measurements have been done: domain width (green), lineal density of APDB (blue), fraction of ordered area (yellow) and angle (orange).

Sb/P (ppm)	0	411	728
Degree of order (η)	0.53	0.48	0.44
Width (nm)	52	61	172
Area ordered (%)	85	81	74
Angle (°)	51	78	94
Lineal density APDB (nm-1 ‰)	1.6	1.3	1.2

Table 3.2 Quantitative study of the ordered domains and the antiphase boundaries.

regions with homogeneous contrast (yellow); the linear density was obtained from different profiles, taken along the layer and perpendicular to the APDB, computing the number considering a threshold on the contrast modulation (blue); finally, the domain width was measured perpendicular to the APDB (green). All the measurements were acquired from several regions of the same area and then the average was taken as the reference value. The results of the measurements are summarized in Table 3.2. For all these geometrical measurements, the error has been estimated as the standard deviation. In addition, the ordered fraction cannot be considered reliable as the intensity thresholds were established in a qualitative way. By plotting the dependence of the four parameters, with the error bars for the geometrical ones, as a function of the flux (Figure 3.5(b)) it can be observed that the angle and the linear density are the only variables with a clear dependence on the flux/order parameter. This agrees with previously reported works[22] where the dependence of the angles of the APBs between ordered domains was already verified. However, a relation between the extension of ordered domains and the degree of order was reported[23] which, a priori, it is in contradiction with the present results as the ordered fraction varies oppositely with the degree of order. Thus, a certain cristalline anisotropy appears in the GaInP:Sb layer due to the presence of the CuPt type B ordering and the APDBs and it changes with the degree of order. Even if the extension of the ordered area cannot be related with the degree of order as could have been expected, a slight increase of the linear density of APDB is observed with growing η.

3.4 Z-constrast imaging

In order to analyze the In/Ga alternation and the dumbbell orientation Z-contrast imaging was essential. Thus, HAADF-STEM images at high magnification were acquired to look at the Z-contrast modulation. An aberration corrected Titan FEI instrument operated at 300 kV was used for high resolution high-angle annular dark-field HAADF imaging in the STEM mode.

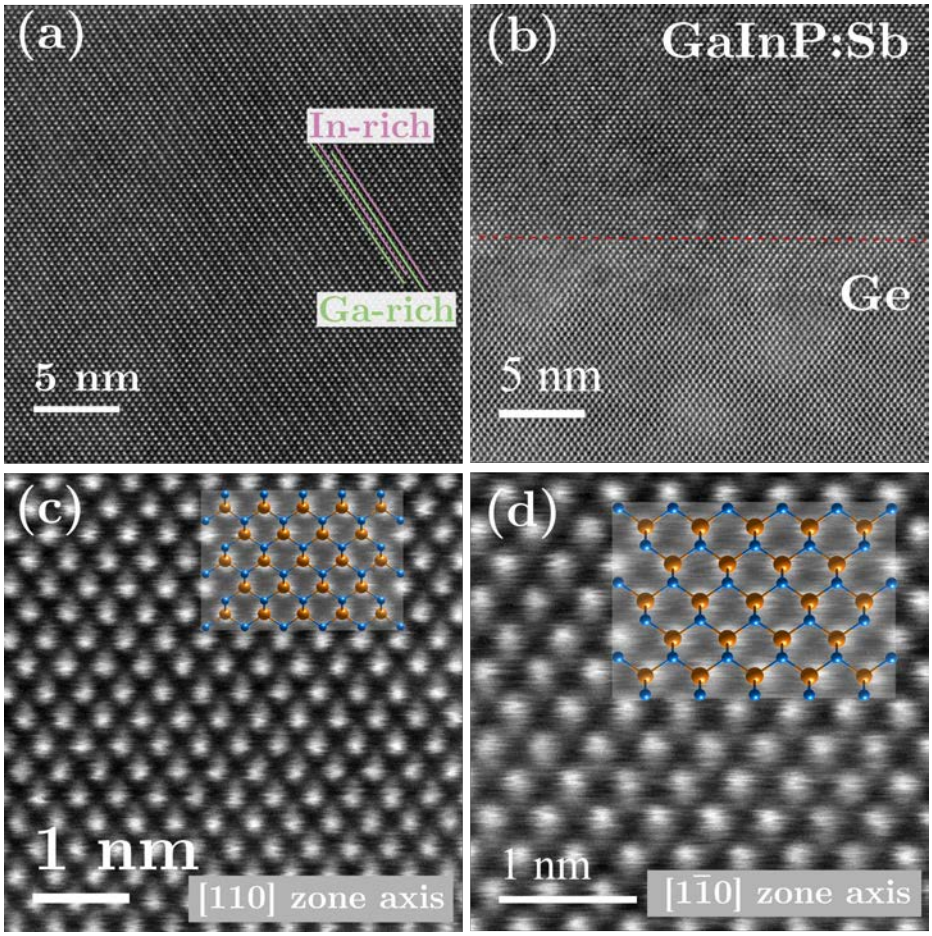

Figure 3.6 HAADF-STEM images of the same sample prepared on the [110] (left) and [1$\bar{1}$0] (right) zone axis. (a) The alternation of brighter (In-rich) and darker (Ga-rich) is visible along the [110] zone axis, on the perpendicular the alternation is not visible (b) (the interface between GaInP and Ge is highlighted in red). (c-d) The change of polarity is shown on a high magnification image, over which the theoretical structure is placed.

3.4.1 Planes alternation and dumbbells polarity

HAADF-STEM images show the double periodicity in the $[1\bar{1}1]$ direction on the $[110]$ zone axis but not on the orthogonal one. The Z-contrast in the HAADF images allows to observe the alternation of brighter and darker planes as highlighted in Figure 3.6(a); however, the ordering disappears on the $[1\bar{1}0]$ zone axis (b). Increasing the magnification, the change in the dumbbell polarity is checked on the $[110]$ zone axis: the group V element occupies the upper position and the group III element the lower one, while in the perpendicular direction this is reversed. In Figure 3.6(c,d) the dumbbells polarity is illustrated by overlapping a scheme of the crystallographic structure along the corresponding directions: the orange balls correspond to In/Ga atoms.

3.4.2 Ordered domains

Referring to the DF two beam imaging (Figure 3.4 (d-f)), the darker regions (APDB) should correspond to regions without the alternation of In and Ga atoms since they appear dark in the dark field mode. It can be checked more carefully at higher magnification computing the inverse Fast Fourier Transform (FFT) filtered using the extra satellite spots of a region with apparent homogeneous order. Figure 3.7 exemplifies the local lack of order in certain regions of the GaInP:Sb layer. The alternation of the Ga and In planes is clearly seen in the HAADF-STEM image (a), where the brighter planes correspond to Indium and the darker planes to gallium. The FFT of the whole region is computed and the satellite spots placed at $\frac{1}{2}(1\bar{1}1)$ are selected to get the inverse FFT (b). The inverse FFT highlights the regions with order by the presence of stripes and the gray regions are apperently regions without ordering.

Two hypotheses could be considered: (I) in the gray regions the alternation is not present or (II) the gray regions correspond to regions with an overlapping of ordered regions, as suggested by [24].

As it has been mentioned in the previous section, the extension of the ordered domains does not fit with the degree of order variations; thus, the second hypothesis (II) was taken into further consideration. In accordance with the study reported in [24], the overlapping could be due to the

superposition of layers with a displacement of half of the unit cell. In order to validate this hypothesis, image simulations were performed.

3.4.3 HAADF image simulations

Rodius from TEM UCA Server was used to build a supercell modelling an overlapping situation but, first, a conventional GaInP cell with order was prepared.

GaInP fully ordered was built by removing the symmetry of an initial 2x2x2 GaP cell [25]. The positions of Ga of the $(1\bar{1}1)$ planes were occupied by In or Ga to get the precise alternation involved by the $CuPt_B$ ordering. The cell parameter was fixed to be double of the one found experimentally, 11.32 Å. Thereon a model with P1-symmetry, 64 non-equivalent atoms structure with $CuPt_B$ ordering was obtained. The lattice parameter was verified by comparison with the experimental diffraction patterns.

The supercell model consists in a superposition of two blocks of GaInP oriented along the $[110]$ zone axis with a displacement of half a unit cell between them in the perpendicular direction, $[00\bar{1}]$. The total thickness of the block is h = 60 Å (around 11 unit cells of GaInP) and it was kept

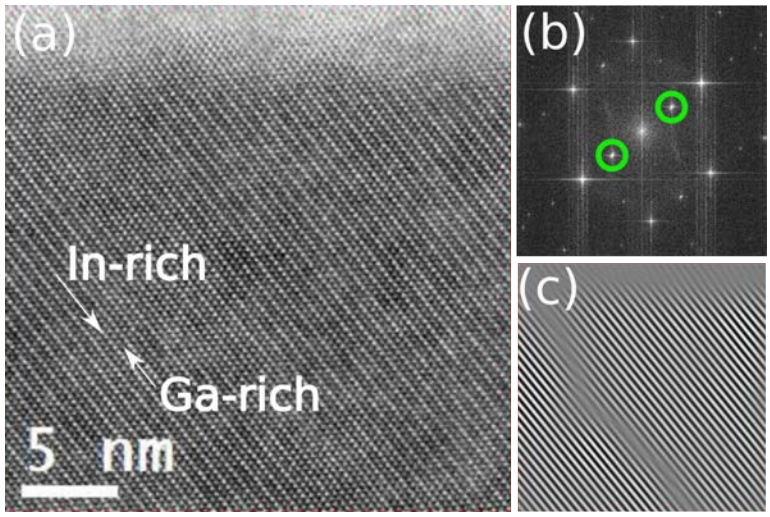

Figure 3.7 (a) HAADF-STEM image of the sample with a flux containing 411 ppm of Sb ($\eta = 0.48$) along $[110]$ zone axis. (b) FFT of the whole area and, highlighted in green, applied mask selecting the satellite spots. (c) Inverse FFT of the masked Fourier Transform, highlighting the ordered regions.

constant. A scheme of this atomistic model is shown in Figure 3.8 (a), where the darkest region (which thickness is given as a fraction of h) corresponds to the displaced block. Several simulations were performed for different thicknesses (t), from 0.2 times h to 0.5 times h.

The simulations were performed using *autoslic* from *computem* by Kirkland[26], and the parameters were set to fit the experimental ones. The voltage of the incident electron beam was set at 300 keV and, as a corrected microscope was used, the spherical aberration at third order was set at 0.3 μm. The objective aperture chosen was of 11.43 mrad. The resolution of the probe was set at 128 x 128 pixels, while the object was made of 512 x 512 pixels. To avoid aliasing, 2048 x 2048 pixels were selected as the sampling

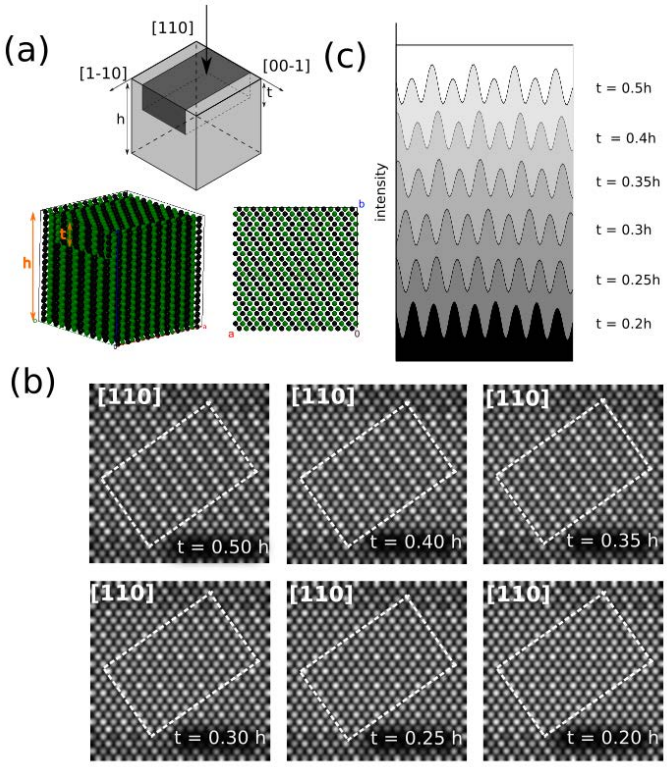

Figure 3.8 : (a) Scheme of the atomistic model used in the HAADF-STEM simulations. (b) HAADF-STEM simulated images for different t values. (c) Intensity profiles (integrated in the highlighted regions in (b)) along the $[1\bar{1}1]$ direction in the simulated HAADF images, showing the evolution of the apparent ordering degree as a function of thickness (t).

of the final image. According to the radius of the HAADF detector the sensitive range started at 74 mrad and ended at approximately 300 mrad.

Several simulations were performed for different thicknesses (t). From the simulated images, the intensity profiles were measured perpendicular to the ordered planes, along the $[1\bar{1}1]$ direction. The results are presented in Figure 3.8(c); for values above t=0.35h the Z-contrast due to ordering is still visible. Nevertheless, for thickness values equal and below t=0.3h the intensity variation flattens out. The simulated HAADF-STEM images (Figure 3.8 (b)) show that the order of (111) In rich/Ga rich planes is easily seen for thick superposed layers and that as the superposed layer gets thinner the ordering becomes indistinguishable. A thin enough ordered region displaced with respect to another underneath ordered region does effectively appear as the characteristic Z-contrast of a sample without order. The correct interpretation of the observed ordered/disordered regions based on Z-contrast is thus a key issue to account for an appropriate accordance with the order parameter estimated from previous PL measurements, giving higher fractions of ordered areas for lower Sb/P ratios and solving the apparent lack of agreement with high order parameter samples with the ordered area fraction or the extension of the ordered domains measured in conventional dark field imaging mode.

3.5 In situ measurements

In situ electrical TEM measurements were performed to observe more carefully the possible effect of the anisotropy on the optoelectronic properties. In order to get relevant data, the setup of the in-situ experiment was prepared thoroughly. For each sample two lamellas were prepared on the orthogonal directions ([110] and [$\bar{1}$10]) and attached to the holder as is sketched in Figure 3.9 (a). This is a simplified sketch of the situation inside the TEM column, and the proportions are not realistic. With this configuration the electron current was measured perpendicular to the APDB for the sample prepared along the [110] zone axis and parallel to the APDB for the orthogonal one (Figure 3.9 (b)).

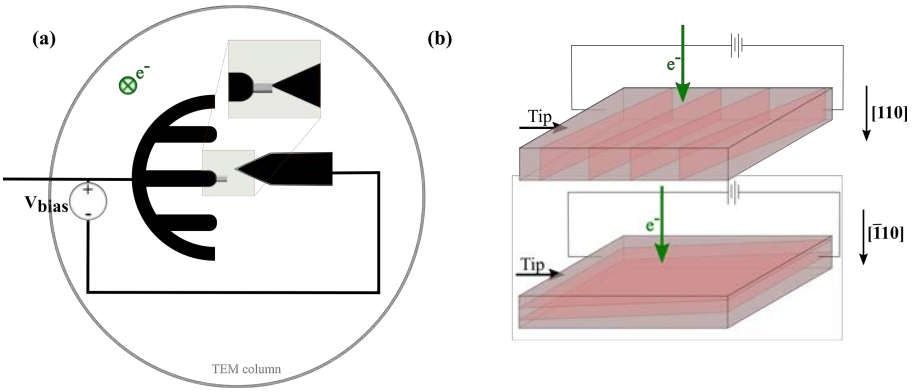

Figure 3.9 In situ measurements set up. (a) Configuration inside the TEM column. (b) Scheme of the lamella contact.

The I(V) curve for both orientations was acquired, which allows to calculate the mobility ratio. The mobility depends on the doping amount, the charge and the resistivity (ρ), which can be determined from the resistivity obtained from the I(V) and the geometry of the GaInP structures obtained from the TEM images and considering the thickness of the TEM lamella to be 100 nm.

$$\boldsymbol{\mu}\left[\frac{cm^2}{Vs}\right] = \frac{100}{\boldsymbol{q}[C]\boldsymbol{N_A}[cm^{-3}]\boldsymbol{\rho}[\Omega m]}$$

The results evidenced a dependence of the mobility anisotropy between degree of order. As can be checked on Table 3.3 the higher the order parameter, the larger the anisotropy. A direct relation of this anisotropy and the presence of the antiphase boundaries can be established. The APDB are defects that can have the role of active recombination centers, as has been reported[27–31]. As highlighted before, the APDB angle and their linear density change within the degree for order. That involves a loss of perpendicularity and an increase in the total number of APDB as the degree of order increases. Thus their impact as recombination centers can also

Sb/P (ppm)	**η**	**N_A ($10^{16}cm^{-3}$)**	**$\rho[1\bar{1}0]$ (Ω·m)**	**$\mu[1\bar{1}0]$ (cm^2/Vs)**	**$\rho[110]$ (Ω·m)**	**$\mu[110]$ (cm^2/Vs)**	**$\frac{\mu[110]}{\mu[1\bar{1}0]}$**
0	0.53	8,9±2,2	63,0±4,0	111±35	11,5±0,5	611±179	5.5
411	0.48	15±4	43,9±0,2	95±24	10,6 0,1	393±102	4.1
1721	0.31	43±11	5,46±0,02	266±68	4,95±0,01	294±74	1.1

Table 3.3 In situ resistivity measurements in both crystal directions compared with the degree of order, the doping of the layers and the Sb/P ratio. The mobility in each crystal direction and their ratio has also been calculated from resistivity values and dopant concentration.

change as a function of η.

3.6 Density Functional Theory calculations

Until now in all the analyses the APDB had a relevant role. However, the simple fact of having an alternation of Ga and In atoms deserves more attention. DFT calculations were considered the best way to study the effect of CuPtB on the optoelectronic properties of the compound.

3.6.1 Cell modelling and structure relaxation

Two conventional cells of $CuPt_B$ ordered and disordered GaInP were modelled. The ordered model was built as already explained in the atomic simulations section, while the disordered one was the same, with the exception that the III-group positions were randomly occupied by Ga and In; a sequence of random numbers was used to avoid any additional ordering. The models (Figure 3.10) correspond to the extreme cases, fully ordered (η=1) (a) and completely random (η=0) (b) in an idealistic model.

	Ordered	Disordered
Lattice parameters	a = 11.27918	a = 11.25265
	b = 11.27918	b = 11.26736
	c = 11.27918	c = 11.27037
Angles	α = 89.9988	α = 89.8153
	β = 90.0178	β = 89.8153
	γ = 90.0176	γ = 89.8153

Table 3.4 Lattice parameter for both structures after the structural relaxation.

First, structural relaxation was performed for both models. Structural relaxation consists in applying small variations in the lattice parameters and/or in the atomic positions in order to minimize the total energy and forces of the whole structure. In the present case VASP, package was used to perform the structural relaxation. The atomic positions and the lattice parameters were tuned until the energy of the system reached the minimum. The exchange potential used was the PBE with a cutoff energy of 200 eV for the plane waves. A 11x11x11 Monkhorst-Pack k-point grid in the Brillouin zone was considered.

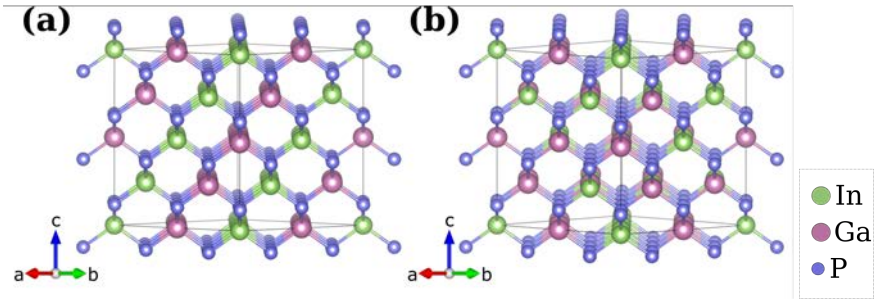

Figure 3.10 GaInP cells prepared for the DFT calculations: (a) ordered GaInP and (b) disorderd GaInP. Both cubic cells have a lattice parameter of 11.32Å.

The resulting structures (summarized in Table 3.4) were slightly different from the original ones and it is important to notice that, after the relaxation, the ordered and the random structures have different lattice parameters.

3.6.2 Density of states: bandgap optimization

Starting from the relaxed structures the Self-Consistency Cycle (SCF) was computed to find the electron density and, from there, the Density of States (DOS), the Energy Loss Function (ELF) and the band structure were calculated. Before that, the SCF cycle was optimized to avoid a bandgap underestimation. In order to increase the bandgap, the generalized gradient approximation (GGA-PBE)[32] including the Hubbard model, which considers an extra onsite Coulomb interaction[33], was used. The effect of using this hybrid method is a controlled expansion of the bandgap; however, the proper value of U_{eff} is found iteratively until optimitzation. In Figure 3.11 the DOS for the ordered GaInP structure is plotted to illustrate the effect of the PBE+U method. For example, by applying a U_{eff} of -15 eV to the phosphorous atoms the bandgap shifts from 0.624 eV (a), with U_{eff} =0, to 1.597 eV (b), an absolute increment of 1eV.

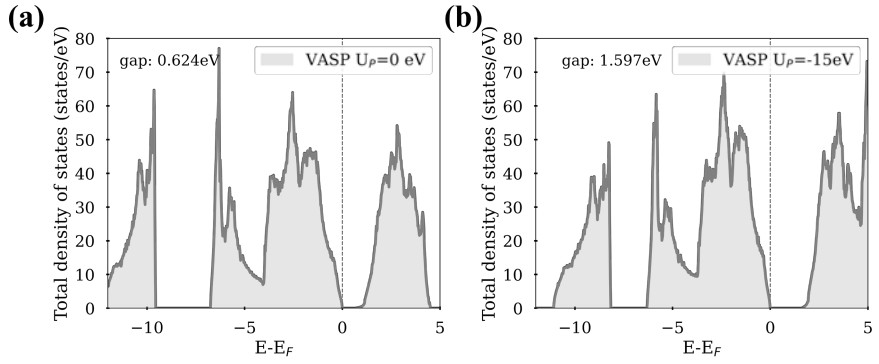

Figure 3.11 Total DOS of the ordered structure (a) PBE approximation and (b) PBE+U approximation.

The proper value of Hubbard potential was found using VASP, as it is faster than WIEN2k. Figure 3.12 (a) shows the values of the bandgap as a function of the value of the U_{eff} applied to the different atoms (P, Ga or In). It is clearly seen that the most influent one is the U_{eff} to P. Figure 3.12 (b)

compares the values of the bandgap as a function of the degree of order for the simulated data, the experimental one and the one approximated, using the quadratic expression reported by Wei [18].

Once the U_{eff} value was stablished to be -18 eV for all atoms of group V (P) for the disordered structure, the same calculation was performed using two different code packages (WIEN2k and VASP) obtaining close results. From that point WIEN2k was used, as it enables to compute the optical properties in an easier way.

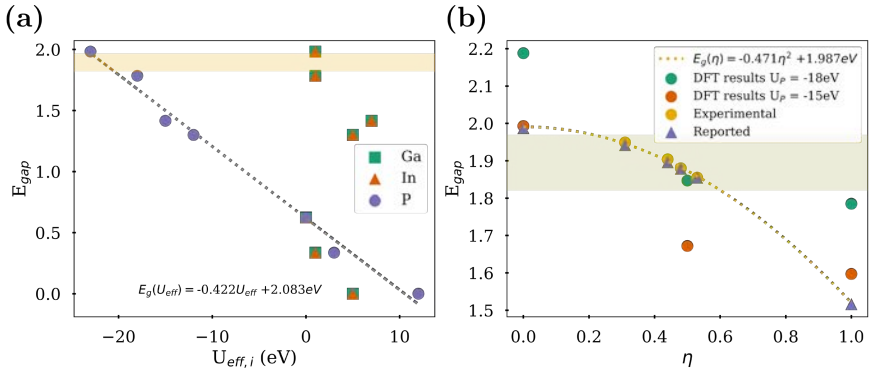

Figure 3.12 Determination of U_{eff}. (a) Values of the energy bandgap for the fully ordered case as a function of the U_{eff} applied to the phosphorus (purple-circle), the gallium (green-square) or indium (orange-triangle). (b) Comparison of the energy bandgap of different idealistic partially ordered models with the experimental (yellow -circle) and fitted data (dashed line). The regions of interest are highlighted in yellow and green.

3.6.3 Optical properties: inter-band transitions

The energy loss function (ELF) and the complex dielectric function (CDF) were computed using the OPTIC[34–36] task of the WIEN2k package[37,38]. The Perdew-Burke-Ernzerhof [39](PBE) functional was used setting RKmax to 7.0 and defining 500 k-points on the Brillouin zone. The energy and charge convergence criteria were set to 0.0001 Ry and 0.001 e, respectively.

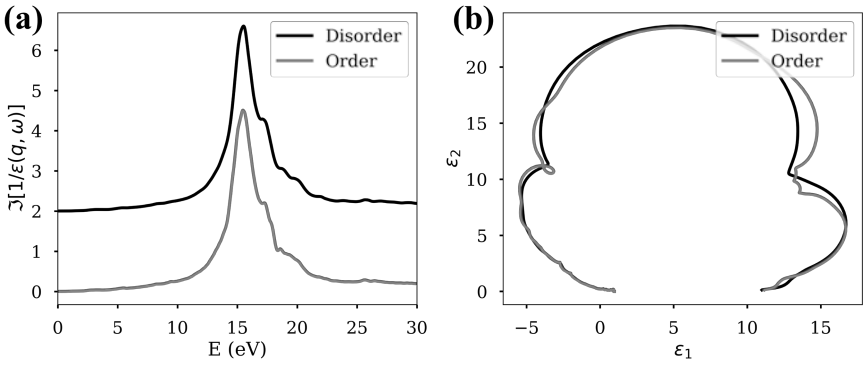

Figure 3.13 (a) Energy loss function (Im[$1/\varepsilon$]) for the ordered and disordered cells and (b) cole-cole diagram for both phases.

As it is shown in Figure 3.13, the ELFs do not present significant difference. However, some difference on the peaks' prominence can be noticed. By plotting the cole-cole diagram, which consists in plotting the imaginary part of the CDF as a function of the real part, it is easy to check the presence of more inter-band transitions for the ordered phase; as the more loops appear on the plot the higher the number of inter-band transitions. In more detail, Figure 3.13 (a) displays the ELF obtained from the DFT calculations for both models; they present a sharp plasmon around 15.5 eV, in good agreement with the experimental results, assigned to the bulk plasmon. It is found to present a positive slope when analyzing the real part of the CDF (Figure 3.14(a-b)) for both structures. The simulations clearly establish that different inter-band transitions are allowed in each case, as the ELF post-peak region shows finer structure for the ordered case. By comparing both cole-cole diagrams, it can be determined that extra inter-band transitions are allowed for the ordered case (Figure 3.13(b)). The inter-band transitions are also visible in the imaginary part of the CDF (ε_2), where they correspond to the main peaks (Figure 3.14(a-b)). The plots show

that, for the ordered structure, there are three sharp peaks, while for the disordered just one is clearly a peak and the other two are shoulders. The DOS alongside with the CDF allows the determination of the nature of these transitions. As shown in Figure 3.14(a,c), for the disordered model, three main inter-band transitions are observed in the ELF at 17, 18.6 and 19.8 eV; they correspond to a transition between the d occupied band to the unoccupied p band(d→p) for In and Ga atoms. Controversely, the ordered model (Figure 3.14 (b,d)) presents an extra transition at 21.5 eV, clearly visible in the ε_2; this transition is a d→p transition for In atoms.

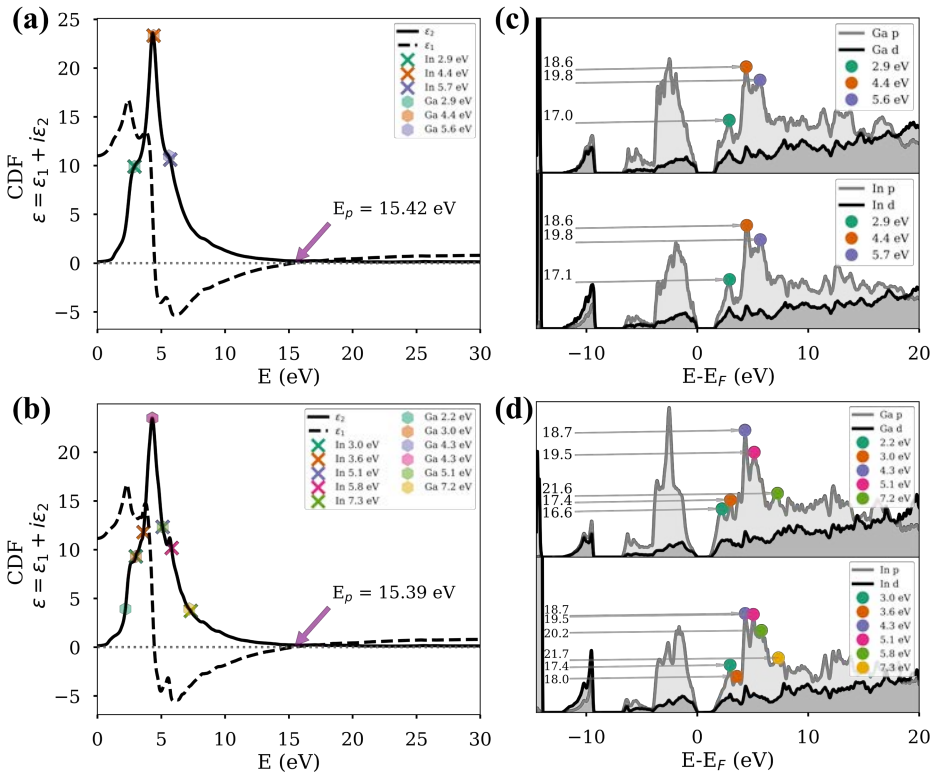

Figure 3.14 CDF computed for the disordered structure (a) and for the ordered structure (b) with plots of the real (solid line) and the imaginary (dashed line) parts of the CDF. The partial density of states for the In and Ga atoms for both structures are plotted, (c) for the disordered structure and (d) for the ordered case. The inter-band transitions are highlighted with the same color on both plots to be uniquely identified.

3.6.4 Effective mass and band structure

The effective mass tensor calculation was performed using perturbation theory for both structures, considering 1k bands in order to compare them with the changes observed in the mobility ratio experimentally calculated from the in-situ TEM electrical measurements. The electron effective masses for the conduction band was found to be 0.092 m_0 for the ordered case and 0.090 m_0 for the disordered one. Also, the effective mass for the heavy (hh) and light holes (lh) were computed for the valence band, which would be responsible for the conductivity in these samples. Table 3.5 shows the

	Ordered	Disordered
E_g	1.785 eV	2.188 eV
m^*_e	0.092 m_0	0.090 m_0
m^*_{hh}	0.234 m_0	0.198 m_0
m^*_{lh}	0.185 m_0	0.189 m_0
E_{hh}-E_{lh}	57 meV	17 meV
E_{hh}-E_{so}	285 meV	107 meV

Table 3.5 Summary of the bandgap energy (E_g), electron effective mass (m^*_e), heavy/light holes effective mass (m^*_{hh}/m^*_{lh}), energy splitting of the valence band (heavy - light holes (E_{hh}-E_{lh}) and heavy hole -split orbit (E_{hh}-E_{so})) computed for both structures.

results, which are in good agreement with the work performed by Emanuelsson, et al. using $\mathbf{k} \cdot \mathbf{p}$ perturbation theory on an eight band model[40,41].

Finally, in order to assess a potential anisotropy in the ordered structure depending on the direction, the band structure was plotted along a very specific k-path. To obtain a comprehensible band structure, a crystallographic structure as simple as possible is needed, with high symmetry and low number of non-equivalent atoms. A high symmetry structure was extracted from the relaxed ordered GaInP cell where the new structure has R3m symmetry, space group 160[42]. The R3m structure presents 4 non-equivalent atomic positions occupied by Ga, In and two P atoms. The lattice parameters were found to be a = b = c =6.96 Å and the angles $\alpha = \beta = \gamma = 33.41^o$.

The Modified Becke-Johnson (MBJ) exchange potential[43] was considered for the high symmetry ordered case in order to increase the bandgap. Spin-orbit splitting was considered to obtain the inverse mass tensor by using the mstar code developed for WIEN2k[44] based on perturbation theory. KVEC from Bilbao Crystallographic Server [45,46] was used to get the proper coordinates of the high symmetry K-points and SeeK-path to visualize the Brillouin zone of our structures[47].

First, DOS and CDF were computed for the new structure to check that no contradiction with the previous P1 model exists. Both, DOS and CDF, did not present any important difference, allowing to consider them equivalent. Then the band-structure along the S_0-Γ-T and T- Γ-M_8 k-path was plotted. The selection of these specific k-points was done to compare the direction where the alternation of In/Ga planes is present and the perpendicular one. In Figure 3.15(a) a 2x2x2 $GaInP_2$ is shown to illustrate the $(\bar{1}\bar{1}1)$ plane in orange, where the order is visible, and the orthogonal $(\bar{1}\bar{1}2)$ in green. The k-path can be added to the First Brillouin Zone and is displayed in Figure 3.15(insets).

The obtained band structure is asymmetric with respect to the Γ point and, as the curvature of the band at the gamma point is related to the effective mass of the electron/hole according to the following expression

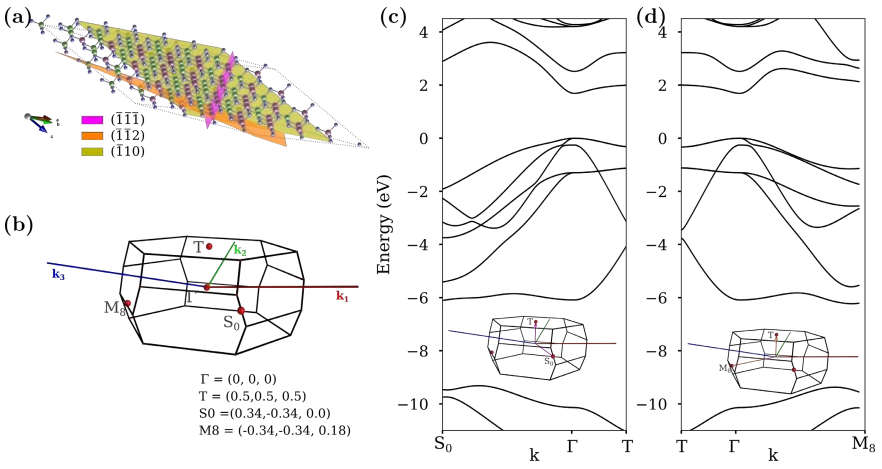

Figure 3.15 2x2x2 $GaInP_2$ R3m supercell with P atoms in blue, Ga in pink and In in green. (-1-12) and (-1-1-1) planes are highlighted in orange and green respectively. (b) First Brillouin Zone of the GaInP R3m. Band structure plotted along the S_0-Γ-T (c) and T- Γ-M_8 (d) k-paths.

(55), an asymmetry depending on the direction of the effective mass is deduced.

$$m^*_{eff} = \hbar \frac{1}{\frac{\partial^2 E_n}{\partial k^2}\Big|_{k_{ex}}} \quad (56)$$

The asymmetry agrees with previously reported works[48,49]. The maximum of the valence band has been fitted to a parabolic function obtaining a different fit by each side of the maximum. The theoretical effective mass ratio has been calculated for the fully ordered case, obtaining a ratio of 1.5. In addition, if the anisotropy is quantified according to the expression $\frac{m_{\parallel}-m_{\perp}}{m_{alloy}} \cong 0.5\, m_e$, where $m_{\parallel}$is the effective mass in the ordering direction and $m_{\perp}$ on the perpendicular one, in agreement of the value reported for the fully ordered case by Franceschetti *et al.*[49] From these results, we can conclude that not only APDBs but also the anisotropic behaviour of the effective mass has a role in the anisotropy of the electrical conductivity of CuPtB type ordered GaInP thin films observed by in-situ TEM.

3.7 Conclusions

The main conclusions of this chapter can be summarized as follows:

- The presence of CuPtB type ordering has been assessed by electron diffraction and HAADF-STEM imaging.
- The antiphase boundaries between ordered domains have been precisely analyzed as a function of Sb/P ratio in the flux combining dark field two beam imaging and atomistic simulations of HAADF images. The effect of having overlapping ordered displaced layers that can mask order related contrast has been analyzed. A dependence of the angle of the APDB with the degree of order has been found.
- The anisotropy of carrier mobility has been studied and quantified using electrical in situ TEM as a function of the APDB orientation. The increase of the ratio between the mobility in two orthogonal directions as the degree of order increases demonstrates the role of the APDBs as a recombination center.

- The effect of atomic ordering on conductivity has been examined from the most fundamental point of view using DFT calculations, reaching the following conclusions:
    - The presence of $CuPt_B$ has a direct effect on the energy bandgap in agreement with the PL measurements.
    - The Ga and In alternation opens the possibility of extra inter-band transitions as demonstrated by the analysis of the CDF and the PDOS.
    - The effective masses of both structures, ordered and disordered, do not present a significant difference as shown by the perturbation theory calculations.
    - In a fully ordered structure a change in the effective mass appears between the direction where the order is visible and the orthogonal directions, as it is apparent from the band structure, indicating an anisotropy of the effective mass.
    - The differences in conductivity are thus shown to be a consequence of the APDBs and of the ordering.

3.8 References

[1] T.N. Lin, S.R.M.S. Santiago, J.A. Zheng, Y.C. Chao, C.T. Yuan, J.L. Shen, C.H. Wu, C.A.J. Lin, W.R. Liu, M.C. Cheng, W.C. Chou, Enhanced Conversion Efficiency of III–V Triple-junction Solar Cells with Graphene Quantum Dots, Scientific Reports. 6 (2016). https://doi.org/10.1038/srep39163.

[2] M. Rudolph, K. Beilenhoff, P. Heymann, Scalable GaInP/GaAs HBT Large-Signal Model, 2000 IEEE MTT-S International Microwave Symposium Digest. 48 (2000) 2370–2376. https://doi.org/10.1109/MWSYM.2000.863291.

[3] Y.-J. Chan, D. Pavlidis, Trap Studies in GaInP/GaAs and AlGaAs/GaAs HEMT's by Means of Low-Frequency Noise and Transconductance Dispersion Characterizations, IEEE TRANSAnIONS ON ELECTRON DEVICES. (1994) 637–642.

[4] J.F. Ahadian, P.T. Vaidyanathan, S.G. Patterson, Y. Royter, D. Mull, G.S. Petrich, W.D. Goodhue, S. Prasad, L.A. Kolodziejski, C.G. Fonstad, Practical OEIC's Based on the Monolithic Integration of GaAs-InGaP LED's with Commercial GaAs VLSI Electronics, 1998. https://doi.org/10.1109/3.687852.

[5] F. Bugge, A. Knauer, S. Gramlich, I. Rechenberg, G. Beister, J. Sebastian, H. Wenzel, G. Erbert, M. Weyers, MOVPE Growth of AlGaAs/GaInP Diode Lasers, Journal of Electronic Materials. 29 (2000).

[6] J.F. Geisz, M.A. Steiner, I. García, S.R. Kurtz, D.J. Friedman, Enhanced external radiative efficiency for 20.8% efficient single-junction GaInP solar cells, Applied Physics Letters. 103 (2013) 041118. https://doi.org/10.1063/1.4816837.

[7] S.P. Philipps, F. Dimroth, A.W. Bett, High-efficiency III-V multijunction solar cells, in: McEvoy's Handbook of Photovoltaics: Fundamentals and Applications, Academic Press, 2018: pp. 439–472. https://doi.org/10.1016/B978-0-12-809921-6.00012-4.

[8] Chiu PT, Law DC, Woo RL, Singer SB, Bhusari D, Hong WD, 35.8% space and 38.8% terrestrial 5J direct bonded cells, IEEE 40th Photovoltaic Specialist Conference. (2014) 11–13.

[9] M.A. Green, K. Emery, Y. Hishikawa, W. Warta, E.D. Dunlop, D.H. Levi, A.W.Y. Ho-Baillie, Solar cell efficiency tables (version 49), Progress in Photovoltaics: Research and Applications. 25 (2017) 3–13. https://doi.org/10.1002/pip.2855.

[10] J.F. Geisz, R.M. France, K.L. Schulte, M.A. Steiner, A.G. Norman, H.L. Guthrey, M.R. Young, T. Song, T. Moriarty, Six-junction III-V solar cells with 47.1% conversion efficiency under 143 Suns concentration,. https://doi.org/10.1038/s41560-020-0598-5.

[11] P. Bellon, J.P. Chevalier, G.P. Martin, E. Dupont-Nivet, C. Thiebaut, J.P. Andre, Chemical ordering in GaxIn1-xP semiconductor alloy grown by metalorganic vapor phase epitaxy., Appl. Phys. Lett. 52 (1988) 567.

[12] A. Gomyo, T. Suzuki, S. Iijima, Observation of Strong Ordering in GaInP alloy semiconductors, Phys. Rev. Lett. 60 (1988) 2645–2648.

[13] P. Bellon, J.P. Chevalier, E. Augarde, J.P. André, G.P. Martin, Substrate-driven ordering microstructure in GaxIn1−xP alloys, Journal of Applied Physics. 66 (1989) 2388. https://doi.org/10.1063/1.344245.

[14] J.K. Shurtleff, R.T. Lee, C.M. Fetzer, G.B. Stringfellow, Band-gap control of GaInP using Sb as a surfactant, Applied Physics Letters. 75 (1999) 1914–1916. https://doi.org/10.1063/1.124869.

[15] E. Barrigón, L. Barrutia, I. Rey-Stolle, Optical in situ calibration of Sb for growing disordered GaInP by MOVPE, Journal of Crystal Growth. 426 (2015) 71–74. https://doi.org/10.1016/j.jcrysgro.2015.05.020.

[16] E. Barrigon, B. Galiana, I. Rey-Stolle, Reflectance anisotropy spectroscopy assessment of the MOVPE nucleation of GaInP on germanium (1 0 0), Journal of Crystal Growth. 315 (2011) 22–27. https://doi.org/10.1016/j.jcrysgro.2010.09.038.

[17] E. Barrigón, L. Barrutia, I. Rey-Stolle, Optical in situ calibration of Sb for growing disordered GaInP by MOVPE, Journal of Crystal Growth. 426 (2015) 71–74. https://doi.org/10.1016/j.jcrysgro.2015.05.020.

[18] S.H. Wei, D.B. Laks, A. Zunger, Dependence of the optical properties of semiconductor alloys on the degree of long-range order,

Applied Physics Letters. 62 (1993) 1937–1939. https://doi.org/10.1063/1.109496.

[19] P. Ernst, C. Geng, F. Scholz, H. Schweizer, Y. Zhang, A. Mascarenhas, Band-gap reduction and valence-band splitting of ordered GaInP2, Applied Physics Letters. 67 (1995) 2347–2349. https://doi.org/10.1063/1.114340.

[20] S.H. Lee, C.M. Fetzer, G. Stringfellow, C.-J. Choi, T. Seong, Step structure and ordering in Zn-doped GaInP., J. Appl. Phys. 86 (1999) 1982.

[21] J.M. Olson, W.E. McMahon, S. Kurtz, Effect of Sb on the Properties of GaInP Top Cells, 4th IEEE World Conference on Photovoltaic Energy Conversion. 1 (2006) 787–790.

[22] L.C. Su, I.H. Ho, G.B. Stringfellow, Effects of substrate misorientation and growth rate on ordering in GaInP, J. Appl. Phys. 75 (1994) 5135–5141.

[23] S.P. Ahrenkiel, M.C. Hanna, Antiphase-boundary extension in single-variant CuPt-B ordered Ga0.47In0.53As on InP, Appl. Phys. Lett. 79 (2001) 1781–1782.

[24] G. Hahn, C. Geng, P. Ernst, H. Schweizer, F. Scholz, F. Phillipp, Investigations on domain boundaries in ordered GaInP using stereo transmission electron microscopy, 1997. https://doi.org/10.1006/spmi.1996.0456.

[25] J. Zemann, Crystal structures, 2 nd edition. Vol. 1 by R. W. G. Wyckoff, Acta Crystallographica. 18 (1965) 139–139. https://doi.org/10.1107/s0365110x65000361.

[26] E.J. Kirkland, Advanced Computing in Electron Microscopy, 2010. https://doi.org/10.1088/1751-8113/44/8/085201.

[27] G. Attolini, C. Bocchi, F. Germini, C. Pelosi, A. Parisini, L. Tarricone, R. Kùdela, S. Hasenohrl, Effects of inhomogeneities and ordering in InGaP/GaAs system grown by MOVPE, Materials Chemistry and Physics. 66 (2000) 246–252. https://doi.org/10.1016/S0254-0584(00)00319-9.

[28] S. Hasenöhrl, J. Novák, R. Kúdela, J. Betko, M. Morvic, J. Fedor, Anisotropy in transport properties of ordered strained InGaP,

Journal of Crystal Growth. 248 (2003) 369–374. https://doi.org/10.1016/S0022-0248(02)01873-0.

[29] J. Novák, S. Hasenöhrl, R. Kúdela, M. Kučera, D. Wüllner, H.H. Wehmann, Resistivity anisotropy in ordered InxGa1-xP grown at 640°C, Applied Physics Letters. 73 (1998) 369–371. https://doi.org/10.1063/1.121837.

[30] L. Chernyak, A. Osinsky, H. Temkin, A. Mintairov, I.G. Malkina, B.N. Zvonkov, Y.N. Saf'anov, Transport anisotropy in spontaneously ordered GaInP2alloys, Applied Physics Letters. 70 (1997) 2425–2427. https://doi.org/10.1063/1.118864.

[31] L. Nasi, G. Salviati, M. Mazzer, C. Zanotti-Fregonara, Influence of surface morphology on ordered GaInP structures, Applied Physics Letters. 68 (1995) 3263–3265. https://doi.org/10.1063/1.116568.

[32] J.P. Perdew, J.A. Chevary, S.H. Vosko, K.A. Jackson, M.R. Pederson, D.J. Singh, C. Fiolhais, Atoms, molecules, solids, and surfaces: Applications of the generalized gradient approximation for exchange and correlation, PHYSICAL REVIEW B. 46 (1992) 6672–6687.

[33] C. Loschen, J. Carrasco, K.M. Neyman, F. Illas, First-principles LDA+U and GGA+U study of cerium oxides: Dependence on the effective U parameter, Physical Review B - Condensed Matter and Materials Physics. 75 (2007) 1–8. https://doi.org/10.1103/PhysRevB.75.035115.

[34] C. Hébert, Practical aspects of running the WIEN2k code for electron spectroscopy, Micron. 38 (2007) 12–28. https://doi.org/10.1016/j.micron.2006.03.010.

[35] A. Eljarrat, X. Sastre, F. Peiró, S. Estradé, Density Functional Theory Modeling of Low-Loss Electron Energy-Loss Spectroscopy in Wurtzite III-Nitride Ternary Alloys, Microsc. Microanal. 22 (2016) 706–716. https://doi.org/10.1017/S1431927616000106.

[36] C. Ambrosch-Draxl, J.O. Sofo, Linear optical properties of solids within the full-potential linearized augmented planewave method, Computer Physics Communications . 175 (2006) 1–14.

[37] P. Blaha, K. Schwarz, G. Madsen, D. Kvasnicka, J. Luitz, WIEN2k: An Augmented Plan Wave Plus Local Orbitals Program for Calculating Crystal Properties, 2014.

[38] P. Blaha, K. Schwarz, F. Tran, R. Laskowski, G.K.H. Madsen, L.D. Marks, WIEN2k: An APW+lo program for calculating the properties of solids, Journal of Chemical Physics. 152 (2020) 74101. https://doi.org/10.1063/1.5143061.

[39] J.P. Perdew, K. Burke, M. Ernzerhof, Generalized Gradient Approximation Made Simple, PHYSICAL REVIEW LETTERS. 77 (1996) 3865–3868.

[40] P. Emanuelsson, M. Drechsler, D.M. Hofmann, B.K. Meyer, M. Moser, F. Scholz, Cyclotron resonance studies of GaInP and AlGaInP, Applied Physics Letters. 64 (1994) 2849–2851. https://doi.org/10.1063/1.111445.

[41] I. Vurgaftman, J.R. Meyer, L.R. Ram-Mohan, Band parameters for III-V compound semiconductors and their alloys, Journal of Applied Physics. 89 (2001) 5815–5875. https://doi.org/10.1063/1.1368156.

[42] A. Jain, S.P. Ong, G. Hautier, W. Chen, W.D. Richards, S. Dacek, S. Cholia, D. Gunter, D. Skinner, G. Ceder, K.A. Persson, Commentary: The materials project: A materials genome approach to accelerating materials innovation, APL Materials. 1 (2013). https://doi.org/10.1063/1.4812323.

[43] D. Koller, F. Tran, P. Blaha, Merits and limits of the modified Becke-Johnson exchange potential, PHYSICAL REVIEW B. 83 (2011) 195134. https://doi.org/10.1103/PhysRevB.83.195134.

[44] O. Rubel, F. Tran, X. Rocquefelte, P. Blaha, Perturbation approach to ab initio effective mass calculations, Computer Physics Communications. 261 (2021). https://doi.org/10.1016/j.cpc.2020.107648.

[45] M.I. Aroyo, D. Orobengoa, G. de La Flor, E.S. Tasci, J.M. Perez-Mato, H. Wondratschek, Brillouin-zone database on the Bilbao Crystallographic Server, Acta Crystallographica Section A: Foundations and Advances. 70 (2014) 126–137. https://doi.org/10.1107/S205327331303091X.

[46] E.S. Tasci, G. de La Flor, D. Orobengoa, C. Capillas, J.M. Perez-Mato, M.I. Aroyo, An introduction to the tools hosted in the Bilbao Crystallographic Server, EPJ Web of Conferences. 22 (2012). https://doi.org/10.1051/epjconf/20122200009.

[47] Y. Hinuma, G. Pizzi, Y. Kumagai, F. Oba, I. Tanaka, Band structure diagram paths based on crystallography, Computational Materials Science. 128 (2017) 140–184. https://doi.org/10.1016/j.commatsci.2016.10.015.

[48] Y. Zhang, A. Mascarenhas, Conduction-and valence-band effective masses in spontaneously ordered GaInP2, PHYSICAL REVIEW B. 51 15–1995.

[49] A. Franceschetti, S.H. Wei, A. Zunger, Effects of ordering on the electron effective mass and strain deformation potential in GaInP2: Deficiencies of the kp model, Physical Review B. 52 (1995) 13992–13997. https://doi.org/10.1103/PhysRevB.52.13992.

Chapter 4: Oxygen Vacancies in Bismuth Oxide

In this Chapter an in-depth study of Bi_2O_3 EELS features as related to Bi oxidation state will be presented. Three different Bi_2O_3 samples with the same nominal stoichiometry were analyzed. Macroscopic spectroscopic techniques were used to assess the presence of oxygen vacancies. A morphological and structural characterization was carried out by atomic resolution transmission electron microscopy. Electron Energy Loss Spectroscopy experimental results were obtained and compared to Density Functional Theory calculations to identify the ELNES signatures indicating oxygen vacancies in Bi_2O_3.

4.1 State of the art – Motivation

Post-transition metal oxides have become increasingly interesting in recent years, as they have been reported to exhibit a wide variety of crystalline structures and magnetic properties due to the hybridization of their d orbitals. In particular, bismuth oxide (Bi_2O_3) is a widely used material in the state-of-the- art of many technological fields such as gas sensors[1,2], optical devices[3,4], and solid oxide fuel cells[5,6]. However, the functional properties of Bi_2O_3 are strongly dependent on its crystalline phase. Bismuth oxide is a polymorph with four main crystallographic phases: the monoclinic α-phase[7], which is stable at low temperature; the tetragonal β[8] and face-centered cubic γ phases [9], which are metastable; and the δ-phase[10], which is stable at high temperatures[11,12]. Figure 4.1 summarizes all the polyphorms of bismuth oxide including their crystallographic information. As can be seen, the number of non-equivalent atoms in the structure depends on the phase.

(a)

α - Bi_2O_3

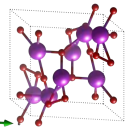

Lattice type P
Space group name P 21/c
Space group number 14

a	b	c	alpha	beta	gamma
5.83000	8.14000	7.48000	90.0000	67.0700	90.0000

Structure parameters

		x	y	z	Occ.
1 Bi	Bi1	0.52000	0.18750	0.63500	1.000
2 Bi	Bi2	0.04000	0.04300	0.22500	1.000
3 O	O1	0.61500	0.27800	0.31600	1.000
4 O	O2	0.63100	0.02700	0.11300	1.000
5 O	O3	0.02400	0.08400	0.46000	1.000

(b)

β - Bi_2O_3

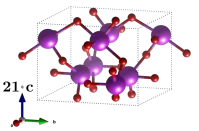

Lattice type P
Space group name P -4 21 c
Space group number 114

a	b	c	alpha	beta	gamma
7.72990	7.72990	5.65870	90.0000	90.0000	90.0000

Structure parameters

		x	y	z	Occ.
1 Bi	Bi	0.02770	0.23010	0.25000	
2 O	O1	0.29000	0.31900	0.02000	
3 O	O2	0.00000	0.50000	0.25000	

(c)

δ - Bi_2O_3

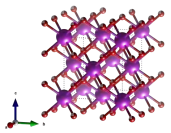

Lattice type F
Space group name F m -3 m
Space group number 225

a	b	c	alpha	beta	gamma
5.66500	5.66500	5.66500	90.0000	90.0000	90.0000

Structure parameters

		x	y	z	Occ.
1 O		0.25000	0.25000	0.25000	0.750
2 Bi		0.00000	0.00000	0.00000	1.000

(d)

γ - Bi_2O_3

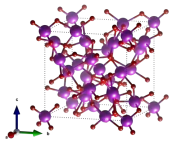

Lattice type I
Space group name I 2 3
Space group number 197

a	b	c	alpha	beta	gamma
10.25010	10.25010	10.25010	90.0000	90.0000	90.0000

Structure parameters

		x	y	z	Occ.
1 Bi	Bi	0.17600	0.32030	0.00960	1.000
2 Bi	Bi(M)	0.00000	0.00000	0.00000	1.000
3 O	O(1)	0.13650	0.24760	0.50380	1.000
4 O	O(2)	0.18740	0.18740	0.18740	1.000
5 O	O(3)	0.88850	0.88850	0.88850	1.000

Figure 4.1 Bi_2O_3 polymorphs with their crystallographic information: (a) monoclinic α- Bi_2O_3, (b) tetragonal β- Bi_2O_3, (c) cubic δ- Bi_2O_3 and (d) γ- Bi_2O_3.

As an example of the relevant differences between phases, the conduction mechanism of α-Bi_2O_3 is mainly electronic, whereas for δ-Bi_2O_3 it is mainly ionic[13,14]. Moreover, with the advent of nanotechnology, a huge miscellany of Bi_2O_3 nanostructures is being reported, from nanocoatings to nanowires, nanotubes, or hollow nanoparticles, each with its own applications and virtues[15–19]. Therefore, when tailoring these complex nanostructures, assessing Bi_2O_3 phase, defects, and other structural properties with high resolution is mandatory.

Obviously, in this context, high-resolution Transmission Electron Microscopy (TEM) is the best tool to evaluate crystalline structural modifications at the nanoscale[20]. Additionally, when coupled with Electron Energy Loss Spectroscopy (EELS), it can also probe chemical and electronic properties of a given material at high resolution. In particular, the band structure of a material is related to low-loss EELS spectra, while information on the oxidation state, coordination, or presence of vacancies of a given element in the sample can be obtained from core loss spectra by analyzing its Energy Loss Near Edge Structure (ELNES)[21]. For bismuth oxide, the accurate analysis of its ELNES will be essential, because its high ionic conductivity is discussed in terms of oxygen vacancy, generation, ordering and transport[13,14,22,23]. However, obtaining this information through the ELNES fine structure is not straightforward and requires previous knowledge on how microscopic properties of the given material alter the spectra. This can only be obtained from reference samples or simulations[24–26].

In the bibliography, EELS measurements of Bi_2O_3 low-loss spectra have only been used to determine band gap energy [23], and there is no reference presenting data from the core loss region. In addition, most of the literature is about studies performed at the macroscopic level and, even though local properties such as the electronic environment of the oxygen would be highly interesting, little experimental work has been done in this matter[27].

In this Chapter, pioneering core and low-loss EELS studies in three different α-Bi_2O_3 samples which exhibit different oxygen conductivity values will be presented. These are the first reported core loss EELS measurements of this material to our knowledge and, as such, how spectral features relate to structural and electronic properties remained unveiled. In order to clarify

and verify the experimental core loss EELS data, Density Functional Theory (DFT) calculations are used to elucidate all the features which appear in the experimental spectra[28–30].

4.2 Material and preliminary characterization

In this section, experimental data from three differnet bismuth oxide samples are presented: commercial Bi_2O_3 powder, ceramic Bi_2O_3 and Bi_2O_3 nanowires. The three samples represent different stages of the nanowires growth process. They were provided by Dr. Carlos Díaz-Guerra from the Universidad Complutense de Madrid. Further details about the sample synthesis can be found in [26,31].

Micro-Raman and micro-photoluminescence (PL) measurements were carried out at room temperature in a Horiba Jovin-Ybon LabRAM HR800 system. In order to collect Raman spectra, the samples were excited by a 633 nm He–Ne laser on an Olympus BX 41 confocal microscope with a 100×objective. A 325 nm He-Cd laser and a 40x objective were used for PL measurements. It should be mentioned that both Raman and PL data were measured on the same samples that were later characterized by TEM-EELS.

Normalized Raman spectra representative of the Bi_2O_3 powders, ceramics and nanowires, are shown in Figure 4.2(a). No significant differences, in terms of peak positions and bandwidths, were found in the Raman spectra of the different samples. Raman bands appear peaked at 84, 119, 139, 152, 184, 210, 280, 313, 411, 448, and 526 cm^{-1}, which are

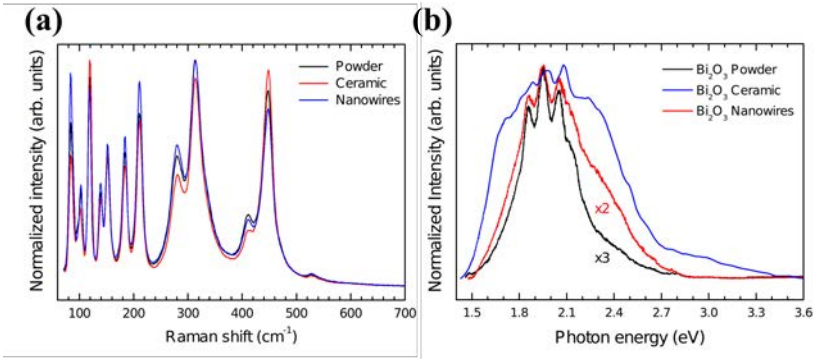

Figure 4.2 (a) Normalized Raman spectra and (b) photoluminescence measurements spectra for the three sample, powder (black), ceramic (red) and nanowires (blue).

characteristic of the α-Bi_2O_3 phase[32–34]. Peaks corresponding to metallic bismuth or other Bi oxides were not detected.

Figure 4.2(b) shows representative PL spectra of the three types of samples investigated that exhibit quite different PL intensities (note the multiplying factors appearing in the figure). In the case of Bi_2O_3 powders, the spectra show three narrow, well-resolved emission bands, peaked at 1.86, 1.95 and 2.05 eV. Besides, two weaker and broader emissions, respectively centred near 2.10 eV and 2.27 eV, can also be appreciated. A higher PL intensity was measured in the Bi_2O_3 nanowires. In addition, an enhancement of the relative intensity of the 2.10 and 2.27 eV shoulders was observed. Ceramic samples exhibit the highest PL intensity. Moreover, luminescence emission from these samples was detected in a wider spectral range. The PL bands observed in the Bi_2O_3 powder and nanowires are also observed in this case, but changes in the peak positions and band widths are evident. Precisely, the peak positions of the abovementioned three narrow emissions observed cantered between 1.86 and 2.05 eV in PL spectra of powders and nanowires, appear shifted 0.3 eV towards higher energies. Furthermore, a clear increase of the relative intensity of the 2.27 eV emission can also be appreciated. Additionally, PL spectra from the ceramic samples show a weak and broad new emission at about 3.0 eV as well as an intense band centered near 1.72 eV.

Trivalent bismuth cations in inorganic compounds exhibit luminescence properties related to their $6s^2$ configuration[35,36]. At room temperature, radiative transitions are mainly assigned to $^3P_1 \rightarrow {}^1S_0$ transitions[35,37] or charge transfer transitions between oxygen ligands and Bi^{3+} ions[36], giving rise to luminescence bands peaked in the (3.1–2.2) eV spectral range under UV excitation. On the other hand, Bi^{2+} ions show PL emission in the range (2.10–1.95) eV under UV excitation. This luminescence has been attributed to $^2P_{3/2}$ (1) $\rightarrow {}^2P_{1/2}$ transitions[37–39] and it is extremely dependent on the local crystal field, which in turn depends on the symmetry and coordination of the surrounding oxygen atoms. Previous luminescence studies of α-Bi_2O_3 ceramic samples annealed in different atmospheres have shown that the 2.10 eV band is related to oxygen vacancies[31]. Other works[40,41] reported that the emission in the low-energy spectral range (below 2.1 eV) can be also attributed to oxygen vacancies that form defect donor states, as supported

by DFT calculations. Wu and Lu[41] also associated the PL emission at this spectral range to oxygen vacancies and stated that the higher the emission intensity, the greater the vacancy density.

4.3 TEM characterization

Scanning TEM (STEM) High Angle Annular Dark Field (HAADF) and EELS measurements from the samples were acquired in a JEOL ARM200cF TEM operated at 200 kV and equipped with a cold field emission gun (c-FEG) and a GATAN Quantum GIF EEL spectrometer. A Gatan double tilt cryo- holder (model 636) was used for the ceramic sample to minimize electron beam damage, with a working temperature of 97 K. The collection and convergence semiangles were 27.78 and 35 mrad respectively throughout all of the EELS measurements. These measurements were performed using the dual-EELS acquisition mode, which allows acquiring both low-loss and core loss EELS spectra simultaneously. The latter were focused in the 520−560 eV energy loss range, were the O K edge can be observed. The dual acquisition enables aligning core loss spectra with the zero-loss peak, therefore making the absolute energy-loss position of different features of the peaks reliable. Single spectra for each sample were obtained by summing larger spectrum images after zero-loss peak alignment. These spectrum images were acquired with atomic resolution, and the corresponding co-acquired HAADF images allow the identification of the zone axis of the crystal during the acquisition as well as making it possible to rule out any beam damage. It was possible to avoid carbon contributions either from the TEM grid or from contamination.

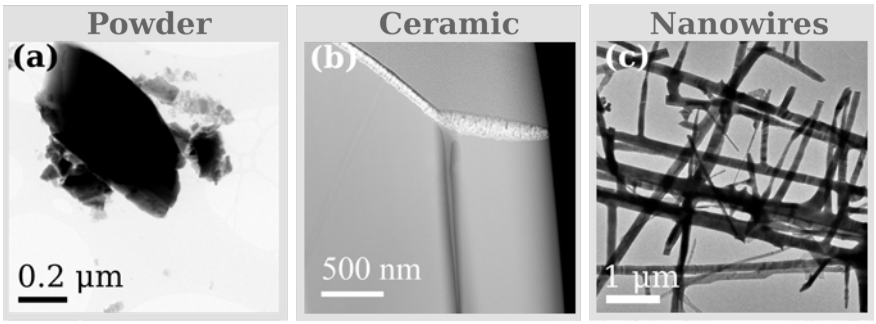

Figure 4.3 Low magnification TEM images of powder (a), ceramic(b) and nanowires(c) of Bi_2O_3.

A previous low magnification characterization of the samples was carried out by conventional TEM. The three samples were observed at 200 keV in a JEOL 2010F and in a JEOL 2100, in order to identify the main morphological features.

The commercial powder sample was prepared for TEM observation by the standard suspension in hexane and drop pouring onto a TEM holey carbon grid. As for the pellet of ceramic, the sample was prepared by the standard FIB lift-out technique[42]. Finally, the Bi_2O_3 nanowires were prepared by suspension and sonication in hexane, followed by pouring a drop of the solution onto a TEM holey carbon grid.

The TEM structural analysis showed that the commercial powder was comprised of crystals with lateral sizes varying from 50 to 500 nm (Figure 4.3(a)). The crystals presented good crystallinity without defects, as can be observed in the High Resolution TEM (HRTEM) image in Figure 4.4(a). On the other hand, TEM characterization of the ceramic evidenced that it consisted of large (several micrometers) α-phase Bi_2O_3 crystals. Figure 4.3(b) corresponds to the edge of the lamella where the protective layers can be identified in the upper-right corner, then two crystals are visible separated by the dark stripe in the middle. Last, the nanowires presented a completely different structure. As can be seen in the low-magnification TEM image, they were found to form hierarchical structures (Figure 4.3 (c)). The HRTEM image shows the good crystallinity of the NWs; however, they are not defect-free, as can be seen, for example, in the lower right corner of the image of the NW cap (Figure 4.4(b)).

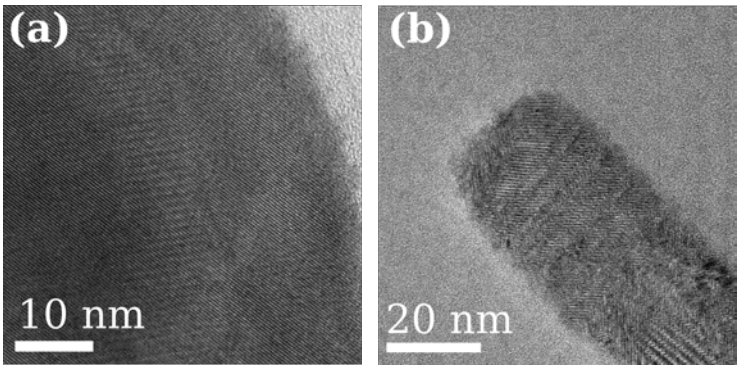

Figure 4.4 HRTEM image of powder sample (a) and the nanowire sample (b).

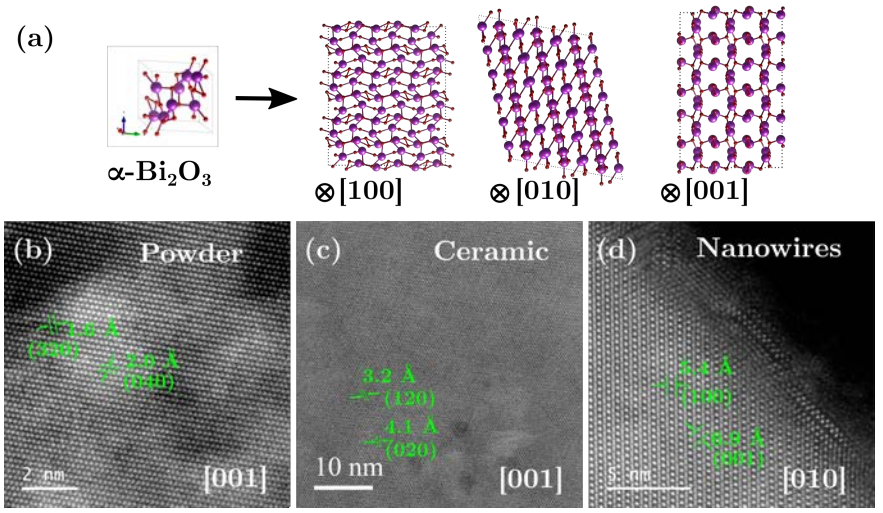

Figure 4.5 (a) $\alpha - Bi_2O_3$ unit cell. 2x2x2 $\alpha - Bi_2O_3$ oriented along the main zone axis, [100], [010] and [001]. HAADF-STEM images of the three samples: (b) powder, (c) pellet and (d) nanowires.

The indexations of the three samples agree with the α-phase of Bi_2O_3, despite sparse, smaller nanowires of the metastable β-Bi_2O_3 nanowires were also observed, but as Raman measurements show, they are not statistically relevant.

STEM-HAADF imaging also showed that the powder and ceramic samples are formed by α-Bi_2O_3, as do most of the nanowires. As it has been mentioned before α-phase is a monoclinic phase, thus the aspect in two different zone axes can be completely different as is highlighted on Figure 4.5 (a). The crystallographic planes have been identified in the STEM-HAADF images, as well as the corresponding zone axes. Figure 4.5 (b) corresponds to a crystal of the powder sample oriented along the [001] zone axis, the (040) and (320) planes can be clearly identified. A crystal of the ceramic is presented in Figure 4.5 (c) where the (120) and (020) planes are highlighted. Figure 4.5 (d) corresponds to the edge of a nanowire oriented along the [010] zone axis; here, large interplanar distances can be seen, which correspond to the (100) and (001) planes.

4.3.1 Electron Energy Loss Spectroscopy

The presence of oxygen vacancies, previously observed by macroscopic spectroscopies, was studied by EELS, because it allows to study locally the changes on the electron configuration. Thus, if there is a change on the atomic coordination, a fingerprint of the alteration will appear on the spectra. The goal was the comparison of the O K edge of all the samples in order to find this particular feature.

Nevertheless, if during the experiment the electron beam induces some beam damage having a direct effect on the electronic configuration, it can be also detected on the O K edge, as a shift of the edge or a splitting due to a possible phase transition or generation of extra oxygen vacancies. As an example Figure 4.6 shows the possible temperature induced phase transitions between the Bi_2O_3 polymorphs. These transitions can be easily triggered by the increase of temperature induced by the electron beam-sample interaction when the beam scans the sample surface.

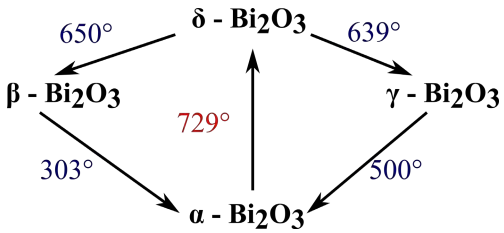

Figure 4.6 Bi_2O_3 solid polymorphs phase transitions.

Therefore, before starting the proper experiment, the robustness of the samples under the electron beam was tested. Unfortunately, all the samples presented some degree of beam damage, and the nanowires happened to be the most sensitive sample under the electron beam. Moreover, the formation of bubbles and changes on the crystalline structure were observed by conventional TEM imaging for long acquisition times.

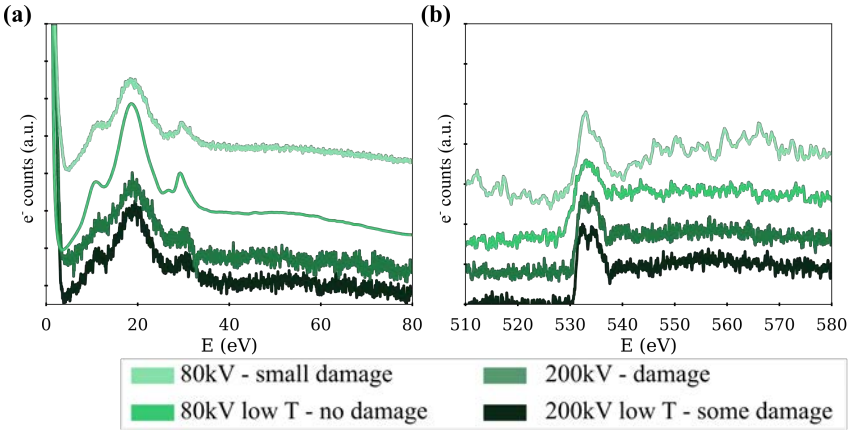

Figure 4.7 Electron beam damage monitoring by acquiring dual EELS on the NWs samples. (a) Low loss and (b) core loss acquired at different experimental conditions.

In order to optimise the experimental conditions to prevent any possible structural and composition modification, a study of the electron damage was carried out. Dual EELS spectra were acquired under different conditions on different microscopes. Figure 4.7 shows the spectra obtained with a Tecnai F30 instrument working at 80 kV and in an ARM working at low temperature both at 200 kV and 80 kV. As can be observed, at 80 kV no damage is produced; however, in this microscope there is not enough spatial resolution. With the probe corrected ARM at low temperature at 200 kV it was possible to avoid irreparable damage reducing the acquisition time to 0.20 s.

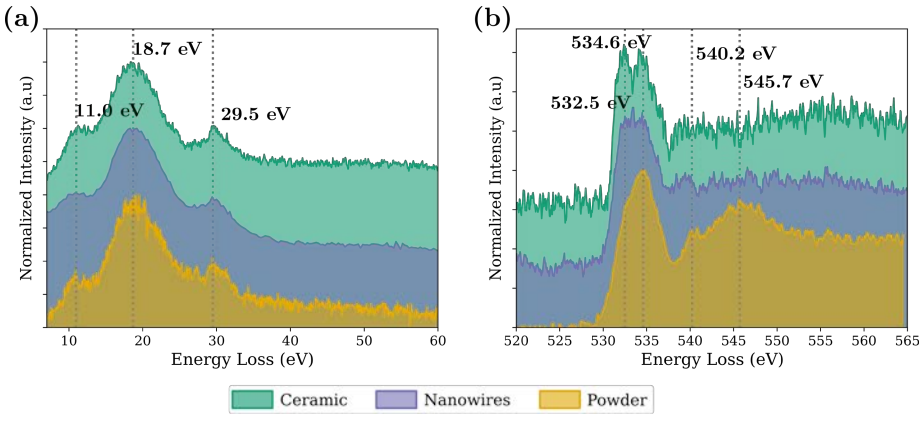

Figure 4.8 Low loss (a) and core loss (b) EELS of the three different samples.

For the ceramic and powder, the experiment was also performed at 200 keV, but at room temperature, as the damage was not as severe, with an acquisition time of 0.05 s for the powder and of 3 s for the ceramic.

Low loss and core loss EELS

The EELS measurements at 200kV for each sample are shown in Figure 4.8. Clear differences between samples appear in the spectra. In order to discuss these differences, the main features have been highlighted.

Concerning the low loss EELS, the three samples are quite equivalent (Figure 4.8 (a)). As can be checked in Figure 4.8 three main peaks appear at 11.0 eV, 18.7 eV and 29.5 eV.

On the other hand, the core loss spectra shows a main peak at 534.6 eV which is at the same position for all samples (Figure 4.8 (b)). This O K edge shows a shoulder at 532.5 eV that varies in height when comparing the commercial powder sample with the other two, which were thermally treated. The shoulder peak intensity goes from being almost 25% lower than the main peak in the commercial powder to being equal in the nanowire and the ceramic. Moreover, the powder shows some additional peaks in the continuum region of the spectrum at 540.2 eV and 545.7eV.

Remarkably, this was the first reported experimental core loss spectrum of α-Bi_2O_3.

4.4 DFT calculations of bismuth oxide

To understand the information from the EELS spectra, DFT simulations were carried out. Initially the same calculations were performed for the α and β phases of Bi_2O_3 in order to ensure that the experimental data correspond to α-Bi_2O_3; in this regard, the low loss features were the key ones. Then, a detailed study of the α phase was performed for the conventional unit cell and for the oxygen deficient case.

The atomistic input models were built according to the crystallographic information of the unit cell (UC) from the α-Bi_2O_3 and the β-Bi_2O_3 structure. The same procedure was followed for both phases. The cutoff energy of the simulation was set at -11.9 Ry, defining the following valence and semicore electrons: $2s^2$ and $2p^4$ for oxygen and $4f^{14}$, $5d^{10}$, $6p^3$ and $6s^2$ for bismuth. Structural relaxations of the crystal were performed until the

total energy was converged to 10^{-5} eV and the residual forces on atoms were below 0.01 eV/Angstrom with 1000 k-points. Importantly, the LDA approximation used in the calculations is known to not reliably calculate absolute onset energies for EELS edges[43].

After the SCF was converged for both phases, the density of states and the low loss, as well as the dielectric function, were calculated; then, the core loss of the α-Bi_2O_3 was computed.

4.4.1 Density of states

Figure 4.9 and Figure 4.10 present the Density of States (DOS) for the α-Bi_2O_3 and β-Bi_2O_3 phases respectively. As can be observed from the DOS, the energy bandgap for both phases agrees with the experimental one. The experimental studies reported an energy bandgap slightly lower than 3 eV [44–47] for both phases, but highly dependent on the sample. The results obtained for the presented calculations were slightly lower for the monoclinic phase, for which the computed bandgap was 2.45 eV (Figure 4.9). For the tetragonal phase, the difference was higher as the obtained value was 1.59 eV (Figure 4.10). To correct for the observed difference, hybrid methods can be applied, as mBJ, and a proper value is reached; however, this can modify the shape of the bands. If the goal is to compare the low loss spectra, this correction does not need to be applied.

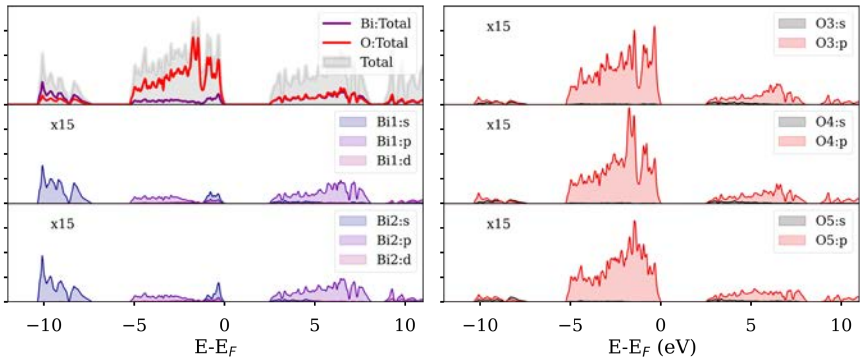

Figure 4.9 DOS and PDOS of α-Bi_2O_3. (top-left) The DOS of the Bi (purple) and O (red) atoms are overlapped to the total DOS of the Bi_2O_3. The rest of the plots show the PDOS for the main orbitals of all the atoms are plotted in purple (Bi) and red (O).

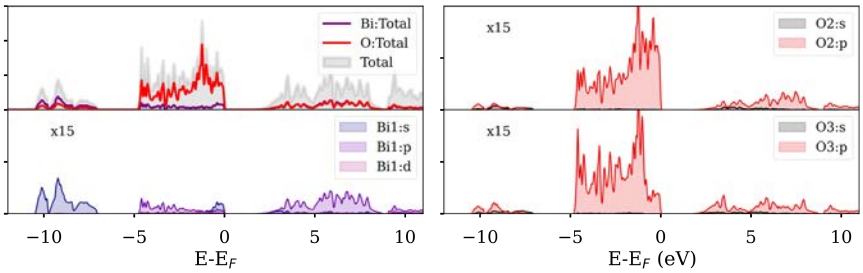

Figure 4.10 DOS β-Bi_2O_3. (top-left) The DOS of the Bi (purple) and O (red) atoms are overlapped to the total DOS of the Bi_2O_3. PDOS for the main orbitals of all the atoms are plotted is purple (Bi) and red (O).

Apart from the bandgap, the energy location of the orbitals has to be noted from the Partial DOS (PDOS). The non-equivalent bismuth atoms in both phases have the 6s orbitals split between -9 eV and just at the top of the valence band. The 6p are split between the valence and conduction band. On the other hand, the non-equivalent oxygen atoms present a clear split of the 2p orbitals between the valence and conduction band. The 5d-Bi and 2s-O do not appear on the plot as they are located at lower energy, and they do not participate on the bonding.

Summarizing, three main regions can be identified on the PDOS for both phases: the low energy, between -11eV and -8eV, occupied by the Bi-6s orbitals and the O-2p; the top of the valence band, between -5 and the Fermi level, where the O-2p coexist with the 6s and 6p-Bi; and, finally, the conduction band, over the bandgap, is occupied by the O-2p and the Bi-6p.

4.4.2 Low loss EELS: phase identification

From the electron density, the complex dielectric function can be calculated for both phases, and, from it, the energy loss function.

The results are plotted in Figure 4.11 (a-b). In Figure 4.11 (a) the Energy Loss Functions (ELF) for both phases are displayed. At first sight they seem equivalent; however, two main differences can be observed. Both phases present two main peaks, one at 18.8 eV and the other at 29.6 eV. However, for the α-Bi_2O_3 first peak appears at 10 eV, while for the β-Bi_2O_3 at 10 eV there is just a shoulder. In addition, between the peak at 20 eV and the peak at 29.6 eV, for the β-Bi_2O_3, an extra peak appears at 25.3 eV. However, it does not appear as clear for the α-Bi_2O_3. By comparison, the

experimental low loss (Figure 4.8(a)) for all three samples can be identified to correspond to α-Bi_2O_3 as the peak at 10 eV is clear in all spectra

The Complex Dielectric Function (CDF) allows to identify the nature of the main peaks of the ELF. The first peak, at 10 eV, corresponds to a surface plasmon resonance as it is placed at a zero crossing of the real part of the CDF and the second and main peak, at 18.8 eV, can be identified as the bulk plasmon as it corresponds to a zero crossing of the ε_1 and a decrease of the ε_2. The small peak at 25.3 eV corresponds to the $O_{4,5}$ edge of bismuth. The last peak corresponds to an intra-band transition as it is associated to a local maximum of the imaginary part of the CDF.

4.4.3 Core loss EELS: oxygen vacancies

As far as the cationic structure is concerned, the samples show no significant differences, all of them being mainly α-Bi_2O_3. However, the experimental EEL core loss spectra show clear differences, and their origin must be elucidated.

The core loss EELS was computed for the α-Bi_2O_3. Specifically, the K edge of the oxygen atoms and the $M_{4,5}$ for the bismuth atoms were calculated. However, from now on, all the interest will be focused on analysing the ELNES of the oxygen K edge, as it is found to be the one affected by the presence of oxygen vacancies.

In order to get a spectrum comparable with the experimental one, the simulation parameters were selected intentionally in agreement. The

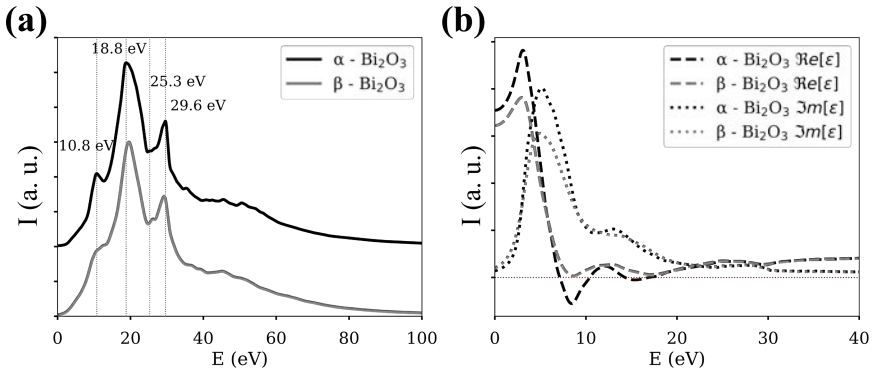

Figure 4.11 (a) Energy loss function of α-Bi_2O_3 (black) and β-Bi_2O_3 (grey). (b) Real (dashed line) and imaginary (dotted line) part of the complex dielectric function.

collection semi angle was set to 35 mrad and the convergence angle to 27 mrad. Likewise, the gaussian broadening of the spectrometer and the Lorentzian core hole lifetime of the edge[48] were set to 0.5 eV and 0.15 eV respectively, to reach the best fit with the experimental data.

As it has been mentioned before, the LDA approximation used typically induces an energy shift. Because of this, a shift of 1.2eV was applied to all simulations. This value was chosen so that the main peak energy, 534.6eV, of the experimental spectrum of the commercial powder matched the maximum of the simulated edge from the unit cell, taking the commercial powder as a reference sample. An important fact to consider is that in the UC of α-Bi_2O_3 there are three different non-equivalent oxygens, each one seeing a different electronic environment in the structure. These positions will be referred as O_I for x=0.2337a, y=0.4533b, z=0.1266c and equivalent positions; O_{II} for x=0.265a, y=0.0294b, z=0.0115c; and O_{III} for x=0.7783a, y=0.3037b, z=0.2080c where a, b, c are the unit cell parameters (see Figure 4.1). The calculations were done for each of the non-equivalent oxygens and then they were weight-averaged having in mind their multiplicity (the number of atoms in each position and equivalents, two for all in this case). The averaged spectrum is the one comparable with the experimental spectrum, as in the experimental one a mix contribution of oxygens is acquired.

The simulated O K edge from the unit cell is shown in Figure 4.12, where the energies of the experimental features are also labelled. An excellent match with the experimental spectrum from the reference Bi_2O_3

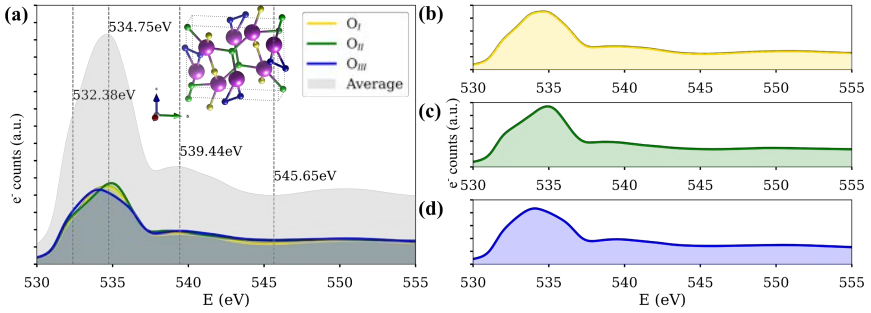

Figure 4.12 Computed O K edge of the oxygen atoms of α-Bi_2O_3. (a) the O-K obtained for each non-equivalent oxygen atom of the unit cell, highlighted on the inset (OI: yellow, OII: green and OIII: blue). The average edge is shown in gray. (b-d) display the contribution of each oxygen separately.

powder can be appreciated: the simulation shows all the features of the experimental spectra, with only small differences in the position of the post-peak (at a lower energy in the simulation) and the last peak (at a higher energy). In contrast, the shoulder is much more intense in the ceramic and nanowire spectra, and both showing a steeper onset than the reference sample. The good match between the powder sample and the UC simulation, whilst small discrepancies show up for nanowire and ceramic, points to significant changes between these samples.

The contributions of oxygen atoms in O_I, O_{II}, O_{III} can also be extracted from the simulated UC, and are shown in Figure 4.12. The total spectra can be evaluated as the sum of these contributions weighted by their multiplicity. In Figure 4.12 (c-d) it is clear that these contributions are different. In fact, the most notable difference is also the height of the shoulder, O_{II} presenting the lowest one, and the main peak distance with respect to the edge onset, O_{II} having the highest one. This fact hints that the difference in the experimental spectra might be due to an imbalance on the occupation of the three oxygen sites. In order to further investigate this, simulations of unit cells with oxygen vacancies were undertaken.

Oxygen deficient simulations

There are a few considerations to take into account when removing an atom from a unit cell in a DFT simulation. Even though a unit cell with one missing oxygen atom might seem a rather small defect in a big crystal, the simulations are performed with periodic boundary conditions, which

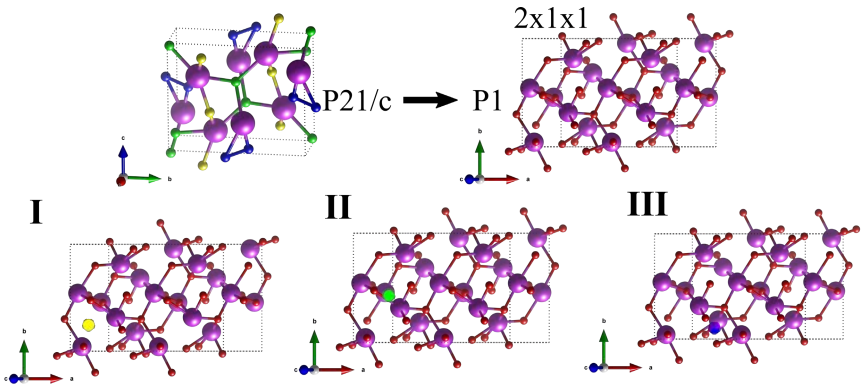

Figure 4.13 α-Bi_2O_3 oxygen identification (O_I: yellow, O_{II}: green and O_{III}: blue). 2x1x1 supercell with the different type of oxygen vacancies.

means actually that an infinite crystal with one less oxygen in each unit cell is being simulated. Because of this, if the vacancy proportion is to be kept low, a large supercell consisting of multiple unit cells in which only one oxygen vacancy is being introduced must be simulated. To keep the computational cost of the simulation reasonable, we chose to simulate a 2x1x1 supercell, which will be referred to as V simulation, with one oxygen atom missing. An oxygen in the O_{II} site was chosen since its contribution was the more resembling to the experimental spectra of the nanowire and the pellet sample. This configuration corresponds to a vacancy concentration of $1/24 \approx 4\%$. The same offset of 1.2 eV applied to the UC simulation was applied to the V simulated spectrum.

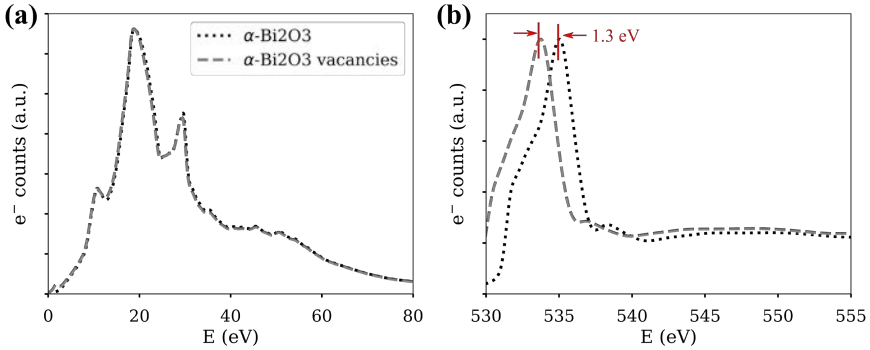

Figure 4.14 Comparison between the computed normalized spectra for the unit cell and for a supercell with 4% of oxygen deficiency. (a) Low loss and (b) core loss EELS.

The calculations were repeated for V in the same way that was done for the UC. UC and V simulations were compared both in the core loss and the low-loss regime (Figure 4.14). Remarkably, almost no differences appear in the low-loss spectra, apart from a small peak at 1.9 eV. Similarly, the experimental low-loss spectrum barely changes between each sample, and unfortunately, at 1.9 eV the zero-loss peak overlaps with the loss function of the samples too much to see any peak of this kind in the experimental data. But the most interesting feature in this comparison is the appearance of a 1.3 eV shift to lower energies of the O K edge in the V simulation. This seems very reasonable if one bears in mind that this shift has also been observed in EELS spectra of other transition metals, such as Fe, Co or Mn, when they are reduced[24,49–51].

The last verification of the effect of the oxygen vacancies was to check if any relationship can be extracted from the number of vacancies and the energy shift. Four supercells of α-Bi_2O_3 were prepared with a different degree of oxygen deficiency. The supercells are summarized in the Table 4.1. For each of the supercells the total number of atoms respect to the number of oxygens is written. The % vacancy is computed as the number of O removed over the total number of O's multiplied by 100.

	0vac@2x1x1	1vac@3x1x1	1vac@2x1x1	2vac@3x1x1
Supercell	2x1x1	3x1x1	2x1x1	3x1x1
Total | #O	40 | 24	60 | 36	40 | 24	60 | 36
O removed	0	1	1	2
% vacancy	0	2.7	4.2	5.5

Table 4.1 Supercells with different oxygen deficiency. For each of the supercells the total number of atoms with respect to the number of oxygens is written. The % vacancy is computed as the number of O removed over the total number of O's multiplied by 100.

By comparing the O K EELS edge position of all the simulations (Figure 4.15) it is clear that the energy shift is proportional to the vacancy concentration.

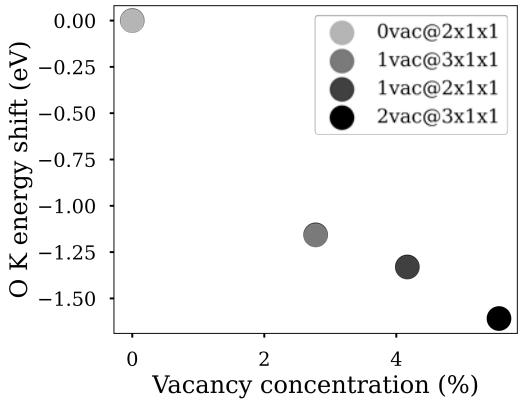

Figure 4.15 O K-edge shift as a function of the vacancy concentration.

In order to perform a rigorous analysis of the core loss spectra from the nanowire and ceramic sample in terms of oxygen vacancies, each configuration of missing oxygen atoms for increasingly large supercells should be simulated. This approach is not feasible in terms of computational

time. In this regard, it must be kept in mind that bismuth is one of the heaviest stable elements on the periodic table, with 83 electrons, 29 of which have been treated rigorously within the DFT formalism (orbitals 4f to 6s as stated in the methods section), and therefore costly to simulate. However, based on the knowledge that the previous simulations have yielded, that vacancies shift the O K edge, and that the main peak and the shoulder features vary for different symmetry sites, the following simple model can be inferred:

	k_1	k_2	k_3	s (eV)
Powder	0.084503	0.084503	0.054324	0
Nanowires	0.113847	1.466080e-12	0.113847	0.452774 eV
Ceramic	0.110796	5.390694e-16	0.110796	0.586514 eV

Table 4.2 k_i and s obtained for the fittings of the computed spectra of oxygen contributions to the three experimental EELS datasets.

$$I_{exp}(\Delta E) = k_1 I_{O_I}(\Delta E - s) + k_2 I_{O_{II}}(\Delta E - s) + k_3 I_{O_{III}}(\Delta E - s) \quad (57)$$

Properly normalized, the k_i parameters represent occupancies of the different oxygen sites and the parameter s accounts for the energy shift that the V simulation demonstrates. This model was used to fit the experimental data and give some grounds for discussion on the presence and nature of oxygen vacancies in the material. Importantly, it must be kept in mind that the positions of the simulated oxygen spectra have been calibrated by using the commercial powder sample, and therefore any property calculated by this method will be relative to this reference. However, this seems reasonable since it is the purest form in which we can obtain this material.

The model was implemented in Python using a Scipy curve fitting routine[52] and the results of the fit of the experimental data are summarized in Figure 4.16.

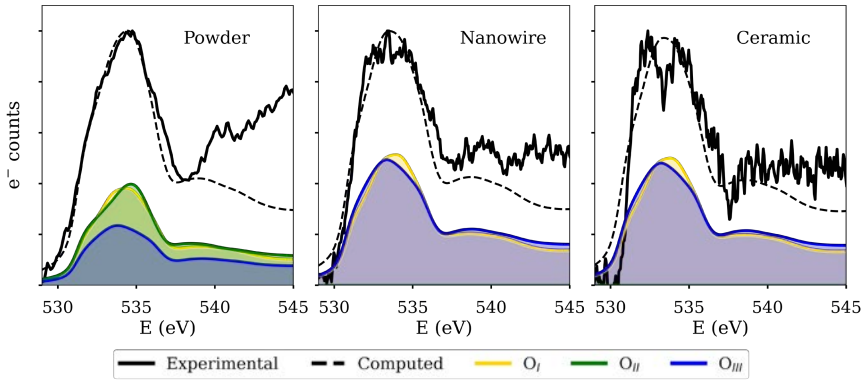

Figure 4.16 Fitting of the core loss experimental spectra from each α-Bi_2O_3 sample with the weighted contributions of each non-equivalent oxygen atoms and an energy shift.

The obtained k_i and s parameters (Table 4.2) show that the occupancy of O_I and O_{III} barely change in the three samples. Nonetheless, a small shift of approximately 0.45 eV for the nanowire sample and 0.58 eV for the pellet is introduced and the occupation of O_{II} drops to zero for these samples. Furthermore, from Figure 4.15 the linear relation between O K edge energy shift and vacancy concentration can be calculated by a linear regression, yielding an r-value of 0.97. From the regression values, the O K shift value of the nanowire and the pellet sample can be translated into approximately 1.2% of oxygen vacant sites in the nanowires and 1.6% in the ceramic sample, relative to the powder. These results would indicate that, although the commercial powder has a certain density of vacancies, they are uniformly distributed in all crystallographic positions while the ceramics and nanowires have a higher concentration of vacancies preferably located at the O_{II} site.

It is important to rule out an orientation dependence of EEL spectra[53] since the samples were not in the same zone axis during the acquisition. In order to explore this possibility, UC simulations for the relevant zone axes were carried out ([100], [010] and [001]). As it can be seen in Figure 4.17, they show no significant differences.

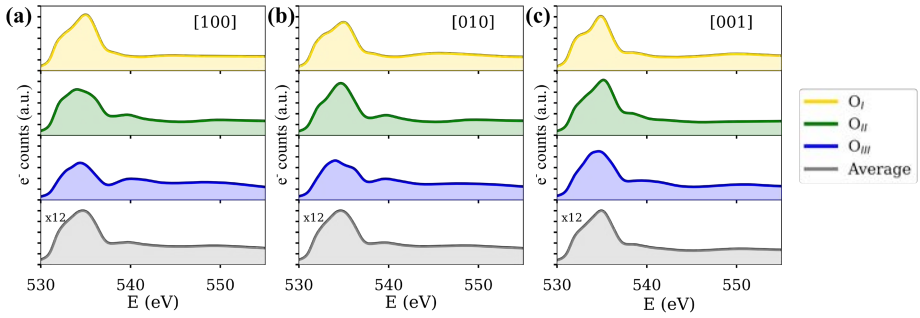

Figure 4.17 EELS simulations as a function of orientation.

The findings are in good agreement with PL results. Previous luminescence studies of α-Bi_2O_3 ceramic samples annealed in different atmospheres had shown that a 2.10 eV band is related to oxygen vacancies[54]. Other works reported that the emission in the low-energy spectral range (≈below 2.1 eV) can also be attributed to oxygen vacancies that form defect donor states[55], and that the higher the emission intensity in this spectral range, the greater the vacancy density[56]. Hence, the higher PL intensity observed in ceramics and nanowires, as compared to that measured in powder samples, as well as the higher relative intensity of the PL emissions in the low-energy spectral range - support the fact that our EELS results reveal a higher concentration of oxygen vacancies in the studied α- Bi_2O_3 nanowires and ceramics.

4.5 Conclusions

The main conclusions of this chapter can be summarized as follows:

- The microstructural differences between three samples of α-Bi_2O_3, powder, ceramic and nanowires, have been observed by low magnification TEM and HAADF-STEM imaging.
- Novel results on the EELS characterization of α-Bi_2O_3 have been reported for the first time.
- DFT calculations have been used to complement the experimental EELS data in order to understand the information present in the spectra.

- Low loss EELS simulations have been employed as a tool for phase identification. The density of states and the complex dielectric function of two different polymorphs of Bi_2O_3, α and β, have been computed.
- Core loss EELS simulations have been carried out, taking into account:
    - Non-equivalent oxygens. The contribution of all the non-equivalent oxygens has been analysed.
    - Orientation dependence. The O K ELNES has been analysed as a function of the orientation.
- Thanks to DFT, a shift on the O K edge has been determined to be a signature of oxygen vacancies in the sample. The amplitude of the shift has been related to the concentration of vacancies.

4.6 References

[1] X. Gou, R. Li, G. Wang, Z. Chen, D. Wexler, Room-temperature solution synthesis of Bi2O3 nanowires for gas sensing application., Nanotechnology. 20 (2009) 495501. https://doi.org/10.1088/0957-4484/20/49/495501.

[2] A. Cabot, A. Marsal, J. Arbiol, J.R. Morante, Bi2O3 as a selective sensing material for NO detection, Sensors and Actuators, B: Chemical. 99 (2004) 74–89. https://doi.org/10.1016/j.snb.2003.10.032.

[3] M. Vila, C. Díaz-Guerra, K. Lorenz, J. Piqueras, E. Alves, S. Nappini, E. Magnano, Structural and luminescence properties of Eu and Er implanted Bi2O3 nanowires for optoelectronic applications, Journal of Materials Chemistry C. 1 (2013) 7920. https://doi.org/10.1039/c3tc31989j.

[4] J. Eberl, H. Kisch, Visible Light Photo-Oxidations in the Presence of a-Bi2O3, Photochemical & Photobiological Sciences. 7 (2008).

[5] E.D. Wachsman, K.T. Lee, Lowering the Temperature of Solid Oxide Fuel Cells, Science. 334 (2011).

[6] G.H. Zhong, J.L. Wang, Z. Zeng, Ionic transport properties in doped δ-Bi2O3, J. Phys.: Conf. Ser. 29 (2006) 1–5. https://doi.org/10.1088/1742-6596/29/1/020.

[7] Lars Gunnar Sillen, Die Kristallstruktur des monoklinen alpha-Bi2O3, Naturwissenschaften. 13 (1940) 206–207.

[8] S.K. Blower, C. Greaves, The structure of β-Bi2O3 from powder neutron diffraction data, Acta Crystallographica Section C Crystal Structure Communications. 44 (1988) 587–589. https://doi.org/10.1107/S0108270187011661/FULL.

[9] S.F. Radaev, V.I. Simonov, Y.F. Kargin, Structural features of γ-phase Bi2O3 and its place in the sillenite family, Acta Crystallographica Section B. 48 (1992) 604–609. https://doi.org/10.1107/S0108768192003847.

[10] G. Gattow, H. Schröder, Über Wismutoxide. III. Die Kristallstruktur der Hochtemperaturmodifikation von Wismut(III)-oxid (δ-Bi2O3), ZAAC - Journal of Inorganic and General Chemistry. 318 (1962) 176–189. https://doi.org/10.1002/zaac.19623180307.

[11] H.A. Harwig, A.G. Gerards, The polymorphism of bismuth sesquioxide, Thermochimica Acta. 28 (1979) 121–131.

[12] H.A. Harwig, On structure of bismuth sesquioxide: the a, b, g, and d-phase., Zeitschrift Für Anorganische Und Allgemeine Chemie. 444 (1978) 151–166.

[13] T. Takahashi, H. Iwahara, T. Arao, High oxide ion conduction in sintered oxides of the system Bi2O3-Y2O3, Journal of Applied Electrochemistry. 5 (1975) 187–195.

[14] P. Shuk, H.D. Wiemhöfer, U. Guth, W. Göpel, M. Greenblatt, Oxide ion conducting solid electrolytes based on Bi2O3, Solid State Ionics. 89 (1996) 179–196.

[15] K.Y. Niu, J. Park, H. Zheng, a. P. Alivisatos, Revealing bismuth oxide hollow nanoparticle formation by the Kirkendall effect, Nano Letters. 13 (2013) 5715–5719. https://doi.org/10.1021/nl4035362.

[16] L. Kumari, J. Lin, Y. Ma, One-dimensional Bi2O3 nanohooks: synthesis, characterization and optical properties, Journal of Physics: Condensed Matter. 19 (2007). https://doi.org/10.1088/0953-8984/19/40/406204.

[17] Y. Qiu, D. Liu, J. Yang, S. Yang, Controlled synthesis of bismuth oxide nanowires by an oxidative metal vapor transport deposition technique, Advanced Materials. 18 (2006) 2604–2608. https://doi.org/10.1002/adma.200600654.

[18] W.E. Mahmoud, A.A. Al-Ghamdi, Synthesis and properties of bismuth oxide nanoshell coated polyaniline nanoparticles for promising photovoltaic properties, Polymers for Advanced Technologies. 22 (2011) 877–881.

[19] B. Sarma, A.L. Jurovitzki, Y.R. Smith, S.K. Mohanty, M. Misra, Redox-induced enhancement in interfacial capacitance of the titania nanotube/bismuth oxide composite electrode, ACS Applied Materials and Interfaces. 5 (2013) 1688–1697. https://doi.org/10.1021/am302738r.

[20] D.B. Williams, C.B. Carter, Transmission Electron Microscopy: A Textbook for Materials Science, 2009. https://doi.org/10.1007/978-1-61779-415-5_23.

[21] R.F. Egerton, Electron Energy-Loss Spectroscopy in the Electron Microscope (3rd Edition), 2011. https://doi.org/10.1007/978-1-4419-9583-4.

[22] S. Boyapati, E.D. Wachsman, N. Jiang, Effect of oxygen sublattice ordering on interstitial transport mechanism and conductivity activation energies in phase-stabilized cubic bismuth oxides, Solid State Ionics. 140 (2001) 149–160.

[23] P. Shuk, H.D. Wiemhöfer, W. Göpel, Electronic Properties of Bi203 Based Solid Electrolytes, Zeitschrift Für Anorganische Und Allgemeine Chemie. 623 (1997) 892–896.

[24] P. Torruella, R. Arenal, F. de la Peña, Z. Saghi, L. Yedra, A. Eljarrat, L. López-Conesa, M. Estrader, A. López-Ortega, G. Salazar-Alvarez, J. Nogués, C. Ducati, P.A. Midgley, F. Peiró, S. Estradé, 3D Visualization of the Iron Oxidation State in FeO/Fe3O4 Core–Shell Nanocubes from Electron Energy Loss Tomography, Nano Letters. 16 (2016) 5068–5073. https://doi.org/10.1021/acs.nanolett.6b01922.

[25] M. Varela, M.P. Oxley, W. Luo, J. Tao, M. Watanabe, a. R. Lupini, S.T. Pantelides, S.J. Pennycook, Atomic-resolution imaging of oxidation states in manganites, Physical Review B - Condensed Matter and Materials Physics. 79 (2009) 1–14. https://doi.org/10.1103/PhysRevB.79.085117.

[26] M. Vila, C. Díaz-Guerra, J. Piqueras, L. López-Conesa, S. Estradé, F. Peiró, Growth, structure, luminescence and mechanicalresonance of Bi2O3nano- and microwires, CrystEngComm. 17 (2015) 132. https://doi.org/10.1039/c4ce01639d.

[27] A. Walsh, G. Watson, D.J. Payne, R.G. Edgell, J. Guo, P.-A. Glans, T. Learmonth, K.E. Smith, Electronic structure of the alpha and delta phases of Bi2O3: A combined ab initio and x-ray spectroscopy study, PHYSICAL REVIEW B. 73 (2006) 235104. https://doi.org/10.1103/PhysRevB.73.235104.

[28] C. Hébert, Practical aspects of running the WIEN2k code for electron spectroscopy, Micron. 38 (2007) 12–28. https://doi.org/10.1016/j.micron.2006.03.010.

[29] C. Hébert-Souche, P.H. Louf, P. Blaha, M. Nelhiebel, J. Luitz, P. Schattschneider, K. Schwarz, B. Jouffrey, The orientation-dependent simulation of ELNES, 2000. https://doi.org/10.1016/S0304-3991(99)00168-0.

[30] C. Hébert, J. Luitz, P. Schattschneider, Improvement of energy loss near edge structure calculation using Wien2k, Micron. 34 (2003) 219–225. https://doi.org/10.1016/S0968-4328(03)00030-1.

[31] M. Vila, C. Díaz-Guerra, J. Piqueras, ARTICLES YOU MAY BE INTERESTED IN, Appl. Phys. Lett. 101 (2012) 71905. https://doi.org/10.1063/1.4747198.

[32] R.J. Betsch, W.B. White, Vibrational spectra of bismuth oxide and the sillenite-structure bismuth oxide derivatives, Spectrochimica Acta Part A: Molecular Spectroscopy. 34 (1978) 505–514. https://doi.org/10.1016/0584-8539(78)80047-6.

[33] S.N. Narang, N.D. Patel, V.B. Kartha, Infrared and Raman spectral studies and normal modes of α-Bi2O3, Journal of Molecular Structure. 327 (1994) 221–235. https://doi.org/10.1016/0022-2860(94)08160-3.

[34] V.N. Denisov, A.N. Ivlev, A.S. Lipin, B.N. Mavrin, V.G. Orlov, Raman spectra and lattice dynamics of single- crystal Bi2O3, Journal of Physics: Condensed Matter. 9 (1997) 4967–4978.

[35] G. Blasse, H. Zhiran, A.J.A. Winnubst, A.J. Burggraaf, The luminescence of yitria stabilized zirconia doped with Bi2O3, Materials Research Bulletin. 19 (1984) 1057–1062. https://doi.org/10.1016/0025-5408(84)90220-4.

[36] Y. Zorenko, V. Gorbenko, T. Voznyak, V. Jary, M. Nikl, Luminescence spectroscopy of the Bi 3 + single and dimer centers in Y 3 Al 5 O 12 :Bi single crystalline films, (2010). https://doi.org/10.1016/j.jlumin.2010.05.013.

[37] Y. Fujio, C.-N. Xu, N. Terasaki, T. Sugiura, T. Sano, K. Manseki, S. Devi, V. Tharmaraj, L. Kumari, J.-H. Lin, Y.-R. Ma, Synthesis of bismuth oxide nanostructures by an oxidative metal vapour phase deposition technique, NANOTECHNOLOGY. 18 (2007) 7. https://doi.org/10.1088/0957-4484/18/29/295605.

[38] A.M. Srivastava, Luminescence of divalent bismuth in M2+ BPO5 (M2+ = Ba2+, Sr2+ and Ca2+), Journal of Luminescence. 78 (1998) 239–243. https://doi.org/10.1016/S0022-2313(98)00010-6.

[39] M. Gaft, R. Reisfeld, G. Panczer, G. Boulon, T. Saraidarov, S. Erlish, The luminescence of Bi, Ag and Cu in natural and synthetic barite BaSO 4,. www.elsevier.nl/locate/optmat (accessed December 9, 2021).

[40] S. Schmidt, E.T. Kubaski, D.P. Volanti, T. Sequinel, ‖ Vinicius, D.N. Bezzon, A.B. Beltrán, S.M. Tebcherani, J.J. Varela, Effect of Pressure-Assisted Heat Treatment on Photoluminescence Emission of α-Bi 2 O 3 Needles, (2015). https://doi.org/10.1021/acs.inorgchem.5b01237.

[41] Y. Wu, G. Lu, The roles of density-tunable surface oxygen vacancy over bouquet-like Bi 2 O 3 in enhancing photocatalytic activity †, Phys. Chem. Chem. Phys. 16 (2014) 4165. https://doi.org/10.1039/c3cp54461c.

[42] L.A. Giannuzzi, B.W. Kempshall, S.M. Schwarz, J.K. Lomness, B.I. Prenitzer, F.A. Stevie, FIB Lift-Out Specimen Preparation Techniques, in: Introduction to Focused Ion Beams, Kluwer Academic Publishers, Boston, 2005: pp. 201–228. https://doi.org/10.1007/0-387-23313-X_10.

[43] D.R. Hamann, D.A. Muller, Absolute and Approximate Calculations of Electron-Energy-Loss Spectroscopy Edge Thresholds, Physical Review Letters. 89 (2002) 126404–4. https://doi.org/10.1103/PhysRevLett.89.126404.

[44] C.-H. Ho, C.-H. Chan, Y.-S. Huang, L.-C. Tien, L.-C. Chao, The study of optical band edge property of bismuth oxide nanowires α-Bi 2 O 3, Phys. Chem. Chem. Phys. 12 (2007) 1843–1850. https://doi.org/10.1364/OE.21.011965.

[45] T. Saison, N. Chemin, C. Chan, O. Durupthy, V. Erie Ruaux, L. Mariey, F.-O. Maug, P. Beaunier, J.-P. Jolivet, Bi 2 O 3 , BiVO 4 , and Bi 2 WO 6 : Impact of Surface Properties on Photocatalytic Activity under Visible Light, J. Phys. Chem. C. 115 (2011) 5657–5666. https://doi.org/10.1021/jp109134z.

[46] Y. Qiu, M. Yang, H. Fan, Y. Zuo, Y. Shao, Y. Xu, X. Yang, S. Yang, Nanowires of a-and b-Bi 2 O 3 : phase-selective synthesis and application in photocatalysis †,. https://doi.org/10.1039/c0ce00508h.

[47] H. Cheng, B. Huang, J. Lu, Z. Wang, B. Xu, X. Qin, X. Zhang, Y. Dai, Synergistic effect of crystal and electronic structures on the visible-light-driven photocatalytic performances of Bi 2 O 3 polymorphs, Phys. Chem. Chem. Phys. 12 (2010) 15468–15475. https://doi.org/10.1039/c0cp01189d.

[48] C. Almbladh, P. Minnhagen, Comments on hole lifetime effects in deep-level spectroscopies*, Physical Review B. 17 (1978) 929–939.

[49] H.K. Schmid, W. Mader, Oxidation states of Mn and Fe in various compound oxide systems, Micron. 37 (2006) 426–432. https://doi.org/10.1016/j.micron.2005.12.004.

[50] A. López-Ortega, A.G. Roca, P. Torruella, M. Petrecca, S. Estradé, F. Peiró, V. Puntes, J. Nogués, Galvanic Replacement onto Complex Metal-Oxide Nanoparticles: Impact of Water or Other Oxidizers in the Formation of either Fully Dense Onion-like or Multicomponent Hollow MnOx/FeOx Structures, Chemistry of Materials. 28 (2016) 8025–8031. https://doi.org/10.1021/acs.chemmater.6b03765.

[51] Z. Wang, J. Bentley, N. Evans, Valence state mapping of cobalt and manganese using near-edge fine structures, Micron (Oxford, England : 1993). 31 (2000) 355–62. https://doi.org/10.1016/S0968-4328(99)00114-6.

[52] SciPy: Open Source Scientific Tools for Python | BibSonomy,. https://www.bibsonomy.org/bibtex/24b71448b262807648d60582c036b8e02/neurokernel (accessed January 12, 2022).

[53] P. Schattschneider, B. Jouffrey, C. Hebert, Orientation dependence of ionization edges in EELS, Ultramicroscopy. 86 (2001) 343–353.

[54] M. Vila, C. Díaz-Guerra, J. Piqueras, Luminescence and Raman study of α-Bi2O3 ceramics, Materials Chemistry and Physics. 133 (2012) 559–564. https://doi.org/10.1016/j.matchemphys.2012.01.088.

[55] S. Schmidt, E.T. Kubaski, D.P. Volanti, T. Sequinel, V.D.N. Bezzon, A. Beltrán, S.M. Tebcherani, J.A. Varela, Effect of

Pressure-Assisted Heat Treatment on Photoluminescence Emission of ??-Bi2O3 Needles, Inorganic Chemistry. 54 (2015) 10184–10191. https://doi.org/10.1021/acs.inorgchem.5b01237.

[56] Y. Wu, G. Lu, The roles of density-tunable surface oxygen vacancy over bouquet-like Bi2O3 in enhancing photocatalytic activity, Phys. Chem. Chem. Phys. 16 (2014) 4165–4175. https://doi.org/10.1039/c3cp54461c.

Chapter 5: Understanding the Verwey transition

At room temperature Fe_3O_4 has a cubic inverse spinel structure (Fd-3m). At T ~ 125 K the cubic structure changes to monoclinic, this is the Verwey transition. The distortion of the structure induces a strong change in the magnetic behaviour of magnetite. Despite the relevance and ubiquitousness of Fe_3O_4, the Verwey transition is still not fully understood. In this Chapter, in-situ TEM is used to carry out the HRTEM and EELS analyses of Fe_3O_4 nanocubes before and after cooling them to below T_V. Evidencies of the Verwey transition are detected by both techniques. DFT calculations are carried out to compare the density of states for different phases with the ELNES of the Fe $L_{3,2}$ edge in Fe_3O_4 and to identify the origin of the ELNES fingerprint indicating a Verwey transition

5.1 State of the art – Motivation

Magnetite (Fe_3O_4) is the oldest known magnetic material, with important significance for physics, engineering, chemistry, geology, medicine and biology[1–22]. At room temperature Fe_3O_4 is a half-metal with a cubic inverse spinel structure (Fd-3m). However, at around $T_V \sim 125$ K the cubic structure distorts to monoclinic and the material undergoes metal-insulator transition (Figure 5.1), known as the Verwey transition[23]. Given the important fundamental implications of this transition in condensed matter physics (e.g., correlated electronic materials), it has been extensively studied during the last decades[24–26]. However, despite the intense research, the Verwey transition remains an open issue.

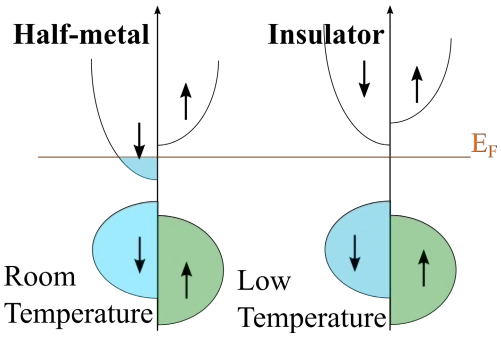

Figure 5.1 Verwey transition: half-metal to insulator.

The monoclinic low temperature phase of Fe_3O_4 is rather complex. In fact, among other factors, the large number of parameters to be refined, the strong twinning (due to the loss of symmetry), the multiple scattering and the self-absorption make the determination of the exact space group of the Verwey phase of Fe_3O_4 by single-crystal diffraction a rather difficult task[27]. Actually, the exact structure of this phase remains controversial, and different monoclinic phases have been proposed, e.g., Cc[28], P2/c[29] and C2/c[27] (displayed in Figure 5.2). The three monoclinic phases present small differences amongst them, just a small distorsion of their unit cell. According to the literature the most suitable one is the P2/c, and it has been assumed in the majority of the studies [30,31].

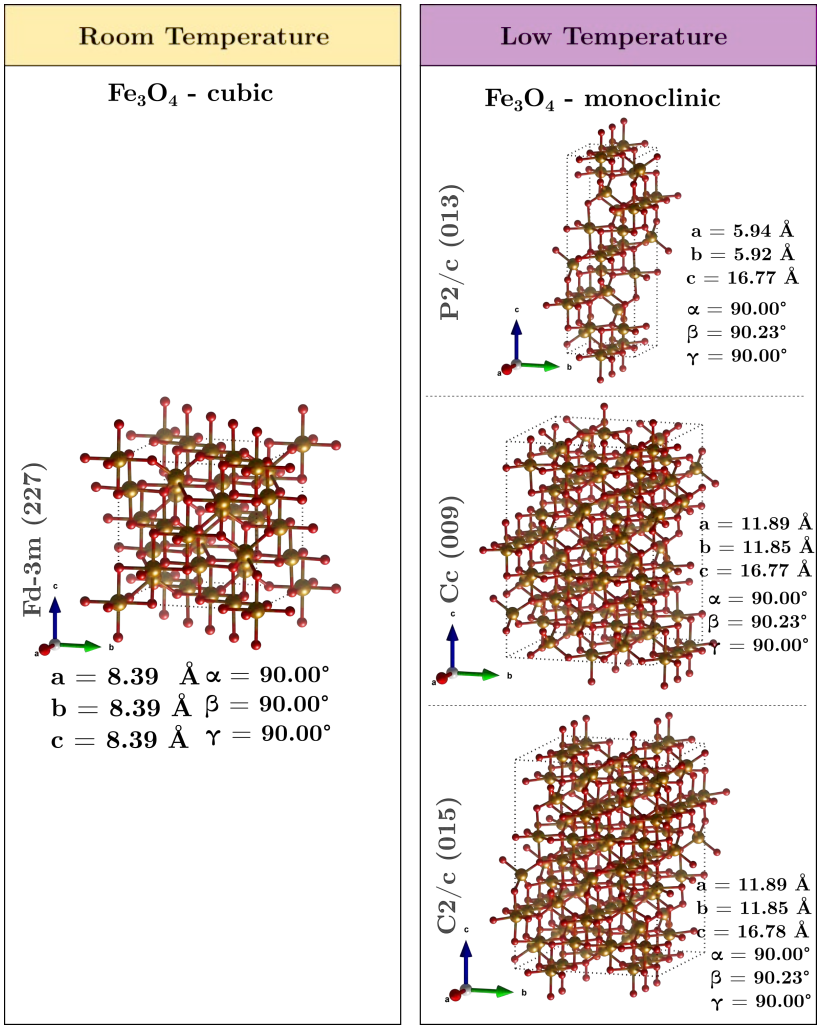

Figure 5.2 Fe_3O_4 crystallographic phases. (Left) magnetite room temperature phase and (right) possible low temperature monoclinic phases. (Fe atoms in brown and O atoms in red).

In nanostructured Fe_3O_4 samples, the interpretation of macroscopic data is rather complex due to the effects of concomitant particle size distributions and the severe peak broadening observed in diffraction methods due to the small crystallite size. Therefore, studies on single sub-30 nm nanoparticles (where T_V starts to significantly decrease from bulk values) are critical to understand the implications of the Verwey transition in the nanoscale. On the other hand, nanostructured samples can provide advantages over single crystal measurements since defects like twinning

(unavoidable in bulk samples) or magnetic domains are often avoided. Although some reports on the electronic, magnetic and transport properties in individual nanoparticles can be found in the literature[32–36], there are no direct evidence of the structural changes involved in the Verwey transition in single Fe_3O_4 nanoparticles.

Electron Energy Loss Spectroscopy (EELS) combined with High Resolution Transmission Electron Microscopy (HRTEM) of a perfect sample by controlling its temperature could be the most suitable way to detect structural and electronic changes due to the Verwey transition[37–39]. However, the interpretation of the obtained results is not straightforward and additional theoretical information is needed. EELS data contain all the information, regarding bonding, oxidation state, etc., and, thus, the Verwey transition is expected to manifest in EELS core loss data, so that a fingerprint can be found. An in-depth understanding of this fingerprint requires DFT simulations.

In this Chapter, the low temperature crystalline phase after the Verwey transition in single Fe_3O_4 nanocubes will be studied by a combination of aberration corrected HRTEM imaging and both experimental and simulated EELS. The transition from cubic to monoclinic crystalline structure below the Verwey temperature (T_V) is assessed both by HRTEM and EELS after in situ cooling from room temperature to 100 K in the TEM sample holder. Density Functional Theory (DFT) calculation is used to analyze the fingerprint of the Verwey transition in the EEL spectra.

5.1.1 Material and preliminary characterization

Fe_3O_4 nanocubes were provided by the Magnetic Nanostructures group of Prof. Josep Nogués from ICN2.

The nanocubes were synthesized following the method previously reported by Kim et al[40]. Briefly, this method consists in the decomposition of iron(III) acetylacetonate in benzyl ether with the presence of oleic acid and 4-biphenylcarboxyilic acid at 290°C. To obtain the Fe_3O_4 nanoparticles, all chemicals were used as supplied without further purification: iron (III) acetylacetonate>97% (Fluka); oleic acid>90% (Sigma); 4-biphenylcarboxylic>99% (Acros Organics); dibenzyl ether>98% (Acros Organics). Iron (III) acetylacetonate (0.71 g) was added to a mixture of

oleic acid (1.27 g) and 4-biphenylcarboxyilic acid (0.4 g) and dibenzyl ether (10 mL). This mixture was degassed at room temperature for 30 min in vacuum (~10^{-2} mbar) under vigorous magnetic stirring. Then, the slurry was heated up to 290 °C at a rate of 20°C/min under argon atmosphere and kept at this temperature for 30 minutes. Finally, the reaction was cooled down to room temperature. To purify the nanocubes, the resulting product was washed twice with a mix of toluene and hexane (4:1) and centrifuged for 5 minutes at 4000 rpm discarding the supernatant. Next, the nanocubes were dispersed in chloroform and centrifuged again. A last step of purification was carried out by resuspension in hexane and centrifugation. Finally, the nanoparticles were resuspended in toluene and stored in the fridge.

In order to check the crystallinity of the sample XRD measurements were carried out using an X'pert PRO MPD from PANalytical with a Cu Kα radiation (λ = 1.540 Å). The crystallite size was calculated using the Debye-Scherrer equation using the 311 peak.

The XRD pattern shown in Figure 5.3(a) confirms that the room temperature structure of the particles is that of a cubic spinel (Fd-3m), consistent with either Fe_3O_4 or γ-Fe_2O_3. The crystallite size, evaluated from the Scherrer equation[41], was found to be 25 nm.

Magnetic characterization was performed using a SQUID magnetometer (MPMS XL, Quantum Design). The temperature dependence of the magnetization was recorded by performing Zero-Field-Cooling (ZFC) and

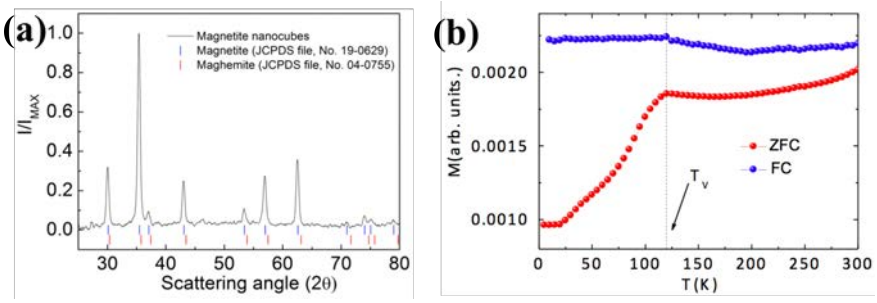

Figure 5.3 (a) XRD pattern of the nanocubes compared to a Fe_3O_4 and γ-Fe_2O_3 references (vertical lines). (b) Zero field cool (ZFC) and field cool (FC) magnetization versus temperature curves (H = 25 Oe) showing the presence of the Verwey transition at around 120 K.

Field-Cooling (FC) measurements between 5 and 300 K under an applied field of 25 Oe.

The temperature dependence of the magnetization exhibits a small maximum in the FC curve and a clear decrease of the magnetization in the ZFC curve, at about 120 K (Figure 5.3(b)). These are typical features of the Verwey transition (T_V = 120 K) for Fe_3O_4[24,25]. The somewhat broad transition probably stems from the particle size distribution, where smaller particles are expected to exhibit lower T_V[31]. Thus, the studied nanoparticles could correspond to Fe_3O_4 nanocubes at room temperature. Around 120K, a change in the magnetization occurs which can be identified as the Verwey transition.

5.2 TEM Characterization

The Verwey transition detected by the magnetic measurements was observed in-situ in the TEM using a cooling sample holder. HRTEM and EELS data were collected before and after reaching T_V. A general TEM characterization was obtained before the in-situ experiment to assess the homogeneity of the nanocubes.

TEM Images were acquired using a JEOL JEM-1400 transmission microscope operating at 120 kV. The TEM specimens were prepared by electron dispersing the particles in hexane and dipping a holey carbon copper grid into a freshly sonicated dispersion.

The analysis of the low resolution TEM images (Figure 5.4(a,c)) shows that the nanoparticles display a cubic morphology with an average edge length of 24 nm and a narrow size distribution, fitted to a log-normal distribution with $\sigma_{log\text{-}norm}$=0.18 (Figure 5.4(b)). The average particle size and standard deviation were estimated by measuring the edge length of more than 200 particles. By HRTEM, the good crystallinity of the nanocubes was observed, as well as the fact that they do not present any defects (Figure 5.4(d)).

The nanocubes were also characterized at room temperature by EELS. Iron (III) oxide (γ-Fe_2O_3) and iron (II,III) oxide (Fe_3O_4) reference spectra were compared with the experimental ones (Figure 5.5).

By comparing the fine structure of the spectra with reference spectra from the literature[42], the nanocubes were confirmed to be Fe_3O_4. Note that the characteristic splitting of the oxygen K pre-peak in γ-Fe_2O_3 is not observed in the experimental data (Figure 5.5) discarding its presence in the sample. No variation of the EEL spectra from the center towards the edges of the particles was detected, confirming the homogeneity of the nanocubes.

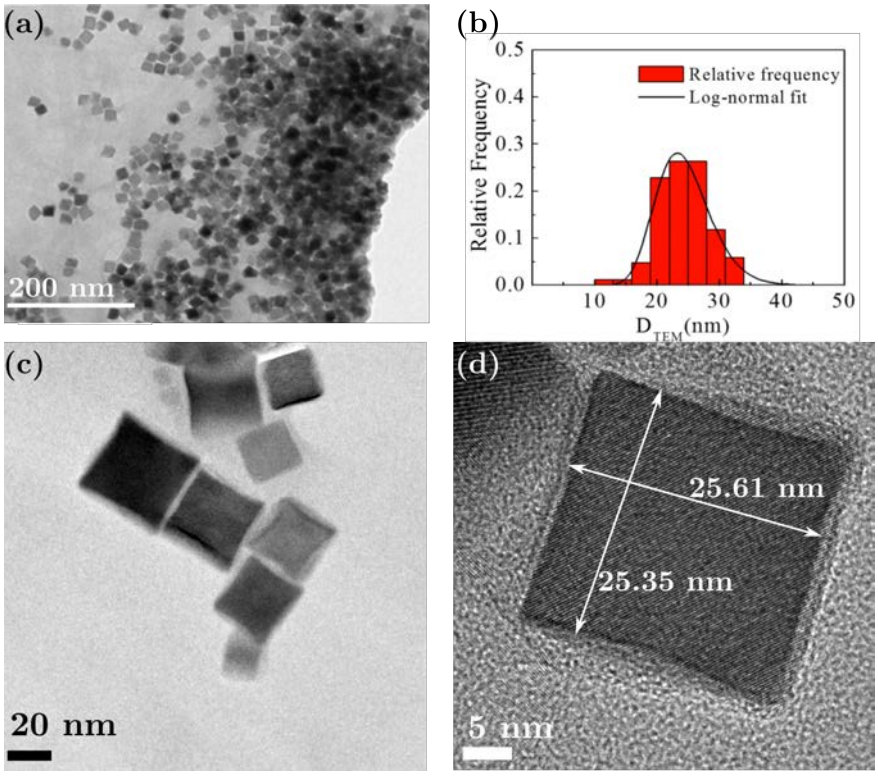

Figure 5.4 (a,c) General TEM image of the nanoparticles. (b) Particle size distribution histogram fitted to a log-normal function. (d) HRTEM image of one isolated nanocube with size annotations.

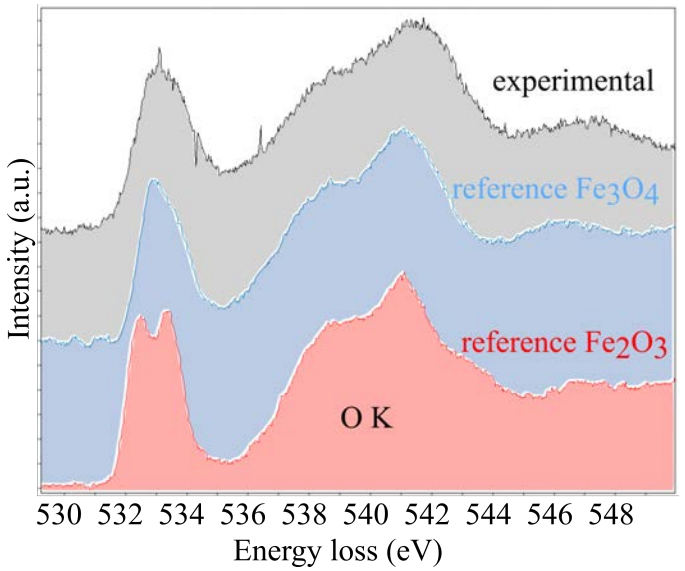

Figure 5.5 Phase determination by core loss EELS comparison. The experimetal EELS spectra (gray) is compared with the references for Fe_2O_3 (red) and the Fe_3O_4 (blue).

5.2.1 In-situ cooling experiment

HRTEM images were acquired in an image corrected Titan 60-300 microscope, operated at 300 kV and equipped with a Schottky field emission electron gun and an aberration corrector in the objective lens. EELS spectra were acquiredin a probe corrected Titan 60-300 microscope equipped with a high brightness XFEG gun and a Wien filter monochromator coupled to a Gatan Tridiem 866 ERS spectrometer. The sample was cooled for the cryo experiments using a liquid nitrogen sample holder from Gatan.

The exact same nanocube was observed at room temperature (RT) and low temperature (LT). The HRTEM image of a nanocube taken at room temperature seen along one of its edges shows the monodomain crystallinity of the cube (Figure 5.6(a)). By computing and indexing the Fast Fourier Transform (FFT) of the HRTEM image, the crystal structure could be assigned to the expected cubic spinel (space group Fd-3m) viewed along the [101] zone axis (Figure 5.6(c)).

Subsequently, HRTEM images were acquired from the same nanocube at 100 K (below Tv) (Figure 5.6(b)). Directly comparing both HRTEM images, the change in the crystalline structure is hinted at. It is worth emphasizing the defect-free structure of the nanoparticle even at 100 K, with no twinning, in contrast to what is often observed in bulk magnetite[43]. In addition, by computing the FFT, the change is evidenced, as extra spots appear (see the spots highlighted in green in Figure 5.6(d)), evidencing the temperature-induced structural modulation. The indexation of the FFT spots of this low temperature (below Tv) phase is compatible with the [100] zone axis of the monoclinic phase proposed in the literature: space group P2/c[29]. Note that the crystal orientation of the observed

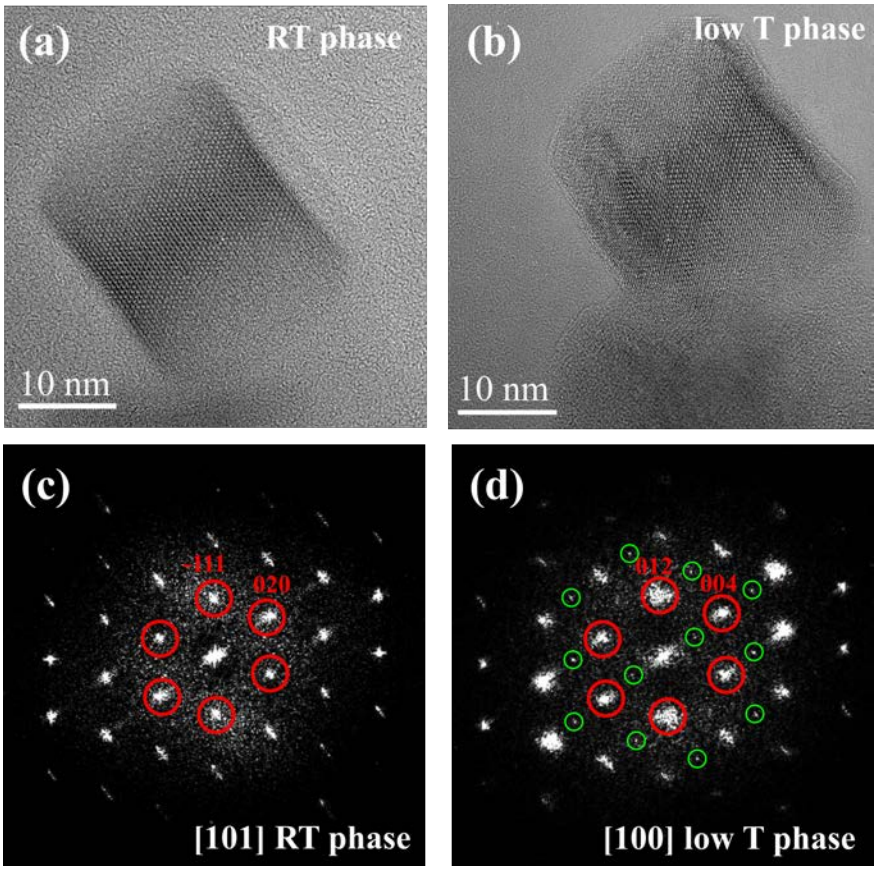

Figure 5.6 HRTEM images obtained from the same nanocube acquired at RT (a) and at 100 K (b) and their corresponding FFTs (c,d). The equivalent spots are marked in red and the additional spots appearing due to the superstructure modulation are marked in green.

nanocube was chosen because of the expected high density of superstructure spots in the reciprocal space for the low temperature monoclinic phase observed along the [100] direction.

Electron energy loss spectra were acquired in the spectrum image mode over single nanocubes. The resulting large datasets were denoised using Principal Component Analysis (PCA) routines in the HyperSpy toolbox[44]. Afterwards, a Richardson-Lucy deconvolution of the zero-loss peak was performed in order to improve energy resolution.

EELS data were obtained from several nanoparticles at room temperature and at 100 K with energy loss ranges including the oxygen K edge at about 532 eV or the iron L_3 and L_2 edges at about 708 eV and 720 eV, respectively.

The iron $L_{3,2}$ edge for the same nanocube at room and low temperature is plotted in Figure 5.7(a). As it can be observed, the general appearance of the edges is the same, there is no shift or splitting in any of the edges. However, if both spectra are overlapped and zoomed on the L_3 edge, at an energy range between 707 eV and 718 eV, as it is shown in Figure 5.7(b), a clear difference is detected. There is an increase in intensity in the first peak of the L_3 doublet at low temperature in comparison with the room temperature spectrum. This difference in the intensity ratio of the L_3 doublet can be directly assigned to the Verwey transition. The ratio of both first peaks of the RT versus the LT is $\frac{3}{4}$. Conversely, no changes were observed in the O K edge.

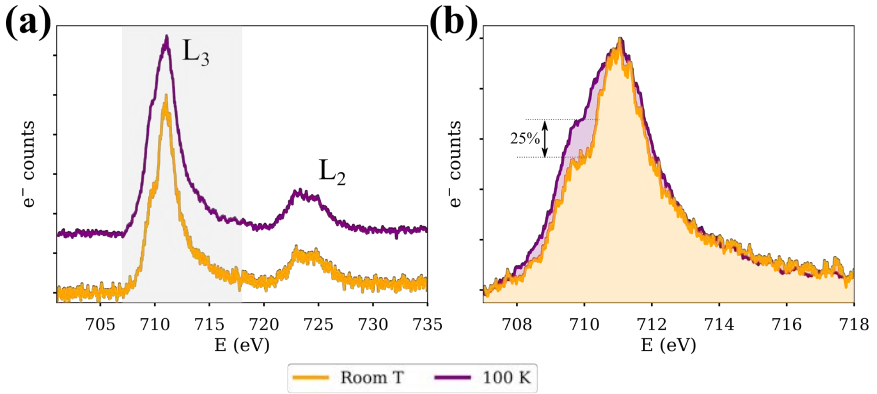

Figure 5.7 Experimetal O K edge ELNES. (a) $L_{3,2}$ Fe edge integrated and processed for the same nanocube after and before reducing the temperature to 100K. (b) Zoom in of gray region of (a) which corresponds to the L_3 Fe.

Thus, by cryo-TEM the Verwey transition was detected. The structural modification appeared in the HRTEM image as a change in the phase contrast modulation and in EELS in the Fe L_3 edge as an increase in the intensity of the first sub-peak. To validate the results and analyze the origin of the edge shoulder, the experiment was complemented with simulations.

5.3 Structural analysis

As it has been presented in the introduction, at room temperature Fe_3O_4 presents an inverse spinel structure (space group 227) with 3 atoms in the asymmetric unit: two iron and one oxygen. These two non-equivalent irons will correspond to the usual positions A and B in the inverse spinel structures ($FeA^{3+}[Fe^{2+}Fe^{3+}]BO_4$). From now on, the irons will be always differentiated as FeA and FeB: the first one corresponds to the one placed in the tetrahedral (T_d) position with spin down and the second one corresponds to the one in the octahedral (O_h) positions with spin up; the same notation will be used in the monoclinic cell. Figure 5.8 illustrates the cubic structure, FeA atoms are highlighted in light blue and FeB in green. The polyhedrons have been superposed to clarify how FeA and FeB can be identified.

The monoclinic structure cannot be identified as an inverse spinel structure because of the present distortion; however, the non-equivalent iron

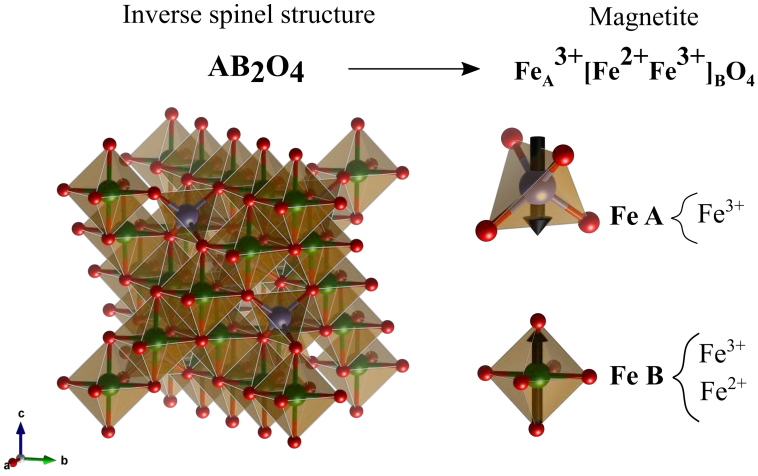

Figure 5.8 Room temperature Fe_3O_4 crystallographic phase, inverse spinel. The octahedral and tetrahedral positions have been indicated.

atoms of the unit cell are, also, placed in the O_h and T_d positions. Thus, the same notation will be used.

The presented structures, i. e. Fd-3m and P2/c Fe_3O_4, were used to index the FFT of the HRTEM images (Figure 5.9 (a,d)). As has been explained, at room temperature the indexation was trivial, it fitted perfectly with the cubic Fe_3O_4 along the [101] zone axis, while for the LT if fitted the monoclinic phase, P2/c, along the [100] zone axis.

Figure 5.9(b,e) shows the calculated sections of the reciprocal space corresponding to the two different cases alongside the experimental FFT, where the low temperature monoclinic phase shows additional spots due to the lower symmetry structural modulation. The calculated FFT is in excellent agreement with the experimental results, where the additional spots found experimentally (highlighted by green circles in Figure 5.9(a,d)) coincide with those found in the simulations (Figure 5.9(e)).

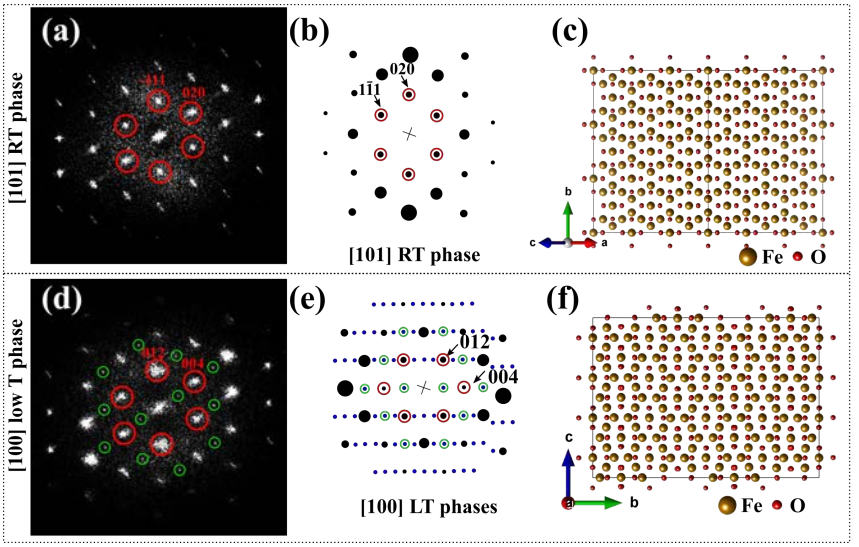

Figure 5.9 Indexation of the FFT. (a,d) FFT for the RT and LT HRTEM images. (d,e) Theoretical diffraction pattern of the RT along the [101] zone axis and LT along the [100]. (c,f) RT and LT crystalline structure viewed along the before mentioned zone axis.

5.4 Electron configuration: Density Functional Theory

DFT simulations were carried out using the cubic and the monoclinic phase of Fe_3O_4 with the aim of understanding the meaning of the variation in the L_3 splitting and explaining the origin of the shoulder.

5.4.1 Structural relaxation

Structural relaxation was performed on both models by VASP. A cutoff energy of 400 eV for the plane waves was used. A 11x11x22 Monkhorst-Pack k-point grid in the Brillouin zone was used for the cubic phase. The number of k-points was decreased for the monoclinic phases as the number of non-equivalent atoms increases. For the P2/c a 6x6x2 Monkhorst-Pack k-point grid was used. In order to increase the bandgap, GGA+U was performed considering the Coulomb energy (U) for the Fe cations; the U value was set according to [45]. The spin configuration was set according to usual inverted spinel ($FeA^{3+}[Fe^{2+}Fe^{3+}]BO_4$) configuration, spin up for octahedral Fe (FeB) cations and down for the tetrahedral ones (FeA).

Fd-3m(227)				P2/c(013)			
Original		Relaxed		Original		Relaxed	
a	8.395 Å	a'	8.3182 Å	a	5.944 Å	a'	5.880 Å
b	8.395 Å	b'	8.3182 Å	b	5.924 Å	b'	5.826 Å
c	8.395 Å	c'	8.3182 Å	c	16.775 Å	c'	16.474 Å
α	90°	α'	90°	α	90°	α'	90°
β	90°	β'	90°	β	90.23°	β'	90.06°
γ	90°	γ'	90°	γ	90°	γ'	90°

Table 5.1 Crystallographic data of the cubic and monoclinic cells after and before the relaxation.

In the structural relaxation all the atomic positions as well as the lattice parameters were let free to be optimized by minimizing the energy. The resulting structures have been summarized in Table 5.1. The cubic relaxed structure presents a slight modification in the lattice parameters but no change in the angles. On the other hand, for the monoclinic structure, changes were found in the lattice parameters as well as on the angles: it

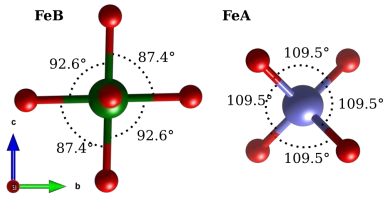

Figure 5.10 Fe_3O_4, 227 space group: FeB and FeA atomic positions.

reached a shape closer to the orthorhombic system, as all the angles were 90° or close.

It is worth to analyse more carefully all the non-equivalent iron positions. As it has been mentioned on the introduction, the Verwey transition induces a distortion of the octahedra and tetrahedra positions and consequently the initial cubic structure is transformed to monoclinic. The distortion can be clearly seen analysing the non-equivalent iron positions. For the cubic structure the octahedra and tetrahedra are regular, all the bonds have the same length and the angles are equal for the tetrahedral Fe and symmetric for the octahedral, as it is illustrated in Figure 5.10. On the other side, for the monoclinic structure either the tetrahedra or octahedra are not regular. Figure 5.11 illustrates the four non-equivalent FeB (O_h) and the FeA (T_d).

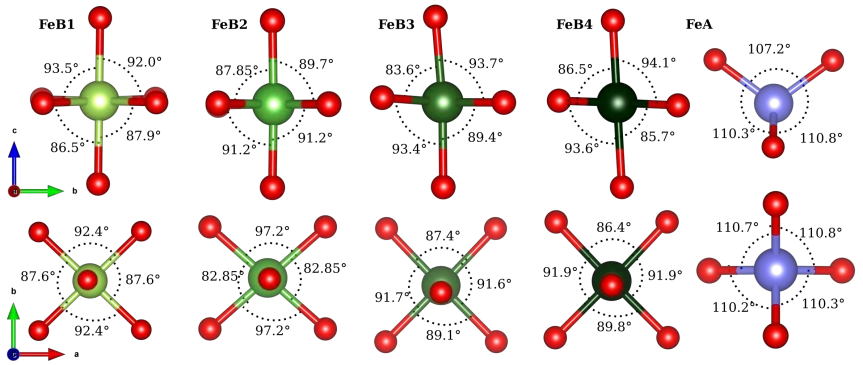

Figure 5.11 Polyhedral distortions for monoclinic Fe_3O_4 on the octahedral and tetrahedral positons.

5.4.2 Density of states

Considering the peculiarities of the Fe_3O_4 after and before the Verwey transition, the density of states is expected to present a clear difference. As

it is explained in the Fundamentals section, because of their different coordination environment, FeA (T_d) and FeB (O_h) should present different crystal splitting (as shown in Figure 5.12), and this is effectively retrieved in the calculations (Figure 5.13). Both positions present a splitting of the d orbitals; however, as it has been commented before, the splitting of the tetrahedral positions (T_d FeA) is smaller than for the octahedral ones and, for that, it will not be studied in as much detail as the O_h FeB, as it is illustrated in Figure 5.12. More specifically, by comparing the cubic structure with the monoclinic one, regular tetrahedra and octahedra will be compared with distorted ones.

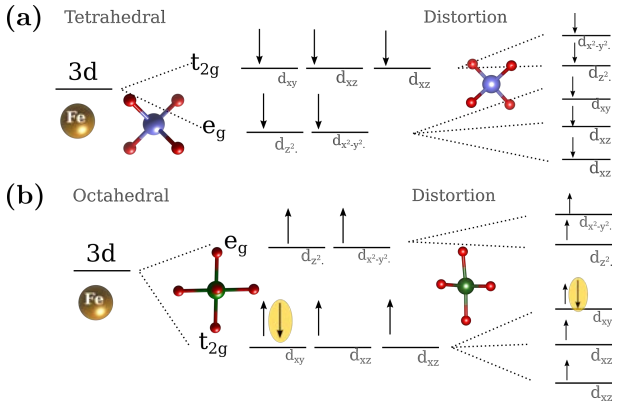

Figure 5.12 Crystal Field Splitting

The theoretical Density of States (DOS) of both phases after structural relaxation was computed by DFT. The resulting DOS are shown in Figure 5.13. As it was expected, cubic magnetite presents a half metallic behaviour (Figure 5.13(a)). The monoclinic phase corresponds to a semiconductor with a narrow bandgap, as shown in Figure 5.13(b). The obtained bandgap for the monoclinic phase was lower than 1eV, 0.351 eV, in good agreement with reported values of experimental data and other first principles calculations[46].

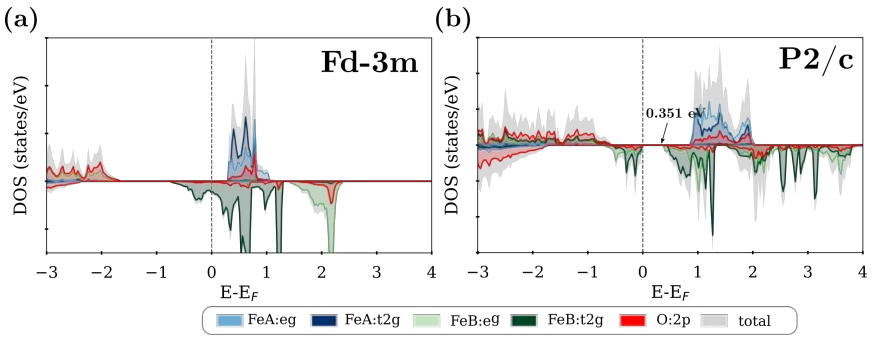

Figure 5.13 PDOS for the RT (a) Fd-3m Fe_3O_4 and the low T (b) P2/c. Represented in gray there is the total DOS, and the PDOS for each element are highlighted in colour (red for oxygen, blue for FeA and green for FeB where t2g and eg orbitals can be distinguished).

The partial DOS of the relevant orbitals around the Fermi energy is presented in Figure 5.13: the 2p-O are plotted in red, the e_g/t_{2g} -FeA in blue and the e_g/t_{2g} -FeB in green. The 3d of FeA are localized at the conduction band; conversely, the 3d of FeB are split between the valence and conduction bands. Indeed, the splitting of the 3d-FeA is small, and t_{2g} and e_g are overlapped.

For the cubic structure, all the tetrahedral/octahedral positions are equivalent, respectively, as illustrated in Figure 5.14 (left), corresponding to the [100] projection of the RT cubic phase. Conversely, for the monoclinic phase (low temperature), four FeB non-equivalent positions are found (Figure 5.14 (right)). The careful study of the partial DOS also reveals that each FeB position exhibits a different orbital splitting. These differences in the orbital splitting translate into a dissimilar magnetic spin moment, as

	Fd-3m	P2/c	Notation	
FeA	-4.04 μ_0	-3.99 μ_0	FeA	-4.00 μ_0
FeB	3.93 μ_0	3.68 μ_0	FeB1	3.60 μ_0
		4.14 μ_0	FeB2	3.70 μ_0
		4.05 μ_0	FeB3	4.05 μ_0
		3.68 μ_0	FeB4	4.14 μ_0

Table 5.2 Spin moments (μ_B) for the FeA and FeB atoms for each crystallographic phase.

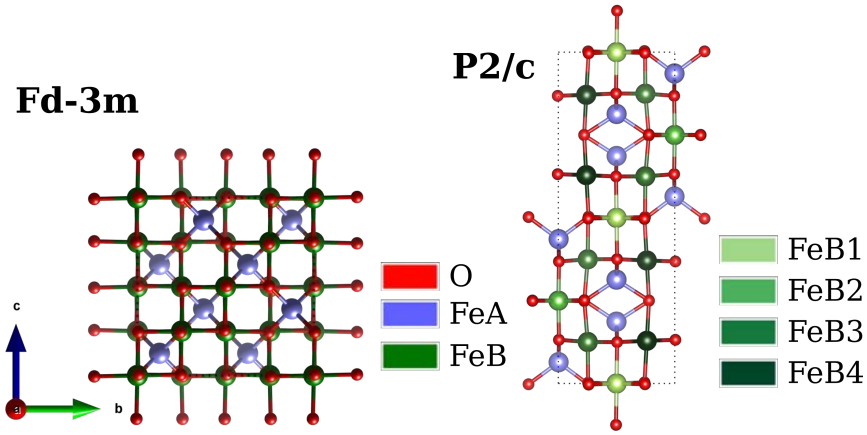

Figure 5.14 Cationic ordering of the RT structure (cubic Fd-3m) and the LT structure (monoclinic P2/c).

summarized in Table 5.2, with values in good agreement with other works[45].

Thus, from the cationic ordering of the FeBs (O_h), the charge ordering and the magnetic spin-ordering are induced.

In the case of magnetite, the room temperature conductivity is attributed to fast hopping of a 3d electron between the Fe^{2+} and Fe^{3+} ions at the B sites of the inverse spinel structure. The extra electron with minority spin in the Fe^{2+} sites occupies the t_{2g} band, as can be seen in the PDOS for magnetite in Figure 5.13(a). Below T_V, this electron hopping freezes and the Fe^{3+} and Fe^{2+} ions arrange themselves in a fixed lattice.

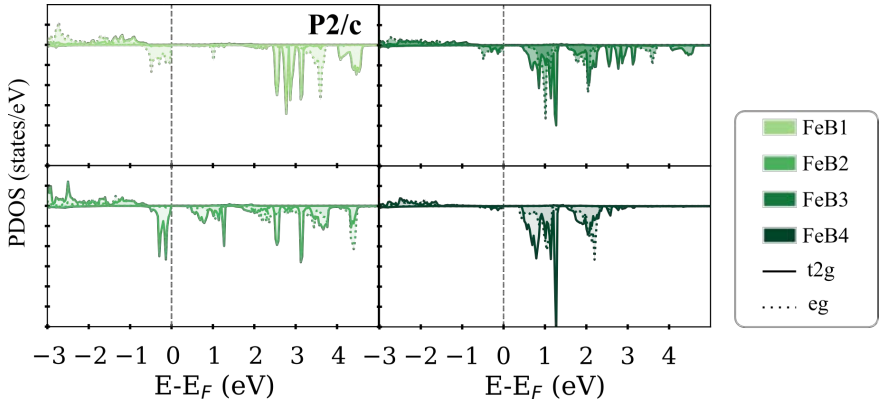

Figure 5.15 PDOS of the P2/c structure showing the difference between the FeB atoms.

This charge ordering is connected to the structural transition to the monoclinic phase through the modification of Fe-O bonds in the BO_6 octahedra. This symmetry breaking results in the splitting of the orbitals in the t_{2g} band (d_{xy}, d_{xz}, d_{yz}) in different ways depending on the crystal site (orbital ordering) (Figure 5.15). From the partial DOS, the splitting of the orbitals has been verified, and it is found that the monoclinic phase presents a splitting of the t_{2g} orbital for the octahedral Fe cations; for the tetrahedral positions the splitting is not large enough to be studied.

5.4.3 ELNES

The final step in the study was to compute the Fe L_3 edge of the LT and RT structures in order to gain more information on the contributions that generate the Energy Loss Near-Edge Structure (ELNES) and, thus, to identify the fingerprint of the Verwey transition on it.

Since changes in the ELNES features in the white lines of transition metals are strongly related to structural changes in the crystal[47–50], the slight differences in the distances and/or angles between nearest neighbour atoms for different phases should give a distinguishable fingerprint in their respective EEL spectra. Hence, since the L_3 energy loss edge in the EELS spectrum corresponds to the transitions from $p^{3/2}$ to d and s levels, the effects of the Verwey transition should be seen as the 3d density of states reflected in the ELNES of the Fe L_3 edge. Specifically, the L_3 splitting represents the t_{2g}-e_g splitting, thus the ELNES will be proportional to the PDOS at the conduction band unoccupied states; the first peak of L_3 would be proportional to t_{2g}-PDOS and the second one to e_g-PDOS, that would include the contribution of all the irons in the cell. As it has been shown before, the splitting of the FeA is negligible. Thus, FeA contribution to the L_3 will be energy localized, while the FeB will highly affect the L_3 splitting.

In order to compare the experimental data with the theoretical predictions, the ELNES simulations for the Fe cations positions was obtained for both the cubic and the monoclinic phases.

A core-hole calculation was carried out, which consists in manually moving the core electron to the conduction band. The self-consistency cycle (SCF) was re-converged for the relaxed structures using the WIEN2k considering the same GGA+U parameters as for VASP and increasing the

number of k-points and the energy range. The relaxed structure was used to compute the ELNES by TELNES[51,52] task of WIEN2k package[53,54].

However, ELNES can be affected by several conditions as for example the sample or spin orientations (as it is a magnetic material). To be sure of which are the effects of both parameters on the spectra, the Fe-L_3 of the cubic phase was computed for different configurations.

Spin orientation: Easy axis

Experimental results show that the easy axis for the room temperature structure (RT) is the [111], while at low temperature (LT) is the [100]. The ELNES of the RT structure was computed with the magnetization parallel to: [111], [100] and [001], which is the default one.

To perform the calculations for different spin orientation and check the "easy axis" direction, the symmetry of the cubic structure was reduced. A seven non-equivalent atoms structure was used as it was the simplest structure able to represent the three chosen spin configurations. This new structure will contain one FeA and three non-equivalent FeB*.

For the new structure GGA+U calculations were preformed using 4x4x4 k-mesh. The effective energy (U_{eff}) was set to 4.5 eV for both iron atoms and J_{eff} to 0.89 eV, as before. The magnetic spin was considered down for the FeA (T_d) and up for the FeB (O_h), as it was done before.

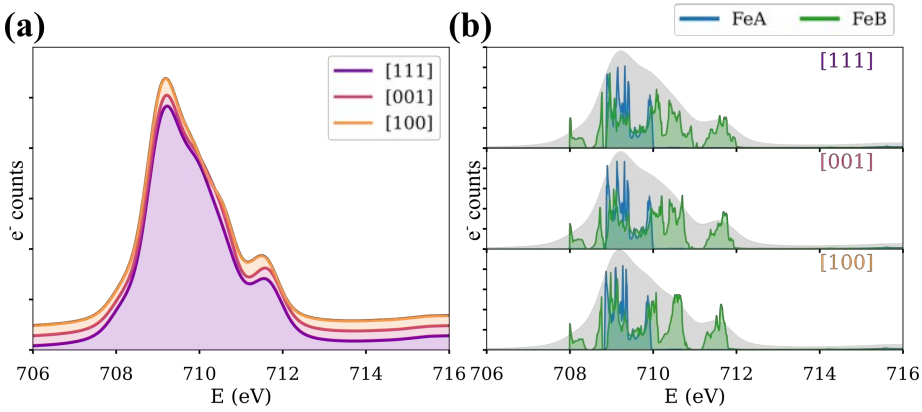

Figure 5.16 Fe L_3 computed for different spin orientations, [111], [001] and [100]. (a) the average of the Fe ELNES computed for all the Fe for each spin orientation. (b) Averaged-broadened Fe L_3 (gray) overlapped by FeA (blue) and FeB (green) ELNES without broadening for each spin-orientation.

In order to include all the transitions in the iron ELNES, the energy range was increased and the k-mesh was reset to 12x12x12. The ELNES was computed for each Fe position and averaged to get the total contribution. The convergence and collection semi angles considered were 6.3 and 19.7 mrad and the acceleration voltage was set to 300 keV, as in the experimental conditions.

Figure 5.16 displays the results of the ELNES computed for the three spin orientations. The plots represent the averaged convoluted spectra with the spectrometer broadening superposed with the pure ELNES, to be able to distinguish the contribution of each cation to the final spectra. In (a) the Fe-L_3 edges for [111], [001] and [100] have been plotted, with a small vertical shift between them for display. The three edges are equivalent, just a small energy shift of the post peak can be noticed. In (b) the edge for each configuration has been overlapped to the ELNES without broadening, which shape clearly reminds of the PDOS, the contribution of the FeA and FeB atoms are colored in blue and green, respectively.

Summarizing, the spin magnetization orientation has not a remarkable effect on the final ELNES. Yet, it produces some changes, and once all the contributions of the FeBs atoms are averaged and convoluted with the broadening, the differences are hinted at.

Sample orientation:

TELNES, the WIEN2k package to compute the ELNES, allows to take into consideration the sample orientation, expressed as a function of the Euler angles (Figure 5.17 (a)).

- α is the signed angle between the x axis and the N axis.
- β is the angle between the z axis and the Z axis.
- γ is the signed angle between the N axis and the X axis.

where x,y,z are the original axes and X,Y,Z are the rotated ones. Which can be related to the rotation matrix:

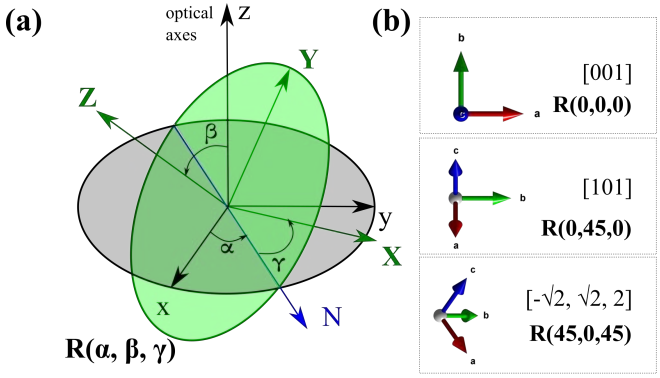

Figure 5.17 (a) Axis rotation according to the Euler angles. The initial axis system is (x,y,z) and the new one the (X,Y,Z). (b) Zone axis of interest and the corresponding rotation angles.

$$R(\alpha,\beta,\gamma) = \begin{bmatrix} \cos(\beta)\cos(\gamma) & -\cos(\beta)\sin(\gamma) & \sin(\beta) \\ \cos(\alpha)\sin(\gamma)+\sin(\alpha)\sin(\beta)\cos(\gamma) & \cos(\alpha)\cos(\gamma)+\sin(\alpha)\sin(\beta)\sin(\gamma) & -\sin(\beta)\cos(\beta) \\ \sin(\alpha)\sin(\gamma)-\cos(\alpha)\sin(\beta)\cos(\gamma) & \sin(\alpha)\cos(\gamma)+\cos(\alpha)\sin(\beta)\sin(\gamma) & \cos(\alpha)\cos(\beta) \end{bmatrix}$$

In the case of study, experimentally, the sample is oriented along the [101] zone axis and the N is considered parallel to the z direction; thus, the applied rotation should be (0,45,0). However, additional orientations have been considered to assess the orientation effects, namely, (0,0,0) and (45,0,45). In Figure 5.17 (b) the studied orientations are listed with the zone axis to which they correspond. By default, if no information about the sample orientation is provided, no preferent direction is considered and all the orientations are averaged.

Figure 5.18 (a) shows the unit cell oriented in the three studied orientations and the average case. The computed Fe L_3 edges are plotted, as for the spin orientation case. However, as before, no perceptible change appears (Figure 5.18 (b)). Thus, the consideration of using the average case would not lead to a wrong conclusion.

After the analysis of the orientation dependence of the Fe-L_3 ELNES, the configuration chosen to be the most suitable one is the average sample orientation with spin orientation according to its easy axis. Thus, for the cubic phase the spin orientation will be [111] and for the monoclinic phase [100].

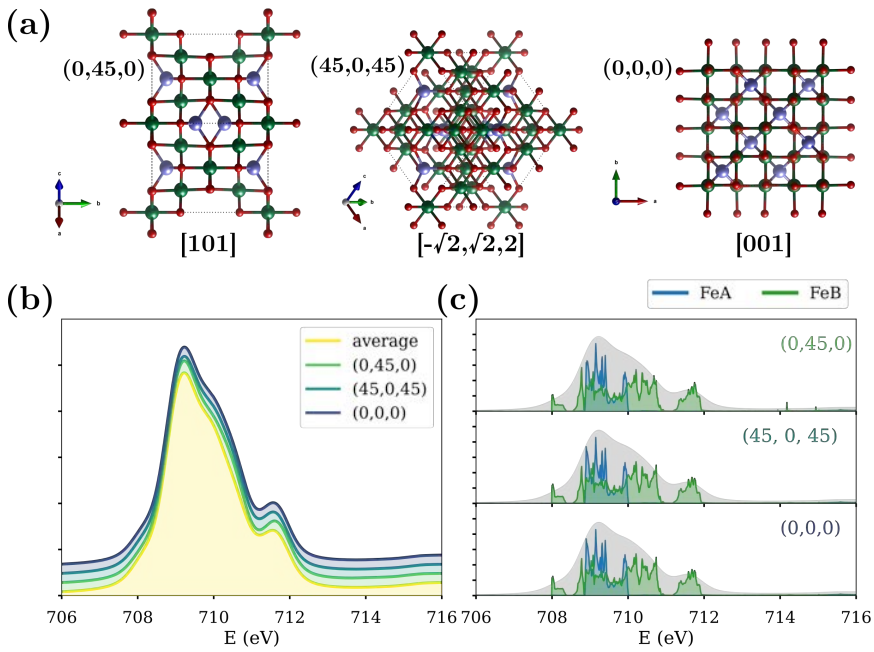

Figure 5.18 Fe L_3 computed for different crystal orientation. (a) Scheme of the three studied crystal orientations with the corresponding Euler angles. (b) Average of the Fe L_3 ELNES computed from all the Fe for each crystal orientation. (c) Averaged-broadened Fe L_3 (gray) overlapped by FeA (blue) and FeB (green) ELNES without broadening for each sample orientation.

Origin of the ELNES features

The detailed study of the Fe L_3 edge for the cubic phase allows to glean evidence of the origin of all the features present in it. Figure 5.19 (a) shows the edge obtained by weight averaging (considering the multiplicity) of all iron contributions (in gray); in addition, the FeA (blue) and the FeB (green) contributions are also distinguished. The FeB is the result of the averaging of all the non-equivalent FeB*; notice that the symmetry of the cubic cell has been reduced in order to consider a [111] spin axis. Thus, it is clear that the main peak is the fingerprint of the FeA (T_d) atoms, while the FeB (O_h) are responsible for the pre- and post- shoulders. In addition, if the pure ELNES without broadening is plotted, a correlation can be seen with the PDOS. The goal was to disentangle the reason for the variation of the pre-peak intensity, and it is clear that, for the case of the cubic phase, it is directly related with the t_{2g}-Fe orbitals.

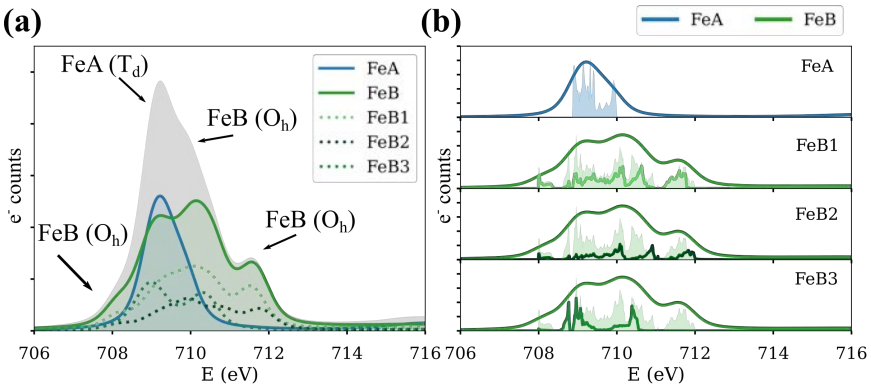

Figure 5.20 Fe L_3 edge of the Fd-3m phase. (a) Averaged Fe-L_3 (gray), overlapped with the FeA (blue) and FeB (green) contributions, the dashed-greenish lines correspond to the FeBs contributions. (b) ELNES with (solid line) and without (solid color) broadening overlapped with the Fe L_3 ELNES.

The same procedure was repeated for the monoclinic structure (P2/c). The spin orientation was the same as the easy axis, [100]. However, as the monoclinic structure has a big number of atoms in the unit cell, computing the ELNES for each of them was not realistic due to the amount of time that would involve. Therefore, the average was computed from the ELNES of one iron of each type (FeA, FeB1, FeB2, FeB3, FeB4).

The results of the ELNES calculations are summarized in Figure 5.20. Conversely to the cubic case, the monoclinic phase presents a clear splitting

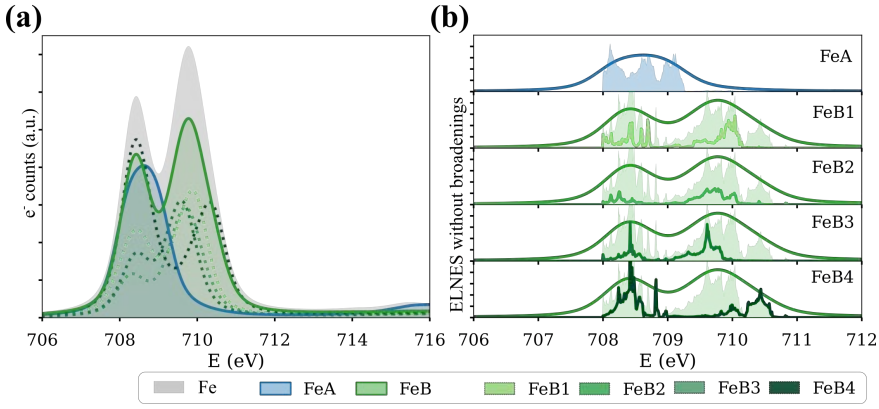

Figure 5.19 Fe L_3 edge of the P2/c phase. (a) Averaged Fe-L_3 (gray), overlapped with the FeA (blue) and FeB (green) contributions, the dashed-greenish lines correspond to the FeBs contributions. (b) ELNES with (solid line) and without (solid color) broadening overlapped to the Fe ELNES.

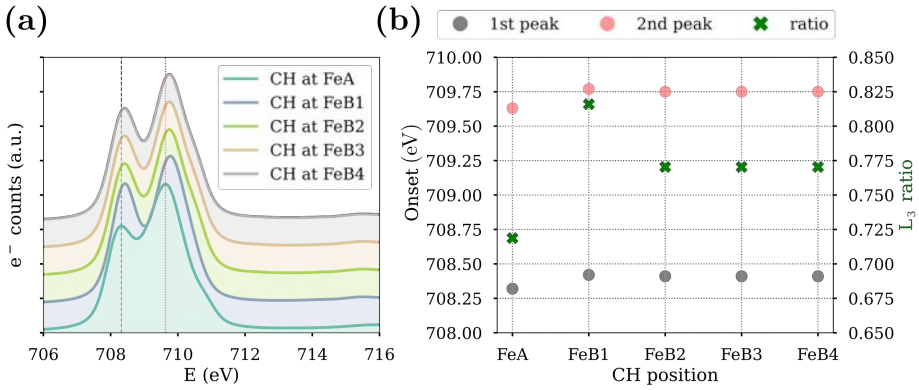

Figure 5.21 Core-hole effect. (a) Fe-L_3 averaged computed considering the CH in different atomic positions. (b) Onset (1st peak-gray and 2nd peak-red) and ratio (green) of the L_3 depending on the atomic position where the core-hole is done.

of the L_3. Two peaks of different intensity can be distinguished. In addition, the post-peak is not detected for the monoclinic case. Taking a closer look, the origin of the main features can be identified. The first peak has the contribution of FeA and FeB, while the second one is mainly composed by FeB contributions. Considering the non-equivalent FeB, it is worth to notice that the FeB4 has an inversion of the ratio of the peaks, and it is the one responsible for the weak post peak feature, as it is seen more clearly in Figure 5.20 (b), where the ELNES without broadening is displayed.

The change in the ELNES due to the core-hole can be really dramatic; to control the real consequences, the same calculation was done considering the core-hole for each of the non-equivalent Fe atoms in the monoclinic structure (FeA, FeB1, FeB2, FeB3, FeB4).

For the core-hole in a FeA(T_d) site, two peaks are clearly distinguished at energies 708.3 eV and 709.6 eV as marked with a grey/red vertical line respectively. Both peaks shift to higher energies for FeB site core-holes (a). In addition, the ratio, defined as the intensity of the second peak over the first one, is lower if the CH is in a FeA site.

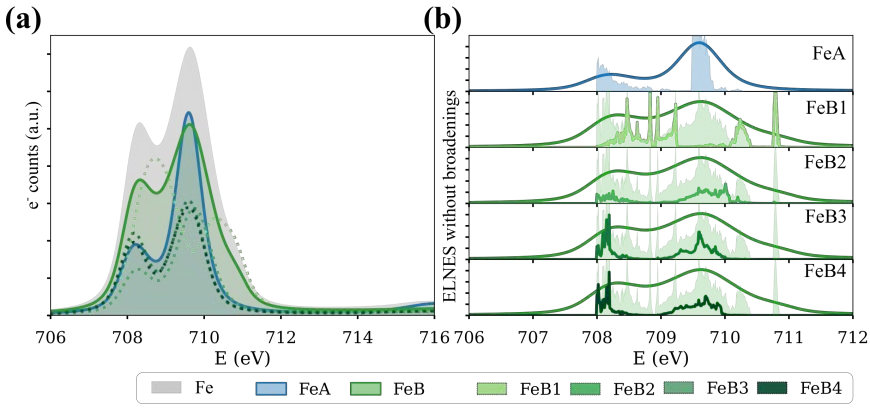

Figure 5.23 Fe L_3 edge with a CH in a FeA position. (a) Averaged Fe-L_3 (gray), overlapped with the FeA (blue) and FeB (green) contributions, the dashed-greenish lines correspond to the FeBs contributions. (b) ELNES with (solid line) and without (solid color) broadening overlapped to the Fe ELNES

By looking at the contributions of each iron atom to the L_3, the origin of the difference is clear: the first peak is the result of the unoccupied FeA 3d and FeB t_{2g}, while the second is mainly due to the FeB contributions. By performing the core-hole on a tetrahedral position it is clear that a splitting of the L_3 occurs as the occupancy of the core orbitals varies, because a core electron has been removed to produce the hole, (Figure 5.22) and the energy splitting increases with respect to the initial tetrahedral

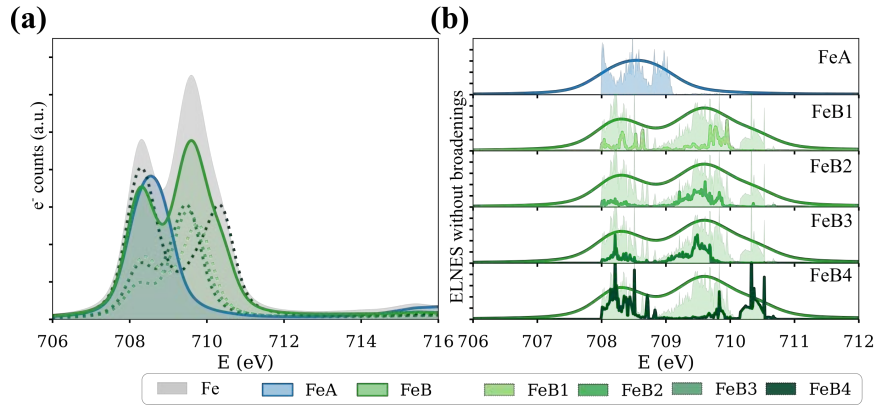

Figure 5.22 Fe L_3 edge with a CH in a FeB position. (a) Averaged Fe-L_3 (gray), overlapped with the FeA (blue) and FeB (green) contributions, the dashed-greenish lines correspond to the FeBs contributions. (b) ELNES with (solid line) and without (solid color) broadening overlapped to the Fe ELNES.

configuration, as a free state is produced. Reproducing the same logic to CH in the octahedral position (FeB) the change is lower as the splitting was already there (as it has been mentioned before the d orbitals were completely split for the distorted octahedra), even if a clear difference in the ratio can be observed, as shown in Figure 5.23.

Summing up, after the detailed study of the Fe L_3 ELNES an univocal relation can be established between the ratio of the peaks and the occupancy of the 3d orbitals. The splitting of the 3d of the O_h position is the key point. Once the Verwey transition happens, and the structure is distorted, the character of the FeB atoms changes, generating four non-equivalent O_h Fe, which have a characteristic splitting, creating a pre-peak at the Fe-L_3 ELNES. The ratio in the splitting is proportional to the occupancy of the t_{2g}/e_g orbitals.

5.5 Conclusions

The principal conclusions of the present chapter can be summarized in the following points:

- The Verwey transition has been analyzed in 25 nm size Fe_3O_4 nanocubes,in-situ in the TEM, by reducing the temperature down to 100 K.
- The crystallographic phase distortion from cubic to monoclinic has been evidenced by phase contrast imaging.
- The RT phase has been stablished to be the cubic one with Fd-3m space group, while the LT fits a monoclinic phase.
- The EELS data show a ratio difference in the Fe L_3 splitting in the same nanocube at RT and LT.
- The origin of the Fe L_3 splitting has been analyzed in depth by comparing the experimental data with DFT calculations.
    - DOS and PDOS of the RT and LT phases have been computed, evidencing the change of behaviour, from half-metal to semiconductor.
    - The cationic ordering has been verified. It fulfills both the charge and spin ordering.

- A detailed study of the Fe L_3 ELNES has been carried out. Its dependence on the sample orientation, magnetic spin axis and core-hole location has been studied.
- DFT calculations have been used to determine the origin of the Verwey fingerprint in the Fe L_3 ELNES, linking it univocally with the PDOS of the FeB atoms.

5.6 References

[1] K. Yoo, B.-G. Jeon, S.H. Chun, D.R. Patil, Y. Lim, S. Noh, J. Gil, J. Cheon, K.H. Kim, Quantitative Measurements of Size-Dependent Magnetoelectric Coupling in Fe $_3$ O $_4$ Nanoparticles, Nano Letters. 16 (2016) 7408–7413. https://doi.org/10.1021/acs.nanolett.6b02978.

[2] R. Bliem, E. McDermott, P. Ferstl, M. Setvin, O. Gamba, J. Pavelec, M.A. Schneider, M. Schmid, U. Diebold, P. Blaha, L. Hammer, G.S. Parkinson, Subsurface cation vacancy stabilization of the magnetite (001) surface, Science (1979). 346 (2014) 1215–1218. https://doi.org/10.1126/science.1260556.

[3] J.-Y. Chen, T.-M. Wong, C.-W. Chang, C.-Y. Dong, Y.-F. Chen, Self-polarized spin-nanolasers, Nature Nanotechnology. 9 (2014) 845–850. https://doi.org/10.1038/nnano.2014.195.

[4] S. de Jong, R. Kukreja, C. Trabant, N. Pontius, C.F. Chang, T. Kachel, M. Beye, F. Sorgenfrei, C.H. Back, B. Bräuer, W.F. Schlotter, J.J. Turner, O. Krupin, M. Doehler, D. Zhu, M.A. Hossain, A.O. Scherz, D. Fausti, F. Novelli, M. Esposito, W.S. Lee, Y.D. Chuang, D.H. Lu, R.G. Moore, M. Yi, M. Trigo, P. Kirchmann, L. Pathey, M.S. Golden, M. Buchholz, P. Metcalf, F. Parmigiani, W. Wurth, A. Föhlisch, C. Schüßler-Langeheine, H.A. Dürr, Speed limit of the insulator–metal transition in magnetite, Nature Materials. 12 (2013) 882–886. https://doi.org/10.1038/nmat3718.

[5] J. Lee, S.G. Kwon, J.-G. Park, T. Hyeon, Size Dependence of Metal-Insulator Transition in Stoichiometric Fe3O4 Nanocrystals, Nano Letters. 15 (2015) 150616160110004. https://doi.org/10.1021/acs.nanolett.5b00331.

[6] S. Lee, A. Fursina, J.T. Mayo, C.T. Yavuz, V.L. Colvin, R.G. Sumesh Sofin, I. V. Shvets, D. Natelson, Electrically driven phase transition in magnetite nanostructures, Nature Materials. 7 (2008) 130–133. https://doi.org/10.1038/nmat2084.

[7] H. Zeng, J. Li, J.P. Liu, Z.L. Wang, S. Sun, Exchange-coupled nanocomposite magnets by nanoparticle self-assembly, Nature. 420 (2002) 395–398. https://doi.org/10.1038/nature01208.

[8] C.T. Yavuz, J.T. Mayo, W.W. Yu, A. Prakash, J.C. Falkner, S. Yean, L. Cong, H.J. Shipley, A. Kan, M. Tomson, D. Natelson, V.L.

Colvin, Low-Field Magnetic Separation of Monodisperse Fe3O4 Nanocrystals, Science (1979). 314 (2006) 964–967. https://doi.org/10.1126/science.1131475.

[9] G.S. Parkinson, Z. Novotny, G. Argentero, M. Schmid, J. Pavelec, R. Kosak, P. Blaha, U. Diebold, Carbon monoxide-induced adatom sintering in a Pd–Fe3O4 model catalyst, Nature Materials. 12 (2013) 724–728. https://doi.org/10.1038/nmat3667.

[10] J. Luo, J. Liu, Z. Zeng, C.F. Ng, L. Ma, H. Zhang, J. Lin, Z. Shen, H.J. Fan, Three-dimensional graphene foam supported Fe3O4 lithium battery anodes with long cycle life and high rate capability, Nano Letters. 13 (2013) 6136–6143. https://doi.org/10.1021/nl403461n.

[11] S.H. Lee, S.-H. Yu, J.E. Lee, A. Jin, D.J. Lee, N. Lee, H. Jo, K. Shin, T.-Y. Ahn, Y.-W. Kim, H. Choe, Y.-E. Sung, T. Hyeon, Self-Assembled Fe $_3$ O $_4$ Nanoparticle Clusters as High-Performance Anodes for Lithium Ion Batteries via Geometric Confinement, Nano Letters. 13 (2013) 4249–4256. https://doi.org/10.1021/nl401952h.

[12] Y. Wu, Y. Wei, J. Wang, K. Jiang, S. Fan, Conformal Fe $_3$ O $_4$ Sheath on Aligned Carbon Nanotube Scaffolds as High-Performance Anodes for Lithium Ion Batteries, Nano Letters. 13 (2013) 818–823. https://doi.org/10.1021/nl3046409.

[13] X. Sun, S. Guo, Y. Liu, S. Sun, Dumbbell-like PtPd–Fe $_3$ O $_4$ Nanoparticles for Enhanced Electrochemical Detection of H $_2$ O $_2$, Nano Letters. 12 (2012) 4859–4863. https://doi.org/10.1021/nl302358e.

[14] A.G. Tomkins, L. Bowlt, M. Genge, S.A. Wilson, H.E.A. Brand, J.L. Wykes, Ancient micrometeorites suggestive of an oxygen-rich Archaean upper atmosphere, Nature. 533 (2016) 235–238. https://doi.org/10.1038/nature17678.

[15] L.M. Gordon, D. Joester, Nanoscale chemical tomography of buried organic–inorganic interfaces in the chiton tooth, Nature. 469 (2011) 194–197. https://doi.org/10.1038/nature09686.

[16] S. Staniland, W. Williams, N. Telling, G. Van Der Laan, A. Harrison, B. Ward, Controlled cobalt doping of magnetosomes in

vivo, Nature Nanotechnology. 3 (2008) 158–162. https://doi.org/10.1038/nnano.2008.35.

[17] Y. Yuan, Z. Ding, J. Qian, J. Zhang, J. Xu, X. Dong, T. Han, S. Ge, Y. Luo, Y. Wang, K. Zhong, G. Liang, Casp3/7-Instructed Intracellular Aggregation of Fe 3 O 4 Nanoparticles Enhances T 2 MR Imaging of Tumor Apoptosis, Nano Letters. 16 (2016) 2686–2691. https://doi.org/10.1021/acs.nanolett.6b00331.

[18] T.P. Almeida, T. Kasama, A.R. Muxworthy, W. Williams, L. Nagy, T.W. Hansen, P.D. Brown, R.E. Dunin-Borkowski, Visualized effect of oxidation on magnetic recording fidelity in pseudo-single-domain magnetite particles, Nature Communications. 5 (2014) 5154. https://doi.org/10.1038/ncomms6154.

[19] M.S. Senn, J.P. Wright, J.P. Attfield, Charge order and three-site distortions in the Verwey structure of magnetite, Nature. (2012). https://doi.org/10.1038/nature10704.

[20] Y. Hou, Y. Liu, X. Yang, H. Mao, Z. Shi, S. Wu, B. Lu, Q.L. Ye, J. Ye, Modulating the Verwey Transition of Epitaxial Magnetite Thin Films by Ionic Gating, Advanced Functional Materials. 31 (2021). https://doi.org/10.1002/adfm.202104816.

[21] T. Kim, S. Sim, S. Lim, M.A. Patino, J. Hong, J. Lee, T. Hyeon, Y. Shimakawa, S. Lee, J.P. Attfield, J.G. Park, Slow oxidation of magnetite nanoparticles elucidates the limits of the Verwey transition, Nature Communications. 12 (2021). https://doi.org/10.1038/s41467-021-26566-4.

[22] R. Nickel, C.C. Chi, A. Ranjan, C. Ouyang, J.W. Freeland, J. van Lierop, Reverse-Engineering Strain in Nanocrystallites by Tracking Trimerons, Advanced Materials. 33 (2021). https://doi.org/10.1002/adma.202007413.

[23] E.J.W. Verwey, Electronic Conduction of Magnetite (Fe3O4) and its Transition Point at Low Temperatures, Nature. 144 (1939) 327–328. https://doi.org/10.1038/144327b0.

[24] F. Walz, The Verwey transition - a topical review, Journal of Physics: Condensed Matter. 14 (2002) R285–R340. https://doi.org/10.1088/0953-8984/14/12/203.

[25] J. García, G. Subías, The Verwey transition—a new perspective, Journal of Physics: Condensed Matter. 16 (2004) R145–R178. https://doi.org/10.1088/0953-8984/16/7/R01.

[26] M. Bohra, N. Agarwal, V. Singh, A Short Review on Verwey Transition in Nanostructured Fe 3 O 4 Materials, (2019). https://doi.org/10.1155/2019/8457383.

[27] J. Blasco, J. García, G. Subías, Structural transformation in magnetite below the Verwey transition, Physical Review B - Condensed Matter and Materials Physics. 83 (2011) 1–7. https://doi.org/10.1103/PhysRevB.83.104105.

[28] M.S. Senn, J.P. Wright, J.P. Attfield, Charge order and three-site distortions in the Verwey structure of magnetite, Nature. 481 (2011) 173–176. https://doi.org/10.1038/nature10704.

[29] J.P. Wright, J.P. Attfield, P.G.. Radaelli, Charge ordered structure of magnetite Fe3O4 below the Verwey transition, Physical Review B. 66 (2002) 1–4. https://doi.org/10.1103/PhysRevB.66.201101.

[30] S. Ruiz-Gómez, L. Pérez, A. Mascaraque, A. Quesada, P. Prieto, I. Palacio, L. Martín-García, M. Foerster, L. Aballe, J. de la Figuera, Geometrically defined spin structures in ultrathin Fe $_3$ O $_4$ with bulk like magnetic properties, Nanoscale. 10 (2018) 5566–5573. https://doi.org/10.1039/C7NR07143D.

[31] J. Lee, S.G. Kwon, J.-G. Park, T. Hyeon, Size Dependence of Metal-Insulator Transition in Stoichiometric Fe3O4 Nanocrystals, Nano Letters. 15 (2015) 150616160110004. https://doi.org/10.1021/acs.nanolett.5b00331.

[32] A. Hevroni, M. Bapna, S. Piotrowski, S.A. Majetich, G. Markovich, Tracking the Verwey Transition in Single Magnetite Nanocrystals by Variable-Temperature Scanning Tunneling Microscopy, The Journal of Physical Chemistry Letters. 7 (2016) 1661–1666. https://doi.org/10.1021/acs.jpclett.6b00644.

[33] A. Hevroni, B. Tsukerman, G. Markovich, Probing magnetization dynamics in individual magnetite nanocrystals using magnetoresistive scanning tunneling microscopy, Physical Review B. 92 (2015) 224423. https://doi.org/10.1103/PhysRevB.92.224423.

[34] Q. Yu, A. Mottaghizadeh, H. Wang, C. Ulysse, A. Zimmers, V. Rebuttini, N. Pinna, H. Aubin, Verwey transition in single magnetite nanoparticles, Physical Review B. 90 (2014) 075122. https://doi.org/10.1103/PhysRevB.90.075122.

[35] P. Poddar, T. Fried, G. Markovich, A. Sharoni, D. Katz, T. Wizansky, O. Millo, Manifestation of the Verwey transition in the tunneling spectra of magnetite nanocrystals, Europhysics Letters (EPL). 64 (2003) 98–103. https://doi.org/10.1209/epl/i2003-00141-0.

[36] Z.H. Li, X. Li, W. Lu, Field-variable magnetic domain characterization of individual 10 nm Fe3O4 nanoparticles, Chinese Physics B. 28 (2019). https://doi.org/10.1088/1674-1056/28/7/077504.

[37] M. Bugnet, G. Radtke, S.Y. Woo, G.-Z. Zhu, G.A. Botton, Temperature-dependent high energy-resolution EELS of ferroelectric and paraelectric BaTiO 3 phases,. https://doi.org/10.1103/PhysRevB.93.020102.

[38] K. Hojou, S. Furuno, K.N. Kushita, H. Otsu, Y. Furuya, K. Izui, In situ EELS and TEM observation of silicon carbide irradiated with helium ions at low temperature and successively annealed, Physics Research B. 116 (1996) 382–388.

[39] A. Song, W. Zhang, H. Sik Jeong, J.-G. Kim, Y.-J. Kim, In situ dynamic HR-TEM and EELS study on phase transitions of Ge 2 Sb 2 Te 5 chalcogenides,. https://doi.org/10.1016/j.ultramic.2008.05.012.

[40] D. Kim, N. Lee, M. Park, B.H. Kim, K. An, T. Hyeon, Synthesis of Uniform Ferrimagnetic Magnetite Nanocubes, J Am Chem Soc. 131 (2009) 454–455. https://doi.org/10.1021/ja8086906.

[41] P. Scherrer, Bestimmung der inneren Struktur und der Größe von Kolloidteilchen mittels Röntgenstrahlen, Kolloidchemie Ein Lehrbuch. 277 (1912) 387–409. https://doi.org/10.1007/978-3-662-33915-2_7.

[42] P. Ewels, T. Sikora, V. Serin, C.P. Ewels, L. Lajaunie, A Complete Overhaul of the Electron Energy-Loss Spectroscopy and X-Ray Absorption Spectroscopy Database: Eelsdb.eu, Microscopy and

Microanalysis. 22 (2016) 717–724. https://doi.org/10.1017/S1431927616000179.

[43] K.P. McKenna, F. Hofer, D. Gilks, V.K. Lazarov, C. Chen, Z. Wang, Y. Ikuhara, Atomic-scale structure and properties of highly stable antiphase boundary defects in Fe3O4., Nat Commun. 5 (2014) 5740. https://doi.org/10.1038/ncomms6740.

[44] F. de la Peña, E. Prestat, V.T. Fauske, P. Burdet, J. Lähnemann, T. Furnival, P. Jokubauskas, M. Nord, T. Ostasevicius, K.E. MacArthur, D.N. Johnstone, M. Sarahan, T. Aarholt, J. Taillon, pquinn-dls, V. Migunov, A. Eljarrat, J. Caron, T. Poon, S. Mazzucco, C. Francis, B. Martineau, actions-user, S. Somnath, T. Slater, N. Tappy, M. Walls, N. Cautaerts, F. Winkler, DENSmerijn, hyperspy/hyperspy: Release v1.6.5, (2021). https://doi.org/10.5281/ZENODO.5608741.

[45] H.T. Jeng, G.Y. Guo, D.J. Huang, Charge-orbital ordering and verwey transition in magnetite, Physical Review Letters. 93 (2004). https://doi.org/10.1103/PhysRevLett.93.156403.

[46] H. Liu, C. di Valentin, Band Gap in Magnetite above Verwey Temperature Induced by Symmetry Breaking, (2017). https://doi.org/10.1021/acs.jpcc.7b09387.

[47] S. Estradé, J. Arbiol, F. Peiró, Ll. Abad, V. Laukhin, Ll. Balcells, B. Martínez, Cationic diffusion in La2⁄3Ca1⁄3MnO3 thin films grown on LaAlO3 (001) substrates, Applied Physics Letters. 91 (2007) 252503. https://doi.org/10.1063/1.2799740.

[48] S. Estradé, J. Arbiol, F. Peiró, I.C. Infante, F. Sánchez, J. Fontcuberta, F. De La Peña, M. Walls, C. Colliex, Cationic and charge segregation in La 2/3 Ca 1/3 MnO 3 thin films grown on " 001... and " 110... SrTiO 3,. https://doi.org/10.1063/1.2981574.

[49] S. Estradé, J.M. Rebled, J. Arbiol, F. Peiró, I.C. Infante, G. Herranz, F. Sánchez, J. Fontcuberta, R. Córdoba, B.G. Mendis, A.L. Bleloch, Effects of thickness on the cation segregation in epitaxial (001) and (110) La2/3Ca1/3MnO3 thin films, Applied Physics Letters. 95 (2009) 072507. https://doi.org/10.1063/1.3211130.

[50] L. Yedra, E. Xuriguera, M. Estrader, A. López-Ortega, M.D. Baró, J. Nogués, M. Roldan, M. Varela, S. Estradé, F. Peiró, Oxide Wizard: An EELS Application to Characterize the White Lines of Transition Metal Edges, Microscopy and Microanalysis. 20 (2014) 698–705. https://doi.org/10.1017/S1431927614000440.

[51] C. Hébert, Practical aspects of running the WIEN2k code for electron spectroscopy, Micron. 38 (2007) 12–28. https://doi.org/10.1016/j.micron.2006.03.010.

[52] C. Hébert, J. Luitz, P. Schattschneider, Improvement of energy loss near edge structure calculation using Wien2k, Micron. 34 (2003) 219–225. https://doi.org/10.1016/S0968-4328(03)00030-1.

[53] P. Blaha, K. Schwarz, G. Madsen, D. Kvasnicka, J. Luitz, WIEN2k: An Augmented Plan Wave Plus Local Orbitals Program for Calculating Crystal Properties, 2014.

[54] P. Blaha, K. Schwarz, F. Tran, R. Laskowski, G.K.H. Madsen, L.D. Marks, WIEN2k: An APW+lo program for calculating the properties of solids, Journal of Chemical Physics. 152 (2020) 74101. https://doi.org/10.1063/1.5143061

Chapter 6: Plasmonic Nanoparticles: gold nanodomes

In this Chapter, novel exotic gold nanoparticles, nanodomes, are analysed with the combination of experimental low loss EELS and Boundary Element Method (BEM) calculations. The possibility of using models with different degrees of complexity is exploited and the used models range from a purely idealistic one to a model built from an experimental tomographic reconstruction. The reliability of the models is assessed by comparing the theoretical results with the experimental ones, reaching a good agreement.

6.1 State of the art – Motivation

The plasmonic response of nanostructures of almost any possible shape has been vastly studied because of their superior light confinement capacity[1–4]. The physical nature of surface plasmons is well understood, i.e., a collective oscillation of the electron charge at the interface between materials with dielectric function of opposite sign[5]. Their outstanding optoelectronic properties make them suitable for a wide range of applications, especially for life sciences, e.g., cancer treatment, drug delivery, improvement of optoelectronic devices[6–10], among others. Interestingly, nanoplasmonics has led to a major change in the biosensing field[11,12] owing to the possibility of merging size reduction, high sensitivity and spectral tunability by simply controlling the size and shape of the sensing structure. To achieve optimized plasmonic structures for each application through the tailored interaction with the electromagnetic fields, a huge variety of simple and complex shapes has been investigated. However, for complex nanostructures the understanding and the prediction of their interaction with the incident light can be difficult. This often hinders the development of optimized structures or leads to lengthy trial and error processes.

To gain a deeper insight, Electron Energy Loss Spectroscopy (EELS) is one of the most powerful techniques for detecting and analyzing the plasmonic response of nanoobjects. The use of electrons instead of photons allows for having a high spatial (subnanometer) and energy (lower than 20 meV) resolutions, as demonstrated by different groups[13–15]. In addition, to fully understand the different plasmonic resonant modes observed in the EELS spectra, Boundary Element Method (BEM) based simulations are often carried out[16,17].

In this chapter the high potential of combining electron tomography, Boundary Element Method (BEM) analysis and EELS measurements to reach a deeper understanding of the optical behavior of complex plasmonic nanostructures is demostrated. In particular, this chapter is focused on spectrally complex plasmonic semi-shells, also denoted as nanodomes. These structures exhibit anisotropic optical properties with wide multiband absorbance spectra, which are conferred by their intrinsic curvature and the thickness gradient across the nanostructure. Their sharp rims make them

interesting for Surface Enhanced Raman Spectroscopy (SERS) or surface enhanced fluorescence and their enhanced absorption is appealing for photothermal applications. Therefore, understanding the origin of their spectral response can contribute to improve their potential applications.

6.2 Material and preliminary characterization

The studied nanoparticles were provided and macroscopically characterized by the Magnetic Nanostructures group of ICN2 lead by Prof. Josep Nogués.

They were fabricated by a combination of colloidal nanolithography and physical vapor deposition, as described elsewhere[18]. Briefly, the nanodomes were obtained by the electrostatic self-assembly of an array of polystyrene nanoparticles of 100 nm diameter on a silicon substrate, followed by the deposition of a gold layer of controlled thickness (between 20 and 40 nm), on the array of particles. This process yields either isolated or small clusters of nanospheres semi covered by a gold layer. After the fabrication process, the nanodomes were directly dispersed in milliQ water by ultrasonication and finally deposited on SiN_3 or SiO_2 grids to avoid any undesired signal on the energy low loss.

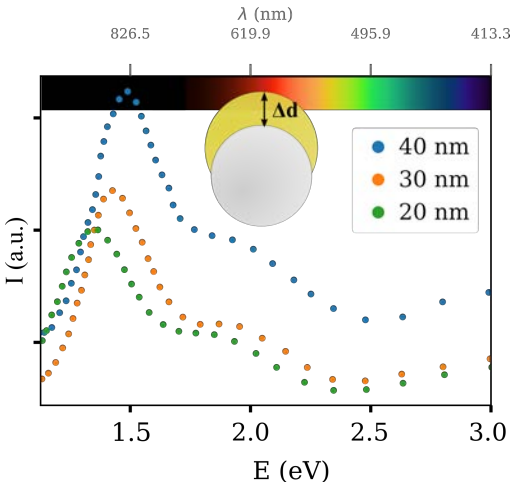

Figure 6.1 Experimental UV-vis spectra of Au nanodomes with different thickness. The inset shows a schematic transversal section of the nanodome with the electron beam direction considered perpendicular to the image.

Macroscopic UV-visible absorbance experiments were conducted using a Lambda25 (PerkinElmer) UV- vis spectrometer in the 1 eV to 3 eV spectral range.

The UV-visible absorbance spectra of the nanodomes corresponding to three different maximum Au thicknessess, (Δd = 20, 30 and 40 nm) dispersed in water (Figure 6.1) present two main extinction peaks. In the case of 20 nm thickness, the peaks are found at 1.36 eV and 1.84 eV, respectively. The experimental results also show a blueshift in the low energy mode as the thickness of the nanodome increases, showing values of 1.42 eV and of 1.48 eV for the 30 nm and the 40 nm shell nanodomes, respectively. However, it is important to emphasize that UV-visible spectroscopy is a spread beam technique, therefore, the obtained information is a convolution from the whole sample, and the acquired spectra are the superposition of the transversal and longitudinal resonant modes, as the nanodomes are randomly oriented in the water dispersion.

6.3 Morphologic and structural characterization

The low magnification Transmission Electron Microscopy (TEM) characterization was performed in a JEOL 2010F TEM operated at 200 kV.

The shape and orientation distribution of the nanodomes were checked by conventional TEM on the 20 nm Au thickness sample. The TEM images of the isolated nanodomes and small nanodome clusters are displayed in

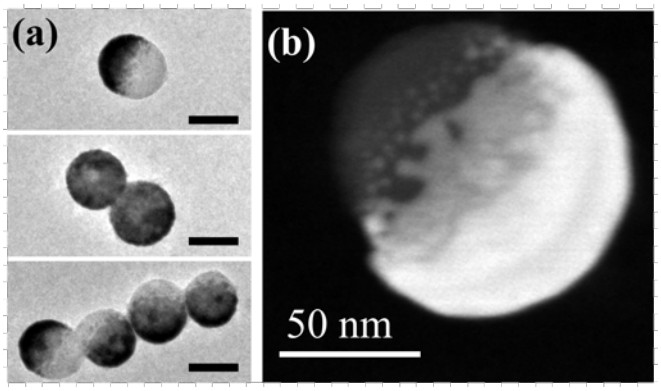

Figure 6.2 Nanodomes morphology. (a) Low magnification image of three different nanodomes clusters dispersed in H_2O and deposited on a SiN_3 grid (scale bar: 100 nm). (b) STEM – HAADF image of one of the isolated nanodomes.

Figure 6.2(a), and a Scanning TEM – High Angular Annular Dark Field (STEM-HAADF) image of an isolated nanodome is shown in Figure 6.2(b). The images show that the gold layer covers roughly half of the polystyrene nanoparticles and confirms that the nanodomes have the expected shape, with an inner-diameter of around 100 nm, corresponding to the polystyrene nanoparticle, plus the deposited gold layer. In addition, it can be noticed that the nanodomes show a rough rim, as defects and small gold particles can be detected along the rim length, which are expected to play an important role in the plasmonic response.

6.3.1 Tomographic reconstruction

As the shape of the nanoobjects is crucial for their plasmonic response, a morphological tomography was carried out to get their 3D structure.

For the electron tomography experiments, a tilt series of HAADF images, from −70 to +70 each 5°, was acquired in a FEI Titan Themis 60-300 instrument at 200 keV. The series was aligned using a combination of the ThermoFisher Inspect3D proprietary software and the TomoJ tool of the ImageJ free software. The reconstruction algorithm of choice was the total variation minimization in 3D (TVM3D), based on the total variation minimization by augmented lagrangian and alternating direction algorithms (TVAL3), described elsewhere[19,20]. The missing wedge artifact was minimized by using TVM3D reconstruction.

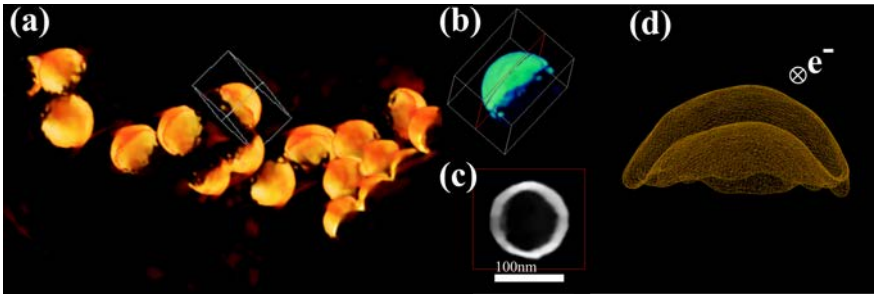

Figure 6.3 (a) HAADF-STEM morphological tomography reconstruction of a group of nanodomes. (b) Isolated nanodome selected as a real model for BEM calculations. (c) Orthogonal cut of (b) to check its sphericity and size. (d) Boundary constituted by the net of points extracted from the tomographic reconstruction, the considered direction of the electron beam is highlighted in the upper-right corner.

A tomographic reconstruction of the shape of a nanodome is given in Figure 6.3, confirming the semi-spherical shape, the thickness gradient and the rim roughness. Figure 6.3(a) shows the aggregate of nanodomes from which the isolated nanodome was extracted (b). By cutting a slice, their hemispherical shape can be checked and its 100 nm diameter size confirmed. It should be noticed that the polystyrene nanoparticles do not appear on the reconstruction because the contrast has been optimized to get all the gold layer details, but they are there. In Figure 6.3(d), the reconstruction in a net of points is shown.

6.4 EELS analysis

The spectral characterization was done by low loss EELS in order to examine the plasmonic resonances detected by UV-vis (Figure 6.1) and to spatially locate them.

The low loss EEL spectrum images were acquired in two probe corrected TITAN High-Base 80-300 and Low-Base 60-300 microscopes, operated at 80 kV and equipped with an XFEG gun, coupled to a Gatan Quantum GIF and a Gatan Tridiem GIF spectrometer, respectively. EELS data at low-loss energies were acquired with an energy resolution between 75 and 180 meV. Spectrum images of 80x80 pixels with 2 nm/pixel size were acquired with a 0.02 eV dispersion and 0.0012 s exposure time. The resolution of the experimental spectra was improved using the Richardson-Lucy deconvolution algorithm in Hyperspy[21]. The final resolution improved a 30% with respect to the acquired data.

The spectral characterization of the isolated nanodomes was performed by low loss EELS (Figure 6.4). Note that, in contrast to the UV-vis, EELS is a highly localized technique with high energy and spatial resolution, which allows the spatial identification of the plasmonic modes. As the plasmonic resonances are highly sensitive to the particle shape, the number of pixels was maximized to reach a good compromise between the acquisition time and the spatial resolution (see the experimental details section) when acquiring a spectrum image from a whole isolated nanodome. To obtain representative spectra, the EELS signal was summed over the square regions highlighted in Figure 6.4(a). The different spectra are shown in Figure 6.4(b), with the colour code indicating the region where they were collected

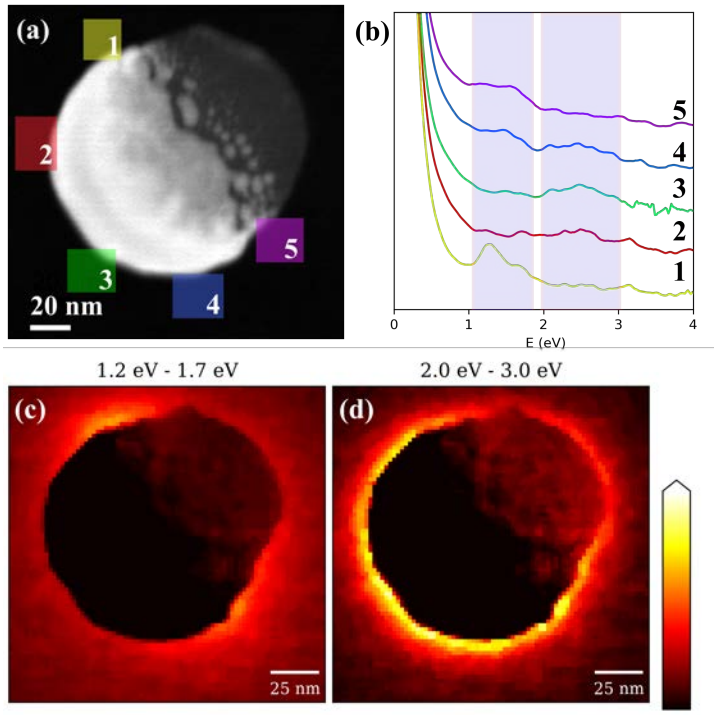

Figure 6.4 (a) Co-acquired HAADF image of an isolated Au nanodome, with color rectangles showing the regions of interest. (b) Integrated spectrum from the corresponding highlighted rectangles in (a). Energy filtered color maps, after intensity integration in energy windows centered in 1.5 eV (c) and 2.4 eV (d).

from. Two main peaks can be observed in the spectra, one centered at 1.5 eV for the spectra obtained at the rim, and another one at 2.4 eV at the top of the nanodomes (i.e., the region with the largest Au thickness). The spatial distribution of their intensities was mapped for the whole nanodome by integrating the signal along two windows of approximately 1 eV width, centered at both peak energies in the original spectrum image (Figure 6.4(c,d)). The lower energy mode clearly appears at both edges of the nanodome, whereas the higher energy mode is more homogeneously distributed and presents the highest intensity at the top of the nanodome.

The same procedure was repeated for other isolated nanodomes as well as for complex structures, such as clusters of nanodomes. A dimer with two coupled nanodomes, each one with a diameter of 75 nm, is shown in Figure 6.5(a). Figure 6.5(b) presents the sum of the experimental EEL spectra in the five highlighted regions of Figure 6.5(a). The main difference with

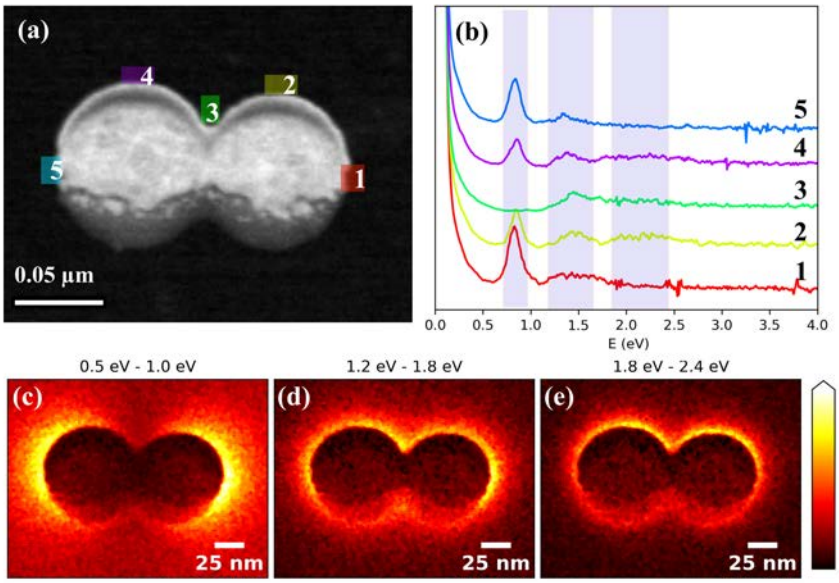

Figure 6.5 (a) HAADF-STEM image of the nanodome dimer from which the EELS spectrum image was acquired. Highlighted in colour are the regions from where the signal was integrated and plotted in (b). (c-e) correspond to the color map of three energy windows highlighted in purple in (b). The first mode, 0.8 eV, is displayed in (c), the second, at 1.5 eV, in (d) and the third, at 2.1 eV, in (e).

respect to the isolated nanodomes is an intense low energy peak detected at 0.8 eV, in addition to the two other modes detected at 1.5 eV and 2.1 eV. Again, energy-filtered color maps were obtained for the three energy windows marked in Figure 6.5(c-e). The maps clearly show that the highest intensity 0.8 eV signal appears at the edges in the longitudinal axis of the dimer. The 0.8 eV signal is sharper and more prominent than the signals detected in the isolated case and, interestingly, it also appears with lower intensity in the top regions of the nanodome dimer together with the peak located at 2.1 eV. In Figure 6.5(d) the 1.5 eV signal appears all around the nanodome. In contrast, at the central region, in the union between the nanodomes, the intensity of the 2.1 eV peak is almost zero, which confirms that the nanodomes are connected by the metal film forming a continuous coverage.

Thus, two different modes are clearly identified for the isolated nanodome and three for the dimer. However, in order to disentangle and better understand the origin of all the signals detected and to assess the

importance of the particle shape on the spectral response, the nanodomes were modelled by BEM based calculations[22–25].

6.5 BEM simulations for low loss EELS comparison

The BEM calculations were performed using the MNPBEM Matlab toolbox from Graz University[26]. The input for the simulation consisted of a 5000 points mesh, which models the nanodome. To simulate the experimentally observed modes, the electron beam was considered as a planar wave perpendicular to the nanodome, as shown in Figure 6.3(d), to recreate the conditions inside the microscope column. The energy beam was considered to be 80 kV, as per the experiment, and the energy step of the spectra was set to 20 meV.

Three different models of the nanodome were used as an input mesh for BEM calculations. The models were (i) an ideal Au semi-shell with constant Au thickness, (ii) a realistic Au semi-shell with a thickness gradient, and (iii) the actual nano-shell geometry obtained from the 3D tomography reconstruction. The first two were built from scratch with the 3D design software Blender[27]. The idealistic one was made by the creation of two concentric spherical surfaces with a given radii difference, which determined the thickness of the dome, Δd; both surfaces were bisected, and an additional mesh was added to close the whole surface. The realistic model was made using a similar approach, i.e., two different spheres with a different diameter were superposed although, in this case, with a certain displacement between the centers of the spheres, thus obtaining a model with the maximum thickness, Δd, equal to the displacement plus the difference of diameters. The meshes were cut by their intersection, obtaining a gradual thickness nanodome. The thickness at the top of the nanodome, Δd, was set to 20 nm for both models, to match the experimental conditions. The last model, the tomographic one, was directly obtained from the reconstruction of the nanodomes HAADF tomography (Figure 6.3). The surface obtained from the reconstruction was simplified by reducing the number of mesh points to have a feasible computational time. Finally, the polystyrene nanoparticle was modeled by a spherical particle in direct contact to the inner part of the Au nanodome.

For the dimer case, the models were built using the same approximation as for the isolated case. The idealistic and realistic models were built by attaching two models of the idealistic and realistic isolated nanodomes, respectively, and the tomographic model was obtained from the reconstruction of a real nanodome dimer. All the used models are summarized in Figure 6.6.

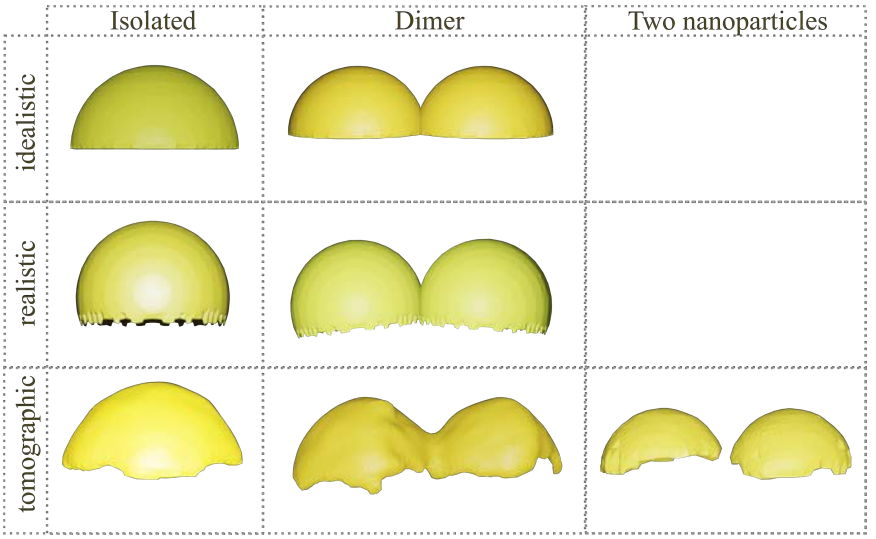

Figure 6.6 Summary of the main models created and used on the BEM simulations: idealistic models, realistic models and tomographic models for the isolated and dimer nanodomes.

The dielectric environment was set to model the corresponding materials. The tabulated gold dielectric function from 0.188 to 1.937 μm wavelength[28] was considered for the Au layer of the nanodome, while for the vacuum and the polystyrene nanoparticle a refractive index of n = 1.00 and n = 1.59 were used, respectively. To reduce the computation time, no substrate was considered in the calculations, although the nanoparticles were deposited either on SiO_2 or SiN_3 for the EELS experiments. Note that neglecting the presence of the high refractive index substrate induces an energy blue-shift on the simulations with respect to the experimental data[24,25]. All the computed spectra have been shifted accordingly 0.1 eV for the SiO_2 and 0.2 eV for SiN_3 to correct for the effect of the substrate.

6.5.1 Isolated nanodomes models

The EELS simulations computed by BEM from all three models (Figure 6.7(a)), show a good overall agreement with the experimental spectra, as shown in Figure 6.7(b,c). All of them clearly exhibit a spectral difference in the EELS signal between the top of the nanodome and the rim. At the rim, p_1, the main signal is located at 1.5 eV for all the three models while at the top, p_2, the signal is around 2.4 eV. However, although the main signals at both locations agree with the experimental data for all the considered models, each model produces some peculiarities. For the ideal model, a second signal appears at p_1 around 1.9 eV with an intensity similar to the main peak at 1.5 eV, which is not observed experimentally. In the realistic model, additional small peaks are detected at slightly higher energy than the main peak. In contrast, for the tomographic model, the two additional small peaks appear at lower and higher energy than the main 1.5 eV peak. Overall, it is clear that the spectral shape simulated from the tomographic

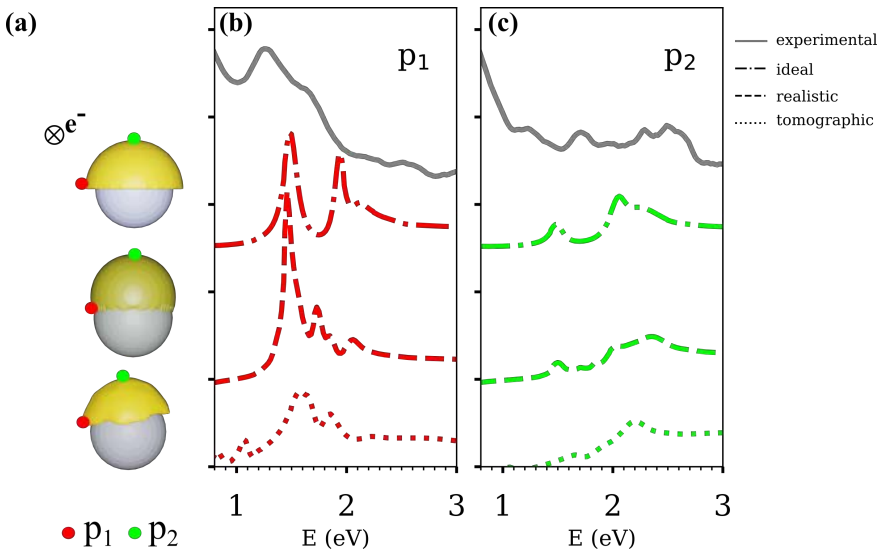

Figure 6.7 (a) Models of isolated nanodomes created for the BEM simulations (from top to bottom): idealistic model, realistic model with a gradual change of thickness and tomographic model obtained from the reconstruction. Comparison of the experimental and computed EELS for the positions p_1, at the rim, in red (b) and p_2, at the top, in green (c).

model displays a better correlation with the experimental results than those simulated from the idealistic and realistic models.

The experimental spectral maps of Figure 6.4 were also compared with similar color maps calculated from the EELS simulations using the three models. These theoretical maps were obtained by integrating a small energy window around the energy peaks found in the spectra (Figure 6.8). In all the cases, the highest intensity signal appears at the rim at 1.5 eV, corresponding to the low energy mode. As can be observed, the tomographic model shows a lower homogeneity in the intensity field distribution at the rim as a consequence of the generated defects during the deposition of the metal layer. Moving towards the top of the nanodome, the low energy mode is attenuated, and the most prominent energy signal appears at 2.4 eV, the high energy mode, thus being in good correlation with the experimental results.

These spectral changes may arise due to the effect of a non-constant thickness of the gold layer of the nanodomes. To achieve a more detailed analysis of the thickness gradient effects, extra models with 30 and 40 nm

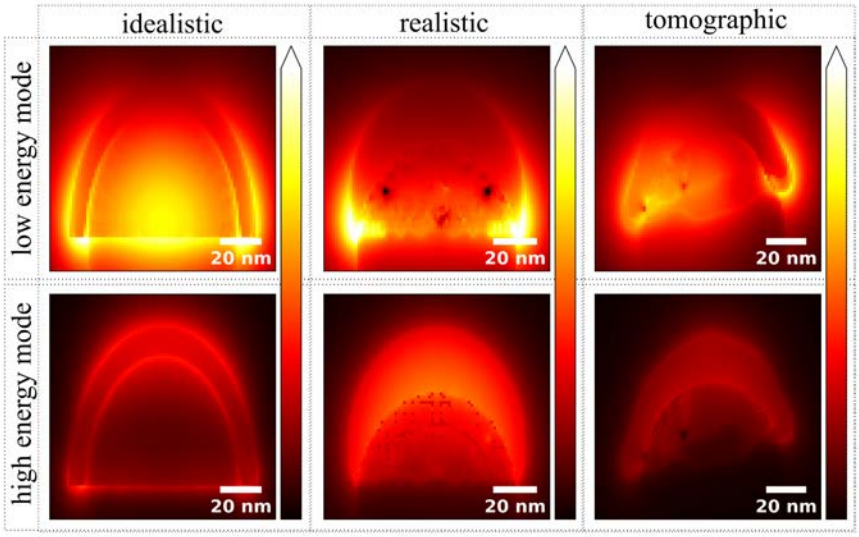

Figure 6.8 Colormaps of the extracted signal of the two detected modes for the simulated spectra of the isolated nanodome according to the three models (idealistic – left; realistic – middle; and tomographic – right). The low energy mode is located at 1.5 eV (top row) and the high energy mode at 2.4 eV (bottom row).

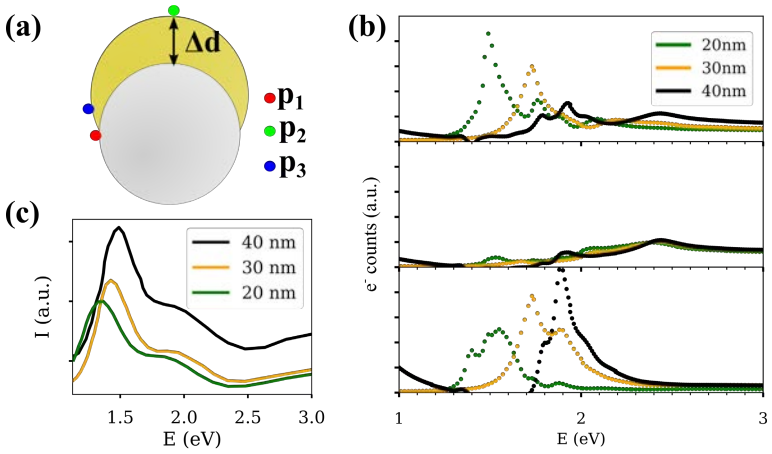

Figure 6.9 (a) Transversal cross section of the realistic model highlighting from where the thickness, Δd, was considered and the points from which the EELS was obtained (p_1, p_2 and p_3). (b) Low loss simulated data at the three points highlighted in (a), considering a nanodome with a thickness of 20 (green), 30 (orange) and 40 nm (black). (c) Experimental UV-vis spectra of the Au nanodomes with different thickness.

Au thickness were constructed based on the realistic model (Figure 6.9 (a)). In this case, the analysis was focused on three points: p_1, the edge of the rim; p_2, at the top of the dome, and p_3, located a few nm from the rim. The comparison of the signal at p_1 and p_3 shows that the intensity of the main peak at 1.5 eV decreases, whereas the next peak located at slightly higher energy increases (Figure 6.9(b)). In addition, when the Au layer thickness increases, a 0.4 eV blueshift in all the peaks is found. Notice that the absolute shift caused by the thickness change is slightly higher than the one detected by UV-vis spectroscopy because, in this case, we avoid averaging effects due to the convolution over a large number of randomly oriented individual nanodomes and the presence of nanodomes clusters, as was the case of the experimental UV-vis measurements. In addition, by comparing p_1 and p_3 a change in intensity and an energy shift is detected just by slightly increasing the thickness, which explains the differences on intensity obtained for the three models shown in Figure 6.7.

Furthermore, the original tomographic model was also used to predict the dependence of the plasmonic response with the size of the particle, keeping its aspect ratio, i.e., the ratio between sphere diameter and Au thickness (Figure 6.10). The simulations show that the low energy peak

shifts to higher energy as the particle size decreases. However, the shift for the high energy peak is almost negligible.

In summary, the macroscopic optical measurements gave a global convolution of all the signals in any possible orientation (Figure 6.1), as shown in prior work where transversal and longitudinal orientations were studied finding two main modes at near infrared and red spectral regions [29]. The use of EELS allows to determine the exact localization of both modes. The low energy mode at 1.5 eV corresponds to the localized surface plasmon located in the rim, and the high energy mode at 2.4 eV corresponds to the one located at the top of the dome, however the contribution of the bulk plasmon cannot be avoided close to the high energy mode[8].

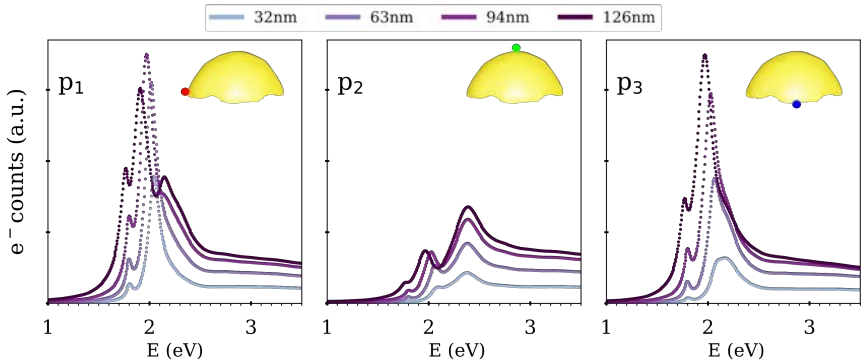

Figure 6.10 Analysis of the plasmonic modes as a function of the nanodome size. The three points from where the EELS signal is calculated: p_1- red-rim, p_2-green-top, p_3-blue-central; the points are highlighted in the insets. Plots of the signal on the selected points for a range of sizes from 0.4 times the size of the experimental nanodome (32nm) to 1.2 times it (126 nm).

6.5.2 Nanodome dimer model

To probe the capacity to predict the behavior of even more complex structures, clusters of nanodomes were also studied. An example is the dimer formed by two coupled nanodomes, each one with a diameter of 75 nm, equivalent to the experimental presented in Figure 6.5.

To explain the new peak detected at 0.8 eV in the dimer characterization of Figure 6.5, again three theoretical models were created to simulate the dimer (Figure 6.11(a)). The response was analyzed at the

rim (p_1), top (p_2) and union points (p_3). As shown in Figure 6.11(b-d), the computed spectra for all the model are in good agreement with the experimental data. The first peak at 0.8 eV is the most intense one, and completely vanishes at the union point. The second peak at 1.5 eV is present all around the rim, and the third mode, 2.1 eV, is more important at the top of the nanodome. Interestingly, comparing the three models, the realistic model agrees better with the experimental spectral shape, as for the isolated nanodome, whereas the idealistic model generates a spectrum where all peaks have a similar intensity, unlike the experimental data. Also in this configuration, the tomographic model gives the best description of the attached nanodomes.

The spatial distribution of the modes was simulated by plotting the color map of the integrated intensity at each mode energy. The first mode (0.8 eV) is mainly located in the rim region in the axis of the dimer, and it shows the highest intensity. The second mode (1.5 eV) appears along the rim and the third mode (2.1 eV) all around the nanodome (Figure 6.12). According to the spatial distribution of the plasmonic modes, the idealistic

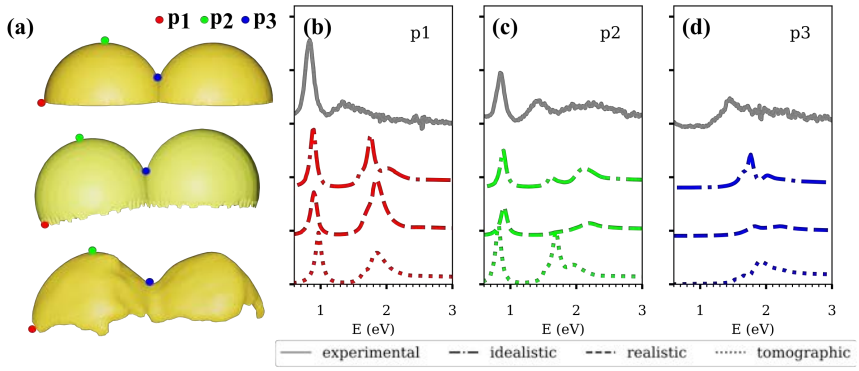

Figure 6.11 (a) Models created for the BEM simulations of the dimer (from top to bottom): idealistic model, realistic model of two realistic/idealistic attached nanodomes and model obtained from the tomographic reconstruction. Comparison of the experimental and computed EELS for the positions p_1 in red (b), p_2 in green (c) and p_3 in blue (d).

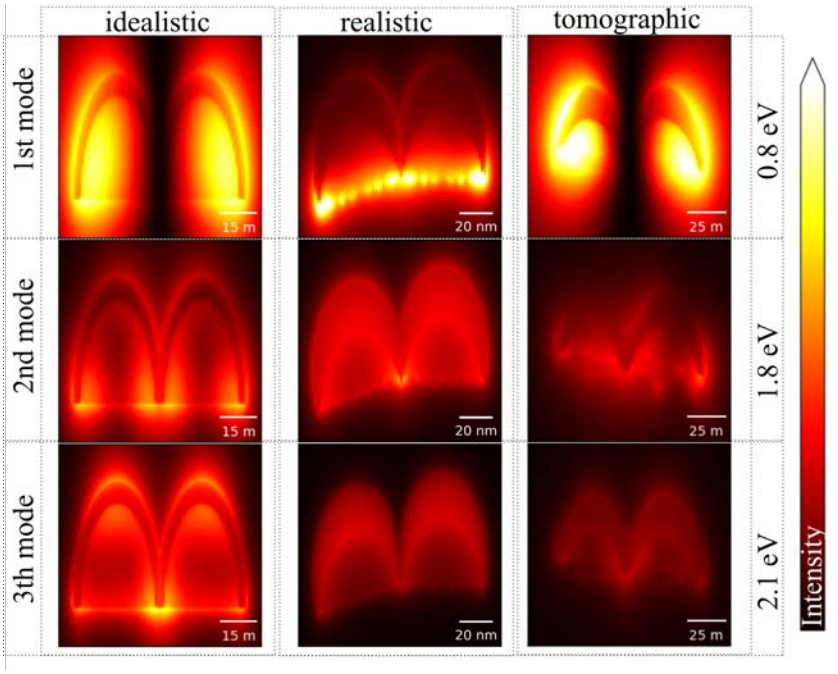

Figure 6.12 Colormaps of the extracted signal of the three detected modes for the simulated spectra of the dimer according to the three models (idealistic – left; realistic – middle; tomographic – right). The first energy mode is located at 0.8 eV (top row), the second energy mode at 1.5 eV(middle row) and the third at 2.1 eV (bottom row).

and, especially, the tomographic reconstructions, are found to be in excellent agreement with the experimental data.

In addition, a calculation of two close but non-touching nanoparticles was also carried out for comparison (Figure 6.13(a)). The dimer simulations were compared with those of the non-touching nanoparticles, as shown in Figure 6.13(a). The obtained results (Figure 6.13(b-d)) do not show the low energy mode, at 0.8 eV, similarly to the isolated case, pointing out that this low energy mode is a characteristic of the dimer and not due to near-field effects between not touching nanodomes.

In conclusion, the 0.8 eV mode detected by the experimental EELS is thus identified as arising from the physical union of two nanodomes and to the rupture of the symmetry creating a low energy resonant mode along the dimer axis, resembling the low energy resonance in gold nanorods, despite of the very complex geometry.

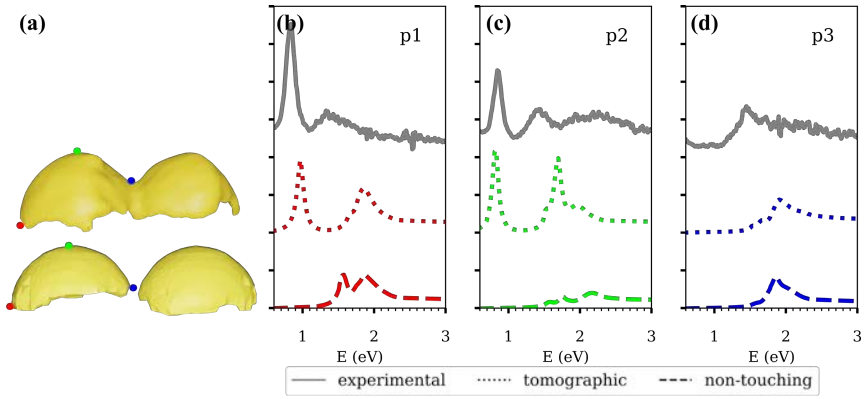

Figure 6.13 (a) Models created for the BEM simulations to compare the dimer with non-touching nanoparticles (from top to bottom): model obtained from the tomographic reconstruction and model created by adding two tomographic individual models. Comparison of the experimental and computed EELS for the positions p_1 in red (b), p_2 in green (c) and p_3 in blue (d).

Notably, this intense resonance does not appear in the UV-Vis measurements (Figure 6.1). This indicates that the individual nanodomes dominate in the optical spectrum. This is confirmed by the low magnification TEM imaging (Figure 6.2), which shows that the majority of the nanodomes are isolated, and only a small fraction of them actually forms dimers.

6.6 Conclusions

This chapter devoted to BEM simulations of gold plasmonic nanodomes can be summarized in the following points:

- The plasmonic response of gold nanodomes has been studied experimentally by UV-vis and low loss EELS.
- Low loss EELS has allowed to locate spatially the origin of the plasmonic resonances.
    - Two main modes have been detected for isolated nanodomes: a low energy (1.5 eV) one at its rim and a high energy (2.4 eV) one at its top.
    - A lower energy mode (0.8 eV) has been detected for dimer structures at the rim of the two nanodomes, but not at.

- TEM tomographic reconstructions of the real nanodomes have been used to obtain reliable morphological information.
- BEM simulations of models with different degrees of complexity (idealistic, realistic and tomographic models) have been performed and the simulated EEL spectra have been obtained for all of them.
- The agreement of the simulations with experimental data as a function of the used model has been analyzed showing good results for most of the models.
- The presented approach can be easily applied to the accurate simulation of other physicochemical properties, and to design new functional materials in a more effective way.

6.7 References

[1] I.C. Bicket, E.P. Bellido, D.M. McRae, F. Lagugné-Labarthet, G.A. Botton, Carving Plasmon Modes in Silver Sierpiński Fractals, ACS Photonics. 6 (2019) 2974–2984. https://doi.org/10.1021/acsphotonics.9b01179.

[2] H. Yu, Y. Peng, Y. Yang, Z.Y. Li, Plasmon-enhanced light–matter interactions and applications, Npj Computational Materials. 45 (2019). https://doi.org/10.1038/s41524-019-0184-1.

[3] T.H. Chow, N. Li, X. Bai, X. Zhuo, L. Shao, J. Wang, Gold Nanobipyramids: An Emerging and Versatile Type of Plasmonic Nanoparticles, Accounts of Chemical Research. 52 (2019) 2136–2146. https://doi.org/10.1021/acs.accounts.9b00230.

[4] H. Yuan, C.G. Khoury, H. Hwang, C.M. Wilson, G.A. Grant, T. Vo-Dinh, Gold nanostars: Surfactant-free synthesis, 3D modelling, and two-photon photoluminescence imaging, Nanotechnology. 23 (2012). https://doi.org/10.1088/0957-4484/23/7/075102.

[5] F.J. García De Abajo, Optical excitations in electron microscopy, Reviews of Modern Physics. 82 (2010) 209–275. https://doi.org/10.1103/RevModPhys.82.209.

[6] C. Martinez-Boubeta, K. Simeonidis, A. Makridis, M. Angelakeris, O. Iglesias, P. Guardia, A. Cabot, L. Yedra, S. Estradé, F. Peiró, Z. Saghi, P.A. Midgley, I. Conde-Leborán, D. Serantes, D. Baldomir, Learning from nature to improve the heat generation of iron-oxide nanoparticles for magnetic hyperthermia applications, Scientific Reports. 3 (2013). https://doi.org/10.1038/srep01652.

[7] M. de la Mata, S. Catalán-Gómez, F. Nucciarelli, J.L. Pau, S.I. Molina, High Spatial Resolution Mapping of Localized Surface Plasmon Resonances in Single Gallium Nanoparticles, Small. 15 (2019) 1902920. https://doi.org/10.1002/smll.201902920.

[8] C. Diaz-Egea, W. Sigle, P.A. van Aken, S.I. Molina, High spatial resolution mapping of surface plasmon resonance modes in single and aggregated gold nanoparticles assembled on DNA strands, 2013. https://doi.org/10.1186/1556-276X-8-337.

[9] P. Güell-Grau, F. Pi, R. Villa, O. Eskilson, D. Aili, J. Nogués, B. Sepúlveda, M. Alvarez, Elastic plasmonic-enhanced Fabry-Perot

cavities with ultrasensitive stretching tunability, Advanced Materials . (2021). https://doi.org/10.1002/ADMA.202106731.

[10] V. Amendola, R. Pilot, M. Frasconi, O.M. Marago, M.A. Iati, Surface plasmon resonance in gold nanoparticles: a review, Journal of Physics: Condensed Matter TOPICAL REVIEW. 29 (2017). https://doi.org/10.1088/1361-648X/aa60f3.

[11] M.-C. Estevez, M.A. Otte, B. Sepulveda, L.M. Lechuga, Trends and challenges of refractometric nanoplasmonic biosensors: A review, Analytica Chimica Acta. 806 (2014) 55–73. https://doi.org/10.1016/j.aca.2013.10.048.

[12] B. Sepúlveda, P.C. Angelomé, L.M. Lechuga, L.M. Liz-Marzán, LSPR-based nanobiosensors, Nano Today. 4 (2009) 244–251. https://doi.org/10.1016/j.nantod.2009.04.001.

[13] O.L. Krivanek, N. Dellby, J.A. Hachtel, J.-C. Idrobo, M.T. Hotz, B. Plotkin-Swing, N.J. Bacon, A.L. Bleloch, G.J. Corbin, M. v Hoffman, C.E. Meyer, T.C. Lovejoy, Progress in ultrahigh energy resolution EELS, (2018). https://doi.org/10.1016/j.ultramic.2018.12.006.

[14] I. Benabdallah, Y. Auad, W. Sigle, P.A. van Aken, M. Kociak, M. Benaissa, Electronic properties of black phosphorus using monochromated low-loss EELS, Materials Science and Engineering B: Solid-State Materials for Advanced Technology. 265 (2020). https://doi.org/10.1016/j.mseb.2020.115002.

[15] L. Guerrini, R. Arenal, B. Mannini, F. Chiti, R. Pini, P. Matteini, R.A. Alvarez-Puebla, SERS detection of amyloid oligomers on metallorganic-decorated plasmonic beads, ACS Applied Materials and Interfaces. 7 (2015) 9420–9428. https://doi.org/10.1021/acsami.5b01056.

[16] F.J. García de Abajo, A. Howie, Retarded field calculation of electron energy loss in inhomogeneous dielectrics, Physical Review B. 65 (2002) 115418. https://doi.org/10.1103/PhysRevB.65.115418.

[17] A. Trügler, U. Hohenester, F.J. García De Abajo, Plasmonics simulations including nonlocal effects using a boundary element method approach, International Journal of Modern Physics B. 31 (2017). https://doi.org/10.1142/S0217979217400070.

[18] Z. Li, A. Lopez-Ortega, A. Aranda-Ramos, J.L. Tajada, J. Sort, C. Nogues, P. Vavassori, J. Nogues, B. Sepulveda, Simultaneous Local Heating/Thermometry Based on Plasmonic Magnetochromic Nanoheaters, Small. 14 (2018). https://doi.org/10.1002/smll.201800868.

[19] M. López-Haro, M. Tinoco, S. Fernández-Garcia, X. Chen, A.B. Hungria, M.Á. Cauqui, J.J. Calvino, A Macroscopically Relevant 3D-Metrology Approach for Nanocatalysis Research, Particle and Particle Systems Characterization. 35 (2018). https://doi.org/10.1002/ppsc.201700343.

[20] C. Li, W. Yin, H. Jiang, Y. Zhang, An efficient augmented Lagrangian method with applications to total variation minimization, Computational Optimization and Applications. 56 (2013) 507–530. https://doi.org/10.1007/s10589-013-9576-1.

[21] F. de la Peña, E. Prestat, V.T. Fauske, P. Burdet, J. Lähnemann, T. Furnival, P. Jokubauskas, M. Nord, T. Ostasevicius, K.E. MacArthur, D.N. Johnstone, M. Sarahan, T. Aarholt, J. Taillon, pquinn-dls, V. Migunov, A. Eljarrat, J. Caron, T. Poon, S. Mazzucco, C. Francis, B. Martineau, actions-user, S. Somnath, T. Slater, N. Tappy, M. Walls, N. Cautaerts, F. Winkler, DENSmerijn, hyperspy/hyperspy: Release v1.6.5, (2021). https://doi.org/10.5281/ZENODO.5608741.

[22] U. Hohenester, A. Trügler, MNPBEM - A Matlab toolbox for the simulation of plasmonic nanoparticles, Computer Physics Communications. 183 (2012) 370–381. https://doi.org/10.1016/j.cpc.2011.09.009.

[23] U. Hohenester, Simulating electron energy loss spectroscopy with the MNPBEM toolbox, 2014. https://doi.org/10.1016/j.cpc.2013.12.010.

[24] J. Waxenegger, A. Trügler, U. Hohenester, Plasmonics simulations with the MNPBEM toolbox: Consideration of substrates and layer structures, Computer Physics Communications. 193 (2015) 138–150. https://doi.org/10.1016/j.cpc.2015.03.023.

[25] J.A. Waxenegger, Simulation of plasmonic nanoparticles situated on substrates, 2016.

[26] U. Hohenester, A. Trügler, MNPBEM - A Matlab toolbox for the simulation of plasmonic nanoparticles, Computer Physics Communications. 183 (2012) 370–381. https://doi.org/10.1016/j.cpc.2011.09.009.

[27] B. Foundation, blender.org - Home of the Blender project - Free and Open 3D Creation Software, Blender.Org. (2018). https://doi.org/10.1002/adfm.201304036.

[28] P.B. Johnson, R.W. Christy, Optical Constants of the Nobel Metals, Physical Review B. 6 (1972) 309[29] Z. Li, A. Aranda-Ramos, P. Güell-Grau, J.L. Tajada, L. Pou-Macayo, S. Lope Piedrafita, F. Pi, A. G. Roca, M.D. Baró, J. Sort, C. Nogués, J. Nogués, B. Sepúlveda, Magnetically amplified photothermal therapies and multimodal imaging with magneto-plasmonic nanodomes, Applied Materials Today. 12 (2018) 430–440. https://doi.org/10.1016/j.apmt.2018.07.00

Chapter 7: General conclusions

This PhD Thesis has been focused on complementing the Transmission Electron Microscopy (TEM) characterization of different relevant materials with theoretical ab initio calculations. In this sense, the physical basis of different simulation methods has been presented in Chapter 2: multislice simulation to compute Z- and phase-contrast images, Density Functional Theory (DFT) calculations to compute low loss and core loss Electron Energy Loss Spectra (EELS) and Boundary Element Method (BEM) based simulations to simulate surface plasmons.

The materials science problems solved through these simulations are the analysis of $CuPt_B$ ordering effects in GaInP (Chapter 3), the influence of oxygen vacancies in the EELS of Bi_2O_3 (Chapter 4), the consequences of the Fe_3O_4 Verwey transition in its electronic structure and how it is observed in EELS (Chapter 5) and, finally, the surface plasmon distribution in gold-nanodomes as a function of the dome shape (Chapter 6).

Chapter 3 GaInP: the effect of atomic ordering on the electronic configuration

This chapter revisits the $CuPt_B$ ordering in III-V semiconductors. The study was done on a set of $Ga_{0.5}In_{0.5}P$ samples with different degree of order controlled by the use of a certain amount of Sb flux during the growth.

The samples were characterized by TEM showing changes linked to the order parameter. The $CuPt_B$ ordering was detected by the presence of a double periodicity on the (111) planes viewed along the [110] zone axis, using Hight Resolution TEM (HRTEM), and the satellite spot corresponding to the superstructure noticed on the diffraction pattern. All the samples samples showed Antiphase Boundaries between ordered Domains (APDB). A deep analysis of the APB was performed, showing a clear dependence of the APB extension angle and linear density with the order parameter.

The possibility of having an overlapping of displaced ordered layers which blurred the measurements of ordered regions was verified by atomic image simulations.

The conductivity anisotropy of the sample due to the ordering and to the APBs was experimentally analysed by in situ TEM electrical measurements. The results showed a clear anisotropy of the conductivity/mobility and, in addition, this anisotropy had a dependence with the order parameter.

Finally, DFT calculations of GaInP with and without ordering were performed to determine the effect of In/Ga alternation on its electronic structure. The decrease of energy band gap and extra inter-band transitions were corroborated with Density of States (DOS) and Complex Dielectric Function (CDF) calculations of the ordered structure in comparison with the disordered one. The anisotropy of the effective mass on the ordering direction was verified by the calculation of the band structure along a specific k-path. Thus, the conductivity anisotropy can be attributed to the APB presence, but the contribution of the anisotropic In/Ga alternation cannot be neglected.

Chapter 4: Oxygen Vacancies in Bi_2O_3

In this chapter a set of α-Bi_2O_3 samples in different forms was studied: commercial powder, ceramic-pellet and nanowires. The goal was to check the existence of oxygen vacancies in the nanowires, previously detected by macroscopic measurements, by their fingerprint in EELS, as no data for α-Bi_2O_3 had been previously reported in the bibliography.

HRTEM and HAADF-STEM showed that the nanowires presented a hierarchical structure respect to the big crystals detected on the powder. The good crystallinity of the grains was conserved on the ceramic sample.

Low loss and core loss EEL spectra of the three samples were acquired showing no differences in the low loss region, or in the Bi $M_{4,5}$ edge, but clear differences in the O K edge. The main difference in the fine structure of the O K ELNES between the three samples was in the splitting ratio of the pre-peak and the main peak.

DFT calculations were used to compute the simulations of the low loss and core loss EELS data; in addition, the careful analysis of the CDF and DOS allowed to determine the origin of the spectral features. The DOS showed a bandgap energy in agreement with the experimental one and the energy distribution of the orbitals: the O-2p and the Bi-6p are split between the conduction and valence band while the Bi-6s are located at the conduction band. The oxygen vacancies fingerprint on the O K edge was analysed by computing the edge for different supercells with different concentration of intentional vacancies concluding that a shift to lower energy is induced as the concentration of vacancies increases.

Finally, the possibility of separating the contribution of each individual oxygen atom in the structure to the ELNES was exploited by fitting the experimental spectra with the computed data in order to determine in which oxygen site it is more probable to find oxygen vacancies.

Chapter 5: Understanding the Verwey transition

The analysis of the structural and electronic changes in Fe_3O_4 due to the Verwey transition was tackled in this chapter. The studied sample was composed by 25 nm edge Fe_3O_4 nanocubes. The macroscopic magnetic measurements showed that bellow 125 K of the nanocube magnetic behaviour changes evidencing the Verwey transition. By X-ray diffraction and EELS, the crystalline structure of the room temperature sample was identified as the cubic Fd-3m. Experimentally, the Verwey transition was observed in situ in the TEM by HRTEM and EELS, verifying that structural changes appear as a contrast modulation; below 125 K the structure became monoclinic in agreement with the P2/c structure.

By comparing the Fe L_3 edge at room and low temperature a difference in the ratio of its splitting was detected. DFT calculations of both phases were performed and an in-depth study of the electronic differences between them was carried out. The structural distortion due to the temperature decrease was directly correlated with the changes in the crystal field splitting and from there to the Fe L_3 splitting.

Chapter 6: Plasmonic Nanoparticles: gold nanodomes

The last chapter is centred on the low energy range of the low loss EELS as the goal was to analyse the plasmonic response of gold nanoparticles. The studied nanoparticles presented an exotic shape, out of the conventional spheres, rods or 2D structures: they were nanodomes on top of polystyrene nanoparticles. By experimental low loss EELS, the energy and spatial distribution of the plasmonic response on the gold nanodome was determined. For isolated nanodomes, two main modes were found, one at low energy (1.5 eV) located at the rim and the other at high energy (2.4 eV) on its top. For dimer structures, an extra lower energy (0.8 eV) mode was detected.

BEM calculations were performed in order to correlate the plasmon modes with the nanodome features. For that, three different models of different degree of complexity were built: the idealistic, the realistic and the tomographic, with the result of the tomographic reconstruction of a real nanodome. EEL spectra were computed for all the models showing the benefits of each of them. In addition, the models were intentionally modified to account for size changes, and the response was analysed. The presented approach can be easily applied to the accurate simulation of other physicochemical properties, and to design new functional materials in a more effective way.

Thus, to conclude, along the presented manuscript, the simulations have been presented as an essential tool to complement TEM studies, linkin the experimental results with the most fundamental aspects determined by the structure of the studied materials.

Appendix A: Acronyms and Abbreviations

2D	Two dimensional
3D	Three dimensional
ADF	Annular Dark Field
AE	All-Electron
BCC	Body Centered Cubic
BEM	Boundary Element Method
BF	Bright Field
BZ	Brillouin Zone
CDF	Complex Dielectric Function
CFT	Crystal Field Theory
CL	Cathodoluminescence
CTEM	Conventional Transmission Electron Microscopy
DDA	Discrete Dipole Approximation
DF	Dark Field
DFT	Density Functional Theory
DOS	Density Of States
EDXS	Energy Dispersive X-ray Spectroscopy
EELS	Electron Energy Loss Spectroscopy
ELF	Energy Loss Function
ELNES	Energy Loss Near Edge Structure
FBZ	First Brillouin Zone

FCC	Face Centered Cubic
FDTD	Finite Difference Time Domain approximation
FEM	Finite Elements Method
FFT	Fast Fourier Transform
GGA	Generalized Gradient Approximation
HAADF	High-Angle Annular Dark-field
HF	Hartree-Fock
HRTEM	High Resolution Transmission Electron Microscopy
KS	Kohn-Sham
LAPW	Linearized Augmented Plane Wave
LDA	Local Density Approximation
LSRP	Localized Surface Resonance Plasmons
MBJ	Modified Becke-Johnson
MD	Molecular Dynamics
MNBEM	Metallic Nanoparticles BEM (code)
NW	Nanowire
PAW	Plane Augmented Wave
PBE	Perdew, Burke and Ernzerhof (approximation)
PDOS	Partial Density Of States
PP	PseudoPotential
QE	Quantum Espresso
RPA	Random Phase Approximation
SERS	Surface Enhanced Raman Spectroscopy
SPP	Surface Plasmon Polaritons

STEM	Scanning Transmission Electron Microscopy/e
TEM	Transmission Electron Microscopy/e
UC	Unit Cell
VASP	Vienna Ab initio Simulation Package
XC	Exchange-correlation term
ZLP	Zero loss peak

Appendix B: Complementary information

On the following you will find some complementary information to the main manuscript, such as tables, figures, or clarifications.

B.1 Definitions and concepts

Poisson equation: $\Delta\,\Phi = f$

Helmholth equation/theorem: Fundamental theorem of calculus that states that any sufficient by smooth, rapidly decaying vector field in the three dimensions can be resolved into the sum of an irrotational vector field and a solenoidal (divergence-free) vector field.

The irrotational vector field is a scalar potential and a solenoidal vector field is a vector potential.

$$-\nabla\phi + \nabla\boldsymbol{A}$$

Free electron model: simple model to describe the behavior of charge carriers in a metallic solid. Involves the following assumptions:

- Free electron approximation.
- Independent electron approximation.
- Relaxation time.
- Pauli exclusion principle.

Non-retarded approximation: neglect the delay experienced by the electromagnetic signal that mediates the electron-sample interaction.

Bloch theorem: states that the solution to the Schrödinger equation in a periodic potential takes the form of a plane wave modulated by a periodic function.

Fresnel diffraction: diffraction phenomenon where either of an electron source and an observation point, or both of them, are located at a finite distance from an object, thus the incident wave or exit wave cannot be regarded as a plane wave.

Time dependent Schrödinger equation: describes the system evolving during time.

$$i\hbar\frac{d}{dt}|\,\Psi(t)\rangle = \widehat{H}\,|\Psi(t)\rangle$$

Hartree-Fock method: method of approximation for the determination of the wave function and the energy of a quantum many-body system in a stationary state. It is a self consistency method.

Mott-Bethe formula: approximation used to calculate atomic electron scattering form factors $f_e(q, Z)$, from atomic X-ray scattering form

factors $f_X(q,Z)$. It simply follows from applying the first-order Born approximation for scattering of e^- via Coulomb interaction and Poisson equation for charge density.

Lorentz Gauge condition:

$$\partial_\mu A^\mu \equiv A^\mu_\mu = 0 \rightarrow \nabla A + \frac{1}{c^2}\frac{\partial \varphi}{\partial t}$$

Green function: it is a mathematic function which is used like a lineal integral operator in the resolution of differential non-homogenous equations with boundary conditions.

Boundary condition of Maxwell theory:

- Tangential electric field $\boldsymbol{E}$ is continuous: $\widehat{e_n} \times (\boldsymbol{E_1} - \boldsymbol{E_2}) = 0$
- Discontinuity of the tangential $\boldsymbol{H}$ fields equals the surface current: $\widehat{e_n} \times (\boldsymbol{H_1} - \boldsymbol{H_2}) = \boldsymbol{j_s}$
- Discontinuity of the normal $\boldsymbol{D}$ equals the surface charge density: $\widehat{e_n} \times (\boldsymbol{D_1} - \boldsymbol{D_2}) = \rho_s$
- Normal component of $\boldsymbol{B}$ is continuous: $\widehat{e_n}\,(\boldsymbol{B_1} - \boldsymbol{B_2}) = 0$

Poynting vector: it represents the directional energy flux of an electromagnetic field:

$$\boldsymbol{S} = \boldsymbol{E} \times \boldsymbol{H} = \boldsymbol{E} \times \frac{1}{\mu}\boldsymbol{B}$$

B.2 Crystallographic files

The structural information of known compounds is compiled in publications, and for the most usual compounds their structural data can be extracted from publications from the mid-20th century. In the last decades, several digital databases (open or not) have been created to facilitate the access to all the researchers. In addition, it is important to remark that some normalized formats exist for the structure files, the most common and used one is CIF file[1], however it is not the only one.

.cif	Imported and exported for almost any software. Includes the symmetry information.
.xyz	Used by all the softwares which work with supercells modelling. Does not consider the symmetry operations, all the atomic positions are included.
.CEL	It is specific of CaRIne[7], important as it allows to plot and play with reciprocal lattice. Includes all the symmetry information.
.xsf	Used by xcrysden [4,5], essential on the electronic band calculations and path selection. Includes the symmetry information.

Table B.1 Most used structure files for visualization

The important point regarding the existence of these standard formats is that they are synchronized with the visualization programs. A huge amount of visualization programs exists; however, the most used open ones are VESTA[2,3] and Xcrysden[4,5]. VESTA can import almost any format file and export to all of them, thus apart of being great to check the structure there is the option to transform formats. Each visualization program is oriented towards the requirements of a specific field of research. VESTA is great on visualization, cell transformation and on customizing the representation, and it is compatible with all the operative systems and a huge amount of file formats; however, it cannot help to identify crystal orientations. This should be done with CaRIne, while for k-path selection Xcrysden is essentia. In order to build huge supercells with an specific shape, Rodius from UCA TEM Server[6] is the best option.

VESTA	Visualization	https://jp-minerals.org/vesta/en/download.html
Xcrysden	K-path selection	http://www.xcrysden.org/
Carine	Reciprocal space	http://carine.crystallography.pagesperso-orange.fr/
UCA TEM server	Phase indentification. Modelling	http://temserver.uca.es/global/home/welcome.htm

Table B.2 Packages for structure visualization and modelling

B.3 Space group list

Triclinic	Monoclinic	Orthorombic	Tetragonal
Trigonal	Hexagonal	Cubic	

1	P1	2	P-1	3	P2	4	P21	5	C2
6	Pm	7	Pc	8	Cm	9	Cc	10	P2/m
11	P21/m	12	C2/m	13	P2/c	14	P21/c	15	C2/c
16	P222	17	P2221	18	P21212	19	P212121	20	C2221
21	C222	22	F222	23	I222	24	I212121	25	Pmm2
26	Pmc21	27	Pcc2	28	Pma2	29	Pca21	30	Pnc2
31	Pmn21	32	Pba2	33	Pna21	34	Pnn2	35	Cmm2
36	Cmc21	37	Ccc2	38	Amm2	39	Aem2	40	Ama2
41	Aea2	42	Fmm2	43	Fdd2	44	Imm2	45	Iba2
46	Ima2	47	Pmmm	48	Pnnn	49	Pccm	50	Pban
51	Pmma	52	Pnna	53	Pmna	54	Pcca	55	Pbam
56	Pccn	57	Pbcm	58	Pnnm	59	Pmmn	60	Pbcn
61	Pbca	62	Pnma	63	Cmcm	64	Cmce	65	Cmmm
66	Cccm	67	Cmme	68	Ccce	69	Fmmm	70	Fddd
71	Immm	72	Ibam	73	Ibca	74	Imma	75	P4
76	P41	77	P42	78	P43	79	I4	80	I41
81	P-4	82	I-4	83	P4/m	84	P42/m	85	P4/n
86	P42/n	87	I4/m	88	I41/a	89	P422	90	P4212
91	P4122	92	P41212	93	P4222	94	P42212	95	P4322
96	P43212	97	I422	98	I4122	99	P4mm	100	P4bm
101	P42cm	102	P42nm	103	P4cc	104	P4nc	105	P42mc
106	P42bc	107	I4mm	108	I4cm	109	I41md	110	I41cd
111	P-42m	112	P-42c	113	P-421m	114	P-421c	115	P-4m2
116	P-4c2	117	P-4b2	118	P-4n2	119	I-4m2	120	I-4c2
121	I-42m	122	I-42d	123	P4/mmm	124	P4/mcc	125	P4/nbm
126	P4/nnc	127	P4/mbm	128	P4/mnc	129	P4/nmm	130	P4/ncc
131	P42/mmc	132	P42/mcm	133	P42/nbc	134	P42/nnm	135	P42/mbc
136	P42/mnm	137	P42/nmc	138	P42/ncm	139	I4/mmm	140	I4/mcm
141	I41/amd	142	I41/acd	143	P3	144	P31	145	P32
146	R3	147	P-3	148	R-3	149	P312	150	P321
151	P3112	152	P3121	153	P3212	154	P3221	155	R32
156	P3m1	157	P31m	158	P3c1	159	P31c	160	R3m
161	R3c	162	P-31m	163	P-31c	164	P-3m1	165	P-3c1
166	R-3m	167	R-3c	168	P6	169	P61	170	P65
171	P62	172	P64	173	P63	174	P-6	175	P6/m
176	P63/m	177	P622	178	P6122	179	P6522	180	P6222
181	P6422	182	P6322	183	P6mm	184	P6cc	185	P63cm
186	P63mc	187	P-6m2	188	P-6c2	189	P-62m	190	P-62c
191	P6/mmm	192	P6/mcc	193	P63/mcm	194	P63/mmc	195	P23
196	F23	197	I23	198	P213	199	I213	200	Pm-3
201	Pn-3	202	Fm-3	203	Fd-3	204	Im-3	205	Pa-3
206	Ia-3	207	P432	208	P4232	209	F432	210	F4132
211	I432	212	P4332	213	P4132	214	I4132	215	P-43m
216	F-43m	217	I-43m	218	P-43n	219	F-43c	220	I-43d
221	Pm-3m	222	Pn-3n	223	Pm-3n	224	Pn-3m	225	Fm-3m
226	Fm-3c	227	Fd-3m	228	Fd-3c	229	Im-3m	230	Ia-3d

B.4 References

[1] I.D. Brown, B. McMahon, CIF: The computer language of crystallography, Acta Crystallographica Section B: Structural Science. 58 (2002) 317–324. https://doi.org/10.1107/S0108768102003464.

[2] K. Momma, F. Izumi, VESTA: a three-dimensional visualization system for electronic and structural analysis, Journal of Applied Crystallography. 41 (2008) 653–658. https://doi.org/10.1107/S0021889808012016.

[3] K. Momma, F. Izumi, VESTA 3 for three-dimensional visualization of crystal, volumetric and morphology data, Journal of Applied Crystallography. 44 (2011) 1272–1276. https://doi.org/10.1107/S0021889811038970.

[4] A. Kokalj, XCrySDen-a new program for displaying crystalline structures and electron densities, (2000).

[5] A. Kokalj, Computer graphics and graphical user interfaces as tools in simulations of matter at the atomic scale, Computational Materials Science. 28 (2003) 155–168. https://doi.org/10.1016/S0927-0256(03)00104-6.

[6] J.A. Pérez-Omil, Interpretación sistemática de imágenes de microscopía electrónica de alta resolución de materiales policristalinos. Estudio de catalizadores metálicos soportados.

Appendix C: Scientific Curriculum

C.1 Education

2018-2022	PhD in Physics Universitat de Barcelona
2014-2015	Master's degree in Nanoscience and Nanotechnology Universitat de Bacelona
2009-2014	Bachelor's degree in Physics Universitat de Barcelona

C.2 Grants awarded

2018-2022	Ayudas para contratos predoctorales para la formación de doctores 2017 (FPI-2017). Proyecto: MAT2016-79455-P. Referencia de la ayuda: BES-2017-080045

C.3 Journal publications

Martín, G; Coll, C; López-Conesa, Ll; Rebled, JM, Barrigón, E; García, I; Rey-Stolle, I; Algora, C; Cornet, A; Estradé, S; Peiró, F, Understanding the anisotropy in the electrical conductivity of CuPtB type ordered GaInP thin films by combining in-situ TEM biasing and first principles calculations. **ACS Appl. Electron. Mater.** (*submitted*)

Das, P. P.; Guzzinati, G.; Coll, C.; Pérez, A. G.; Nicolopoulos, S.; Estradé, S.; Peiró, F.; Verbeeck, J.; Zompra, A. A.; Galanis, A. S. Reliable Characterization of Organic & Pharmaceutical Compounds with High

Resolution Monochromated EEL Spectroscopy. **Polymers (Basel).** 2020, 12 (7), 1–11.

Pennington, R. S.; Coll, C.; Estradé, S.; Peiró, F.; Koch, C. T. Neural-Network-Based Depth-Resolved Multiscale Structural Optimization Using Density Functional Theory and Electron Diffraction Data**. Phys. Rev. B** 2018, 97 (2), 1–10.

Coll, C.; López-Conesa, L.; Rebled, J. M.; Magén, C.; Sánchez, F.; Fontcuberta, J.; Estradé, S.; Peiró, F. Simulation of STEM-HAADF Image Contrast of Ruddlesden-Popper Faulted LaNiO3 Thin Films. **J. Phys. Chem. C** 2017, 121 (17).

Torruella, P.; Coll, C.; Martín, G.; López-Conesa, L.; Vila, M.; Díaz-Guerra, C.; Varela, M.; Ruiz-González, M. L.; Piqueras, J.; Peiró, F.; Estradé, S. Assessing Oxygen Vacancies in Bismuth Oxide through EELS Measurements and DFT Simulations. **J. Phys. Chem. C** 2017, 121 (39).

Blanco-Portals, J.; Berestok, T.; Torruella, P.; Coll, C.; López-Conesa, L.; Guardia, P.; Coy, L. E.; Cabot, A.; Estradé, S.; Peiró, F. Atomistic Modelling and High Resolution Electron Microscopy Simulations of CeO2 nanoparticles. **Appl. Phys. Lett**. 2017, 111 (22).

Coll, C.; Barrigón, E.; López-Conesa, L.; Rebled, J.; Barrutia, L.; Rey-Stolle, I.; Estradé, S.; Algora, C.; Peiró, F. The Effect of Sb-Surfactant on GaInP $CuPt_B$ Type Ordering: Assessment through Dark Field TEM and Aberration Corrected HAADF Imaging. **Phys. Chem. Chem. Phys**. 2017, 19 (15), 9806–9810.

C.4 Conference contributions

Coll, C.; Martín, G.; López-Conesa, L.; Rebled, J. M.; Barrigón, E.; García, I.; Rey-Stolle, I.; Algora, C.; Cornet, A.; Estradé, S.; Peiró., F.

Understanding of GaInP Electronic Properties by a Combination of DFT and In-Situ TEM. In **XXXVI Trobades Científiques de la Mediterrània Josep Miquel Vidal «Microscòpies i espectroscòpies: accedint a la nanoescala**; 2021(oral).

Coll, C.; Martín, G.; López-Conesa, L.; Rebled, J. M.; Barrigón, E.; García, I.; Rey-Stolle, I.; Algora, C.; Cornet, A.; Estradé, S.; Peiró, F. DFT and In-Situ TEM for the Understanding of GaInP Electronic Properties. In **Microscopy at the Frontiers of Science**; 2021 (oral).

Coll, C.; López-Conesa, L.; Muro-Cruces, J.; Roca, A. G.; Trushkina, Y.; Salazar-Álvarez, G.; Fernández-Pacheco, R.; Magén, C.; Estradé, S.; Peiró, F.; Nogués, J. Verwey Transition on Iron Oxide Nanocubes Elucidated by Electron Energy Loss Spectroscopy and Density Functional Theory Simulations. In **Microscopy at the Frontiers of Science,** Zaragoza, 2019 (oral).

Coll, C.; Bicket, I.; Sepúlveda, B.; Blanco-Portals, J.; López Haro, M.; Nogués, J.; Botton, G.; Estradé, S.; Peiró, F. EELS Plasmon Mapping of Gold Nanodomes Assessed by BEM Simulations. In **4a Reunión de la red de excelencia imagine**, Cádiz, 2019 (oral).

Coll, C.; López-Conesa Muro-Cruces, J.; Roca, A. G.; Trushkina, Y.; Salazar-Álvarez, G.; Fernández-Pacheco, R.; Magén, C.; Estradé, S.; Peiró, F.; Nogués, J. Combination of Density Functional Theory Simulations and Electron Energy Loss Spectroscopy as a New Way for the Understanding of the Verwey Transition. In **EUROMAT 2019**, Symposium D2 - Analytical transmission electron microscopy,1st - 5th September, Stockholm, Sweden; 2019 (oral).

Coll, C.; Martin, G.; López-Conesa, L.; Barrigón, E.; Barrutia, L.; Rey-Stolle, I.; Algora, C.; Estradé, S.; Peiró, F.; Cornet, A. In-Situ TEM Assessment of the Anisotropic Electrical Conductivity of GaInP CuPt B Type Ordering. In **XV Congreso Nacional de Materiales | I Iberian Meeting on Materials Sicence**; 4-6 July, Salamanca, 2018 (oral).

Torruella, P.; Ruiz-Caridad, A.; Walls, M.; Roca, A. G.; Lopez-Ortega, A.; Blanco-Portals, J.; Lopez-Conesa, L.; Nogues, J.; Peiro, F.; Estrade, S. Determination through EELS of Cation Inversion in Oxide Nanoparticles In **11e edition des Journées EELS 2018** Porquerolles, Francia 11-14, Junio, 2018 (poster).

Coll, C.; Estradé, S.; Peiró, F. Elucidating the Electronic Structure of Complex Compound through DFT+EELS Analysis. In **2a Reunión de la red de excelencia imagine**; 2018 (oral).

Pennington, R. S.; Coll, C.; Estradé, S.; Peiró, F.; Zuo J-M. Shao, Y.-T.; C.T., K. Improved Characterization and Depth-Resolved Structural Optimization of Ferroelectric Materials Using Density Functional Theory and Electron Diffraction Data. In **19th International Microscopy Congress - IMC19**, Session: Instrumentation and Techniques (IT6 - Diffraction techniques), 9-14 Septiembre, 2018 (invited talk).

Coll, C.; Torruella, P.; Martín, G.; López-Conesa, L.; Vila, M.; Díaz-Guerra, C.; Varela, M.; Ruiz-Gonzalez, M. L.; Piqueras, J.; Estradé, S.; Peiró., F. Study of Oxygen Deficient Alpha-Bi_2O_3 Combing EELS + DFT. In **Annual Meeting of the Institute of Nanoscience and Nanotechnology of the UB (IN2UB)**; 2018 (poster).

Peiró F; López-Conesa, J.; Coll, C.; Rebled J.M; Blanco J.; Barrigón E; Barrutia L,; Rey-Stolle, I,; Algora, C,; Magén C.; Sánchez F.; Fontcuberta J.; Berestok T; Torruella P.; Guardia P.; Coy E.; Cabot A.; Estradé S. Some Clues and Misconceptions from High Resolution Scanning-Transmission Electron Microscopy of Advanced Functional Materials. In **Caribbean Conference on Functional Materials (CARIBMAT 2018),** Cartagena de Indias, Colombia, 6th-10th February, 2018 (invited talk).

J.Blanco-Portals; T.Berestok; P.Torruella; C.Coll; L.López-Conesa; P.Guardia; E.Coy; A.Cabot; S.Estradé; F.Peiró. High-Resolution Electron

Microscopy and High-Angle Annular Dark-Field Image Simulation of CeO2 Nanoparticles. In **IN2UB Annual Meeting,** 2018 (poster).

Torruella, P; Coll, C.; Estrader, M.; López-Ortega, A.; Baró, M. D.; Varela, M.; Peiró, F.; Estradé, S. Application of Clustering Analysis to Electron Energy Loss Spectroscopy (EELS). In **11e edition des Journées EELS 2018** Porquerolles, Francia 11-14, Junio, 2018 (oral).

Peiró, F.; López-Conesa, L.; C., C.; Rebled, J.; Barrigón, E.; Barrutia, L.; Rey-Stolled, I.; Algora, C.; Magén, C.; Sánchez, F.; Fontcuberta, J.; Torruella, P.; Estradé, S. Simulations to Avoid Misconceptions from High Resolution Scanning-Transmission Electron Microscopy of Advanced Functional Materials. In **NanoTech Poland International Conference and Exhibition**, Section A: Advanced nanomaterials, Poznań, Poland, 7th - 9th June, 2018 (invited talk).

Coll, C.; Torruella, P.; Martin, G.; López, L.; Vila, M.; Díaz-Guerra, C.; Varela, M.; Ruiz-Gonzalez, M. L.; Piqueras, J.; Estradé, S.; Peiró., F. EELS + DFT on the Study of Oxygen Deficient α-Bi_2O_3. In **19th International Microscopy Congress - IMC19**; 2018 (poster).

Coll, C.; López-Conesa, L.; Rebled, J. M.; Barrigón, E.; Barrutia, L.; Rey-Stolle, I.; Algora, C.; Estradé, S.; Peiró, F. Analysis of $CuPt_B$ Ordering in GaInP Combining Aberration-Corrected Transmission Electron Microscopy and Atomic Simulations. In **Microscopy at Frontiers of Science 2017 (MFS2017),** Zaragoza, 5-8 Septiembre, 2017 (oral).

Blanco-Portals J; Berestok, T.; Torruella, P.; Coll, C.; López-Conesa, L.; Guardia, P.; Coy, E.; Cabot, A.; S., E.; Peiró, F. Atomistic Modelling and High Resolution Electron Microscopy Simulations of CeO2 Octapods. In **Microscopy at Frontiers of Science 2017 (MFS2017),** Zaragoza, 5-8 Septiembre 2017 (oral).

Blanco-Portals J; Berestok, T.; Torruella, P.; Coll, C.; López-Conesa, L.; Guardia, P.; Coy, E.; Cabot, A.; S., E.; Peiró, F. Assessment of Octopod

Morphology of Branched Ceria Nanocrystals. In **5th Nano Today Conference**, Waikola Hawaii, 6-10 December, 2017 (oral).

López-Conesa, L.; Coll, C.; Rebled, J. M.; Pesquera, D.; Dix, N.; Sánchez, F.; Herranz, G.; Fontcuberta, J.; Magén, C.; Casanove, M. J.; Peiró., F.; Estradé, S. Advanced (S)TEM - EELS Characterization of Functional Oxides. In **2017 EMN/CC Barcelona Meeting**; 2017 (oral).

Estradé, S.; Yedra, L.; Eljarrat, A.; López-Conesa, L.; Rebled, J. M.; Torruella, P.; Martín, G.; Coll, C.; Plana, S.; Ruiz-Caridad, A.; Blanco, J.; Peiró, F. My Hovercraft Is Full of EELS: Making the Most of Core-Loss Electron Energy Loss Spectroscopy for Materials Science. In **Microscopy at Frontiers of Science 2017 (MFS2017),** Zaragoza, 5-8 Septiembre 2017 (invited talk).

Torruella, P, Coll, C.; Martín, G.; López-Conesa, L.; Vila, M.; Díaz-Guerra, C.; Varela, M.; Ruiz-González, M. L.; J., P.; Estradé, S.; Peiró, F. EELS as Tool to Assess Microscopic Properties of Bismuth Oxide. In Enhanced Data Generated by Electrons, **8th International Workshop on Electron Energy Loss Spectroscopy and Related Techniques**, Okuma, Okinawa, Japan, May 14th - 19th; 2017 (poster).

Coll, C.; López, L.; Barrigón, E.; Barrutia, L.; Rey-Stolle, I.; Algora, C.; Estradé, S.; Peiró, F. $CuPt_B$ Ordering in GaInP Layers Assessment through Aberration-Corrected TEM HAADF Images and Simulations. In **EUROMAT 2017, European Congress and Exhibition in Advanced Materials and Processes**, Thessaloniki (Grecia), 17-22 Septiembre, 2017 (oral).

Blanco-Portals, J.; Berestok, T.; Torruella-Besa, P.; Coll, C.; López-Conesa, L.; Guardia, P.; Cabot, A.; Estradé, S.; Peiró, F. Elucidation of the Structure of Octapod Branched Ceria Nanocrystals by Transmission Electron Microscopy: Contrast Simulations and Electron Tomography. In **NanoTech Poland International Conference and Exhibition,**

Section A: Preparation and characterization of advanced nanomaterials, Poznań, Poland, 1st - 3rd June 2017 (invited talk).

Torruella, P.; Coll, C.; Martín, G.; López-Conesa, L.; Vila, M.; Díaz-Guerra, C.; Varela, M.; Ruiz-González M.L. Piqueras, J.; Peiró, F.; Estradé. S. EELS Assessment of Oxidation State in Bi_2O_3. In **FFSCI Nanoscience and EMN Croatia Meeting**, Dubrovnik, May 3th-7th, 2017 (invited talk).

Coll Benejam, C. IN2UB Seminar: Clues and Pitfalls of Advanced TEM in Some Materials for Optoelectronics and Energy Applications. In **Seminari IN2UB**; 2017 (oral).

Coll, C.; Torruella, P.; Vila, M.; Díaz-Guerra, C.; Piqueras, J.; Estradé, S.; Peiró, F. DFT Simulations of α-Bi_2O_3 and β-Bi_2O_3 EEL Spectra. In **10ème édition des Journées de l'EELS**, Tarragona, 28-30 June 2016 (oral).

López-Conesa, L; Coll, C; Rebled, J.M.; Magén, C; Sánchez, F; Fontcuberta; J; Estradé, S; Peiró, F. Strain Relaxation Mechanisms in LaNiO3 Thin Films. In **13rd Workshop of IMAGINE, Materials at Sub-Ångstrom resolution, meeting of the Consolider Project** CSD2009-00013, Facultad de Ciencias, Universidad de Cádiz, Cádiz 9-10 de Junio 2016 (oral).

Coll, C.; López-Conesa, L.; Magén, C.; Sanchez, F.; Fontcuberta, J.; Estradé, S.; Peiró, F. Simulation of STEM-HAADF Image Contrast of Ruddlesden Popper Faulted LaNiO3 Thin Films. In **16th European Microscopy Conference (EMC2016)**, 28th August-2nd September Lyon, France, 2016 (poster).

Torruella, P.; Eljarrat, A.; Martín, G.; Rebled, J. M.; López-Conesa, L.; Coll, C.; Ruiz, A.; Plana, S.; Estradé, S.; Peiró, F. EELS Tomography: Recovering the Spectrum Volume from MVA Methods. In **10ème édition des Journées de l'EELS**, Tarragona, 28th 30th June; 2016 (oral).

Coll, C.; Torruella, P.; Vila, M.; Díaz-Guerra, C.; Piqueras, J.; Estradé, S.; Peiró, F. DFT Simulations of α-Bi_2O_3 and β-Bi_2O_3 EEL Spectra. In **13rd Workshop of IMAGINE, Materials at Sub-Ångstrom resolution**, meeting of the Consolider Project CSD2009-00013, Facultad de Ciencias, Universidad de Cádiz, 9-10 de Junio 2016 (oral).

Torruella, P.; Eljarrat, A.; Coll, C.; López-Conesa, L.; Martín, G.; Vila, M.; Díaz-Guerra, C.; Piqueras, J.; Estradé, S.; Peiró, F. Energy Loss Spectroscopy of Bi_2O_3. In **Microscopy at the Frontiers of Science (MFS)**, Oporto, 9-11 Septiembre, 2015 (oral).

Coll, C.; López, L.; Barrigón, E.; Barruita, L., Rey-Stolle, I.; Estradé, S.; Peiró, F. Degree of Ordering as a Function of Sb Content in $In_{0.5}Ga_{0.5}P$ Layers for Tandem Solar Cells. In **10th Spanish Conference on Electron Devices (CDE),** Aranjuez, 11-13 Febrero 2015 (oral).

López-Conesa, L.; Rebled, J. M.; Coll, C.; Barrigón, E.; Rey-Stolle, I.; Estradé, S.; Peiró, F. Effect of Sb Content in the Ordering of $(In_{0.5}Ga_{0.5})P$ Layers for Tandem Solar Cells. In **Microscopy of Semiconducting Materials (MSM-XIX)**; 2015 (oral).

López-Conesa, L.; Rebled, J.; Coll, C.; Barrigón, E.; Barrutia, L.; Rey-Stolle, I.; Estradé, S.; Peiró, F. Control of $CuPt_B$ Ordering in In0.5Ga0.5P Layers for Tandem Solar Cells as a Function of Sb Flux. In **XXIII International Materials Research Conference**, 17-21 Agosto Cancun, Mexico; 2015 (oral).

Coy, L. E.; Graczyk, P.; Coll, C.; Bassas, J. M.; Rodriguez, L.; Mielcarek, S.; Ventura, J.; Ferrater, C.; Polo, M. C.; Estrade, S.; Peiro, F.; Mroz, B.; Varela, M. Thin Films of Multiferroic Gd2(MoO4)3 (Ferroelastic-Ferroelectric) Grown on STO(001) Ans Si(001) by PLD. In **European Materials Research Society Fall Meeting, 2015 Fall Meeting**, Symposium J, Ferroic perovskites for advanced materials - Materials for

electronics and optoelectronic applications away from silicon, Warsaw 15th-18th September, 2015 (oral).

C.5 Research Stage

McMaster University – CCEM (Canada)
Under the supervision of Prof. Gianluigi Botton
January 2018 – April 2018

C.6 Workshops and schools

2019 August	WIEN2k - WORKSHOP - DFT based simulations of solids with the WIEN2k code
Austria	TU Wien
2018 May	Workshop: High Performance Computing for Next Generation Nanomaterials & Nanodevice Enginering
Spain	Institut Català de Nanociència i Nanotecnologia (ICN2)
2017 June	CCEM Summer School on Electron Microscopy
Canada	McMaster University –Canadian Center for Electron Microsocpy
2017 May	QEM2017 Quantitative Electron Microscopy
France	CEMES-CNRS
2016 July	European Summer Workshop: Transmission Electron Microscopy of Nanomaterials (TEM-UCA 2016)
Spain	Universidad de Cadiz
2016 July	Curso microscopía electrónica de transmisión: más allá de la frontera de la resolución atómica
Spain	Universidad Complutense de Madrid

C.7 Supervision of research projects

2016	Characterization of crystallographic defects in LaNiO3 through TEM image simulations (Treball Final de Grau del Grau en Física)	Joan Carles Bastons
2017	Simulation study of crystalline Bi_2O_3 (Treball Final de Grau del Grau en Física)	Adrià Bonet
2019	Characterization by HRTEM of plasmonic nanoparticles (Treball Final de Grau del Grau en Física)	Marta Oliva
2019	Crystallographic characterization of a BFMO layer grown on STO through HRTEM imaging and simulation (Treball Final de Grau del Grau en Física)	Nikolas Deco
2020	Moiré pattern identification in gold nanoparticle-topped silicon nanowires by HRTEM (Treball Final de Grau del Grau en Física)	Silvia Alzina

Appendix D: Resum en català

La microscòpia electrònica de transmissió (TEM), des de la seva implementació per Ernst August Friedrich Ruska i Max Knoll el 1931, ha estat una tècnica essencial en el camp de la nanociència i la nanotecnologia. Al principi, la resolució real era només una petita fracció de la resolució potencial esperada pel fet d'utilitzar electrons com a font de "llum". La longitud d'ona dels electrons accelerats a centenars d'electró-volts havia de suposar una resolució subatòmica; tanmateix, totes les aberracions relacionades amb les lents electromagnètiques provocaven una disminució dramàtica d'aquesta. A més, la resolució energètica estava molt afectada per l'aberració cromàtica del feix d'electrons. Actualment, tots aquests problemes inicials s'han resolt amb el desenvolupament dels correctors d'aberració esfèrica de les lents i els monocromadors. Des que la resolució atòmica, juntament amb la resolució energètica de 10 meV, són una realitat per als investigadors, s'han establert nous i ambiciosos horitzons per a la microscòpia electrònica de transmissió, com l'obtenció d'imatges dels orbitals electrònics[1], l'obtenció d'imatge de la distribució de fonons[2], o el monitoratge d'àtoms en temps real[3] entre d'altres.

La TEM es podria descriure en el seu aspecte més fonamental com l'anàlisi del resultat de l'impacte dels electrons amb un compost o una estructura específica[4]. A partir d'aquest impacte, es poden obtenir diferents dades ràpidament classificables entre imatge i espectroscòpia.

Hi ha tres modes principals d'operació que produeixen com a resultat una imatge: contrast de fase, contrast de nombre atòmic i contrast de difracció. El primer, el mode de contrast de fase, recull la imatge generada per la interferència dels feixos difractats per la interacció del feix paral·lel d'electrons amb la mostra cristal·lina, a causa de la dispersió elàstica coherent. El tipus més comú d'imatge generada és la imatge d'alta resolució (HRTEM). La segona en ordre d'importància és la imatge de contrast de nombre atòmic. Quan un feix d'electrons altament focalitzat incideix sobre la mostra, aquests electrons són dispersats incoherentment i recollits per un detector anular; a cada píxel de la imatge final, formada a mesura que el

feix rastreja la mostra, la intensitat és aproximadament proporcional al quadrat del número atòmic dels àtoms presents en aquell punt. Les imatges de camp fosc anul·lar (ADF) i de camp fosc anul·lar d'alt angle (HAADF), segons el diàmetre del detector, són les imatges de contrast Z comuns. D'altra banda, les imatges de contrast de difracció són les que es formen degut a la difracció coherent que té lloc només per a orientacions cristal·logràfiques concretes i que s'obtenen seleccionant punts de difracció específics per formar la imatge; les més comunes són les imatges de camp clar (BF) i les de camp fosc (DF), depenent de si inclouen o no el feix directe; tanmateix, es pot fer servir una configuració més específica com les condicions de dos feixos quan es considera només una reflexió excitada.

Pel que fa a les tècniques espectroscòpies associades a la TEM, encara que es poden instal·lar diversos detectors a la columna per realitzar anàlisis de raigs X d'energia dispersiva (EDX) o de catodoluminescència (CL), l'Espectroscòpia de Pèrdua d'Energia dels Electrons (EELS) és la tècnica espectral amb millor resolució energètica i espacial que es pot fer dins de la columna del TEM[5]. L'EELS consisteix en analitzar el nombre d'electrons que han perdut una quantitat d'energia determinada, és a dir, el nombre d'electrons per canal d'energia. Quan la mostra és irradiada amb el feix d'electrons, la majoria dels electrons la travessen sense perdre energia, originant el Pic de Zero Pèrdues (ZLP), mentre els altres han perdut part de la seva energia. Així, l'EELS està fortament correlacionat amb els electrons que han patit dispersió inelàstica; no obstant, no és totalment independent de la dispersió elàstica.

L'espectre EEL cobreix tot el rang de pèrdues d'energia, des de 0 eV fins a milers d'electró-volts. En funció del rang d'energia es poden distingir les regions de baixes pèrdues i de pèrdues profundes; com es pot entendre fàcilment, les baixes pèrdues corresponen a les pèrdues de baixa energia, des de zero fins a uns 80 eV, i les pèrdues profundes d'energia a la resta de l'espectre. Tanmateix, la diferència entre les baixes pèrdues i les pèrdues profundes rau en la informació que contenen; a baixes energies la dispersió inelàstica degut a la interacció amb els electrons de la capa externa és la principal contribució, mentre que a pèrdues de més energia la seva contribució disminueix i, els pics d'ionització dels electrons de la capa interna apareixen com les característiques més destacables. Els pics

d'ionització són una empremta dels elements presents a la mostra analitzada, i l'estructura de pèrdua d'energia dels electrons a prop dels pics (ELNES) conté la informació corresponent a l'estat d'oxidació i a la configuració orbital.

Gràcies a les últimes millores en la resolució energètica i espacial, es pot extreure directament des de l'espectre adquirit una gran quantitat d'informació i un conjunt de dades experimentals molt gran; no obstant això, per a una comprensió més profunda, la majoria de les vegades també es necessita el suport dels càlculs teòrics[6,7]. La física de l'estat sòlid, amb consideracions quàntiques, pot contribuir a una descripció precisa dels sistemes estudiats.

Mentre que en el passat, la ciència dels materials, la física de l'estat sòlid, la mecànica quàntica i la química eren disciplines molt separades, avui dia es fusionen en el camp de la nanociència i la nanotecnologia. Quan la mida de l'objecte es redueix a la nanoescala, els efectes quàntics ja no es poden menysprear, ja que qualsevol canvi en la síntesi pot modificar alhora l'estructura, que exerceix un paper essencial en les propietats del compost[8].

Així, la modelització s'ha convertit en un pas essencial en la síntesi i la caracterització de materials. El coneixement de l'estructura permet calcular la interacció dels electrons amb qualsevol estructura cristal·lina ben descrita i generar imatges i espectres comparables amb les dades experimentals, però no només com a comprovació, sinó per obtenir-ne una visió més profunda. La interacció dels electrons amb la matèria s'ha de calcular resolent l'equació de Schrödinger dels electrons que interactuen amb la mostra[9–11]. La mostra, el sistema, es pot considerar com un potencial periòdic.

L'obtenció d'imatges, el mesurament, el modelatge i la manipulació de la matèria són la base del prometedor camp de la nanociència, i es poden dur a terme utilitzant un TEM, però no sense el suport continu dels càlculs teòrics.

Aquesta tesi doctoral utilitza tres tipus principals de càlculs per interpretar les dades del TEM: simulacions atòmiques aplicades a l'obtenció d'imatges, càlculs basats en el mètode d'elements de contorn (BEM) per a les distribucions de plasmons superficials i la teoria del funcional de la densitat (DFT) per a l'anàlisi d'EELS. Tot i que es presentin per separat,

no són independents; l'essència sempre és la mateixa, però depenent dels resultats desitjats es necessiten diferents consideracions.

Les simulacions atòmiques apareixen com a solució per obtenir imatges comparables amb les dades del TEM. En les simulacions atòmiques la mostra es modela com un potencial periòdic determinat pel potencial atòmic de cada element de la mostra, calculat mitjançant DFT. Els resultats s'obtenen per la interacció entre els electrons, l'ona plana, i el potencial periòdic de la mostra. El mètode més utilitzat per simplificar el problema és el mètode multi-llesca, el multislice.

Els càlculs basats en DFT són els més utilitzats per resoldre problemes de molts cossos. El DFT simplifica el problema trobant la densitat d'electrons de tot el sistema en lloc de treballar amb cada electró individualment. Aleshores, una vegada trobada la densitat electrònica, s'obté directament l'estructura electrònica del compost i es poden calcular les propietats optoelectròniques per comparar-les amb les dades experimentals. Així, els càlculs teòrics permeten aprofundir en la configuració electrònica a més de generar dades de referència per comparar-les amb les experimentals.

El BEM, en lloc de considerar la mostra com una disposició atòmica, defineix els límits del nanoobjecte, la resposta plasmònica del qual es vol estudiar, en el nostre cas. Utilitzant la funció dielèctrica dels diferents materials implicats, obtinguda a partir de DFT o experimentalment, el model queda perfectament definit. La resposta plasmònica es troba resolent les equacions de Maxwell del sistema definit.

Tot i això, la lògica essencial de tots aquests procediments computacionals és la mateixa, la "mostra" (el compost d'interès) es modela utilitzant descripcions de la disposició atòmica o dels límits, el feix d'electrons es descriu segons les condicions experimentals en què s' ha realitzat l'experiment i, finalment, s'introdueix la física dels problemes de molts cossos. L'observable que cal simular determinarà la precisió en la formulació dels càlculs.

Aquesta Tesi Doctoral s'ha centrat en la realització de càlculs teòrics que permetin comprendre i extreure la major quantitat d'informació possible de les dades experimentals de TEM, i de les tècniques espectroscòpiques relacionades, concretament, l'espectroscòpia EELS. En aquest sentit, al

Capítol 2 s'han presentat les bases físiques de diferents mètodes de simulació: simulació multislice per calcular imatges de contrast Z i de contrast de fase, càlculs (DFT) per calcular dades EELS de baixa pèrdua i de pèrdues profundes i, simulacions basades en BEM per a plasmons de superfície.

Els problemes de la ciència dels materials resolts mitjançant aquest tipus de simulacions són l'anàlisi dels efectes d'ordenació tipus $CuPt_B$ al GaInP (Capítol 3), la influència de les vacants d'oxigen a l'EELS del Bi_2O_3 (Capítol 4), les conseqüències de la transició Verwey del Fe_3O_4 en la seva estructura electrònica i com s'observa a l'EELS (Capítol 5) i, finalment, la distribució de plasmons superficials als nanodomes d'or en funció de la forma de la cúpula (Capítol 6).

Capítol 3 GaInP: l'efecte de l'ordenament atòmic a la configuració electrònica.

Aquest capítol revisa l'ordenament $CuPt_B$ en semiconductors III-V. L'estudi es va realitzar sobre un conjunt de mostres de $Ga_{0.5}In_{0.5}P$ amb diferent grau d'ordenació controlat per l'ús de diferents quantitats de flux de Sb.

Tot el conjunt de mostres es va caracteritzar per TEM mostrant canvis lligats al paràmetre d'ordre. L'ordenament del $CuPt_B$ es va detectar per la presència d'una doble periodicitat als plans (111) vistos al llarg de l'eix de la zona [110], utilitzant TEM d'alta resolució (HRTEM), i per la presència d'un punt satèl·lit corresponent a la superestructura al patró de difracció. Tot el conjunt de mostres mostrava fronteres de separació (APBD) entre els dominis ordenats. Es va fer una anàlisi en profunditat dels APBD, mostrant una dependència clara de l'angle d'extensió dels APBD i de la densitat lineal amb el paràmetre d'ordre.

La possibilitat que es produeixi un solapament de les capes ordenades desplaçades que podria desdibuixar les mesures de les regions ordenades es va verificar mitjançant simulacions d'imatge amb resolució atòmica.

L'anisotropia de la conductivitat de la mostra deguda a l'ordenament i a les APBDs es va analitzar experimentalment mitjançant mesuraments elèctrics TEM in situ. Els resultats van mostrar una anisotropia clara de la

conductivitat/mobilitat i, a més, aquesta anisotropia tenia una dependència amb el paràmetre d'ordre.

Finalment, es van realitzar càlculs DFT del GaInP amb i sense ordre per determinar l'efecte de l'alternança In/Ga en la seva estructura electrònica. La disminució de la banda d'energia prohibida i les transicions interbandes addicionals es van corroborar amb els càlculs de densitat d'estats (DOS) i la funció dielèctrica complexa (CDF) de l'estructura ordenada en comparació amb la desordenada. L'anisotropia de la massa efectiva a la direcció d'ordenació es va verificar mitjançant el càlcul de l'estructura de bandes al llarg d'una trajectòria k específica. Així, l'anisotropia de la conductivitat es va poder atribuir a la presència de l'APBD, sense menystenir la contribució de l'alternança In/Ga a la anisotropia de la massa efectiva.

Capítol 4: Vacants d'oxigen en Bi_2O_3.

En aquest capítol es va estudiar un conjunt de mostres de α-Bi_2O_3 en diferents formes: pols comercial, ceràmica-pellet i nanofils. L'objectiu era comprovar la presència de vacants d'oxigen als nanofils, prèviament detectades per mesures macroscòpiques, mitjançant la seva empremta digital a l'EELS, ja que no existien dades per a α-Bi_2O_3 a la bibliografia.

HRTEM i HAADF-STEM van mostrar que els nanofils presentaven una estructura jeràrquica respecte als cristalls grossos detectats a la pols, conservant-se la bona cristal·linitat dels grans a la mostra ceràmica.

Es van adquirir els espectres EEL de baixes pèrdues i de pèrdues profundes de les tres mostres, que no van mostrar diferències a la regió de baixes pèrdues, ni a la vora del Bi $M_{4,5}$, però sí a la vora d'O K. La diferència entre les tres formes d'ELNES d'O K radicava en la relació de d'intensitats entre el pre-pic i el pic principal.

Es van utilitzar càlculs DFT per calcular les simulacions de les dades EELS de baixa pèrdua i de pèrdues profundes; a més, un anàlisi detallat de la CDF i la DOS va permetre determinar l'origen de les característiques espectrals. La DOS va mostrar una energia de banda prohibida que concorda amb l'experimental i la distribució energètica dels orbitals: l'O-2p i el Bi-6p, es divideixen entre la banda de conducció i la de valència, mentre que

el Bi-6s es situa a la banda de conducció. La petjada de les vacants d'oxigen a la vora d'O K es va analitzar calculant la vora per a diferents supercel·les amb diferents concentracions de vacants, concloent que les vacants indueixen un desplaçament cap a una energia més baixa.

Finalment, es va explotar la possibilitat de separar la contribució de cada àtom d'oxigen individual a l'estructura a l'ELNES ajustant els espectres experimentals amb les dades computades per determinar en quina de les possibles posicions de l'oxigen era més probable trobar vacants.

Capítol 5: Comprensió de la transició de Verwey.

En aquest capítol s'aborda l'anàlisi dels canvis estructurals i electrònics al Fe_3O_4 deguts a la transició de Verwey. La mostra estudiada estava composta per nanocubs de Fe_3O_4 de 25 nm de aresta. Les mesures magnètiques macroscòpiques van mostrar que per sota de 125 K el comportament magnètic dels nanocubs canvia evidenciant la transició de Verwey. Mitjançant difracció de raigs X i EELS es va identificar l'estructura cristal·lina de la mostra a temperatura ambient com cúbica, Fd-3m. Experimentalment, la transició de Verwey es va observar in situ al TEM mitjançant HRTEM i EELS, verificant que els canvis estructurals apareixen com una modulació de contrast i, que per sota de 125 K l'estructura es torna monoclínica, compatible amb l'estructura P2/c.

Comparant la vora del Fe L_3 a temperatura ambient i a baixa temperatura es va detectar una diferència en la relació del desdoblament. Es van fer càlculs DFT de les dues fases i es van estudiar en profunditat les diferències electròniques entre elles. La distorsió estructural deguda a la disminució de la temperatura es va correlacionar directament amb els canvis en el desdoblament del camp cristal·lí i per això al desdoblament del Fe L_3.

Capítol 6: Nanopartícules plasmòniques: nanodomes d'or.

El darrer capítol es centra en el rang de baixa energia de l'EELS de baixes pèrdues, ja que l'objectiu era analitzar la resposta plasmònica de les nanopartícules d'or. Les nanopartícules estudiades presentaven una forma exòtica, fora de les convencionals esferes, varetes o estructures 2D: eren

nanodomes d'or sobre nanopartícules de poliestirè. Mitjançant EELS experimental de baixes pèrdues es va determinar l'energia i la distribució espacial de la resposta plasmònica de les nanodomes d'or. Per a les nanodomes aïllades, es van trobar dos modes principals, un de baixa energia (1,5 eV) situat a la vora i un altre d'alta energia (2,4 eV) a la part superior. En el cas de les estructures en forma de doblet (dues nanodomes enganxades per un dels extrems), es va detectar un mode addicional de menor energia (0,8 eV).

Es van realitzar càlculs BEM per correlacionar els modes plasmònics amb les característiques de les nanodomes. Per fer-ho, es van construir tres models diferents de diferent grau de complexitat: l'ideal, el realista i el tomogràfic, amb el resultat de la reconstrucció tomogràfica d'una nanodoma real. Es van calcular els espectres d'EEL per a tots els models mostrant els avantatges de cadascun. A més, es van deformar els models i es va analitzar la resposta: per exemple, el pic de baixa energia es desplaça a una energia més baixa a mesura que augmenta el diàmetre, mentre que el pic d'alta energia no es desplaça. L'enfoc presentat es pot aplicar fàcilment a la simulació precisa d'altres propietats fisicoquímiques i al disseny de nous materials funcionals de manera més eficaç.

A mode de conclusió, al llarg del manuscrit presentat les simulacions han demostrat ser una eina essencial per complementar els estudis de TEM, per vincular els resultats experimentals amb els aspectes més fonamentals determinats per l'estructura dels materials estudiats.

[1] L. Pardini, S. Löffler, G. Biddau, R. Hambach, U. Kaiser, C. Draxl, P. Schattschneider, Mapping Atomic Orbitals with the Transmission Electron Microscope: Images of Defective Graphene Predicted from First-Principles Theory, (2016). https://doi.org/10.1103/PhysRevLett.117.036801.

[2] R. Qi, N. Li, J. Du, R. Shi, Y. Huang, X. Yang, L. Liu, Z. Xu, Q. Dai, D. Yu, P. Gao, Four-dimensional vibrational spectroscopy for nanoscale mapping of phonon dispersion in BN nanotubes, Nature Communications. 12 (2021). https://doi.org/10.1038/s41467-021-21452-5.

[3] R. Manzorro, Y. Xu, J. Vincent, R. Rivera, D. Matteson, P. Crozier, Atom Detection in Time-resolved TEM Image Series: Application of Computer Vision Techniques to Noise-degraded Frames, Microsc. Microanal. 27 (2021). https://doi.org/10.1017/S1431927621008011.

[4] D.B. Williams, C.B. Carter, Transmission Electron Microscopy: A Textbook for Materials Science, 2009. https://doi.org/10.1007/978-1-61779-415-5_23.

[5] R.F. Egerton, Electron Energy-Loss Spectroscopy in the Electron Microscope, 2016. https://doi.org/10.1093/acprof:oso/9780198716525.003.0015.

[6] P.E. Batson, N. Dellby, O.L. Krivanek, Sub-angstrom resolution using aberration corrected electron optics, Nature. 418 (2002) 617–620. https://doi.org/10.1093/oxfordjournals.jmicro.a050032.

[7] M. Haider, S. Uhlemann, E. Schwan, H. Rose, B. Kabius, K. Urban, Electron microscopy image enhanced, Nature. 392 (1998) 768–769.

[8] R.P. Feynman, There's Plenty of Room at the Bottom, XXIII (1960).

[9] J.G. Lee, Computational Materials Science, 2017. https://doi.org/10.1016/s1380-7323(04)80014-1.

[10] E.J. Kirkland, Advanced Computing in Electron Microscopy, 2010. https://doi.org/10.1088/1751-8113/44/8/085201.

[11] Earl J. Kirkland, Advanced Computing in Electron Microscopy, 1998.